

**STRUCTURAL ANALYSIS AND OPTIMIZATION OF AIRCRAFT WINGS
THROUGH DIMENSIONAL REDUCTION**

A Dissertation
Presented to
The Academic Faculty

By

Darshan Sarojini

In Partial Fulfillment
of the Requirements for the Degree
Doctor of Philosophy in the
School of Aerospace Engineering

Georgia Institute of Technology

May 2021

Copyright © Darshan Sarojini 2021

**STRUCTURAL ANALYSIS AND OPTIMIZATION OF AIRCRAFT WINGS
THROUGH DIMENSIONAL REDUCTION**

Approved by:

Professor Dimitri N. Mavris
School of Aerospace Engineering
Georgia Institute of Technology

Dr. Jason A. Corman
School of Aerospace Engineering
Georgia Institute of Technology

Professor Dewey H. Hodges
School of Aerospace Engineering
Georgia Institute of Technology

Mr. Robert W. Martin
Aircraft Certification Office (ACO)
Federal Aviation Administration

Professor Graeme J. Kennedy
School of Aerospace Engineering
Georgia Institute of Technology

Date Approved: March 10th, 2021

Science is a way of thinking much more than it is a body of knowledge

Carl Sagan

Dedicated to my late grandparents, Murigeppa and Sushila Sheshgiri

ACKNOWLEDGEMENTS

It has been a truly wonderful experience pursuing a Ph.D. degree at Georgia Tech. I would like to express my sincere gratitude to my professors, colleagues, and friends, without whom this journey would not be possible.

Firstly, I would like to express my gratitude toward my advisor, Dr. Dimitri Mavris. Dr. Mavris created a lab environment conducive to exploring projects on different topics. Dr. Mavris' mentoring has profoundly impacted my way of thinking about a given problem and conducting research. He has always been supportive of all my endeavors and pushed me out of my academic comfort zone. Thank you, Dr. Mavris.

Secondly, I would like to acknowledge and thank my thesis committee members – Dr. Dewey Hodges, Dr. Graeme Kennedy, Dr. Jason Corman, and Mr. Robert Martin. The feedback and suggestions offered by the committee have helped improve the quality of my thesis. Dr. Hodges, thank you for always being available to talk to throughout my Ph.D. journey. You provided me new directions I could explore when I was stuck in my research, and my interactions with you have helped shape my career outlook. Dr. Kennedy, the structural optimization class taught by you was instrumental in exposing me to the fundamentals I heavily relied on while working on this thesis. Your guidance and advice immensely helped me execute the thesis and shortened the time I would have otherwise needed to complete it. Dr. Corman, working with you closely through the various projects has been a wonderful experience. I am delighted to have worked with a mentor whom I could reach out to at any time and willing to help debug a problem for hours till it worked. Demonstrating my work on realistic problems would not have been possible without the RADE toolkit, which you have spearheaded and developed into a powerful aircraft design tool. Mr. Martin, working on projects with you was my first exposure to aeroelasticity, flight dynamics, and loads. Your mentoring helped me appreciate the complexity of aircraft design, how certification requirements play a vital role, and how to tackle such a complex

problem.

I am proud to have been a part of the Aerospace Systems Design Lab. I want to thank all the students and research engineers at ASDL. Working on different topics and collaborating with people from all around the world has been an enriching experience. I would particularly like to thank David Solano, Dushhyanth Rajaram, Evanthia Kallou, Christian Perron, Manish Pohkrel, Aroua Gharbi, Ruxandra Duca, Mayank Bendarkar, Evan Harrison, Burak Bagdatli, and Jimmy Tai.

I am thankful for all the close friendships, both new friends I made here, and my friends from Belgaum and Bangalore. A Ph.D. journey is not an easy one, and there were times when it was overwhelming. The support of my friends helped me through the difficult times and made this journey a fun one. I want to give a shout-out to the ASHA Atlanta chapter that has been one of my non-academic life highlights at Georgia Tech.

Finally, I would like to thank my family. My late grandparents Murigeppa and Sushila Sheshgiri, are why I am here today and whom I miss dearly. My father, Gurappa Shetty, has been a constant source of encouragement and love.

TABLE OF CONTENTS

Acknowledgments	v
List of Tables	xiii
List of Figures	xvi
List of Acronyms	xxii
Chapter 1: Motivation	1
1.1 Introduction	1
1.1.1 Aircraft Certification	1
1.1.2 Certification-By-Analysis	2
1.1.3 Certification-Driven Virtual Design	3
1.1.4 Chapter Outline	6
1.2 Simulation-Based Early-Stage Aircraft Design	6
1.3 Challenges in Simulation-Based Early-Stage Aircraft Design	9
1.4 Summary	10
1.5 Document Outline	12
Chapter 2: Background and Literature Review	14
2.1 Physical Decomposition of the Internal Structure of Aircraft Wings	14

2.1.1	Smearing of Stiffeners	16
2.1.2	Summary	17
2.2	Computation of Dynamic Loads	17
2.2.1	Example 14 CFR Manuever: 14 CFR 25.331(c)(2)	18
2.2.2	Rigid Structure Assumption	20
2.2.3	Stickmodel approach	24
2.2.4	Beam Model Generation	27
2.2.5	Modal approach	29
2.2.6	Higher-fidelity methods	31
2.2.7	Critical load determination	32
2.2.8	Summary	34
2.3	Aircraft Wings Structural Analysis Methods	34
2.3.1	Beam Theories for Structural Analysis	37
2.3.2	1-D Analysis Beam Theories	39
2.3.3	Structural Failure Theories	43
2.3.4	Summary	44
2.4	Multi-Disciplinary Design Optimization (MDO)	45
2.4.1	Constraint Aggregation Techniques	47
2.4.2	Adjoint	49
2.4.3	Summary	51
2.5	Summary of Literature Review	51
Chapter 3: Proposed Method		53

3.1	Reduction of 3-D Features to 2-D	54
3.2	Reduction of 3-D Wingbox to 1-D	57
3.3	1-D Analysis	59
3.4	1-D solution to 3-D fields	65
3.5	Structural Optimization for Dynamic Loads	65
3.5.1	Design Variables	66
3.5.2	Adjoint for Dynamic Simulations	66
3.6	Summary of Proposed Approach	70
3.7	Experimental Plan	71
Chapter 4: Research Questions and Hypothesis Testing		76
4.1	RQ 1.1 – 3-D Feature to 2-D	76
4.1.1	Challenges in Stiffness Matching	79
4.1.2	Stiffness Matching using Orthotropic Materials	80
4.1.3	Experiment for Hypothesis 1.1	84
4.1.4	Results	86
4.1.5	Summary	90
4.2	RQ 1.2 – 3-D Wingbox to 1-D	92
4.2.1	Information from 3-D Geometry	93
4.2.2	VABS for Cross-Sectional Analysis	93
4.2.3	Limitation of using VABS for Sizing	97
4.2.4	Rectangular Box Wingbox	98
4.2.5	Experiments: Cross-Section Properties Computation and Stiffness Matching	101

4.3	RQ 1.3 – 1-D Analysis	104
4.3.1	Influence of Ribs on the Structural Response of the Wingbox	105
4.3.2	Experiment: Displacement Comparison to Shell Model	110
4.4	RQ 1.4 – 3-D Stress/Strain Recovery	112
4.4.1	Experiment: Stress Comparison to Higher-Fidelity Methods	113
4.4.2	Stress Recovery for Box Cross-Sections	115
4.5	Structural Analysis Computation Time	124
4.6	RQ 2.1 – Gradient with Adjoint Method	127
4.6.1	Illustration on Spring-Mass-Damper System	129
4.6.2	Gradient of a Solid Beam subjected to Axial Stress	131
4.6.3	Gradient of a Box-Beam using Automatic Differentiation	136
4.6.4	Summary	138
4.7	RQ 2.2 – Structural Optimization	139
4.7.1	Optimization of a Solid Rectangular Cantilever Beam	139
4.7.2	Optimization of a Box-Beam ‘Wing-Like’ Structure	142
	Chapter 5: Application	152
5.1	Static Load Optimization	155
5.2	Dynamic Load Optimization	158
5.2.1	Gust Simulation	159
5.2.2	Optimization	161
	Chapter 6: Summary	163

Chapter 7: Concluding Remarks	175
7.1 Limitations and Future Work	175
7.1.1 Applicability of Beam Theory	175
7.1.2 Aero-Servo Elastic MDAO	176
7.1.3 Ribs in the Wingbox	178
7.1.4 Additional Experiments to Validate the Method	182
7.2 Conclusions	183
Appendix A: Nonlinear Timoshenko Beam Theory	185
A.1 Definitions of Matrices	185
A.2 Residual System of Equations	189
Appendix B: Rapid Airframe Design Environment (RADE)	195
Appendix C: Variational Asymptotic Method (VAM)	202
C.1 Cross-Sectional Analysis using VAM	202
C.1.1 First-Order Analysis	212
C.2 1-D Beam Analysis with GEBT	217
Appendix D: Description of Test Case Geometries	219
D.1 ‘Wing-Like’ Box Beam	219
D.2 PEGASUS Concept Aircraft	222
D.3 Common Research Model (CRM) Aircraft	226
Appendix E: 1-D Analysis Implementation Verification and Validation	228

E.1	Comparison to known Analytical Formulae	228
E.2	Representative Business Jet	228
E.3	‘Wing-Like’ Box Beam	229
Appendix F: Cross-Sectional Properties of a Box-Beam		232
F.1	Objective Function	232
F.2	Box-Beam Cross-Sectional Properties Computation	232
Appendix G: Gradient of Stress Constraints using Symbolic Differentiation . .		237
References		260
Vita		262

LIST OF TABLES

1.1	FAA certification cost estimates	2
1.2	FAA certification timelines	3
2.1	Rib design morphological matrix	16
2.2	Methods used in the literature for aerodynamics and structural dynamics . .	32
2.3	Quantities tracked by the nonlinear Timoshenko beam theory	40
2.4	Quantities tracked by GEBT	42
3.1	Workstation configuration for all experiments	73
4.1	Stiffness values for a rectangular section	79
4.2	Stiffness values for a square section	79
4.3	Variable bounds used to match S_{44} in gradient-based optimization	84
4.4	Variable bounds used to match S_{44} and S_{22} in gradient-based optimization .	84
4.5	Dimensions of plate	85
4.6	Dimensions of single stiffener cases	85
4.7	Dimensions of two stiffeners case	86
4.8	Loading Conditions	87
4.9	PEGASUS root rib stiffness matrix	102
4.10	PEGASUS tip rib stiffness matrix	102

4.11	Static sizing of components of PEGASUS wing subjected to 1g loads. All masses in lbs	109
4.12	Static sizing of components of CRM wing subjected to 1g loads. All weights in lbs	110
4.13	Comparison of displacement and stress response of the geometry seen in Fig. D.2e	115
4.14	3-D geometry, aerodynamics and shell model execution time	125
4.15	VbS model execution time	126
4.16	Box cross-section beam model execution time	127
4.17	BbcVS model execution time	128
4.18	SMD parameters	130
4.19	SMD adjoint results	131
4.20	Gradient comparison between adjoint method and central differences (step-size: 1×10^{-8}) for 20 design variables for stress aggregated constraint $c_{1,KS}$	135
4.21	Comparison of time (in seconds) to compute the gradient between finite-difference and adjoint method	136
4.22	Gradient comparison between adjoint method and central differences (step-size: 1×10^{-8}) for 16 design variables for von-Mises stress aggregated constraint $c_{vm,KS}$	138
4.23	Parameters used for solid rectangular cross-section optimization studies	141
4.24	Optimization results for different initial guesses	142
4.25	Comparison of structural sizing for static and dynamic loads	142
4.26	Comparison of structural sizing for different constraints	149
4.27	Comparison of structural sizing for static and dynamic analysis	150
4.28	Breakdown of computation time (in seconds) of dynamic solver	150
5.1	Design variables for optimization of PEGASUS wing	157

5.2	Weight and computational time comparison for static sizing	158
5.3	Gust simulation settings	160
5.4	Weight and computational time comparison for static sizing	162
6.1	Quantities required for adjoint solver	172
D.1	Dimensions held constant for all five geometries shown in Fig. D.2	222
D.2	Dimensions varied for the five geometries shown in Fig. D.2	222
D.3	Baseline OML & flight condition values for PEGASUS aircraft	223
D.4	Baseline structural topology values	224
D.5	Baseline OML & flight condition values	227
D.6	Baseline structural topology values	227
E.1	Analytical test cases to validate beam code	228
E.2	Thicknesses of spars and skin for validation study	229
E.3	Comparison of displacements (m) for validation study	230
G.1	Symbolic variables used in the formulation for automatic differentiation	237
G.2	Symbolic Functions at the Beam Level	239
G.3	Symbolic Functions at the Stick Model Level	239
G.4	Symbolic Functions for Constraint Aggregation	240
G.5	Derivative functions for optimization	240

LIST OF FIGURES

1.1	Boeing 787 certification [5]	2
1.2	Shift to simulation-based virtual design	4
1.3	Unconventional aircraft configurations (Images taken from NASA)	5
1.4	Aircraft early-stage design process	8
1.5	A coupled aircraft early-stage design process	10
2.1	Breakdown of main components of an aircraft wingbox	15
2.2	Aircraft wing rib	15
2.3	Smearing of stiffeners onto the base plate	17
2.4	Elevator deflection inputs for checked-pitch maneuver	19
2.5	Aircraft rigid-body dynamics simulation framework	21
2.6	Flowchart for the computation of structural loads time history	21
2.7	Notional depiction of displacement matching approach to stickmodel generation	28
2.8	Process of building load envelope based on maneuvers	33
2.9	Process flowchart describing the sequence of calculations for VAM	39
2.10	Aircraft stick model	42
2.11	Static aeroelastic design process	48

3.1	Complexity of an aircraft wingbox rib	54
3.2	Methods to obtain equivalent section	56
3.3	Stickmodel representation of a representative business jet	62
3.4	Jacobian matrix $\left[\frac{\partial \vec{r}}{\partial \vec{x}} + k_0 \frac{\partial \vec{r}}{\partial \vec{x}} \right]$ structure for three beams joined to another	62
3.5	Presence of aperiodicity in the form of soft-stiff sections along the span of a aircraft wing represented as a beam	63
3.6	Internal structure of the aircraft wing. Taken from Moors et al. [38]	64
3.7	Flowchart of the proposed method	72
3.8	Thesis execution summary	75
4.1	Local smearing approach (Repeated from Fig. 3.2c)	78
4.2	Rectangular and square cross section	79
4.3	CasADi flowchart to generate function for optimization	82
4.4	Parametrization used for test cases	85
4.5	Test cases used in this work	86
4.6	3-D FEM simulations for loading case 3	87
4.7	Specimen 2, method 1 displacement results for load cases 1 and 2	88
4.8	Specimen 2, method 2 displacement results for load cases 2 and 3	89
4.9	Specimen 2, method 3 displacement results for load cases 2 and 3	89
4.10	Specimen 2, method 3 displacement results for load case 1	89
4.11	Specimen 3 displacement vs. span results	90
4.12	Specimen 4 displacement vs. span results	91
4.13	Information from 3-D geometry needed to generate the beam model	94

4.14	Computation of wingbox cross-sectional properties using VABS	95
4.15	2-D cross-section and mesh used as input for VABS	96
4.16	Beam representation	97
4.17	2-D mesh of cross-section with stringers	98
4.18	Rectangular box cross-section assumption and parameters	99
4.19	Computation of wingbox box cross-sectional properties	99
4.20	Flowchart to correct the rectangular box cross-section stiffness with information from VABS	100
4.21	Comparison of the widths and heights of the rectangular box cross-section before and after the stiffness has been corrected	103
4.22	PEGASUS wingbox	104
4.23	Modal response due to insertion of a rib	107
4.24	Qualitative comparison of static response displacement contour of PEGASUS concept wing subjected to 1g loads	107
4.25	Comparison of static response of nodes along PEGASUS concept wing span subjected to 1g loads	108
4.26	Comparison of gust response of tip node PEGASUS concept wing	109
4.27	Displacement response comparison between Nastran shell model and VbS model	111
4.28	Displacement response comparison between Nastran shell model and rectangular box-beam model when averaged height method is used (Fig. 4.18)	112
4.29	Displacement response comparison between Nastran shell model, VbS model, rectangular box-beam model, and BbcVS model	112
4.30	von-Mises stress comparison between VABS beam model (left) and 3-D solid element FEM model (right)	114
4.31	von-Mises stress contour comparison of shell and VABS beam model	116
4.32	von-Mises stress comparison of shell and VbS	116

4.33	Points in each beam cross-section where stresses are computed	118
4.34	Shear sign convention	120
4.35	Generalized Stress matrix	121
4.37	von-Mises stress comparison of shell and beam models	122
4.36	Comparison between VbS model and BbcVS model for the PEGASUS concept	123
4.38	Workflow summary for symbolic gradients and functions	137
4.39	Structural optimization XDSM	140
4.40	Initial guesses given to the optimizer	141
4.41	Optimization of a cantilever beam subjected to sinusoidal tip load	142
4.42	Cross-section height distribution along span of the beam for static and dynamic constant tip loading	143
4.43	Study 1 bending moment, torsional moment and shear loads with interpolated section numbers and highlighted main sections in red	145
4.44	Optimum solution for study 1	146
4.45	Solutions for different constraints in study 2	147
4.46	Study 2 bending moment, torsional moment and shear loads with interpolated section numbers and highlighted main sections in red	149
4.47	Optimum solution for study 3	151
5.1	XDSM for structural optimization of wingbox using analytical beam corrected by VABS	154
5.2	Aerodynamic load distribution for the PEGASUS wing	156
5.3	Static sizing thickness distribution	158
5.4	Gust load time history for the PEGASUS wing	160
5.5	Comparison of thicknesses between static maneuvers sizing and gust sizing	161

5.6	Comparison of area and weights between static maneuvers sizing and gust sizing	162
6.1	Summary of research	173
7.1	Coupled aircraft early-stage design process (Repeated from Fig. 1.5)	176
7.2	Dimensionality of stiffeners	177
7.3	Notional structural multi-fidelity field surrogate model	182
A.1	Aircraft stick model	185
A.2	Cross section properties. Figure based on [53].	188
B.1	XDSM for structural sizing using RADE	196
B.2	Parametric features of the geometry pre-processor shown for a horizontal tail of the CRM aircraft	197
B.3	Parametric mesh generation capability: geometry and mesh of mesh of wing and empennage of the CRM	197
B.4	AVL model of a B777	198
B.5	Subsystems treated as concentrated masses and attached to the structure via rigid body elements	199
C.1	Schematic of Beam Deformation	203
D.1	Box beam geometry parametrization	220
D.2	Box beam geometries considered	221
D.3	OpenVSP model of the PEGASUS aircraft	223
D.4	Wireframe view of the PEGASUS wingbox	224
D.5	Wing OML and ribs view of the PEGASUS wingbox	225

D.6	PEGASUS concept wing shell models	225
D.7	AVL model of the PEGASUS aircraft	226
D.8	Geometry and mesh of mesh of wing and empennage of the CRM	226
E.1	Error between implemented code and known analytical solution for static loads	229
E.2	Dynamic simulation. At 0 seconds, gravity is turned on. At 7.5 seconds, the beam let into free-fall.	230
E.3	Representative business jet simulation	231
E.4	Percentage error of displacements for validation study	231
F.1	Wingbox and cross-section	232
G.1	XDSM for gradient computation using automatic differentiation and adjoint method	238

LIST OF ACRONYMS

.bdf Bulk Data File.

AD Automatic Differentiation.

AVL Athena Vortex Lattice.

B777 Boeing 777 Wide-Body Large Twin-Aisle Aircraft.

BbcVS Box-Beam corrected by VABS Stickmodel.

BDF Backward Difference Formula.

CFD Computational Fluid Dynamics.

CFR Code of Federal Regulations.

CG Center of Gravity.

CRM Common Research Model.

DLM Doublet Lattice Method.

DoF Degrees of Freedom.

DSM Design Structure Matrix.

E-B Euler-Bernoulli.

FAA Federal Aviation Administration.

FARs Federal Aviation Regulations.

FEM Finite Element Method.

IML Inner Mold Line.

KS Kreisselmeier–Steinhauser.

MDO Multi-Disciplinary Optimization.

OML Outer Mold Line.

PEGASUS Parallel Electric-Gas Architecture with Synergistic Utilization Scheme.

RADE Rapid Airframe Design Environment.

ROM Reduced Order Model.

TOGW Take-Off Gross Weight.

VABS Variational Asymptotic Beam Sectional Analysis.

VAM Variational Asymptotic Method.

VbS VABS-based Stickmodel.

VLM Vortex Lattice Method.

SUMMARY

Federal Aviation Regulations (FARs) are critical drivers of aircraft design. Early-stage aircraft design involves a tight coupling between structural dynamics, aerodynamics, and flight mechanics, with time-dependent loads arising from the considerations of the FARs. The current state-of-the-art decouples the time-domain simulation from the structural failure computation due to high computational costs associated with time-domain structural failure computation. The need to account for the dynamic loads specified by the FARs while simultaneously achieving low structural weight for fuel efficiency in early-stage aircraft design motivates the following question: *How to enable computationally efficient structural analysis and optimization of early-stage aircraft wing design, considering dynamics?*

Existing methods simplify the dynamic loads to equivalent static ones and design the structure using shell-based analysis. Other literature approaches use computationally efficient beam models for structural sizing but make assumptions on the geometry and/or material distribution. Higher-order beam theories for structural analysis have been successfully applied to the design of slender structures subjected to time-dependent loads, like rotorcraft blades. While aircraft wings can be considered slender structures, aperiodicity, and inhomogeneity along the span render beam theory ineffective.

The present work aims to bridge this gap by proposing a method for analyzing 3-D structures through dimensional reduction. The use of the Variational Asymptotic Method (VAM) is explored for the systematic reduction of 3-D structures to 1-D models and further, recover 3-D stresses and strains after solving the 1-D problem.

A stiffness matching approach is proposed to dimensionally reduce 3-D features such as stiffeners by locally smearing them on the base plate. The proposed method allows for stiffeners of varying dimensions, topology, and spacing to be smeared. The stiffness matching further allows the beam cross-sectional properties computed from VAM to be equal to a

box-beam cross-section. The equivalence enables the use of Euler-Bernoulli type analytical stiffness computation while retaining the accuracy of VAM. Analytical expressions allow for rapid evaluation of the beam properties and stress recovery and further permit the use of Automatic Differentiation (AD) to obtain partial derivatives. The proposed structural analysis method is applied to the wing structural analysis of a novel distributed electric propulsion aircraft – NASA’s PEGASUS concept, and the open-source Common Research Model (CRM).

A general adjoint method for dynamic simulations is presented and applied to a nonlinear Timoshenko beam theory. It combines general beam residual equations with an adjoint method to extract gradient information from the load time-history. Aggregated constraints implemented for sizing are stress-based, combining axial stresses at the beam corners with shear stresses from torsion and external loads at both corners and mid-sections. CasASDi, an open-source tool for nonlinear optimization and algorithmic differentiation, is used to generate expressions and calculate derivatives for the relevant equations used for analysis and optimization. Numerical tests are conducted to test the accuracy of the adjoint computations and scalability as the number of design variables increase.

A structural optimization framework is developed for the beam-based dynamic analysis method presented, allowing for the structure’s sizing under strength-based failure considerations. The PEGASUS concept is used as a testbed to demonstrate the sizing capabilities. The structure is sized for FARs specified maneuver loads – static 2.5g and -1.0g, and dynamic gusts.

Findings show that: 1) the use of VAM allows for the systematic extraction of beam properties for aircraft wings, 2) the displacement and stress response of the aircraft using beam models match reasonably well against those produced by shell-based models, 3) for dynamic simulations the derived adjoint method computes accurate gradients efficiently to be used in structural optimization, 4) sizing of aircraft wings for 14 CFR specified maneuvers using the proposed approach produces a 6% error compared to shell-based method,

but with a 7.8x speed-up.

The proposed approach provides improvements on the existing literature methods- it is computationally efficient, provides reasonable accuracy for early-stage structural sizing and weight prediction, and includes dynamic effects. The computational efficiency makes it well-suited for many-query applications like optimization, uncertainty quantification, and generating data for surrogate modeling.

CHAPTER 1

MOTIVATION

1.1 Introduction

1.1.1 Aircraft Certification

Federal Aviation Administration (FAA) certification requirements are of central importance to the process of aircraft design. An airframe manufacturer carries out computational analyses, flight tests and extensive ground tests on a proposed design to gain confidence that it can withstand loads prescribed by regulatory standards. Such exhaustive tests are necessary for a design to be deemed safe, durable and reliable [1, 2].

Critical loads (also called sizing loads) often occur during dynamic maneuvers, during which the motion of aircraft itself contributes significantly to the developed loads. Catastrophic failures can occur due to large and unforeseen dynamic loads. This phenomenon is evidenced by the vertical stabilizer structural failure on American Airlines Flight 587. The investigation revealed that large loads had developed on the vertical tail due to the first officer's rapid, aggressive, and oscillatory rudder inputs. The rudder inputs were in response to a wake turbulence encounter and caused the loads on the vertical tail to exceed the aircraft's ultimate design load limits [3].

The Federal Aviation Administration (FAA) defines regulations on the structural integrity of the airframe [4], called 14 Code of Federal Regulations (CFR). 14 CFR often involve a consideration of critical loads occurring during *dynamic maneuvers*. Maneuvers such as 14 Code of Federal Regulations (CFR) 25.331(c)(2), commonly known as the *Checked Pitch Maneuver*, and 14 CFR 25.351, commonly referred to as the *Rudder Kick Maneuver* provide critical loads which size the horizontal tail and vertical tail, respectively. Following the American Airlines Flight 587 incident, the FAA has proposed to add a new

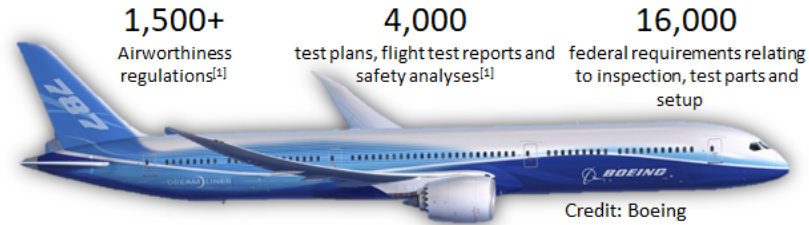


Figure 1.1: Boeing 787 certification [5]

load condition to the design standards for transport category airplanes – 14 CFR 25.353-rudder control reversal conditions.

To demonstrate compliance with 14 CFR, airframe manufacturers must show that the aircraft can sustain the loads defined by the FAA. Fig. 1.1 shows the number of regulations, requirements, and tests performed for the Boeing 787 certification program.

1.1.2 Certification-By-Analysis

In the past, limited computing resources and inaccurate simulation capabilities resulted in heavy reliance on physical testing. Making prototypes and performing physical tests for certification is an expensive endeavor, as shown in Table 1.1. Numerous studies show that when issues are discovered too late in the design process, the unforeseen redesign and fixes are costly [6]. There has been an increase in certification cost and time over the past few decades [7]. For instance, the Airbus A380 faced a delay in its entry into service by almost two years [8, 9]. Boeing has experienced similar cost challenges and delays with its commercial 787 aircraft. The Boeing 787 entered into service more than three years late and tens of billions of dollars over budget in development costs [10, 11].

Table 1.1: FAA certification cost estimates

Light Sport Aircraft	Primary Category	Normal
~\$125,000	~\$1,000,000	~\$25,000,000

With the growth in computational power and numerical simulations’ accuracy over the

past few decades, a potentially cheaper option presents itself to airframe manufacturers. The aircraft can be simulated, designed, and tested virtually, reducing the number of physical tests. The paradigm-shift towards *certification-by-analysis* is seen in reports by airframe manufacturers. For example, Airbus claimed a reduction of 40% [12] in wind tunnel testing time for the development of the A350.

Table 1.2 shows the number of days to obtain certification for some recent aircraft development programs. Despite the reduction in physical testing and increased usage of numerical simulations, the time taken for certification is increasing.

Table 1.2: FAA certification timelines

Aircraft	Application Date	Certification Date	Years
C500	07/16/1968	09/09/1971	3.2
A330	07/17/2000	05/17/2004	3.8
A380	12/20/2001	12/12/2006	5.0
B787	10/01/2006	08/26/2011	4.9
GVII	09/30/2013	10/11/2019	6.0

1.1.3 Certification-Driven Virtual Design

Design is naturally an iterative process. Design entails picking specific values for the parameters specifying the system, determining the system’s response, and assessing if the response is satisfactory. If the response is not satisfactory, the designer changes the values of parameters and determines the system’s response again. Design entails repeating the simulation with different parameter values to discover a design that satisfies all the specified requirements.

Not only can simulation-based tools, be used for certification-by-analysis, but can also be used to virtually design the aircraft. The shift from experiment-based design to simulation-based design is shown in Fig. 1.2. For example, the Boeing 777 aircraft was designed virtually [13].

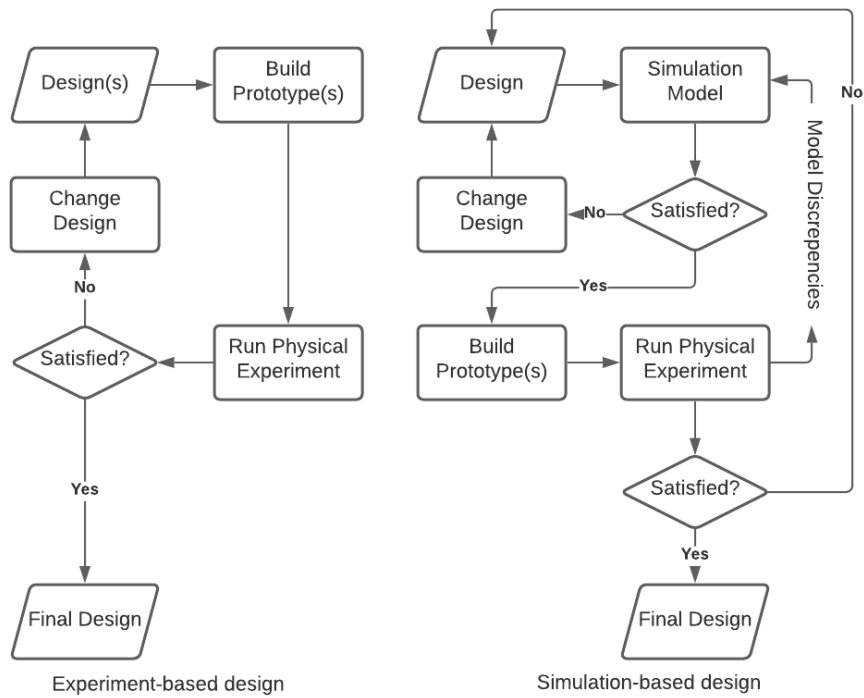


Figure 1.2: Shift to simulation-based virtual design

The certification requirements are constraints the system must satisfy. A satisfactory aircraft design must sustain all the forces applied to it, as specified by the 14 CFR. The design must also meet some performance requirements. For aircraft, fuel efficiency and reduction in emissions are major important performance metrics.

Aircraft have become more complex over the past few decades. The increase in complexity is in part due to aggressive environmental goals put forth by NASA's [14] 'N+i' programs, which have spurred organizations to develop new concepts in a bid to meet demands/projections in the decades to come. Consequently, novel designs featuring several technologies related to advanced materials (e.g. composites), efficient propulsion, and aerodynamics have emerged, as shown in Fig. 1.3.

With new technologies or concepts, the FAA adds additional certification requirements to ensure the design is safe, durable, and reliable. Considering the lack of historical data for these new concepts and the expense of physical testing, using physics-based simulations is



(a) Truss-braced wing



(b) Box-wing concept



(c) Blended wing body concept



(d) D8 concept

Figure 1.3: Unconventional aircraft configurations (Images taken from NASA)

paramount. These simulations that consider certification requirements enable *certification-driven virtual design* of aircraft.

As described earlier, the process of design is iterative. The term *many-query* [15] has been used in the literature to describe applications that require evaluation of a model multiple times. Since the model will be evaluated many times, a single model evaluation must be as computationally efficient as possible for the overall process to be computationally efficient.

Optimization is an example of many-query applications, where the algorithm provides guesses of the design parameters to the model to evaluate objectives and constraints. The algorithm iteratively hones-in on the optimum. Gradient-based optimization algorithms have been shown to be computationally efficient for a large number of design parameters [16]. To use gradient-based optimization algorithms the model must provide, in addition to the objective function value and constraint functions values, the *gradient* of the functions with respect to the design parameters.

Other many-query applications include sensitivity analysis, design-space exploration, trade studies, uncertainty quantification [17], and surrogate model data generation. For these applications, the gradient is not necessary, but if available enables the use of more efficient gradient-enhanced methods [18].

1.1.4 Chapter Outline

Summarizing the requirements based on the discussion so far, a simulation-based virtual design framework must:

1. Account for dynamic maneuvers defined by 14 CFR
2. Be capable of handling new concepts and technologies
3. Have low computation cost to allow for design-space exploration and optimization

This chapter lays the foundation for formulating the main high-level motivating research question that this work investigates. The current early-stage aircraft design process used by airframe manufacturers is first introduced. The rationale for the process and how it meets the requirements is explained. This is followed by identification of the limitations and gaps in the current state-of-the-art. Finally, the discussion is summarized with observations leading to the motivating question this dissertation aims to tackle.

1.2 Simulation-Based Early-Stage Aircraft Design

There is competition among airframe manufacturers to increase fuel efficiency, both from a cost perspective and to meet the aggressive environmental goals. The efficiency can be assessed qualitatively using the Breguet range equation:

$$R = \frac{V}{g} \frac{1}{SFC} \frac{L}{D} \ln \left(1 + \frac{W_{fuel}}{W_{payload} + W_{structure}} \right) \quad (1.1)$$

where L/D is the lift to drag ratio, SFC the specific fuel consumption, V the velocity at cruise, W_{fuel} the fuel weight, $W_{payload}$ the payload weight, and $W_{structure}$ the structural weight. As seen, the aircraft range can be improved by improving the aerodynamic efficiency, L/D , or decreasing the structural weight, $W_{structure}$, or improving the propulsive efficiency, SFC . In other words, for a given desired range, the fuel used can be decreased. Neglecting propulsive considerations, reducing the required fuel for a given flight mission is achieved by improving aerodynamics and decreasing the aircraft's structural weight. Thus, novel aircraft have high aerodynamic efficiency and low structural weight fraction, which yields inherently flexible wings and nonlinear structural and flight dynamics.

Some examples of unconventional configurations proposed are shown in Fig.1.3. The Boeing truss-braced wing [19] and the D-8 concept [20] feature high aspect ratio wings. The blended wing body concept [21], and the joined wings concept [22, 23] also feature large structural deformation. The aeroelastic response of most unconventional aircraft concepts is nonlinear due to nonlinearities in the structural and aerodynamic responses. An accident that highlights the importance of nonlinear multi-disciplinary analysis is the crash of Helios aircraft. The Helios was a very high aspect ratio wing aircraft that crashed due to gust disturbance. The cause of the accident as determined by the investigation panel [24] was "lack of adequate analysis methods led to an inaccurate risk assessment of the effects of configuration changes leading to an inappropriate decision to fly an aircraft configuration highly sensitive to disturbances." Thus, the tools to design aircraft need to account for the nonlinearity [25] and be applicable to unconventional design concepts.

Fig. 1.4 shows the notional aircraft early-stage design process followed today (synthesized from multiple literature sources [26, 27]). There are two main groups: the *Loads group* and the *Stiffness and Stress group*. The following assumptions are made:

1. The aircraft's Outer Mold Line (OML) has been fixed
2. The engine has been sized and an engine deck is available to obtain thrust as a function of throttle setting, Mach number and altitude

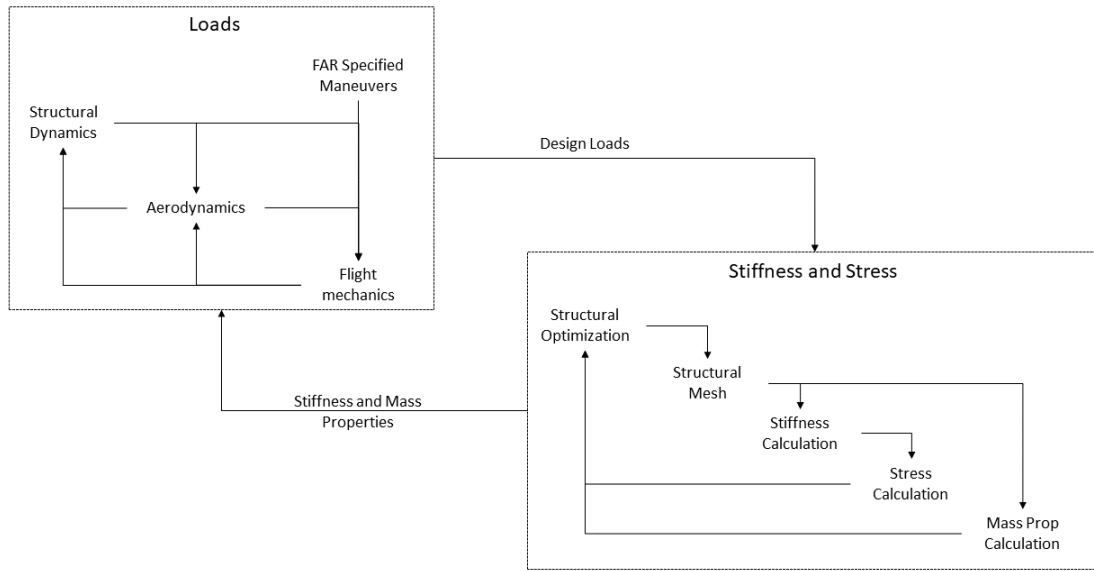


Figure 1.4: Aircraft early-stage design process

Consider the Loads group seen in Fig. 1.4. This group provides the set of critical loads experienced by the aircraft during its mission and due to maneuvers defined by 14 CFR [28]. Computational tools used here must account for a tight coupling between aerodynamics, structural dynamics, and flight mechanics. To efficiently perform these *dynamic simulations* (has a time-varying behavior), the tools used typically reduce the Degrees of Freedom (DoF) to reduce the computational burden [29, 30, 31].

The Loads group communicates the critical loads to the Stress and Stiffness Group using a *load envelop*. High fidelity structural modules with a large number of DoF compute deformation and check for structural failure [32, 33]. The stress and stiffness group sizes the structure to withstand the loads. In doing so, the mass properties and stiffness of the components are determined. These two groups iterate with each other to size the wing's internal structure, ensuring it can withstand the critical loads experienced by it during flight.

In the preceding discussion of early-stage aircraft design, it is noted that the dynamic maneuvers defined by 14 CFR – key drivers in the design process – are considered by the Loads Group. The dynamics necessitate the use of models with low DoF. On the other

hand, the Stress and Stiffness group use models with larger DoF to accurately account for technologies such as composite and the complexities of the aircraft's internal structure. Using low DoF models for the expensive dynamic simulations and high DoF models for the relatively inexpensive static simulations allows for the overall computational cost, allowing for efficient design space exploration and optimization [34, 28, 35].

1.3 Challenges in Simulation-Based Early-Stage Aircraft Design

In the design framework shown in Fig. 1.4, the two groups are decoupled. There is an “over-the-wall” transfer of data between the two groups while performing the iterations. In large organizations, these iterations are time-consuming. The two groups may be geographically separated or make modeling assumptions the other group may not know. Such organizational barriers increase the overall design time. Also, the simulation approach does not account for the coupling between the two multi-disciplinary analyses:

- The simplifications the loads group makes to obtain a low DoF model do not accurately capture the complexities of the aircraft's internal structure, nor can they fully account for composites. Section 2.2 discusses these issues.
- The stress and stiffness group simplifies the dynamic loads to equivalent static loads. The process produces many load cases, on the order of thousands. Standard methods developed downselect to load cases on the order of hundreds. Sizing occurs for these reduced load cases. Section 2.3 discusses these issues.

A coupled framework with simultaneous loads generation and structural sizing would overcome the challenges stated above and reduce design cycle time. Fig. 1.5 shows such a framework. This dissertation argues that one of the most significant challenges for such a framework is the trade-off between accuracy and computational cost. On the one hand, running dynamic simulations with large DoF has a prohibitively high computational cost.

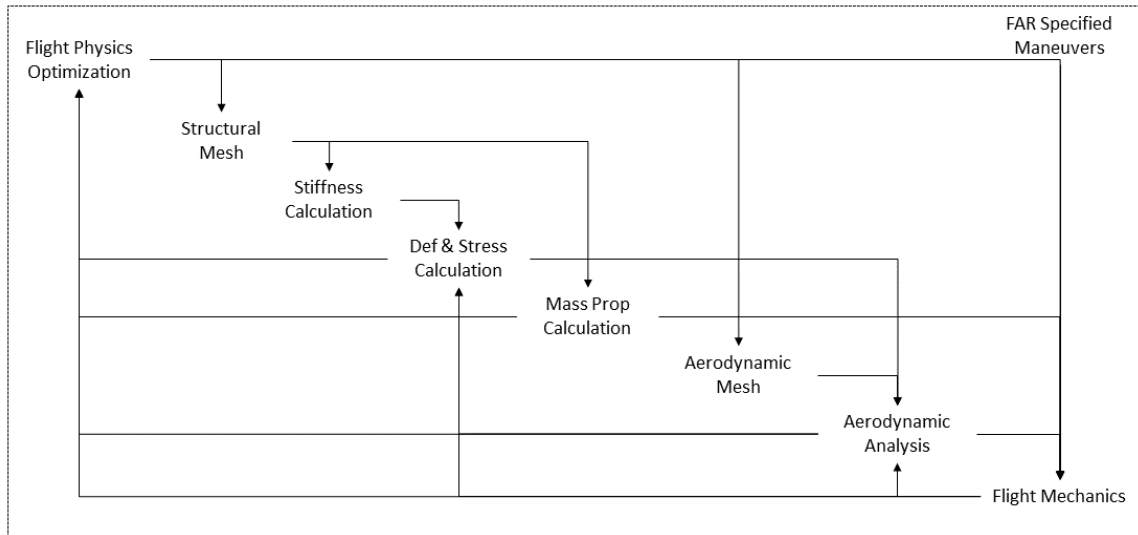


Figure 1.5: A coupled aircraft early-stage design process

On the other hand, the simplifications used to create low DoF models results in insufficient accuracy to correctly predict structural yielding and structural failure.

1.4 Summary

Aircraft design must account for the dynamic maneuvers specified by 14 CFR. The growth of the computational power and improvement in simulation capabilities over the last few decades have afforded the possibility of certification-driven virtual design. Adopting these methods in the early stages of design requires a low computational cost to run the simulation while repeatedly changing design parameters to allow for efficient design space exploration and optimization.

This chapter provided an overview of the current state-of-the-art decoupled design process and outlined how it meets the design framework requirements. It then highlighted the limitations of the framework and proposed a coupled framework. Finally, it elucidated the challenges to implementing the coupled framework. A summary of the discussion in this chapter is presented as the following observations:

Observations 1

- 1.1 Dynamic maneuver certification requirements from 14 CFR are key-drivers in the aircraft design process.
- 1.2 There is a paradigm shift towards using simulation-based tools for certification-by-analysis and certification-driven virtual design.
- 1.3 The simulation tool must have low computational cost to facilitate many-query applications, with a gradient computation capability preference.
- 1.4 The current state-of-the-art decoupled design process adopted faces two issues- 1) organizational barriers and 2) reliance on modeling assumptions.
- 1.5 The desired coupled framework is impractical due to the trade-off between accuracy and computational cost in structural failure assessment.

Deferring details on the specific deficiencies in the state-of-the-art to Chapter 2, the motivating question for the work in this dissertation is introduced.

Motivating Question

How to account for dynamics while maintaining computational efficiency in structural analysis and optimization of early-stage aircraft wing design?

The observations serve as high-level reasons to justify a focus on developing a model with the following characteristics:

Desired Capabilities

- Couple dynamic simulation and structural failure assessment
- Incorporate geometric intricacies and new material technologies
- Easily obtain gradients

The desired capabilities stated above require an accurate, yet computationally efficient model. Thus, the research objective may be stated as:

Research Objective

Develop a framework for aircraft wing design that

1. Dimensionally reduces complex 3-D structures to produce a low DoF structural analysis model
2. Obtain the gradient of the structural analysis model in the time-domain

1.5 Document Outline

The remaining chapters of this dissertation are organized as follows:

- **Chapter 2** presents relevant background information on certification, dynamic loads generation, structural analysis and multi-disciplinary optimization.
- **Chapter 3** addresses the gaps in the literature and proposes, at a high level, a structural analysis and optimization method
- **Chapter 4** dives into each component of the proposed method. This includes descriptions of the research questions, the hypotheses to solve the research questions, the toy problems and test cases to prove/disprove the hypotheses, and the results of

each experiment.

- **Chapter 5** applies the proposed method to the design of the wings of a novel distributed-electric propulsion aircraft, the PEGASUS concept.
- **Chapter 6** summarizes the contributions and the main findings of this dissertation.
- **Chapter 7** outlines the limitations of this dissertation. Some potential avenues for future research are explored. Finally, concluding remarks are provided.

CHAPTER 2

BACKGROUND AND LITERATURE REVIEW

To meet certification-by-analysis, one has to show that the aircraft structure is safe throughout its mission. There are three aspects to consider: what does the internal structure look like (Section 2.1), what the loads it experiences (Section 2.2), and can the aircraft sustain the loads without failure (Section 2.3). Also, for a certification-driven design, we need to size the aircraft to sustain the loads. Section 2.4 explores Multi-Disciplinary Optimization (MDO) and structural optimization methods.

2.1 Physical Decomposition of the Internal Structure of Aircraft Wings

The load bearing component of an aircraft wing is the wingbox. Fig. 2.1 shows a typical wingbox. It consists of skin, spars and ribs each playing a role in the overall capacity to resist loads. The construction is usually semi-monocoque, where the skin resists tension and shear while the stiffeners resist compression. The skin is stiffened by stringers that run along the span of the wing. The primary function of the spar webs is to resist the shear and torsional loads. If we isolate the rib itself (Fig. 2.2), we see that it is a complex structure. The rib has four primary functions:

1. Maintain the airfoil shape of the wing
2. Transfer air pressure loads from the skins to the spars
3. Resist fuel pressure loading
4. Diffuse local concentrated loads such as engine pylon mounts and movable surface attachments

In the rib's design, it is idealized as a chord-wise beam that transfers the loads from the skin to the spars. The rib feet transfer the load from the skin to the rib body. The horizontal stiffeners resist the shear loads, while the vertical stiffeners resist the compressive loads due to air pressure. The rib has cut-outs within it, either to reduce weight or to allow for servicing or system holes. The system holes are necessary to enable hydraulic lines to pass through the rib. These geometric intricacies make the design of an aircraft wing complex. Gharbi et al. [36], Mills and Burley [37], and Gunther et al. [38] give descriptions of the complexity involved in the design of aircraft wings and ribs.

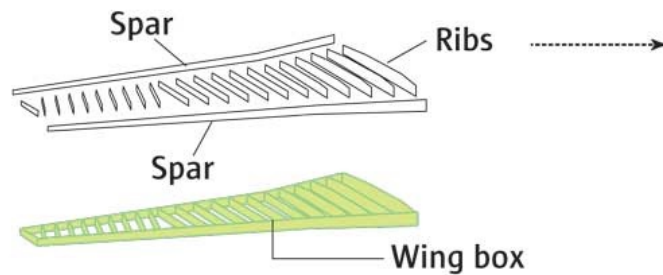


Figure 2.1: Breakdown of main components of an aircraft wingbox

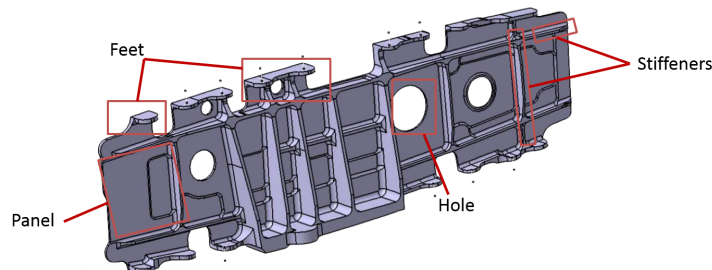


Figure 2.2: Aircraft wing rib

The complexity of the structural design of aircraft components arises from many features that each component is comprised of. Each of these features has a particular role and undergoes a unique design process. Consider the rib discretized into n rows and m columns. Each cell is called a panel. Hence there are $m \times n$ panels. Several configuration decisions are made in each design operation, such as what type of holes to include in a panel or what shape of castellation is used. Further, each configuration chosen needs to be sized hence having its own design variables. In order to estimate the scale of the problem,

Table 2.1: Rib design morphological matrix

Feature	Number in one rib			Example	
No of rows	m			3	
No of columns	n			14	
No of panels	$m \times n$			42	
No of vertical stiffeners	$m + 1$			4	
No of horizontal stiffeners	$m \times n$			42	
Feature Configurations			Combinations	Example	
Stiffener section profile	Blade	T	Hat	$3 \times [(m \times n) + (m + 1)]$	138
Holes	Manhole	Lightening	System	$3 \times (m \times n)$	126
Booms	Simple	Double		$2 \times (m + 1)$	16
Cleats	Type 1	Type 2	Type 3	$2 \times 3 \times n$	84
Seal plate				$2 \times n$	28

the morphological matrix is used, which provides a structured and systematic way of generating a large number of possibilities. Including all the design parameters of the wing rib into the morphological matrix would result in a massive number of design decisions that need to be made for each rib as illustrated in Table 2.1.

2.1.1 Smearing of Stiffeners

Models of wings based on equivalent plate representation are common in the literature. The complexities of the features shown in Fig. 2.2 are smeared onto the base plate, as shown in Fig. 2.3. Basic smearing approaches were explored as far back as 1951 in a NACA-TN-2289 report [39] and in 1965 by Hedgepath and Hall [40]. More recently, Collier et al. [41, 42] extended the Classical Lamination Theory (CLT) to stiffened panels. Yu [43] generalized VAM-based plate theory to model the constitutive behavior of composite plates.

The methods in the literature to perform smearing make assumptions on the stiffeners. As seen in Fig. 2.3, all three stiffeners are of the same blade stiffener topology. Each stiffener is also of the same dimensions. A uniform stiffener spacing of a is assumed. These assumptions allow for analytical formulae to compute the material properties of the

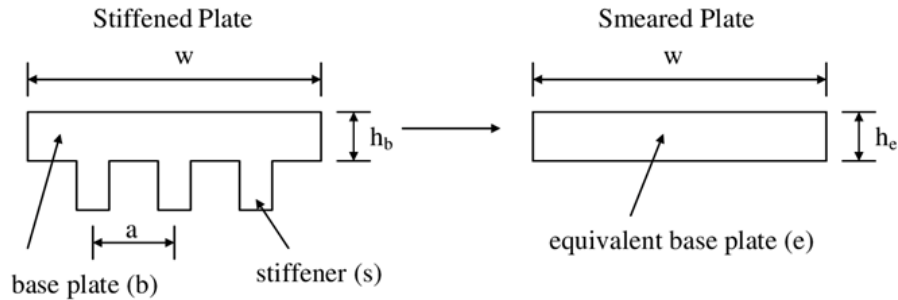


Figure 2.3: Smearing of stiffeners onto the base plate

equivalent plate.

2.1.2 Summary

The literature on internal structure of the wing is summarized as the following observations:

Observations: Internal Structure of Wing

- Internal structure of the wing is very complex with a very large number of design variables.
- Computationally intractable to consider all the variables in early-stages of design.
- Methods in literature consider the effect of stiffeners through smearing
- Creating equivalent 2-D structures for stiffeners of varying topology, dimensions and rib spacing has not been done in the literature

2.2 Computation of Dynamic Loads

The primary goal of the loads group shown in Fig. 1.4 is to provide a set of critical loads the airframe will experience. The critical loads are communicated through the use of the *Load Envelope*. The process of generating a load envelope and a description of it is explained

next. As stated earlier, 14 CFR place requirements on the structural integrity of all certified aircraft.

2.2.1 Example 14 CFR Maneuver: 14 CFR 25.331(c)(2)

14 CFR 25.331(c)(2) is named the *Checked-Pitch Maneuver*. This maneuver is typically the one that results in the most critical loads on the horizontal tail. The checked pitch maneuver (nose up or nose down) consists of the aircraft's pitching motion generated through control input from the pilot, then checked or stopped with an opposite control input. The maneuver is precisely described in the text of 14 CFR 25.331(c)(2) in terms of control deflection as a function of time, achieved load factor, and pilot force. The function that describes the yoke displacement over time is given as

$$\delta(t) = \delta_{max} \sin(\omega t), \quad \text{for } 0 \leq t \leq t_{max} \quad \text{and} \quad \omega \leq \omega_{max} \quad (2.1)$$

with:

- δ_{max} : the maximum yoke deflection, as limited by the control system stops, control surface stops, or by pilot effort as prescribed in 14 CFR 25.397.
- $t_{max} = \frac{3\pi}{2\omega}$
- ω : circular frequency (rad/sec) of the control deflection taken equal to the undamped natural frequency of the short period rigid mode of the airplane, with active control system effects included where appropriate.
- $\omega_{max} = \frac{\pi V}{2V_A}$: with V the speed of the airplane at entry of the maneuver and V_A the design maneuvering speed.

Eq. 2.1 is modified to account for achievable load factors. If the maximum load factor is not reached with the control input specified by Eq. 2.1, then the pilot must hold the control surface deflected until the load factor is reached but for no more than five seconds. On the

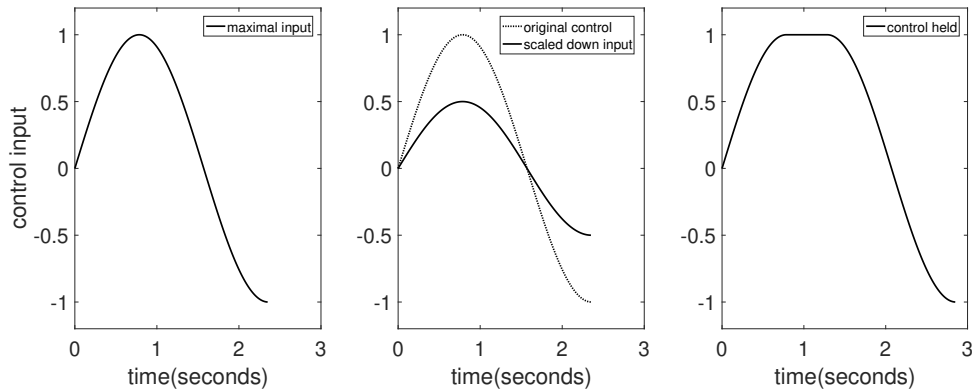


Figure 2.4: Elevator deflection inputs for checked-pitch maneuver

other hand, the maximum prescribed positive load factor must not be exceeded. In such cases, the flight deck pitch control deflection amplitude should be scaled down. Figure 2.4 shows examples of these types of longitudinal control inputs.

Furthermore, the loads do not need to be recorded after the time for which the load factor goes below zero (respectively, above 2.5) during the second phase of the nose up (respectively, nose down) maneuver, in which case the maneuver can be stopped. 14 CFR specifies that the maneuver may be stopped if the pilot's effort to control the airplane falls outside the ranges prescribed by 14 CFR 25.397- viz, 300 lbf.

The simulator must perform the maneuver for entry speeds between the design maneuvering speed V_A and the design dive speed V_D . To correctly implement 14 CFR 25.331(c)(2), the simulation must perform the checked pitch maneuver for several points in the aircraft flight envelope corresponding to speeds between those two values. The flight condition is defined by the entry speed, starting altitude, and loadout of the aircraft (weight and CG position). For each flight condition, the dynamics of the aircraft are different. Consequently, both the circular frequency of the control input ω and the maximum control deflection δ_{max} need to be computed for each case to generate the appropriate control input for the pilot.

The simulation step involves a tight coupling between aerodynamic, structural dynamics, and flight mechanics, as seen in the loads group of Fig. 1.4. Next, we review the tools used in the literature to perform these simulations.

2.2.2 Rigid Structure Assumption

The simulator can find the airframe’s critical loads by assuming the aircraft to be rigid and only considering the interactions between aerodynamics, propulsion, and flight mechanics. Goron et al. [44] adopted such an approach. The authors simulated the checked-pitch maneuver for a business jet through the entire flight envelope and three weight configurations. An aircraft dynamics model is defined by

1. Mass properties
2. Aerodynamic characteristics which describe the total forces and moments at a reference point as a function of aircraft states and control surface deflections
3. Propulsive performance (engine deck) which defines the propulsive loads at the reference point as a function of altitude, Mach number and throttle

Fig. 2.5 shows such an environment represented as a Design Structure Matrix (DSM). The user specifies a desired maneuver in the *Maneuver block*. The *Controller block* compares the desired maneuver to the current state of the aircraft and produces a control vector \vec{u} . The control vector specifies all control surface deflection and throttle settings on the vehicle. The *Vehicle block* contains within it the mass properties, aerodynamics, and propulsion. Given the current state vector, \vec{x} , and control vector \vec{u} , the vehicle block calls appropriate methods to compute the loads due to gravity, aerodynamics, and propulsion. The net loads, \vec{F} and \vec{M} , are sent to the *Equations of Motion block* which computes the time derivative of the states vector, $\dot{\vec{x}}$. The time derivative of the states vector is integrated forward in time using an appropriate time-integration scheme to obtain the states vector at the next time step, \vec{x} at $t_i + \Delta t$. The entire loop is time-marched till the final time t_f .

External loads acting on the lifting surface is obtained from the state’s time history. The proposed method involves dividing the lifting surface into sections, or “strips”, with known aerodynamic characteristics and mass properties, and then calculating the forces and

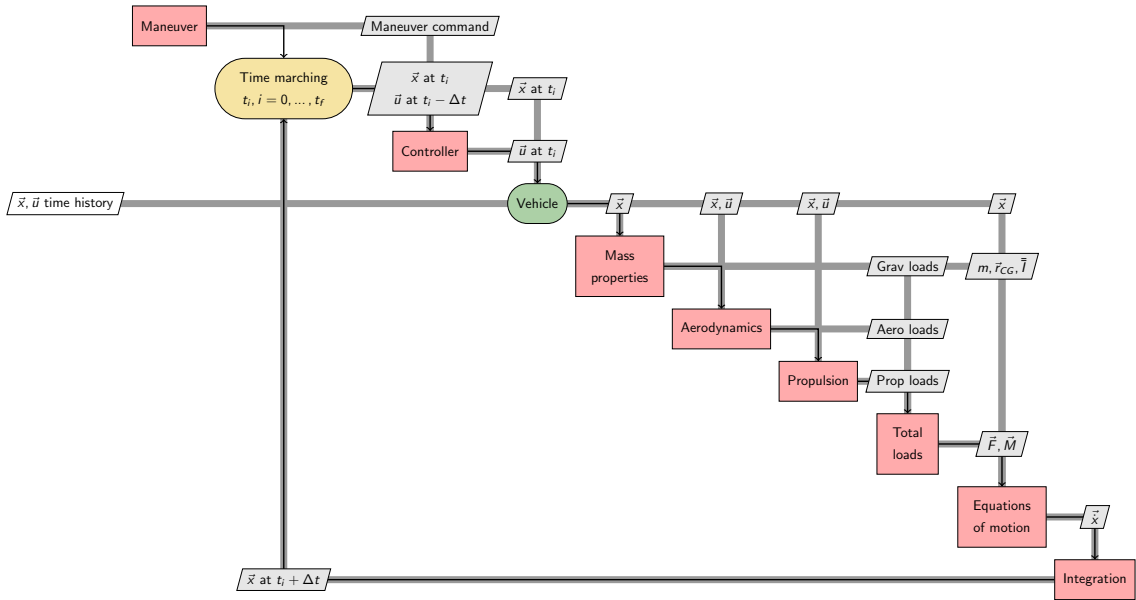


Figure 2.5: Aircraft rigid-body dynamics simulation framework

moments that develop on each strip at each time step. Finally, the most severe loads are found from the time history of loads for each flight condition. Fig. 2.6 shows a high-level flowchart of this process.

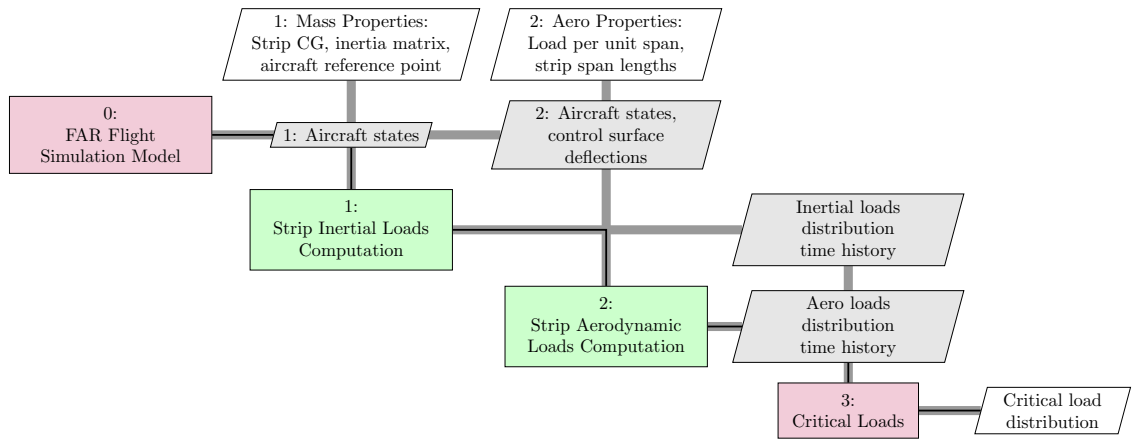


Figure 2.6: Flowchart for the computation of structural loads time history

Equations of Motion

The equations of motion are cast about a fixed reference point O rather than the CG. This enables, for instance, the dynamics of a moving CG (e.g., due to decreasing fuel mass or fuel transfer) to be modeled. The force and moment equations in vector form are given below.

$$\vec{F}_{total} = m \left(\dot{\vec{V}}_0 + \vec{\omega} \times \vec{V}_0 + \ddot{\vec{r}}_g + \dot{\vec{\omega}} \times \vec{r}_g + 2 \vec{\omega} \times \dot{\vec{r}}_g + \vec{\omega} \times (\vec{\omega} \times \vec{r}_g) \right), \quad (2.2)$$

$$\vec{M}_{total} = \bar{\bar{I}} \dot{\vec{\omega}} + \vec{\omega} \times \bar{\bar{I}} \vec{\omega} + m \vec{r}_g \times \left(\dot{\vec{V}}_0 + \vec{\omega} \times \vec{V}_0 \right), \quad (2.3)$$

where \vec{r}_g is the position vector running from O to the center of gravity (CG) of the aircraft, $\vec{V}_0 = \{u, v, w\}^T$ the velocity of the reference point O, $\vec{\omega} = \{p, q, r\}^T$ the angular velocity of the aircraft, and $\bar{\bar{I}}$ the mass moment of inertia matrix of the aircraft about O. The more specific case where the reference point O coincides with the CG can be obtained by setting $\vec{r}_g = 0$ in the above. Kinematic relationships are used to obtain the derivatives of the Euler angles ϕ , θ , and ψ from the angular rates p , q , and r , and also derivatives of the position x_0 , y_0 , and z_0 of the reference point O from the velocities u , v , and w . The resulting system of 12 nonlinear ordinary differential equations (in $u, v, w, p, q, r, \phi, \theta, \psi, x_0, y_0, z_0$) for six degrees-of-freedom rigid body motion is numerically integrated to obtain the motion history of the aircraft during the maneuver.

Inertial Loads Computation

The concept of inertial loads allows for the generalization of equilibrium, which is fundamentally a statics concept, to the case of dynamics problems through D'Alembert's principle and the notion of *dynamic equilibrium*. The equations of motion of strip 'k', subjected

to *externally applied* forces $\sum \vec{F}_{ext}^{(k)}$ and moments $\sum \vec{M}_{ext}^{(k)}$, are given by

$$\sum \vec{F}_{ext}^{(k)} = m_{strip}^{(k)} \vec{a}_{strip}^{(k)} \implies \sum \vec{F}_{ext}^{(k)} + \left[-m_{strip}^{(k)} \vec{a}_{strip}^{(k)} \right] = \vec{0} \quad (2.4)$$

and similarly

$$\sum \vec{M}_{ext}^{(k)} + \left[-\bar{I}_{strip}^{(k)} \dot{\vec{\omega}} - \vec{\omega} \times \left(\bar{I}_{strip}^{(k)} \vec{\omega} \right) \right] = \vec{0} \quad (2.5)$$

By definition, the inertial loads, namely the inertial force $\vec{F}_i^{(k)}$ and the inertial moment $\vec{M}_i^{(k)}$, enforce the dynamic equilibrium conditions $\sum \vec{F}_{ext}^{(k)} + \vec{F}_i^{(k)} = \vec{0}$ and $\sum \vec{M}_{ext}^{(k)} + \vec{M}_i^{(k)} = \vec{0}$. They are equal to the terms within brackets in Eq. 2.4 and Eq. 2.5. Thus, the inertial force $\vec{F}_i^{(k)}$ and moment $\vec{M}_i^{(k)}$ acting on strip ‘ k ’ are given by

$$\vec{F}_i^{(k)} = -m_{strip}^{(k)} \vec{a}_{strip}^{(k)} \quad (2.6)$$

$$\vec{M}_i^{(k)} = -\bar{I}_{strip}^{(k)} \dot{\vec{\omega}} - \vec{\omega} \times \left(\bar{I}_{strip}^{(k)} \vec{\omega} \right) \quad (2.7)$$

with

$$\vec{a}_{strip}^{(k)} = \dot{\vec{V}}_0 + \vec{\omega} \times \vec{V}_0 + \ddot{\vec{r}}_{strip}^{(k)} + \dot{\vec{\omega}} \times \vec{r}_{strip}^{(k)} + 2\vec{\omega} \times \dot{\vec{r}}_{strip}^{(k)} + \vec{\omega} \times (\vec{\omega} \times \vec{r}_{strip}^{(k)}) \quad (2.8)$$

where $\vec{V}_0 = \{u, v, w\}^T$ is the velocity of the aircraft reference point O, $\vec{\omega} = \{p, q, r\}^T$ is the aircraft angular velocity, and $\vec{r}_{strip}^{(k)}$ is the strip’s CG position relative to the aircraft reference point O. The time derivatives of the position vector $\vec{r}_{strip}^{(k)}$ are zero since the strip’s CG location is assumed to be fixed relative to the reference point. It is worth noting that this inertial force depends on the mass properties of the strip (through $m_{strip}^{(k)}$), the position of the mass element (through $\vec{r}_{strip}^{(k)}$), and on the kinematics of the aircraft (through \vec{V}_0 , $\dot{\vec{V}}_0$, $\vec{\omega}$, and $\dot{\vec{\omega}}$). These calculations are performed for every simulation time step, resulting in time histories of the inertial forces and moments on each strip of the lifting surface.

2.2.3 Stickmodel approach

Duca et al. [45] performed uncertainty analysis on the rigid-body simulations performed by Goron et al. [44]. The authors highlighted the necessity to compute the center of gravity's location accurately and capture aeroelastic effects. Sarojini et al. [46] developed a framework to couple the rigid-body simulations performed by Goron et al. [44] with aeroelastic considerations. Their approach considered the aircraft to be beams joined to one another. The authors used a nonlinear Timoshenko beam theory.

In a series of papers by Nguyen and colleagues, the authors derived the equations for flexible aircraft's flight dynamics. The authors used an Euler-Bernoulli beam theory formulation for structural dynamics and the vortex-lattice code, Vorview, to obtain the aerodynamic loads. Theodorsen's theory accounts for unsteady effects. In an early paper, Nguyen [47] derived the equations for strain in a beam where the bending deflections were coupled to the torsional deflection via the slope of the wing pre-twist angle. Subsequently, the flight dynamics equations for six DoF motion of the aircraft were coupled to the structure's elastic response [48]. In [49], a detailed derivation of the aeroelastic angle of attack in the presence of deformation was presented. The paper also provided the partial derivatives of the angle of attack with respect to the states being solved-for. Ting et al. [50], developed a static aeroelastic model coupled with a three degree-of-freedom longitudinal trim flight dynamics model. The equilibrium equations were written in the stability axes. Analytic expressions for the Jacobian matrix were provided. The system was solved through Newton iterations. Thus, at any given flight condition, the trim aeroelastic configuration of the wing could be determined. They showed that the "trim angles of attack for the flexible models are higher than that of the rigid models due to the effect of the aeroelastic bending and torsion on the aeroelastic angle of attack." In [29], the authors investigated the inertial force effect on aircraft elasticity with geometric nonlinearity due to rotational and tension stiffening. The axial, bending, and torsion stiffnesses were fully coupled in the stiffness matrix. The partial differential equations which describe the coupled bending and torsion

motion of the wing due to aerodynamic, propulsive, and inertial forces were derived. The equations were solved using FEM with Hermite shape functions.

Drela [51] simplified the nonlinear beam equations derived by Rivello [52] to only account for wing up-down bending. The beam equations were coupled to a lifting line theory with roll rate, yaw, and yaw rate effects. The coupled nonlinear system was solved simultaneously using a Newton system for the structural and aerodynamic states. Subsequently, the tool ASWING [53] was developed, which coupled the flight dynamics equations with the aeroelastic system. ASWING uses the nonlinear Timoshenko beam theory developed by Minguet [54], an unsteady lifting-line model, and a structural damping model. Time marching was based on a 2nd order Backward Difference Formula (BDF).

Patil et al. [55, 56] modeled the aircraft as a set of beams attached to one another. Each beam was modeled using the geometrically exact mixed variational formulation. These equations are geometrically exact in the sense of no ad-hoc assumptions were made in their derivation. The aerodynamic analysis was performed using the finite-state approach. The finite-state aerodynamic theory of Peters and co-workers [57, 58, 59] allowed for a state-space representation of the aerodynamic problem with a low number of states. This theory includes compressibility effects and captures dynamic stall using the ONERA stall model. Finite elements in space and time were used to march in time and get the system's dynamic nonlinear behavior. Patil et al. [60] investigated the effects of structural and aerodynamic nonlinearities on static aeroelastic solution, flutter solution and, limit-cycle oscillations. The method was applied to the Goland wing. Patil and Hodges [61, 25] showed the importance of accounting for nonlinearities for highly curved and high aspect ratio wings, such as the HALE aircraft. They also showed the necessity of using correct cross-sectional analysis because the aeroelastic results are susceptible to the cross-sectional stiffness parameters. Chang et al. [62] extended the work to model multiple beams joined together to allow for fuselage and tails to be modeled.

Milne et al. [63, 64] showed the concept of a *mean axis* that “decouples the equations

of motion for flight dynamics from the equations for structural dynamics for small deformations”. Shearer, in the thesis [31] and paper [65], coupled the flight dynamics governing equations at a reference point on the aircraft with structural dynamics equations of GEBT and the aerodynamics equations of the finite-state theory. The propagation through time was performed using a novel modified Newmark time-marching scheme. The concept of mean axis was generalized to account for large deformations [66].

Murua et al. [67] coupled an unsteady vortex-lattice method (UVLM) with a nonlinear beam model to model the dynamics of a free-flying flexible aircraft. The UVLM is a time-domain aerodynamic model and provides a direct coupling to the time-domain beam theories. The UVLM also captures the interference effects between the lifting surfaces and the non-planar wakes, and is thus a higher-fidelity method than lifting-line or finite-state approaches.

Tuzcu, in the thesis [68] and papers [69, 70], developed a framework for aeroservoelasticity with both rigid-body motion and elastic deformations. The rigid-body motion consisted of six ODEs and beam ODEs for elastic deformation. All equations were written directly in the time-domain (state-space representation). It was shown that a zeroth order form exists for the maneuvers of the aircraft. In a paper by Tuzcu and Meirovitch [71], the authors investigated the coupling between rigid-body motion and aeroelasticity. Their investigation demonstrates that “it is not always safe to treat separately rigid body and flexibility effects in a flexible flying aircraft.” Meirovitch et al. investigated the impact of a flexible aircraft undergoing a time-varying pitch maneuver [72], and illustrated the drawbacks of using the mean axes to decouple the rigid-body motion from the elastic deformations inertially [73].

Neto et al. [74] developed an inertially coupled formulation that allows for an arbitrary choice of body-fixed reference frame, with small deformation assumptions. A thorough literature review of the mean axes and other axes systems was presented in the paper. The general framework was specialized to three-axes system commonly used in the literature.

2.2.4 Beam Model Generation

Hajela and Chen [75] presented an equivalent beam model. This approach represents the span-wise distribution of sectional moments of inertia and the torsional constant for a built-up wing structure for an equivalent beam. This kind of representation was referred to as a *stick model*. The section properties are scaled to account for shear lag effects. The use of a nominal “average material” concept to link geometrical data to cross-sectional stiffness properties has been explored. Gern et al. [76] used a hexagonal wing box, where the thickness of the six sides of a hexagon was varied to match the structure’s stiffness. Bindolino et al. [77] use a rectangular shape. Piperni et al. [78] presented another method for generating the stick model. They used thin-walled, single-cell sections to represent the wing box. Each wing box section was modeled with a set of skin-stringer panels, front and rear spars, and upper and lower spar caps.

Displacement Matching Approach

The idea of the displacement matching approach is shown notionally in Fig. 2.7. A higher-fidelity model, typically a 3-D shell model, is created. Unit loads are applied to the higher-fidelity model, and the displacement response is found. A beam model of the same length is created, and the same loading is applied. The beam stiffness constant, EI in this example, is found by matching the displacements as:

$$\delta_{shell} = \delta_{beam} \implies \delta_{shell} = \frac{FL^3}{3EI} \implies EI = \frac{FL^3}{3\delta_{shell}} \quad (2.9)$$

Elsayed et al. [79] presented a methodology for extracting an aircraft wing’s stiffness properties using its 3-D finite element model to be used in the stickmodel. A step-by-step approach is enumerated to obtain the bending stiffnesses I_{xx} , I_{yy} and I_{xy} , and the torsional stiffness I_{zz} , where the terms are as defined in the paper.

Palacios et al. [80] developed a method to construct a 1-D model from built-up 3-D

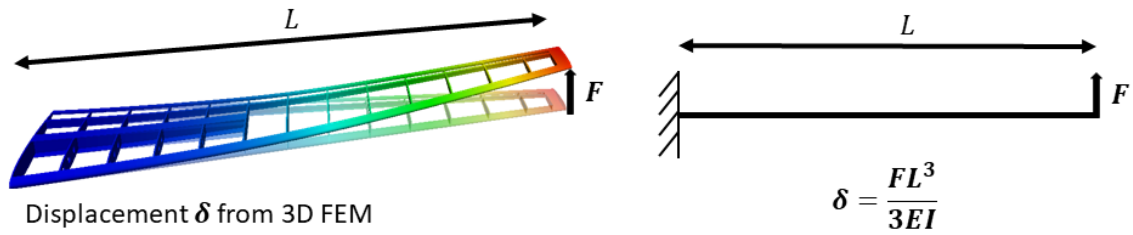


Figure 2.7: Notional depiction of displacement matching approach to stickmodel generation

FEM models. The 1-D beam model is written in modal coordinates, which reduces the number of degrees-of-freedom. Static condensation [81] of the 3-D FEM model is used to obtain the coefficients.

Cirillo [82] extracts beam stiffnesses and mass parameters from detailed FEM models. The stiffness of the empennage (horizontal tail, vertical tail, rudder) was extracted. The method is validated using modal analysis where the beam frequencies were compared to detailed FEM modal analysis frequencies.

Guyan Reduction

Guyan reduction is a mathematical technique commonly used in FEM analysis of structures. In FEM, the structure is represented as a mesh with a finite number of nodes, with each node having upto six degrees of freedom. For aerospace structures, the resulting stiffness matrix is very large and is computationally expensive to solve. The idea of Guyan reduction is to reduce the total DoF. The unloaded DoF are expressed in terms of the loaded DoF. The linear system solved in FEM is

$$\vec{f} = \mathbf{K} \cdot \vec{d} \quad (2.10)$$

where \mathbf{K} is the stiffness matrix, \vec{d} the displacement vector, and \vec{f} the applied force vector. The force vector is partitioned into a loaded ($\vec{f} \neq 0$) and unloaded ($\vec{f} = 0$) portions as:

$$\begin{bmatrix} \mathbf{K}_{ll} & \mathbf{K}_{lu} \\ \mathbf{K}_{ul} & \mathbf{K}_{uu} \end{bmatrix} \begin{bmatrix} \vec{d}_l \\ \vec{d}_u \end{bmatrix} = \begin{bmatrix} \vec{f} \\ \mathbf{0} \end{bmatrix} \quad (2.11)$$

Writing out the second equation

$$\mathbf{K}_{ul} \cdot \vec{d}_l + \mathbf{K}_{uu} \cdot \vec{d}_u = 0 \longrightarrow \vec{d}_u = -\mathbf{K}_{uu}^{-1} \mathbf{K}_{ul} \vec{d}_l \quad (2.12)$$

Substituting \vec{d}_u into the first equation gives:

$$[\mathbf{K}_{ll} - \mathbf{K}_{lu} \mathbf{K}_{uu}^{-1} \mathbf{K}_{ul}] \vec{d}_l = \vec{f} \quad (2.13)$$

Thus, the condensed stiffness matrix $[\mathbf{K}_{ll} - \mathbf{K}_{lu} \mathbf{K}_{uu}^{-1} \mathbf{K}_{ul}]$ is equivalent to the original problem, but expressed in terms of the loaded DoF.

2.2.5 Modal approach

A common approach used is the frequency-domain approach of representing the structural deformation using a set of orthogonal modes. This approach will be referred to as *modal approach*. A brief summary of the process is given next. Consider the equation of motion in time-domain

$$[M]\{\ddot{u}\} + [B]\{\dot{u}\} + [K]\{u\} = \{P(t)\} \quad (2.14)$$

where $\{u\}$ is the displacement at nodal locations, $\{\dot{u}\}$ the velocity, $\{\ddot{u}\}$ the acceleration, $\{P(t)\}$ the external forces, $[K]$ the stiffness matrix, $[B]$ the damping matrix, and $[M]$ the mass matrix. For a detailed finite element model, there can be thousands of grid points, each having upto 6 degrees of freedom. This makes the matrices defined to be quite large.

It is possible to solve an eigenvalue problem (neglecting damping) of the form

$$(\omega_i^2[M] + [K])\{\phi_i\} = \{0\} \quad (2.15)$$

to obtain the natural frequencies, ω_i , and the mode shapes ϕ_i . These mode shapes satisfy orthogonality such that

$$\{\phi_i\}^T[M]\{\phi_i\} = \{\phi_i\}^T[K]\{\phi_i\} = 0 \quad (2.16)$$

To use modal analysis in dynamic response, we assume the displacement vector to be a linear combination of low frequency modes

$$\{u(t)\} = [\phi_h]\{\xi(t)\} \quad (2.17)$$

where n_h are the number of low frequency modes considered. The equation to be solved reduces to

$$[M_{hh}]\{\ddot{\xi}\} + [B_{hh}]\{\dot{\xi}\} + [K_{hh}]\{\xi\} = \{P_h(t)\} \quad (2.18)$$

where $[M_{hh}] = [\phi_h]^T[M][\phi]$ is the generalized mass matrix, $[K_{hh}] = [\phi_h]^T[K][\phi]$ the generalized stiffness matrix, $[B_{hh}] = [\phi_h]^T[B][\phi]$ the generalized damping matrix, and $\{P_h(t)\} = [\phi_h]^T\{P(t)\}$ the generalized force vector. The assumption in Eq. 2.17 reduces the number of degrees of freedom to be solved to n_h , and hence reduces the computational time for flutter analysis and dynamic response. A detailed derivation of using modal analysis for dynamic response of structures is given by Hurty [83]. Waszak and Schmidt [84] explain the use of modal analysis in aeroelastic analysis. Lagrange's equations are derived coupling the aircraft rigid body states and the generalized coordinates associated with structural deformation. In obtaining the generalized forces, aerodynamic strip theory was used. The mode shapes (assumed to known from FEM) were used to influence the attack's aeroelastic angle. The paper also derives practical mean axes constraints.

The use of modal analysis is implemented in NASTRAN's SOL 145 (flutter) and SOL 146 (Dynamic Aeroelasticity) and is widely used in industry and academia. van Schoor and von Flotow [85] used FEM to obtain the mode shapes of the structure. Schmidt and Raney [86] used "elastic mode shapes to simulate an aircraft model with both longitudinal and lateral rigid body dynamics coupled with flexible structures." Pedro and Bigg [87] used "normal modes to develop an environment that incorporates pilot and gust modeling to study flexibility effects on piloted aircraft response." Karpel and colleagues [88, 89, 90, 30] used a frequency-domain formulation. They also developed state-space time-domain models for the control design process. They showed that "the state-space equations of motion are more suitable for time simulations and the interaction with control design algorithms with some accuracy loss because of the rational approximation." Saltari et al. [91] also derived the coupled equations of flight dynamics and elastic deformation with the beam structure on a mean axis. Recently, Medeiros et al. [92] used a modal analysis approach for nonlinear analysis

2.2.6 Higher-fidelity methods

The use of CFD, either Euler or Navier-Stokes equations, for aircraft design considering flight dynamics and aeroelasticity, is still computationally demanding [93]. One of the reasons for the high computational time is the need to perform mesh deformation every time the structure deforms. Palacios and Cesnik [94] coupled an Euler CFD solver for aerodynamics with a 1-D nonlinear beam theory for structural dynamics. 3-D displacements were recovered using the Variational Asymptotic Beam Sectional Analysis (VABS) [95] tool. They applied the method to a HALE aircraft. Garcia [96] coupled a nonlinear 12 DoF beam theory model with CFD to predict aeroelastic characteristics of a swept high-aspect ratio wings at transonic speeds. Garcia showed that the "washout due to the strong bending-torsion coupling inherent in swept wings." Garcia also showed a difference in the system's response between linear and nonlinear modeling. Raveh and Karpel [97, 98] use

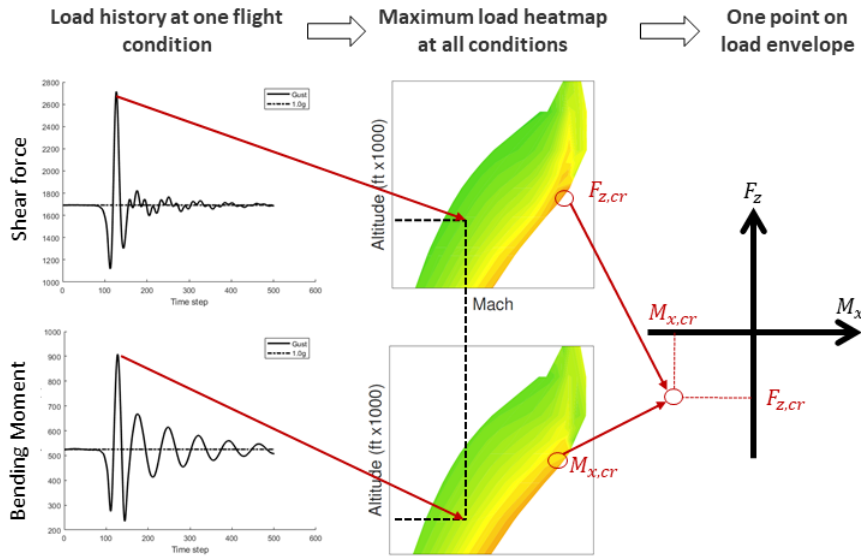
Table 2.2: Methods used in the literature for aerodynamics and structural dynamics

Discipline	Method	Paper
Aerodynamics	Lifting line	[51, 53]
	Lattice methods	[49, 50, 67]
	Finite-state theory	[56, 61, 66, 65]
	CFD	[93, 96, 94], [97, 98, 99]
Structural Dynamics	Modal Analysis	[83, 84, 86, 87], [88, 89, 90, 30, 97, 98]
	StickModel	[47, 48, 49, 50, 29], [51, 53], [56, 61, 66, 65, 94]
	FEM	[99]

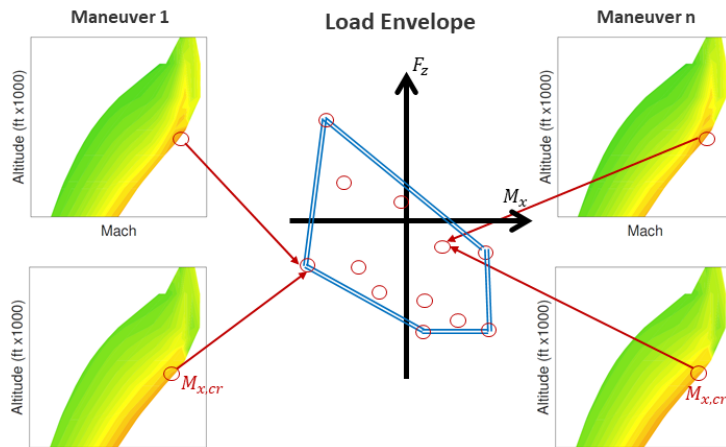
modal analysis for the structure and time-accurate CFD used to obtain generalized aerodynamic forces.

2.2.7 Critical load determination

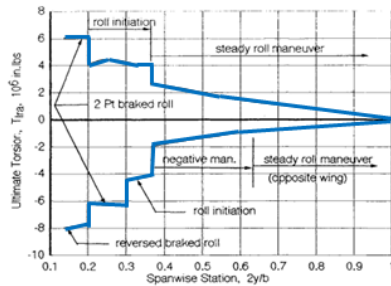
14 CFR provide all the necessary information to precisely simulate the maneuver. An example maneuver was described in Section 2.2.1. When such a simulation is executed for a given flight condition, a load time history is obtained, as shown in the left of Fig. 2.8a. The peak shear force and bending moment for this condition correspond to a single point on the flight envelope. Repeating this process for every point in the flight envelope allows for a heat map to be generated, as shown in the middle of Fig. 2.8a. The most critical loads here are used to populate a single point on the load envelope, as shown to the right of Fig. 2.8a. Performing several such maneuvers results in multiple points on the load envelope, as shown in Fig. 2.8b. The load envelope shown in Fig. 2.8b is representative of one for the horizontal tail. Representative load envelopes for the wing and vertical tail are shown in Fig. 2.8c and Fig. 2.8d respectively. The above is the general process of obtaining critical loads for which the airframe must be sized. The simulation step involves a tight coupling between aerodynamic, structural dynamics, and flight mechanics as seen in the loads group of Fig. 1.4.



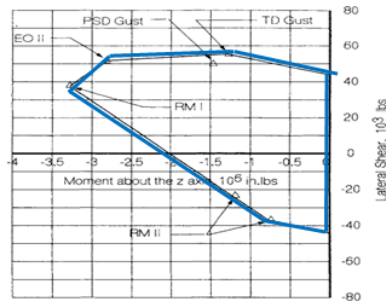
(a) Dynamic simulation of one maneuver to obtain a point on the load envelope



(b) Multiple maneuvers to build a load envelope



(c) Representative max/min plot for spanwise torsion of a wing [100]



(d) Representative load envelope of a vertical tail [100]

Figure 2.8: Process of building load envelope based on maneuvers

The approach described above is very conservative. Other approaches exist in the literature to convert dynamic loads into a set of static load cases [101, 102, 103, 104, 105, 106]. For practical aerospace problems, this leads to a large number of static load cases. Standard approaches have been developed in the industry to downselect to a set of critical load cases for which sizing is performed.

2.2.8 Summary

The literature on loads generation is summarized as the following observations:

Observations: Loads Generation

- The aircraft loads generation process is a time-domain problem requiring dynamic simulations, with strong coupling among the disciplines of structures, aerodynamics, flight mechanics, and propulsion.
- For the analysis to be computationally tractable, the methods in the literature focus on low DoF models.
- The intent of the analysis is focused on obtaining a load history and critical loads. There is sparse literature on coupling the loads' generation with structural analysis and structural failure computation.
- Methods to obtain the low DoF stiffness and mass matrices for dynamics rely on running a shell model.

2.3 Aircraft Wings Structural Analysis Methods

Methods of Megson [107] and Peery [108] are typical of traditional aircraft structural analysis. Here, idealizations were used to reduce the problem to plates, shells, or beams. The methods described are highly decoupled and thus simple enough to solve by hand. For

example, the vertical stiffeners were idealized as a beam-column of varying cross-sections between the upper and lower skin. Axial, shear, and lateral loading were applied to it. The beam can be treated as simply-supported with rotational restraints, thus providing any fixation degree at the upper and lower skin attachments, between pinned and fully fixed.

Strength of materials based calculations continues to be used today to predict stresses and strains in skin and stringers [109]. Nui's Airframe Structural Design book [110] provides the equations to test for the strength given input geometry, loading, and material properties. These equations can be coded to automate the process and are being used for structural design [111]. Takahashi and Lemonds [112] sized the structure based on tensile, compressive, and buckling considerations to produce a minimum wing weight. Multiple loading conditions were used to size the skin, transverse wing stringers, and wing spar caps.

Altus and Kroo [113] represented the wing as a box beam and performed MDO using the Optimizer-Based Decomposition (OBD) architecture, coupling aerodynamics and structural analysis. The wingbox structural weight was computed empirically. Ning and Kroo [114, 115] performed trade studies for a C-wing configuration. The wingbox was treated as a box-beam. Stresses were computed using the strength of materials calculations. The structural weight prediction was based on a single loading parameter – the root wing bending. Xu and Kroo [116] consider the aircraft conceptual design accounting for maneuver load alleviation, gust load alleviation, and natural laminar flow.

Elham et al. [117] also represented the wing as a box-beam to obtain the wingbox weight. The secondary weights of the aircraft (flaps, slats, etc.) were obtained from empirical methods. Sizing was performed using the strength of material analytical formulae. Aerodynamic loads were obtained using AVL and XFOIL.

Hajela [118, 75] represented the wing by equivalent beam models and provided a method to estimate the optimum weight. The structural optimization method used was a fully stressed design. Stresses were obtained using Euler-Bernoulli beam theory equations. The method was applied to a joined-wing configuration.

Giles [119, 120] represented the wing box as an equivalent plate. The width and thickness of the plate can be varied along the span. The skin was assumed to be made of orthotropic layers. The Rayleigh-Ritz method was used to obtain the approximate static solution. Krishnamurthy and Mason [121] presented an equivalent plate method to match the stiffness and natural frequency of an aircraft wing. The method depended on the solution of a full FEM model to obtain the displacement field. Riks [122] presented a finite strip approach for the buckling and post-buckling analysis of wing box stiffened skin-panels. Sexstone [123] developed a methodology to use the tool Equivalent Laminated Plate Solution (ELAPS) tool to perform aircraft mass property analysis. The paper described the structural analysis and weight analysis capability of the tool. These approaches idealized the wings to be stiffened plates/shells.

Bindolino et al. [77] represented the wingbox as a rectangular box beam. CFD analysis was used to obtain the loads. The beam load resultants were used to compute the skin and web panel shear stresses. MDO was carried out using NASTRAN SOL200. Ajaj et al. [124] assumed the wingbox to be a thin-walled beam. Sizing of components were done using closed-form equations based on beam theory and strength of materials formulae. The weight of secondary wing structures was estimated using semi-empirical equations. Gern et al. [76] developed a bending weight calculation process for the strut-braced wing. The wing box was assumed to be comprised of top and bottom plates which resist the bending moment. The loads on the wing were computed using a VLM.

The preceding discussion shows that beam models are used for their low computational cost and provide reasonable accuracy. The subsequent subsections will explore beam models in more detail.

2.3.1 Beam Theories for Structural Analysis

Variational Asymptotic Method (VAM)

The Variational Asymptotic Method (VAM) is a rigorous beam theory approach in the literature. Appendix C provides all the mathematical machinery of VAM applied to beams. This section provides an overview of the method and references to literature on the development, implementation, validation, and application.

The Variational Asymptotic Method (VAM) was developed by Hodges et al. [125] to perform structural analysis in a computationally efficient manner. Fig. 2.9 shows the overall process. When applied to beams, VAM splits the analysis into three parts.

The first part deals with the 2-D cross-sectional analysis. Unlike existing beam theories such as Euler-Bernoulli and Timoshenko beam theory, VAM does not assume the cross-section is rigid- the cross-section is allowed to warp. The 2-D cross-sectional analysis aims to determine the warping, stiffness matrix, and mass matrix. VAM employs asymptotic expansion of the energy functional (instead of a system of differential equations [126, 127, 128]) in terms of the small parameters (a, l, R) and makes the modeling more compact and variationally consistent; i.e., all variables follow naturally from a minimization problem based on the variational principle. Minimizing the cross-section's strain energy functional, with a constraint on the average warping over the entire cross-section, provides the warping variable's solution. The derivative of the strain energy then provides the stiffness matrix. Similarly, the derivative of the kinetic energy provides the mass matrix.

The second part is the 1-D nonlinear analysis phase. The stiffness and mass matrices at cross-sections along the span of the structure produce a beam model. Section 2.3.2 provides details of two beam theories from the literature. The beam analysis solution results in displacement and load resultant solutions along the 1-D beam reference line.

The final part is the recovery of 3-D displacements, strains, and stresses. Using the 1-D displacements and warping solutions, one can extract the 3-D displacements at each node

of the cross-sections using VAM equations. The displacement solutions and the solutions of forces, moments, and momentum yield 2-D strains. The 3-D strains, and consequently, 3-D stresses, are obtained by transforming the 2-D strains to 3-D strains using warping variables.

Rajagopal and Hodges [129] made some recent advancements to the cross-sectional analysis with regards to taper and cross-sectional obliqueness. Chen et al. [130] presented a comprehensive validation study for a VAM-based beam analysis against 3-D FEM for rotor blade structures. Gupta et al. [131] validated the method for thin-walled beams.

Based on VAM, the Variational Asymptotic Beam Section (VABS) [132] and the Geometrically Exact Beam Theory (GEBT) [133] were implemented for 2-D cross-sectional analysis and 1-D beam analysis, respectively. Liu and Yu [134, 135, 136] have developed an approach to solve complex sections using Mechanics of Structural Genome (MSG) where a 3-D structural genome is identified and used to solve heterogeneous beams, but with periodic appearances of the identified structural genome.

VAM-based methods have been successfully used in the analysis and design of rotorcraft blades [137, 138, 139], wind turbines [140, 141], and very flexible aircraft such as HALE [142]. However, its applicability to the analysis and design of commercial aircraft has been limited.

Other Higher-Order Beam Theory Methods

Carrera et al. [143, 144] used a component-wise model where each component (stringers, panels, ribs) has a unique 1-D formulation. The authors obtained both the displacement field and stresses. The wing box was simplified to stringers, skin, and spars in the paper. In [143], the authors considered a NACA 2415 airfoil shape as the cross-sectional geometry. Pagani [145, 146] extended the formulation by Carrera to include dynamic response and aeroelastic effects. Recently, the Carrera Unified Formulation (CUF) has been applied to beams [147] and shells [148, 149]. Another higher-order theory for cross-sectional analysis

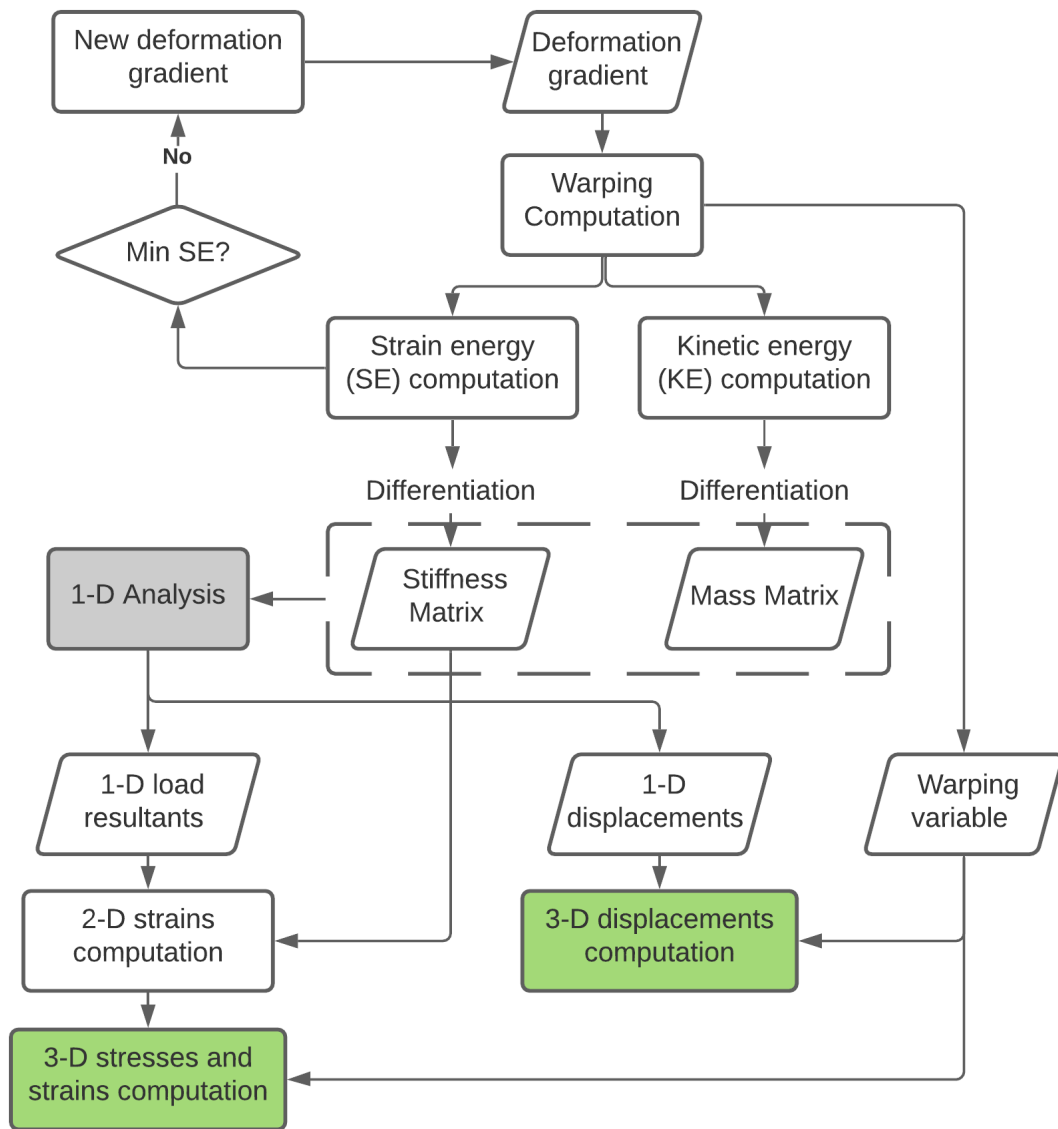


Figure 2.9: Process flowchart describing the sequence of calculations for VAM

is BEam Cross-sectional Analysis Software (BECAS) [150]. The code is written in Matlab and works for anisotropic materials and inhomogeneous beams of arbitrary cross-section.

2.3.2 1-D Analysis Beam Theories

In this section two nonlinear beam theories that have been applied to the dynamic analysis of aircraft are presented.

Nonlinear Timoshenko Beam Theory

Drela [53] presents an aero-servo-elastic tool named ASWING. The documentation of ASWING contains all the equations of a nonlinear Timoshenko beam theory developed for the structural dynamic analysis of aircraft [54]. Appendix A contains equations and algorithms to implement the beam theory. Here, a summary is presented.

The quantities tracked at each node are shown in Table 2.3. They include nodal positions, Euler angles, translational and angular velocities, translational and angular accelerations, and reaction forces and moments.

Table 2.3: Quantities tracked by the nonlinear Timoshenko beam theory

Variable	Body-fixed axes for “i”-th node
$\vec{r}_i = \{x_i, y_i, z_i\}$	Position
$\vec{r}_i = \vec{u}_i = \{u_i, v_i, w_i\}$	Nodal velocities
$\ddot{\vec{r}}_i = \ddot{\vec{u}}_i$	Nodal acceleration
$\vec{\theta}_i = \{\psi, \theta, \phi\}$	Euler angles triad
$\vec{\omega}_i = \{p_i, q_i, r_i\}$	Nodal angular rates
$\dot{\vec{\omega}}_i$	Nodal angular acceleration
$\vec{F}_i = \{F_x, F_y, F_z\}$	Force resultant
$\vec{M}_i = \{M_x, M_y, M_z\}$	Moment resultant

With a state vector defined as $X = \{\vec{r}, \vec{\theta}, \vec{F}, \vec{M}, \vec{u}, \vec{\omega}\}^T$, the governing structural equations can be written in residual form as $R(X, \dot{X}) = 0$, where the quantities in \dot{X} are the time derivatives of the quantities in X . First order finite differencing can be used to relate the states to their derivatives as follows:

$$X_n = \frac{1}{t_n - t_{n-1}} X_n + \frac{-1}{t_n - t_{n-1}} X_{n-1} \quad (2.19)$$

For each node there are 18 variables to be solved for. If n is the number of nodes for a flexible surface, each flexible surface has $18n$ unknowns. The equations to solve the system

are:

1. Element equations

- (a) $3(n - 1)$ Force equilibrium equations
- (b) $3(n - 1)$ Moment equilibrium equations
- (c) $3(n - 1)$ Moment-curvature relationships
- (d) $3(n - 1)$ Strain-displacement relationships

2. Boundary conditions

- (a) 6 conditions at the root
- (b) 6 conditions at the tip

3. Nodal equations

- (a) $3n$ transformations: $\vec{r}_i = \vec{u}_i$
- (b) $3n$ transformations: $\vec{\theta}_i = [C] \vec{\omega}_i$ (matrix C relates the Euler angle rates to angular velocities)

In addition, there are 12 equation-variable pairs for each “joint” in the system. Joints are used to transfer forces and moments from one beam to the other. They also enforce the constraints that the relative position and orientation between the beams (at the joint) must remain invariant. The structural dynamics formulation for this work uses nonlinear beam theory including shear deformation, for which the discretized equations are presented in Appendix A. Fig. 2.10 shows a notional representation of the aircraft represented as a stickmodel.

Geometrically Exact Beam Theory (GEBT)

GEBT is a beam theory code implemented by Yu and Blair [133]. It utilizes the mixed variational formulation of the geometrically exact intrinsic beam theory developed by Dr.

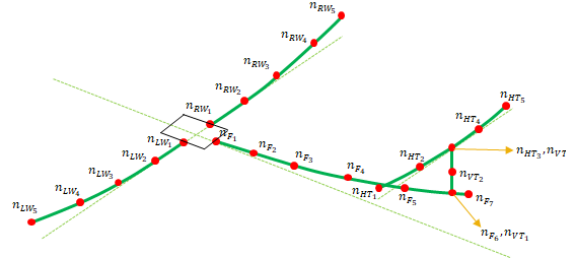


Figure 2.10: Aircraft stick model

Hodges [151]. The equations of GEBT are summarized in Appendix C.

GEBT uses a right-hand coordinate system. The beam coordinate system is denoted by x_1 , x_2 and x_3 , where x_1 is along the beam axis and x_2 and x_3 are the local Cartesian coordinates of the cross section. For static and dynamic analysis, GEBT tracks the quantities shown in Table 2.4.

Table 2.4: Quantities tracked by GEBT

Variable	Description
$\{u_1, u_2, u_3\}$	Position
$\{\theta_1, \theta_2, \theta_3\}$	Euler angles triad
$\{F_1, F_2, F_3\}$	Force resultant
$\{M_1, M_2, M_3\}$	Moment resultant
$\{P_1, P_2, P_3\}$	Linear momentum
$\{H_1, H_2, H_3\}$	Angular momentum

GEBT has the capability to perform the following types of analyses:

1. Static
2. Steady-state
3. Dynamic
4. Eigenvalue

For dynamic analysis, the load history is provided to GEBT in the form of time functions.

Discontinuous Beams

Curvature discontinuities along the span of the beam result from flexural-stiffness jumps, which reflect abrupt changes in the material properties and/or the cross-section geometry. There exist methods in the literature to handle discontinuities for so-called 2-D Euler-Bernoulli beams [152, 153, 154]. The methods described have not been applied to the spatial beam theories typically used for aircraft dynamic load prediction and stress analysis.

2.3.3 Structural Failure Theories

Consider a state of stress at a point represented in matrix form as:

$$\begin{bmatrix} \sigma_{11} & \sigma_{12} & \sigma_{13} \\ \sigma_{12} & \sigma_{22} & \sigma_{23} \\ \sigma_{13} & \sigma_{23} & \sigma_{33} \end{bmatrix} \quad (2.20)$$

It is possible to find principal stresses σ_1 , σ_2 , and σ_3 for this state of stress. For metallic components where ductile fracture is the primary failure mechanism a number of theories exist [155]:

- Rankine or Maximum Principal stress theory: $\max(\sigma_1, \sigma_2, \sigma_3) \leq \sigma_Y$
- Tresca or Maximum Shear Stress Theory: $\sigma_1 - \sigma_3 \leq \sigma_Y$
- von-Mises Criterion - Maximum Shear Strain Energy Theory:

$$\frac{1}{\sqrt{2}} \sqrt{(\sigma_1 - \sigma_2)^2 + (\sigma_2 - \sigma_3)^2 + (\sigma_1 - \sigma_3)^2} \leq \sigma_Y$$

where $s\sigma_Y$ is the yield stress of the material. The von-Mises criteria are the most widely used failure theory used.

For composite materials, it is more common to use strains instead of stresses when defining failure criteria. In this work a simplification is made to only consider metallic components, though the method developed can be applied to composite materials as well. A

detailed treatment of composite material failure is given by Carlson and Kardomateas [156] and Talreja and Singh [157]

2.3.4 Summary

The literature on structural analysis is summarized as the following observations:

Observations: Structural Analysis

- Aircraft wings are complex structures with intricate features, each responsible for bearing the loads
- In the early stages of design, stiffeners' effect is included in the model through the smearing approach. Creating equivalent 2-D structures for stiffeners of varying topology, dimensions, and rib spacing is not done in the literature
- Shell models are the most common structural analysis methods for the wing-box.
- Beam models have been used for structural analysis, but with assumptions on the geometry or material or using simple beam theories. The use of higher-order beam theory considering technologies has been explored for loads but not for structural analysis
- Existing 1-D beam theories do not work well in the presence of aperiodicity along the span of the beam
- Higher-order beam theory methods have been used for the structural analysis and design of rotorcraft blades, but not aircraft wings

2.4 Multi-Disciplinary Design Optimization (MDO)

Multidisciplinary design optimization (MDO) has emerged as a powerful tool with a wide range of applications. MDO methods account for the interdisciplinary interaction of systems that involve multiple disciplines. It enables the true optimum of the coupled system to be determined. Aircraft design is inherently a multidisciplinary process. Fig. 1.4 showed some of the disciplines involved in the early-stage design process. This section explores the literature on MDO as it pertains to aircraft design.

Cavagna [158, 159] and his group developed a tool named NeoCASS to perform structural sizing and optimization considering aeroelasticity. The toolkit provided the flexibility to use varying levels of fidelity in the structural and aerodynamic disciplines. It used a combination of physics-based methods and semi-empirical regressions to perform sizing.

Piperni et al. [160, 78, 161] described an MDO environment named VADOR. Aerodynamics was considered through the use of CFD. Skin, cap, stringers, and spars were considered, and structural sizing was performed assuming a shell model. Loads were obtained from the aeroelastic analysis, where a stickmodel was used. The stickmodel was extracted from the full FEM. Asymmetric Subspace Optimization (ASO) MDO architecture was used. Deblois and Abdo [162] decomposed the aircraft design problem into smaller sub-problems, optimized each sub-problem, and ensured consistency with the top-level optimizer. Sizing was performed based on two critical maneuvers defined in 14 CFR 25.331(b): 2.5g and -1g. For both metallic and composite components, skin and stringers in each bay were sized to consider both stress and buckling considerations [163]. Metallic components were sized using a genetic algorithm, whereas composite ones were sized using an interior point method.

Maute et al. [164] coupled 3-D Euler equations with 3-D FEM to optimize a nonlinear aeroelastic system for steady-state conditions. Gradient-based optimization was used to arrive at a local optimum. The gradients for the coupled system were found using the

adjoint method.

Kennedy [165] developed a parallel finite-element code called Toolkit for the Analysis of Composite Structures (TACS). The code was designed for the analysis of stiffened, thin-walled, composite structures. Skins, spars, and ribs were represented as shell elements in the formulation. TACS allows for the parallel-analysis and gradient evaluation using the adjoint method for aircraft components. In a series of papers, Kennedy et al. [32, 166, 167, 168, 169, 170, 171] performed high-fidelity aerostructural optimization for aircraft wings.

In [168], the aerodynamic code was solved using GMRES with a block Jacobi ILU preconditioner. TACS used GMRES and the Krylov method GCROT to solve the non-symmetric, linear systems. The geometry parametrization for both aerodynamic and structural meshes was based on free-form deformation (FFD) volumes. Panel strength and buckling constraints were imposed. The constraints were aggregated using Kreisselmier-Stienhauser (KS) constraint aggregation technique. Multiple KS functions aggregating similar structural components were used, rather than using a single KS function overall stress constraints in the entire structure. Four aerostructural solvers (nonlinear block Jacobi, Newton Krylov, nonlinear block Gauss–Seidel and approximate Newton Krylov methods) are compared based on solution times. The authors concluded that the Newton Krylov approach was an efficient and robust solution technique.

In [32], aeroelasticity was considered with the aerodynamic analysis performed using a panel method, and structural analysis performed using TACS. Blade stiffeners were included in the structure with associated design variables and were smeared into the panels. A parallel Newton Krylov method was described for the solution of the coupled aerostructural system of equations.

Jacobson et al. [99] used higher-fidelity methods to optimize a wing subjected to dynamic aerodynamic loading. The structure was represented using high DoF shell elements. The unsteady aerodynamics was computed using CFD. The objective function for optimization was evaluated using time-averaged quantities. The maximum stress over the con-

sidered time interval was imposed as the structural constraint. The authors did not couple the aeroelastic model with aircraft flight dynamics in this work.

Hwang and Martins [172] developed an open-source geometry modeling tool named GeoMACH. GeoMACH was created with the intent of a geometry-centric approach to MDAO. In a review paper by Martins and Hwang [173], the authors detailed various approaches to obtain the derivatives of computational models. The authors note that gradient-based optimization for a large number of design variables requires fewer function evaluations than meta-heuristic optimizers. In another review paper, Martins and Lambe [174] survey multidisciplinary design-optimization architectures that have been presented in the literature. Jasa et al. [175] developed an open-source aerostructural optimization named OpenAeroStruct. OpenAeroStruct uses a panel method to obtain the loads. The structure is modelled as a circular beam using E-B beam theory. OpenAeroStruct has recently been enhanced to use a wingbox structure [176]. Static aeroelastic considerations were considered while performing optimization.

Based on the preceding discussion, it was seen that most MDO methods assume static analysis. A DSM for static aero-structural MDO is shown in Fig. 2.11. These MDO methods allow for the simultaneous aerodynamic shape and internal structural optimization. However, current MDO methods in the literature do not account for dynamics.

2.4.1 Constraint Aggregation Techniques

When performing structural optimization, the constraints imposed are usually on strength and buckling criteria. Consider a simple von-Mises yield stress criteria for isotropic metallic components:

$$\sigma(\zeta, x, \mu) \leq \sigma_Y \implies g = \frac{\sigma(\zeta, x, \mu)}{\sigma_Y} - 1 \leq 0 \quad (2.21)$$

where ζ is a point in the structural domain Ω , x the state variables of the governing equations being solved, μ the design variables, and σ_Y the yield stress value of the material. As it is not possible to know apriori where the maximum stress will occur in the structure, it

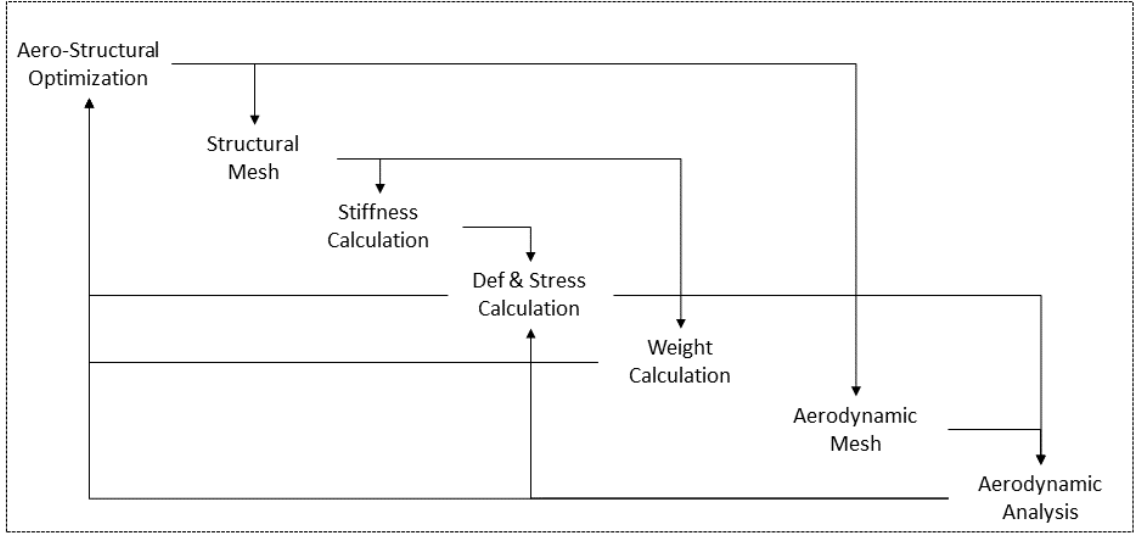


Figure 2.11: Static aeroelastic design process

is necessary to impose this constraint throughout the structure. In a discretized setting, this results in a stress constraint at every nodal point of the mesh. Such a formulation drastically increases the size of the optimization problem.

One way to deal with the large number of constraints is to find the maximum stress violation and impose it as a constraint:

$$\max_{\zeta \in \Omega} g \leq 0 \quad (2.22)$$

However, the max function is not differentiable and thus gradients cannot be found. Instead, a smooth function, c , can be constructed such that

$$\lim_{\rho \rightarrow \infty} c(\rho, g) = \max_{\zeta \in \Omega} g \leq 0 \quad (2.23)$$

where ρ is a parameter of the constraint aggregation function that controls its non-linearity. Thus the function $c(\rho, g)$ can be imposed as a constraint in the optimization problem. The readers are referred to Lambe et al. [177] for further details.

Implementing constraint aggregation for dynamic loads and simulations poses addi-

tional challenges. The constraint that must be imposed is that stress at every point in the structure must be less than the yield stress throughout the dynamic maneuver. As it is not possible to know apriori at which time the maximum stress will occur, stress constraints are placed at every spatial location and at every time. In literature, a large number of such constraints are typically handled using constraint aggregation techniques *spatially* [178, 179, 180]. Limited attention in literature [181, 182] has been given to imposing stress constraints using aggregation techniques in both space and time. This poses a challenge as the maximum stress over time must be used to size the structure. For these computational challenges, the dynamics loads obtained are converted into a set of static critical load cases, and structural sizing is performed for the static loads.

2.4.2 Adjoint

Consider a vector of state variables $x \in \mathbb{R}^{n_x}$ and a vector of design variables $\mu \in \mathbb{R}^{n_\mu}$. Consider a function of interest $F(x(\mu), \mu) : \mathbb{R}$, and governing equations written in residual form $R(x(\mu), \mu) = 0 : \mathbb{R}^{n_x}$. Given values for μ , the residual system of equations is first solved to obtain x . The function of interest can then be computed. The adjoint method is an efficient method to compute the total derivative (gradient) $\frac{df}{d\mu}$. Differentiating the function of interest gives

$$d_\mu F = F_x x_\mu + F_\mu \quad (2.24)$$

where $F_x \in \mathbb{R}^{n_x}$, $x_\mu \in \mathbb{R}^{n_x \times n_\mu}$, and $F_\mu \in \mathbb{R}^{n_\mu}$. Next consider the residual system of equations:

$$R(x(\mu), \mu) = 0 \implies d_\mu R = 0 \quad (2.25)$$

Expanding the total derivative,

$$d_\mu R = R_x x_\mu + R_\mu = 0 \implies x_\mu = -R_x^{-1} R_\mu \quad (2.26)$$

Substituting the above into the derivative of the function of interest gives:

$$d_\mu F = F_x x_\mu + F_\mu \quad (2.27)$$

$$= F_x [-R_x^{-1} R_\mu] + F_\mu \quad (2.28)$$

$$= [-F_x R_x^{-1}] R_\mu + F_\mu \quad (2.29)$$

The bracketed term in the last equation can be viewed as the following linear system solution:

$$R_x^T \lambda = -F_x^T \quad (2.30)$$

where λ is called the *adjoint vector*. Eq. 2.30 is called the *adjoint system*. The derivative of the function of interest can now be written as:

$$d_\mu F = R_\mu \lambda^T + F_\mu \quad (2.31)$$

Thus the required gradient is computed as a two-step process:

1. First, solve the adjoint system Eq. 2.30 for λ
2. Compute the gradient using Eq. 2.31

It should be noted that no assumptions were made on the form of the function of interest F or the residual system of equations R . They may be linear or nonlinear equations. The adjoint system, Eq.2.30 is always a linear system. The reader should see Bradley [183] or Johnson [184] for further details.

Current literature focuses on the use of adjoint method in shell model structural sizing for *static* loads. The adjoint method for time-dependent problems poses challenges in computational time and computational memory [183]. As previously said, dynamic simulations with models which have large DoFs is computationally intractable for many-query applications such as optimization. Further, the adjoint method requires the entire state history

of the forward-simulation to be stored and used in the adjoint-simulation [181, 182]. For models with large DoF this can be gigabytes of data for a single simulation.

2.4.3 Summary

The literature on MDO is summarized as the following observations:

Observations: MDO
<ul style="list-style-type: none">• Multi-disciplinary optimization methods have become mature in the literature for static loads• For a large number of design variables, gradient-based optimization is needed. The efficient computation of gradients can be done with the adjoint method.• To deal with a large number of constraints typical in structural optimization, constraint aggregation techniques are used

2.5 Summary of Literature Review

In this chapter, we explored literature in the context of the question *How do we simulate, predict structural failure, and design aircraft to show compliance with 14 CFR regulations?* Four categories of literature were explored- what does the internal structure look like, what the loads on the aircraft, can the aircraft sustain the loads without failure, and multi-disciplinary design optimization. The gaps in the literature are summarized as the following:

Gaps in the literature

- Dynamic Loads
 - Gap 1: Coupling the loads generation with structural failure computation
 - Gap 2: Systematic extraction of beam stiffness constants accounting for couplings without running higher fidelity tools
- Internal Structure
 - Gap 3: Creating equivalent 2-D structures for stiffeners of varying topology, dimensions and rib spacing
- Structural Analysis
 - Gap 4: Existing 1-D beam theories do not work well in the presence of aperiodicity along the span of the beam
 - Gap 5: Simple beam theories used for stress recovery with limited considerations for airfoil shape and composites
 - Gap 6: Using VAM for structural analysis of aircraft wings
- Multi-Disciplinary Optimization (MDO)
 - Gap 7: MDO methods simplify simulations to statics
 - * Gap 7a: Adjoint in the time-domain applied to aircraft structural optimization
 - * Gap 7b: Constraint aggregation methods not extended for dynamics

CHAPTER 3

PROPOSED METHOD

First, recall the motivating question and research objective:

Motivating Question

How to account for dynamics while maintaining computational efficiency in structural analysis and optimization of early-stage aircraft wing design?

Research Objective

Develop a framework for aircraft wing design that

1. Dimensionally reduces complex 3-D structures to produce a low DoF structural analysis model
2. Obtain the gradient of the structural analysis model in the time-domain

Chapter 2 explored the literature and found existing methods to perform the dimensional reduction of structures. However, the methods have limitations or gaps that listed at the end of the chapter.

This chapter draws from the dimensional reduction methods from the literature to propose a computationally efficient structural analysis method for aircraft wings. Where there are limitations or gaps in the literature to apply the methods directly, research questions are formulated to fill the gaps. Solutions are hypothesized to answer the research questions.

3.1 Reduction of 3-D Features to 2-D¹

In the literature, it is evident that aircraft structures are complex. Fig. 3.1 (repeated from Fig. 2.2) shows the complexity of an important 3-D feature- the rib. It was observed that considering all the complexities early in the design was infeasible and not considered in the literature.

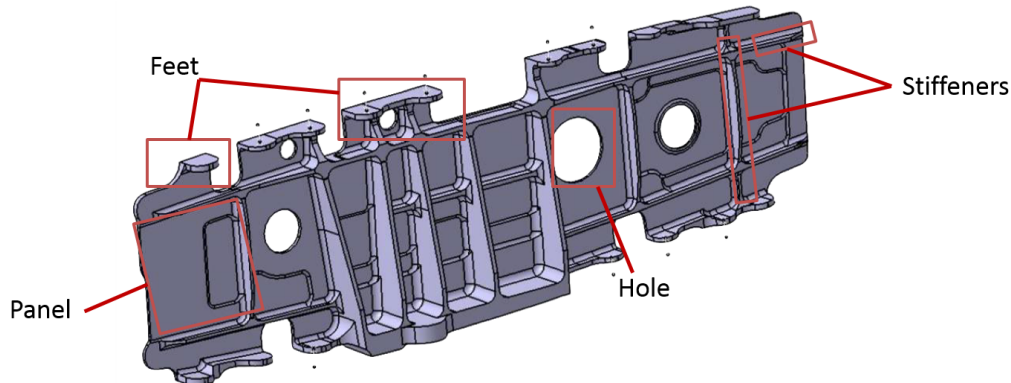


Figure 3.1: Complexity of an aircraft wingbox rib

The response of a rib depends mainly on its length and cross-sectional properties. The cross-sectional properties are dependent on two factors:

1. The cross-section geometric shape
2. Material properties and additional information such as layup orientation if composite materials are involved

A change in the cross-section geometric shape produces a significantly larger effect on the component's overall sectional properties than a change in material properties. It is for this reason that designers add stiffeners to a component. The addition of a stiffener makes a structure stiffer in one or more modes or avoid stress concentration in a particular region. In ribs, stiffeners oppose buckling and crushing loads. As the wing deflects upwards, it induces a buckling load on the upper skin panels. The addition of stringers opposes the

¹The method and results of this section have been published in a prior work [185, 186]

buckling of the skin panel. Thus, most aerospace structures are made of thin-walled stiffened panels that are more effective and efficient than a thicker panel at carrying the types of loads experienced by the aircraft.

For the reasons above, in the early stages of design, a subset of the rib's intricate components- the load-bearing stiffeners (vertical and horizontal)- are included. There is existing literature on techniques to include the effect of the stiffeners. The idea is shown notionally in Fig. 3.2a. The response of the structure with stiffener(s) (hereafter referred to as *built-up structure*) can be obtained by finding the response of a structure without the stiffener (hereafter referred to as *equivalent structure*) by modifying the material properties of the equivalent structure such that its energy is the same as that of the built-up structure.

Two approaches to generate the equivalent structure are shown in Fig. 3.2b and Fig. 3.2c. Fig. 3.2b shows the smearing approach that is extensively used in plate theory [187]. Here, the stiffener properties are smeared entirely on the base plate, thus having an equivalent plate of a uniform anisotropic material, whose material properties are now represented as a general 6×6 matrix, c_{ij} . The limitations of this method are:

1. Different stiffener topologies (such as blade stiffeners, hat stiffeners, T-stiffeners) on a single rib/skin cannot be accounted-for
2. Even for a single stiffener topology, the dimensions of each stiffener on the rib/skin must remain the same
3. Uniform spacing between the stiffeners is assumed

Thus a research question is formulated as

Research Question 1.1

How can an equivalent plate be created that accounts for stiffeners of varying topology, dimensions and non-uniform spacing?

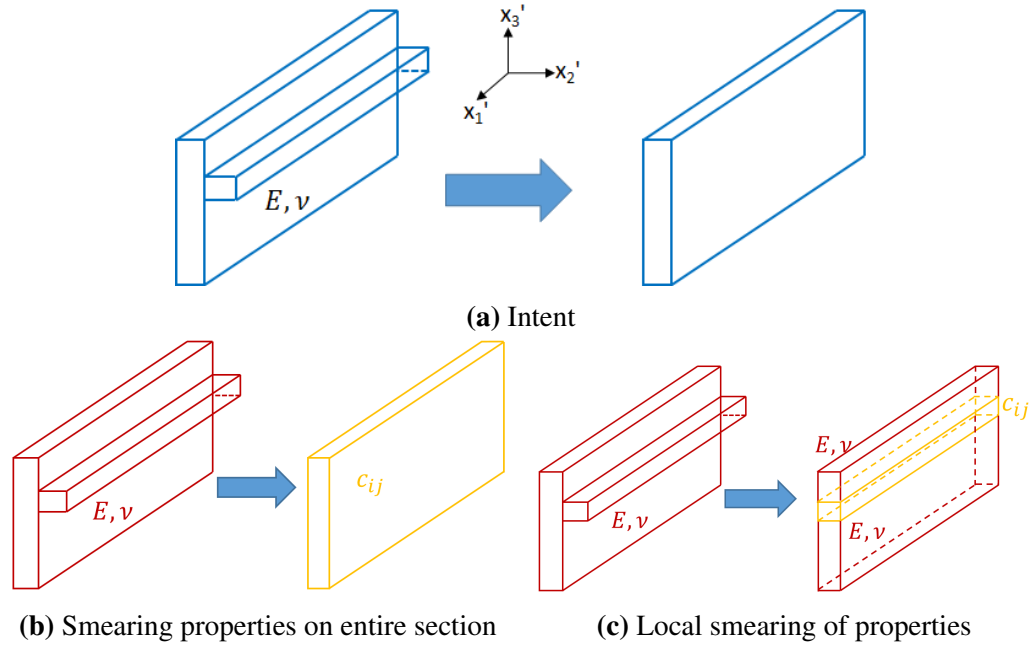


Figure 3.2: Methods to obtain equivalent section

This work proposes a new local smearing approach. The equivalent structure is treated as a composite plate as shown in Fig. 3.2c. The region where the stiffener is attached to the base-plate is modified to have anisotropic properties. The rest of the structure is unaltered.

In a prior work [185], the authors showed that it is possible to obtain equivalent orthotropic properties to match stiffness components in some (not all) directions. They did so by running many cases and fitting a surrogate model to understand the influence material properties have on the stiffness matrix. Creating a surrogate model is cumbersome, and a new one is required for every shape or dimension changes of the cross-section. Here, we generalize the approach to work for any arbitrary cross-section without generating surrogate models.

The problem is posed as a stiffness matching optimization. It boils down to finding the anisotropic material constants c_{ij} shown in Fig. 3.2. Given the sensitivities of the elements in the stiffness matrix S with respect to the material constants, it is possible to set up the

following optimization statement:

$$\begin{aligned} & \underset{c_{ij}}{\text{minimize}} \quad S_{\text{builtup}} - S_{\text{equivalent}} \\ & \text{subject to} \quad \text{Bounds on } c_{ij} \end{aligned} \tag{3.1}$$

The hypothesis for RQ 1.1 thus becomes

Hypothesis 1.1

If

1. smearing the stiffener of the built-up structure to the corresponding portion of the equivalent structure, thereby, accounting for the effects of stiffeners of varying topology, dimensions and spacing, and subsequently,
2. the anisotropic material properties of the composite equivalent structure computed as a stiffness matching minimization problem

converges to within first order optimality criteria,

Then,

the structural response of this equivalent structure matches that of the built-up structure.

3.2 Reduction of 3-D Wingbox to 1-D

In the literature on the generation of stickmodels (Section 2.2.4), it was observed that the current approaches rely on the generation of a higher fidelity model and using a displacement matching approach to obtain the beam stiffness properties. The higher fidelity model used is typically a shell model. Generating a shell model entails meshing the 2-D surfaces that form the shell model, applying appropriate boundary conditions, and applying appropriate material properties to each shell. In design, this process has to be done parametrically

and is a cumbersome step. Specialized tools [159, 32, 188] have been developed over years of implementation to facilitate this, but these tools are not always available open-source. It was noted that a gap in the literature exists to obtain the beam stiffness properties without running a higher fidelity model.

In the structural analysis literature (Section 2.3.1), it was observed that methods exist to obtain the beam stiffness properties. These methods rely on assumptions of the cross-sectional geometry. It is common to assume the cross-section to be a hollow circle [175] or a hollow rectangle [118, 77]. Such assumptions neglect the airfoil shape and result in inaccurate stiffness computation. An open-source tool – OpenAeroStruct [176] does account for the airfoil shape in the cross-sectional properties computation. However, less accurate beam theory analytical formulae are used. Further, the material is assumed to be metallic (isotropic), and thus composite materials cannot be used. Based on the aforementioned gaps, a research question is formulated as

Research Question 1.2

How to compute beam cross-sectional properties for a wingbox airfoil cross-section of arbitrary shape and material definition?

Higher-fidelity beam models such as VAM-based VABS (Section 2.3.1) exist in the literature to systematically compute the cross-sectional properties of any arbitrary shape and accounting of composite and anisotropic materials. VABS has been successfully applied to the analysis of rotorcraft blades, wind turbines, and the HALE aircraft. However, VABS has not been applied to the structural analysis of aircraft wings due to the aperiodicity and inhomogeneity along the beam’s span. This work proposes to use VABS for aircraft structural analysis. The hypothesis for RQ 1.2 is:

Hypothesis 1.2

If

VAM-based VABS is applied to an aircraft wingbox cross-section

Then,

beam cross-sectional properties of a wingbox airfoil of arbitrary shape can be calculated

3.3 1-D Analysis

It was noted that accurate beam theories exist to solve the 1-D analysis in the literature. Given loads (or load time history), the time marching scheme propagates the beam theory equations of motion forward in time to obtain a time history of nodal states given in Table 2.3.

Consider the beam governing equations written in residual form $R(X, \dot{X}) = 0$. The solver will attempt to find the values of the unknowns (elements of X) by driving the residuals of non-linear system of equations to zero. To start the time marching, the states from the trim solution can be given as the initial conditions. The residual system is solved using Newton iterations. The pseudo-code for the solver is given in Algorithm 1.

A key step in Algorithm 1 is a linear system solve $\left[\frac{\partial \vec{r}}{\partial \vec{x}} + k_0 \frac{\partial \vec{r}}{\partial \dot{\vec{x}}} \right] \vec{\delta}_x = -\vec{r}$. The form of

Algorithm 1: Structural Dynamics Time Marching

```
1 while  $t < t_{final}$  do
2    $t = t + \Delta t$ 
3    $\vec{x}_n = \vec{x}_{n-1}$  // Guess from previous solution
4    $\dot{\vec{x}}_n = 0$ 
5    $k_0 = \frac{1}{\Delta t}, k_1 = -k_0$ 
6   Convergence Flag = 0
7    $\vec{x} = \vec{x}_n, \dot{\vec{x}} = \dot{\vec{x}}_n$  // Initialize for current time step
8   while Convergence Flag  $\neq 1$  do
9     Compute residual vector  $\vec{r}$ 
10    Compute Jacobians  $\frac{\partial \vec{r}}{\partial \vec{x}}, \frac{\partial \vec{r}}{\partial \dot{\vec{x}}}$ 
11     $\left[ \frac{\partial \vec{r}}{\partial \vec{x}} + k_0 \frac{\partial \vec{r}}{\partial \dot{\vec{x}}} \right] \delta_x = -\vec{r}$  // Solve Linear System
12    if  $\|\vec{r}\|_2 < \epsilon$  then
13      Convergence Flag = 1
14    end
15    else
16       $\vec{x} = \vec{x} + \delta_x$  // New guess for  $\vec{x}$ 
17       $\dot{\vec{x}} = k_0 \vec{x} + k_1 \dot{\vec{x}}_{n-1}$ 
18    end
19  end
20   $\vec{x}_n = \vec{x}, \dot{\vec{x}}_n = \dot{\vec{x}}$  // Converged solution at a time step
21 end
```

the Jacobian of the linear system is as follows:

$$J = \begin{bmatrix} \frac{\partial Res_1|_{n_1}}{\partial r_x|_{n_1}} & \frac{\partial Res_1|_{n_1}}{\partial r_y|_{n_1}} & \cdots & \frac{\partial Res_1|_{n_1}}{\partial \omega_z|_{n_1}} & \frac{\partial Res_1|_{n_1}}{\partial r_x|_{n_2}} & \cdots & \frac{\partial Res_1|_{n_1}}{\partial \omega_z|_{n_n}} \\ \frac{\partial Res_2|_{n_1}}{\partial r_x|_{n_1}} & \frac{\partial Res_2|_{n_1}}{\partial r_y|_{n_1}} & \cdots & \frac{\partial Res_2|_{n_1}}{\partial \omega_z|_{n_1}} & \frac{\partial Res_2|_{n_1}}{\partial r_x|_{n_2}} & \cdots & \frac{\partial Res_2|_{n_1}}{\partial \omega_z|_{n_n}} \\ \vdots & \vdots & \vdots & \vdots & \vdots & \vdots & \vdots \\ \frac{\partial Res_{12}|_{n_1}}{\partial r_x|_{n_1}} & \frac{\partial Res_{12}|_{n_1}}{\partial r_y|_{n_1}} & \cdots & \frac{\partial Res_{12}|_{n_1}}{\partial \omega_z|_{n_1}} & \frac{\partial Res_{12}|_{n_1}}{\partial r_x|_{n_2}} & \cdots & \frac{\partial Res_{12}|_{n_1}}{\partial \omega_z|_{n_n}} \\ \frac{\partial Res_1|_{n_2}}{\partial r_x|_{n_1}} & \frac{\partial Res_1|_{n_2}}{\partial r_y|_{n_1}} & \cdots & \frac{\partial Res_1|_{n_2}}{\partial \omega_z|_{n_1}} & \frac{\partial Res_1|_{n_2}}{\partial r_x|_{n_2}} & \cdots & \frac{\partial Res_1|_{n_2}}{\partial \omega_z|_{n_n}} \\ \vdots & \vdots & \vdots & \vdots & \vdots & \vdots & \vdots \\ \frac{\partial Res_{12}|_{n_n}}{\partial r_x|_{n_1}} & \frac{\partial Res_{12}|_{n_n}}{\partial r_y|_{n_1}} & \cdots & \frac{\partial Res_{12}|_{n_n}}{\partial \omega_z|_{n_1}} & \frac{\partial Res_{12}|_{n_n}}{\partial r_x|_{n_2}} & \cdots & \frac{\partial Res_{12}|_{n_n}}{\partial \omega_z|_{n_n}} \end{bmatrix} \quad (3.2)$$

The Jacobian has a specific structure: the first 18 rows are the derivatives of 18 residual equations for the first node, rows 19 to 36 are the derivatives of 18 residual equations of node 2, etc. The first column is the partial derivative of a residual equation w.r.t. variable r_x at node 1. Columns 1-18 are the partial derivatives of a residual equation w.r.t. \vec{x} variables at the 1st node, columns 19-36 are the partial derivatives of a residual equation w.r.t. \vec{x} variables at the 2nd node, and so on. The Jacobian will have $18n \times 18n$ terms in it per beam.

In the presence of joints, six force and moment balance equations are removed from each node and replaced with six kinematic constraints. Hence, the appropriate rows in the Jacobian must be modified. Further, the Jacobian must be augmented with 12 rows and columns corresponding to each joint's equations. The sparse Jacobian nature for a case with three beams joined together is shown in Fig. 3.4.

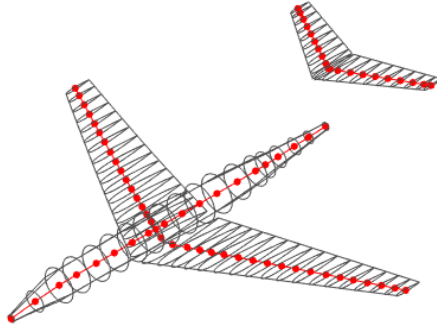


Figure 3.3: Stickmodel representation of a representative business jet

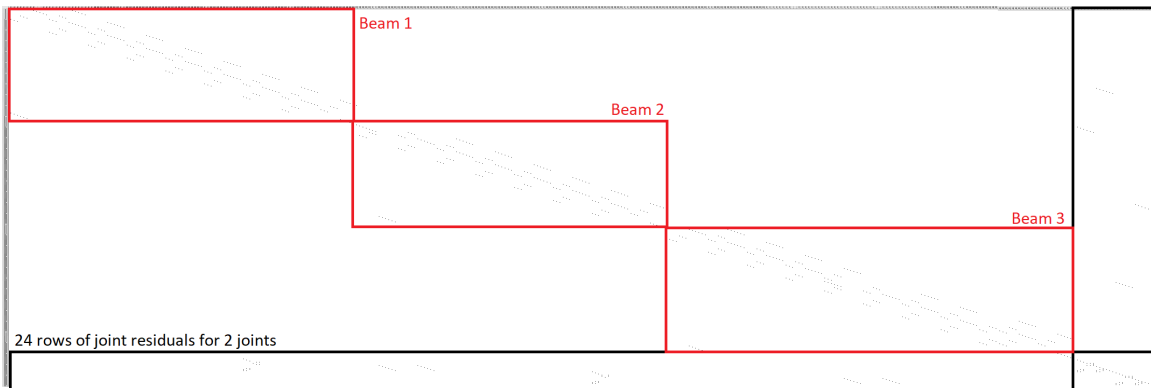


Figure 3.4: Jacobian matrix $\left[\frac{\partial \vec{r}}{\partial \vec{x}} + k_0 \frac{\partial \vec{r}}{\partial \vec{x}} \right]$ structure for three beams joined to another

For aircraft wings, the 1-D beam analysis poses a unique challenge. This is depicted notionally in Fig. 3.5. In the case that the 3-D part is complex, i.e., if it consists of discontinuous beam/strip-like elements such as stiffeners, along the length, then the need for an equivalent model arises (e.g., consider the presence of stiffened ribs in a beam-like structure as shown in Fig. 3.5a). The 3-D parts are dimensionally reduced to 2-D structures as shown in Fig. 3.5b, using a stiffness matching process described in Section 3.1. Each 2-D section is now theoretically made of a composite material whose properties depend on the choice of the matrix matching process from Section 3.1.

The overall structure now comprises regions with lower stiffness – those regions that only have skin, spars, and stringers, and regions of higher stiffness – those regions that have skin, spars, and stringers, and the composite rib. Referring to Fig. 3.6, we see that the ribs are located at discrete small regions along the span of the wingbox. This results in an

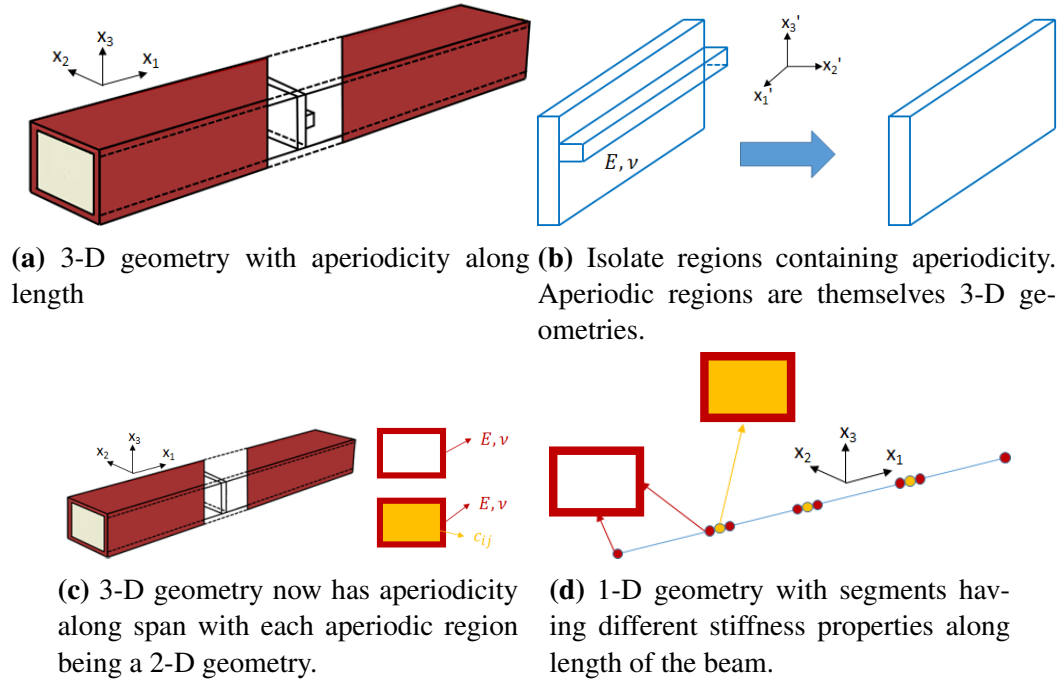


Figure 3.5: Presence of aperiodicity in the form of soft-stiff sections along the span of an aircraft wing represented as a beam

overall structure that is beam-like with *aperiodicity* along the span as shown in Fig. 3.5c and Fig. 3.5d.

Consider the baseline PEGASUS concept wing described in Appendix D.2. When represented as a beam, the static solver properties are:

- Jacobian matrix size: $\mathbb{R}^{342 \times 342}$
- Condition number: 367.60×10^9
- Rank: 342

It is noted that this matrix has a high condition number, even for simple beams. The soft-stiff sections cause numerical ill-conditioning in the Jacobian matrix, resulting in a singular matrix. The ill-conditioning is exacerbated for very thin structures close to yielding, which are typical in aerospace structures. Thus, robustly solving the 1-D analysis in an optimization framework is challenging.

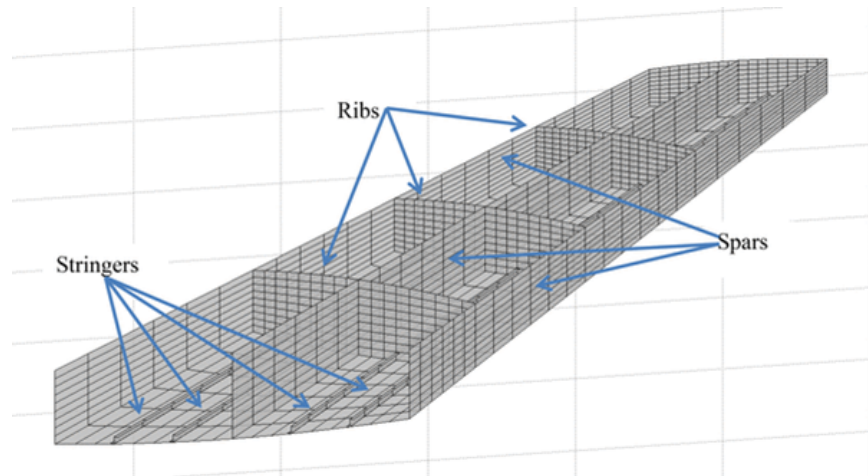


Figure 3.6: Internal structure of the aircraft wing. Taken from Moors et al. [38]

Exploring the pre-conditioning method to solve this problem is relegated to future work. Instead, in this work, the effect of neglecting the ribs will be considered. It is seen in the literature aircraft sizing neglecting the ribs produces reasonably good estimates of the weight [112, 176]. These effects will be studied further and quantified. The research question here is stated as:

Research Question 1.3a

How much accuracy is lost in the structural response and sizing calculations of the aircraft wingbox when its ribs are neglected?

Research Question 1.3b

How accurate is the displacement response when the wingbox structure is represented as a beam model?

3.4 1-D solution to 3-D fields

It was noted in Section 2.3.3 that to predict structural failure requires the computation of stress and strain fields on the entire wing structure. Simple beam theories such as E-B theory and Timoshenko theory have analytical formulae for the prediction of stress. These methods produce reasonable accuracy but do not predict stress concentrations accurately. The methods have also only been applied to the static analysis of aircraft structures [189]. The research question is stated as:

Research Question 1.4

How can stress and strain field time-history computations be made accurate and efficient when the aircraft wingbox structure is subjected to dynamic loads?

Higher-order beam theories, such as VABS, can more accurately predict the stress concentrations and work for dynamic analysis [189]. VABS has been applied for rotorcraft blades, but not to aircraft wings. The hypothesis is stated as

Hypothesis 1.4

If
VAM-based VABS is applied to aircraft wings,
Then,
it accurately computes stress and strain field time histories.

3.5 Structural Optimization for Dynamic Loads

The beam-based low DoF structural analysis method is now used to size aircraft wings. First, a scoping exercise is done to limit the number of design variables considered in this

dissertation. An adjoint method is proposed to obtain the required gradients for optimization. Finally, the structural optimization problem considered is formally stated.

3.5.1 Design Variables

It was noted in Section 2.1 that the wing's internal structure is complex, and only a subset of the variables are sized in the early stages of design. It was also noted in Section 3.1 that the stiffeners' primary function is to resist crushing loads on the rib and buckling of the skin panels. However, due to the limitations of beam theories pointed-out in Section 3.3, the ribs are not considered in this work. The sizing of stringers due to buckling loads is well-established in the literature [112, 110]. Due to the above reasons, the stiffeners are not considered in this work.

The primary wingbox consisting of the front spar, rear spar, upper skin, and lower skin will be considered in this work. The design variables considered are similar to other beam-based structural sizing tools [176]. However, dynamic simulations will be considered in this work instead of static ones in the literature.

3.5.2 Adjoint for Dynamic Simulations

It was noted in the literature on MDO (Section 2.4) that for a large number of design variables, gradient-based optimization is computationally efficient. Section 2.4.2 shows that the adjoint method is an efficient approach to obtaining the gradient. Current literature focuses on using the adjoint method in shell model structural sizing for *static* loads.

The adjoint method for dynamic loads has its own set of challenges. The governing equations for many systems of interest are second-order differential equations in time. It is possible to convert any second-order system into a first-order system using standard approaches. Any set of governing equations can be written generically in the form:

$$\mathbf{R}(\mu, \mathbf{x}, \dot{\mathbf{x}}, t) = \mathbf{0} \quad (3.3)$$

where $\mu \in \mathbb{R}^{n_\mu}$ represents the design variables, \mathbf{x} and $\dot{\mathbf{x}} \in \mathbb{R}^{n_x}$ are the state variables and their first derivatives w.r.t. time (denoted by t). It will also be observed that the chosen form of representing the system lends itself to a simple derivation of the adjoint system of equations.

Several methods exist for integrating the numerical differential-algebraic equations arising from the governing equations. Each method treats the discrete system of algebraic equations differently (for instance, requiring solutions from different time steps). Therefore, the adjoint system must be derived separately for each method. The adjoint system of equations is derived for the Backward Difference Formula (BDF) scheme due to its stability properties in this work. The state approximation of the BDF scheme is given by:

$$\mathbf{S}_i = \frac{1}{\delta_i} \sum_{j=0}^p \alpha_j \mathbf{x}_{i-j} - \dot{\mathbf{x}}_i \quad (3.4)$$

where α_k are the standard BDF coefficients.

In this work, a second order ($p = 2$) BDF scheme is implemented. The time derivative at a time instant is defined as:

$$\dot{\mathbf{x}}_i = \alpha_0 \mathbf{x}_i + \alpha_1 \mathbf{x}_{i-1} + \alpha_2 \mathbf{x}_{i-2} \quad (3.5)$$

with $\alpha_0 = \frac{1.5}{\delta_i}$, $\alpha_1 = \frac{-2}{\delta_i}$, and $\alpha_2 = \frac{0.5}{\delta_i}$. At each time-step, Newton iterations ($l = 0, 1, \dots$) are used to converge the system. The update to the state vector is:

$$\mathbf{x}_i^{l+1} = \mathbf{x}_i^l + \delta_{\mathbf{x}} \quad (3.6)$$

with

$$\left[\frac{\partial \mathbf{R}}{\partial \mathbf{x}_i^l} + \alpha_0 \frac{\partial \mathbf{R}}{\partial \dot{\mathbf{x}}_i^l} \right] \delta_{\mathbf{x}} = -\mathbf{R}^l \quad (3.7)$$

In the context of design through numerical optimization, an objective/constraint func-

tional can be expressed as a sum over time as:

$$f(\mu) = \int_0^T F(\mu, \mathbf{x}, \dot{\mathbf{x}}, t) dt \approx \sum_{i=0}^n \delta_i F_i(\mu, \mathbf{x}_i, \dot{\mathbf{x}}_i, t_i) \quad (3.8)$$

Here, the integrand F can be any arbitrary function of the state and design variables. What follows is a summary of the equations that will be used for the discrete-time adjoint system of equations [181]. The Lagrangian can be written as follows:

$$\mathbf{L} = \sum_{i=0}^n \delta_i F_i + \sum_{i=0}^n \delta_i \lambda_i^T \mathbf{R}_i + \sum_{i=0}^n \phi_i^T \mathbf{S}_i \quad (3.9)$$

where \mathbf{R}_i is the residual of the governing equations, \mathbf{S}_i the state approximations using the BDF scheme, λ and ϕ the corresponding Lagrange multipliers respectively, δ the step size in time, and subscript i denotes position in time.

Setting the partial derivative of the Lagrangian w.r.t. to the state variables to zero will reduce to a linear system of the following form at each time step, i :

$$\left(\frac{\partial \mathbf{R}_i}{\partial \mathbf{x}} + \alpha_0 \frac{\partial \mathbf{R}_i}{\partial \dot{\mathbf{x}}} \right)^T \lambda_i = - \left(\frac{\partial F_i}{\partial \mathbf{x}} + \alpha_0 \frac{\partial F_i}{\partial \dot{\mathbf{x}}} \right) - \left(\sum_{j=1}^p \alpha_j \frac{\partial \mathbf{R}_{i+j}^T}{\partial \dot{\mathbf{x}}} \lambda_{i+j} - \sum_{j=1}^p \alpha_j \frac{\partial F_{i+j}^T}{\partial \dot{\mathbf{x}}} \right) \quad (3.10)$$

After solving for the adjoint variable at each time step, the derivative of the functional of interest w.r.t. design variables can be found as:

$$\frac{\partial f}{\partial \mu} = \sum_{i=0}^n \delta_i \frac{\partial F_i}{\partial \mu} + \sum_{i=0}^n \delta_i \lambda_i^T \frac{\partial \mathbf{R}_i}{\partial \mu} \quad (3.11)$$

Eq. 3.10 shows that the adjoint method requires the entire state history of the forward-simulation to be stored and used in the adjoint-simulation [181, 182]. For models with large DoF, this data can be on the order of gigabytes in size for a single simulation.

Another challenge in implementing structural sizing for dynamic loads is the handling

of constraints. The constraint that must be imposed is that stress at every point in the structure must be less than the dynamic maneuver's yield stress. As it is not possible to know apriori at which time the maximum stress will occur, stress constraints are placed at every spatial location and at every time. In literature, a large number of such constraints are typically handled using constraint aggregation techniques *spatially* [178, 179, 180]. There exists some literature on imposing stress constraints using aggregation techniques in both space and time [181, 182]. However, to the best of the authors' knowledge, there have been no studies on performing aircraft wingbox design using gradient-based optimization techniques considering dynamics in-the-loop. This poses a challenge as the maximum stress overtime must be used to size the structure. For these computational challenges, the dynamics loads obtained are converted into static critical load cases, and structural sizing is performed for the static loads. The research question to address these gaps is stated as

Research Question 2.1

How can the gradient of aggregated strength-based failure criteria be computed efficiently during structural dynamic simulations?

In this work, for a given residual system of equations, the adjoint method for time-dependent problems solved with the stable BDF (Eq. 3.10 and Eq. 3.11) will be shown to require computation of six terms. This generalization allows for a generic adjoint solver to be implemented. The structure will be represented as beams to alleviate the computational costs- both runtime and memory. Stresses are obtained at points on each cross-section of the beam (space) and at each time-step of the simulation (time). The Kreiselmeier–Steinhauser (KS) constraint aggregation method will be extended to aggregate stress constraints in both space and time. The hypotheses for this research question is stated as:

Hypothesis 2.1

If

low DoF beam models, in place of high DoF shell models are used to represent the structure,

Then,

the computational cost (runtime and memory) reduces significantly.

And if

the spatial Kreisselmeier–Steinhauser (KS) constraint aggregation function is extended to include temporal aspects,

Then,

accurate predictions of the maximum strength constraint violation during the dynamic simulation are obtained.

Finally, if

the six quantities (Eq. 3.10 and Eq. 3.11) required for the adjoint method are computed for the beam model and the modified Kreisselmeier–Steinhauser (KS) constraint aggregation function,

Then,

the gradient of aggregated strength-based failure criteria can be computed efficiently during structural dynamic simulations.

3.6 Summary of Proposed Approach

Fig. 3.7 shows a flowchart with the steps of the proposed approach. The salient features of the novel structural analysis and optimization method are:

- The use of stiffness matching allows for stiffeners of varying topology, dimensions, and spacing to be smeared into the base plate creating an equivalent structure. This

process is referred to as 3-D Feature to 2-D.

- Using a higher-fidelity beam theory allows for the systematic reduction of the 3-D wingbox to a 1-D beam for any arbitrary cross-section and material definition.
- It is hypothesized that for early-stage aircraft design, the ribs may be neglected and the structural response and sizing will remain within acceptable error.
- Using a higher-fidelity beam theory allows for the accurate computation of stress and strain fields.
- The adjoint method in the time-domain for beams with constraint aggregation over cross-sections and time-steps produces an accurate and efficient gradient computation method.

The optimization problem solved in this dissertation is given as:

$$\begin{array}{ll}
 \underset{\text{Skin, Spar Thicknesses}}{\text{minimize}} & \text{weight} \\
 \text{subject to} & \mathbf{R}(\mu, \mathbf{x}, \dot{\mathbf{x}}, t, P, E) = \mathbf{0} \quad \text{Beam theory residual equations} \\
 & c_{vm,KS} \leq 0 \quad \text{Aggregated strength failure constraint} \\
 \text{data} & P(t)(\text{N}), E(\text{Pa}), \\
 & \sigma_y(\text{Pa}), \rho(\text{kg/m}^3)
 \end{array} \tag{3.12}$$

3.7 Experimental Plan

The overarching research objective is to develop a structural analysis and optimization method to size aircraft wings subjected to dynamic loads in a computationally efficient manner. This objective is broken down into two research questions: the first on structural

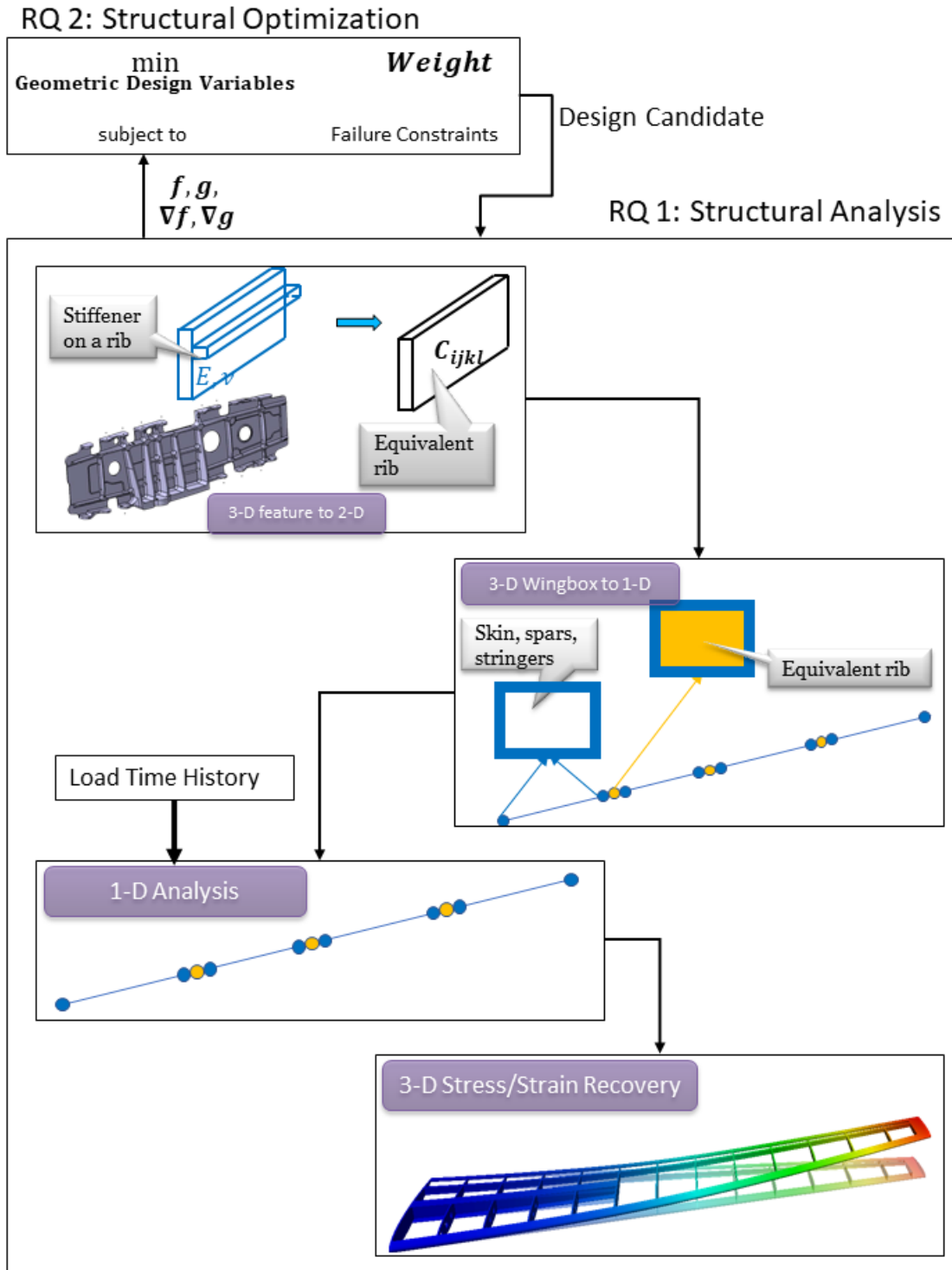


Figure 3.7: Flowchart of the proposed method

analysis, and the second on structural optimization, as described in this chapter and shown pictorially in Fig. 3.7.

Table 3.1: Workstation configuration for all experiments

Component	Installed Part
Processor	Intel(R) Core(TM) i7-7700T CPU @ 2.90GHz (8 CPUs)
RAM	16384 MB
Display	Intel(R) HD Graphics 630
Disk Drives	THNSN5512GPUK NVMe TOSHIBA 512 GB

The experiments have two parts to validate the stated hypotheses: accuracy and computational efficiency. A shell/solid element model will be assumed to be the ground truth in all the experiments. The accuracy of lower DoF model generated in this thesis will be compared to the higher fidelity model. While running the models, computational efficiency metrics such as the number of function calls and clock time will be measured. The overarching hypothesis is that the lower DoF will have better computational efficiency than the higher-fidelity models while retaining accuracy.

For RQ1 pertaining to the structural analysis, the metrics that will be measured are the displacement field, stress field, and analysis clock time. For RQ 2 pertaining to structural optimization, the metrics that will be measured are the optimized thickness distribution, optimized weight, and the number of function calls and clock time for the optimizer to converge.

All the numerical experiments are run on a desktop workstation whose configuration is given in Table 3.1. It should be noted that the workstation has up to eight cores. The implementation of the proposed method is performed in MATLAB. MATLAB's *profile* functionality is used to measure the clock time and the number of function calls. MATLAB's *spmd* functionality is used to run VABS in-parallel on four cores.

As was seen in Fig. 1.3, many of the novel aircraft concepts feature high aspect ratio wings. It is desirable that the proposed method be applicable to both existing conventional tube-and-wing configurations, as well as novel high aspect ratio wings. The method will be applied to two aircraft configurations:

1. The Common Research Model (CRM) that is representative of a wide-body twin-aisle aircraft similar to the Boeing-777 aircraft. This aircraft will demonstrate the method's applicability to existing conventional tube-and-wing configurations. A detailed description of this model is given in Appendix D.3.
2. The Parallel Electric-Gas Architecture with Synergistic Utilization Scheme (PEGASUS) concept developed by NASA. This concept has two hybrid-electric engines on each wing, with the outboard engine at the wing tip. The concept has a high aspect ratio of 11.06. A detailed description of this concept is given in Appendix D.2.

The rationale for the entire thesis, the components of it, and the planned experiments are summarized in Fig. 3.8.

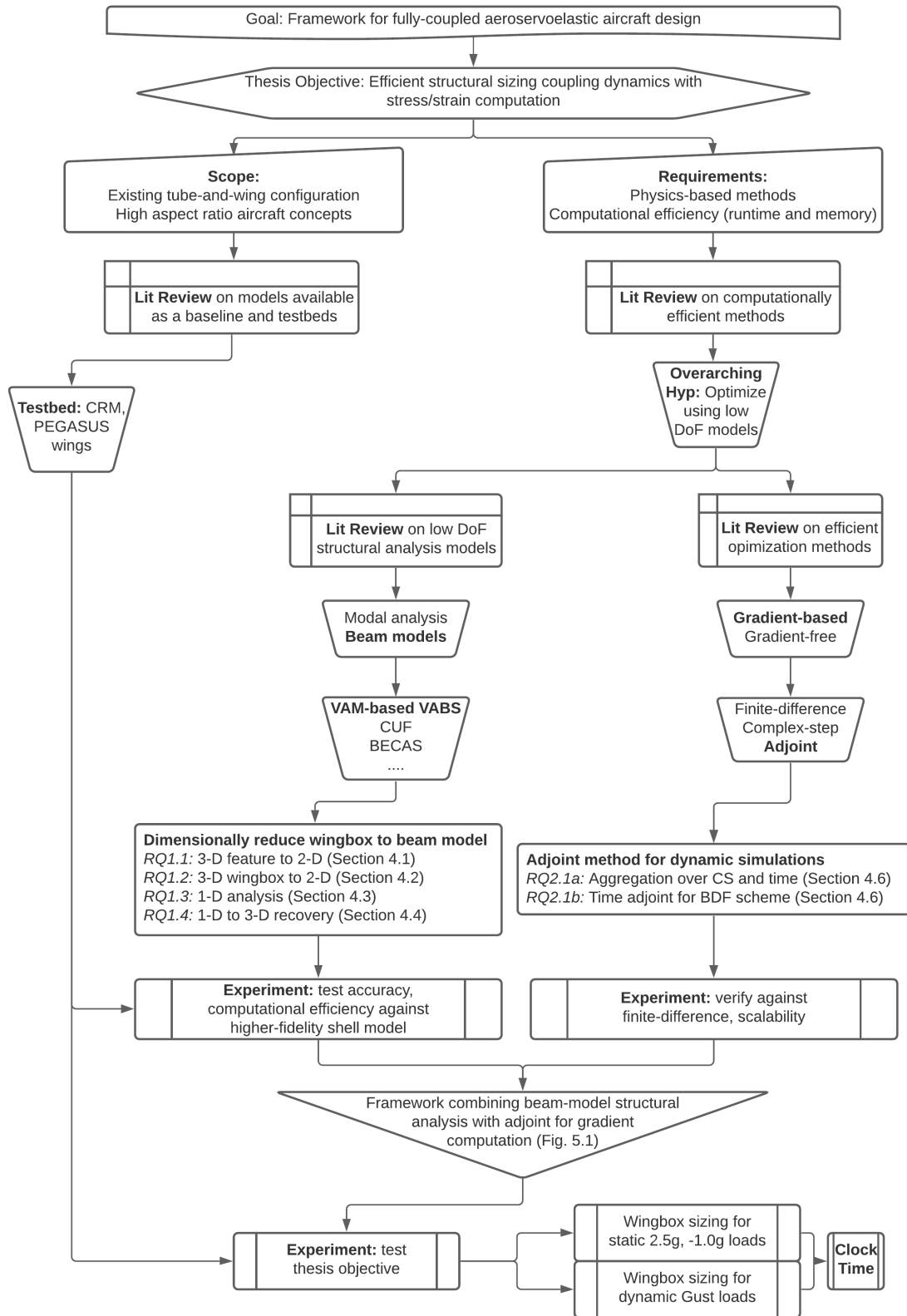


Figure 3.8: Thesis execution summary

CHAPTER 4

RESEARCH QUESTIONS AND HYPOTHESIS TESTING

The overall research objective is repeated here:

Research Objective
Develop a framework for aircraft wing design that <ol style="list-style-type: none">1. Dimensionally reduces complex 3-D structures to produce a low DoF structural analysis model2. Obtain the gradient of the structural analysis model in the time-domain

Chapter 3 proposed a computationally efficient structural analysis and optimization method for advanced aircraft design. It laid out the research questions to address the literature gaps and formulated hypotheses to tackle the research questions.

In this section, the research questions will be explored in-depth. For each hypothesis, an experimental plan is laid-out to test the hypothesis. Experiments are carried out, and the results are discussed. The geometry of the test case problems used in this chapter are discussed in detail in Appendix D.

4.1 RQ 1.1 – 3-D Feature to 2-D¹

The gap this research question addresses relates to the smearing approach of creating an equivalent plate taking stiffeners into account. The literature’s smearing approach assumes stiffeners of the same topology, same dimensions, and uniform rib spacing. To address this

¹The challenges have been published in aprior work [185]. The method and results have been publish in aprior work [186]

gap, the research question was:

Research Question 1.1

How can an equivalent plate be created that accounts for stiffeners of varying topology, dimensions and non-uniform spacing?

A local smearing approach was proposed as a solution to the research question. This is shown in Fig. 4.1. The hypothesis is stated as:

Hypothesis 1.1

If

1. smearing the stiffener of the built-up structure to the corresponding portion of the equivalent structure, thereby, accounting for the effects of stiffeners of varying topology, dimensions and spacing, and subsequently,
2. the anisotropic material properties of the composite equivalent structure computed as a stiffness matching minimization problem

converges to within first order optimality criteria,

Then,

the structural response of this equivalent structure matches that of the built-up structure.

The stiffness matching optimization problem of Hypothesis 1.1 is:

$$\begin{aligned} & \underset{c_{ij}}{\text{minimize}} && S_{\text{builtup}} - S_{\text{equivalent}} \\ & \text{subject to} && \text{Bounds on } c_{ij} \end{aligned} \tag{4.1}$$

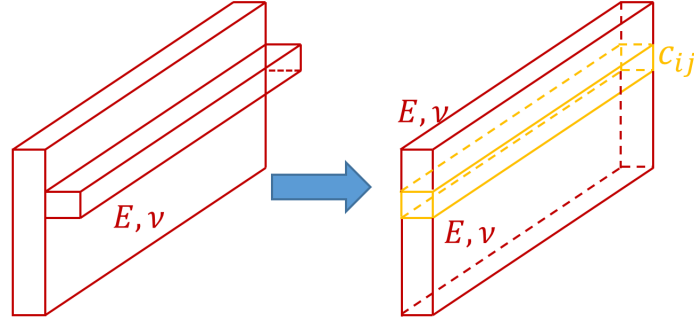


Figure 4.1: Local smearing approach (Repeated from Fig. 3.2c)

Writing out the terms explicitly using the zeroth-order approximation, i.e., classical stiffness matrix

$$\begin{aligned}
 & \underset{c_{ij}}{\text{minimize}} \quad \begin{bmatrix} S_{11} & S_{12} & S_{13} & S_{14} \\ S_{21} & S_{22} & S_{23} & S_{24} \\ S_{31} & S_{32} & S_{33} & S_{34} \\ S_{41} & S_{42} & S_{43} & S_{44} \end{bmatrix} \text{builtup} \quad - \quad \begin{bmatrix} S_{11} & S_{12} & S_{13} & S_{14} \\ S_{21} & S_{22} & S_{23} & S_{24} \\ S_{31} & S_{32} & S_{33} & S_{34} \\ S_{41} & S_{42} & S_{43} & S_{44} \end{bmatrix} \text{equivalent} \\
 & \text{subject to} \quad \text{Bounds on } c_{ij}
 \end{aligned} \tag{4.2}$$

where

$$c_{ij} = E \begin{bmatrix} c_{11} & c_{12} & c_{13} & c_{14} & c_{15} & c_{16} \\ c_{21} & c_{22} & c_{23} & c_{24} & c_{25} & c_{26} \\ c_{31} & c_{32} & c_{33} & c_{34} & c_{35} & c_{36} \\ c_{41} & c_{42} & c_{43} & c_{44} & c_{45} & c_{46} \\ c_{51} & c_{52} & c_{53} & c_{54} & c_{55} & c_{56} \\ c_{61} & c_{62} & c_{63} & c_{64} & c_{65} & c_{66} \end{bmatrix} \tag{4.3}$$

Eq. 4.3 is the material matrix which must be determined in the optimization process. In the most general case of anisotropic materials, this matrix is symmetric with 21 independent terms.

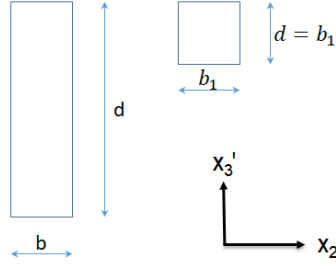


Figure 4.2: Rectangular and square cross section

Table 4.1: Stiffness values for a rectangular section

Stiffness	Axis	Formula
Axial	1	Ebd
Bending	2	$E\frac{bd^3}{12}$
Bending	3	$E\frac{db^3}{12}$

Table 4.2: Stiffness values for a square section

Stiffness	Axis	Formula
Axial	1	$E_{eq}b_1^2$
Bending	2	$E_{eq}\frac{b_1^4}{12}$
Bending	3	$E_{eq}\frac{b_1^4}{12}$

4.1.1 Challenges in Stiffness Matching

The present work is based on matching stiffness properties of two cross-sections of different shapes by altering material properties to enable partial smearing. However, matching stiffness properties entirely (i.e., matching all 21 elements of the 6×6 stiffness matrix for cross-sections of different shapes) is often not easy and, at times, infeasible. To clearly explain this challenge, consider a prismatic isotropic beam made of a material with Young's modulus E and rectangular cross-section, as shown in Fig. 4.2, of width b and depth d . The analytical expressions for axial and bending stiffness properties of this section are given in Table 4.1. Using the current approach, if a square section of side b_1 and homogeneous, isotropic material properties with Young's Modulus E_{eq} is chosen to be a section of equivalent stiffness, then the analytical expressions for corresponding stiffness properties are shown in Table 4.2.

As seen, it is impossible to vary the material property E_{eq} in such a way that the axial

and the two different bending stiffness components all match. For a beam made of a rectangular cross-section, the two flexural stiffness values would be different instead of a beam made of a square cross-section. Hence, the material properties in the equivalent section generated would have to be different in different directions for appropriate stiffness matching. Isotropic materials cannot have such behavior, but orthotropic or anisotropic materials do possess such characteristics and may help get the equivalent section's stiffness matrix to match the stiffness matrix of the original cross-section.

4.1.2 Stiffness Matching using Orthotropic Materials

For orthotropic materials there are 9 independent material parameters. These parameters appear in the 6×6 material matrix as below:

$$E \begin{bmatrix} c_{11} & 0 & 0 & c_{14} & 0 & c_{16} \\ & c_{22} & 0 & 0 & 0 & 0 \\ & & c_{33} & 0 & 0 & 0 \\ & & & c_{44} & 0 & c_{46} \\ & & & & c_{55} & 0 \\ & & & & & c_{66} \end{bmatrix} \quad (4.4)$$

Choosing an Initial Guess

As an initial guess, the material properties are chosen such that the 6×6 material matrix is not fully populated. The non-zero elements of that matrix are found by identifying the anisotropic material matrix possessing properties of an orthotropic material is given by the

inverse of the matrix in the equation below

$$\begin{pmatrix} \sigma_{11} \\ \sigma_{12} \\ \sigma_{13} \\ \sigma_{22} \\ \sigma_{23} \\ \sigma_{33} \end{pmatrix} = \begin{bmatrix} \frac{1}{E_1} & 0 & 0 & -\frac{\nu_{12}}{E_1} & 0 & -\frac{\nu_{13}}{E_1} \\ 0 & \frac{1}{G_{12}} & 0 & 0 & 0 & 0 \\ 0 & 0 & \frac{1}{G_{13}} & 0 & 0 & 0 \\ -\frac{\nu_{12}}{E_1} & 0 & 0 & \frac{1}{E_2} & 0 & -\frac{\nu_{23}}{E_2} \\ 0 & 0 & 0 & 0 & \frac{1}{G_{23}} & 0 \\ -\frac{\nu_{13}}{E_1} & 0 & 0 & -\frac{\nu_{23}}{E_2} & 0 & \frac{1}{E_3} \end{bmatrix} \begin{pmatrix} \gamma_{11} \\ 2\gamma_{12} \\ 2\gamma_{13} \\ \kappa_1 \\ \kappa_2 \\ \kappa_3 \end{pmatrix} \quad (4.5)$$

Further, orthotropic materials properties can be chosen so that the moduli in different directions bear the same value, which matches the axial and at least one flexural stiffness. As the axial stiffness depends on the cross-sectional area, the material properties of the equivalent cross-sections are chosen such that

$$E_1 = E_2 = E_3 = k_A E \quad (4.6)$$

where E is the Young's modulus of the built-up section, E_1 , E_2 , E_3 are chosen to be orthotropic baseline values for the equivalent section, and the area factor k_A is given by

$$k_A = \frac{\text{Area of built-up section}}{\text{Area of equivalent section}} \quad (4.7)$$

The shear stiffness values are chosen to be

$$G_{12} = \frac{E_1}{2(1 + \nu_{12})}, \quad G_{13} = \frac{E_1}{2(1 + \nu_{13})}, \quad G_{23} = \frac{E}{2(1 + \nu_{23})} \quad (4.8)$$

where $\nu_{12} = \nu_{23} = \nu_{13} = \nu$, for simplicity. This process helps to choose a baseline material matrix that would help match the axial stiffness, transverse shear stiffnesses, and one of the two bending stiffnesses (which was bound to happen) right at the start of the stiffness matching process. This baseline matrix would be used during the matching process and iterated upon to find a suitable material matrix that matches the two stiffness matrices in

consideration. It is important to note that the two bending stiffness values vary differently, as pointed out earlier in this section, because of the two cross sections' dimensions under consideration.

Obtaining the gradients

To use gradient-based optimization, an efficient method to obtain the gradient of the stiffness matrix with respect to the material matrix is needed. The authors use automatic differentiation to obtain the gradients using the package CasADi [190]. CasADi allows for custom functions to be defined in terms of symbolic variables. The 9 parameters of Eq. 4.4 are defined as CasADi SX symbolics. The function of interest is the minimization statement in Eq. 4.1. The process of building a function for optimization with the gradients is shown in Fig. 4.3.

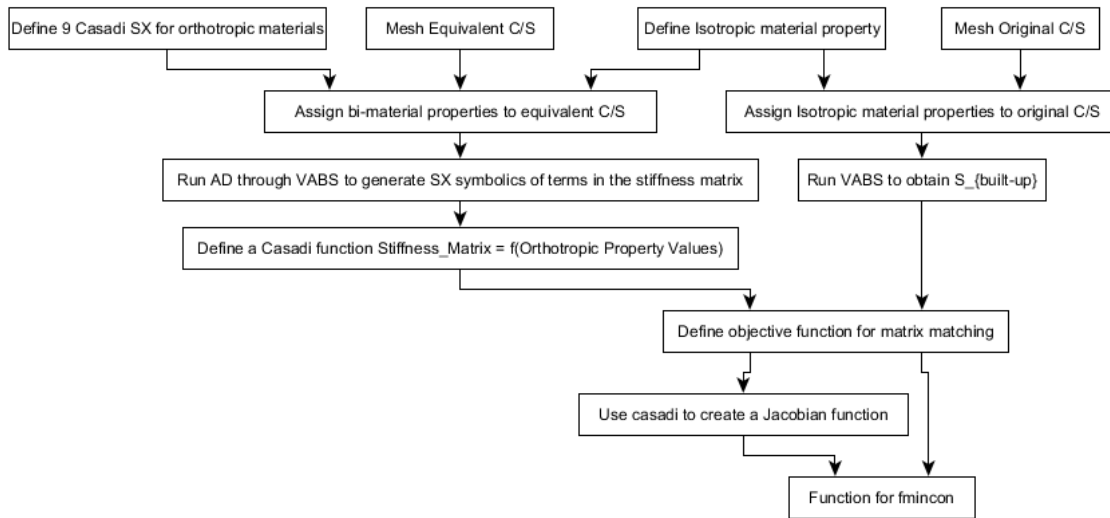


Figure 4.3: CasADi flowchart to generate function for optimization

Optimization methods

The optimization is carried out using Matlab's `fmincon` function. The 4×4 stiffness matrix is symmetric and hence has ten independent parameters. It was found that it is not possible to minimize all ten independent parameters exactly. The optimization problem is relaxed to

match terms along the diagonal of the stiffness matrix. The following objective functions are tested:

- **Method 1:** *Analytical initial guess developed in Section 4.1.2.* With this method it is expected that one of the bending stiffness (S_{33}) matches exactly, with a slight mismatch of axial stiffness (S_{11}). Thus the displacement for the equivalent section should match that of the original section for loading case 2 (Table 4.8 row 2).
- **Method 2:** *Matching S_{44} using gradient-based optimization.* The optimization problem is posed as

$$\begin{aligned} & \underset{c_{ij}}{\text{minimize}} && S_{44}^{\text{builtup}} - S_{44}^{\text{equivalent}} \\ & \text{subject to} && \text{Bounds on } c_{ij} \end{aligned} \quad (4.9)$$

The bounds set for the variables is given in Table 4.3. It is seen that the upper bound of c_{11} has been set to 10 times the Young's Modulus. Thus, in order to match the bending stiffness in the z -direction, it is necessary to incur a large mismatch in the axial stiffness.

- **Method 3:** *Matching bending stiffness E_{44} and torsional stiffness S_{22} using gradient-based optimization.* The optimization problem is posed as

$$\begin{aligned} & \underset{c_{ij}}{\text{minimize}} && \left\| \begin{bmatrix} S_{22} & S_{24} \\ S_{42} & S_{44} \end{bmatrix}_{\text{builtup}} - \begin{bmatrix} S_{22} & S_{24} \\ S_{42} & S_{44} \end{bmatrix}_{\text{equivalent}} \right\|_F \\ & \text{subject to} && \text{Bounds on } c_{ij} \end{aligned} \quad (4.10)$$

with the bounds on the variables given in Table 4.4. It should be noted that the lower bounds on c_{22} and c_{33} are negative. This is necessary in order to match both the bending stiffness and torsional stiffness. The resulting equivalent plate cannot be physically created, but is mathematically possible. The equivalent plate is used to

Table 4.3: Variable bounds used to match S_{44} in gradient-based optimization

	c_{11}	c_{14}	c_{16}	c_{22}	c_{33}	c_{44}	c_{46}	c_{55}	c_{66}
lb	1	0	0	0.1	0.1	1	0.5	0.1	1
ub	10	1	1	1	1	1000	1	1	1000

Table 4.4: Variable bounds used to match S_{44} and S_{22} in gradient-based optimization

	c_{11}	c_{14}	c_{16}	c_{22}	c_{33}	c_{44}	c_{46}	c_{55}	c_{66}
lb	1	0	0	-10	-10	1	0.5	0.1	1
ub	10	1	1	1	1	1000	1	1	1000

accurately recover the displacement under applied loading, but the original plate can be used to recover stresses.

4.1.3 Experiment for Hypothesis 1.1

A simple problem is constructed to illustrate stiffness matching: a prismatic plate of length L with stiffeners. The geometric quantities of the cross-section are shown parametrically in Fig. 4.4. Four variants are created as shown in Figs. 4.5a, 4.5b, 4.5c and 4.5d.

1. Specimen 1: A plate without any stiffeners. The dimensions of the plate are given in Table 4.5.
2. Specimen 2: A single small stiffener is added onto the plate. The dimensions and location of the stiffener are given in Table 4.6 row 1.
3. Specimen 3: A single large stiffener is added onto the plate. The dimensions and location of the stiffener are given in Table 4.6 row 2.
4. Specimen 4: Two stiffeners of different dimensions and locations Table 4.7

All of the four specimens are beam-like. On an aircraft wing, they are representative of a rib with horizontal stiffeners. VABS can be run for each of these cases directly to

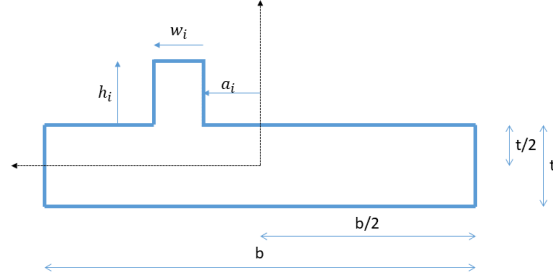


Figure 4.4: Parametrization used for test cases

Table 4.5: Dimensions of plate

Dimension	Value	Unit
Length	0.75	m
Width (b)	0.17	m
Thickness (t)	0.01	m

obtain the 4×4 classical stiffness matrix. The nonlinear Timoshenko beam theory code described in Section A is used for the 1-D analysis. *Cantilever beam* boundary conditions are applied. *Tip loading* is applied in-turn on the x , y and z axes, respectively. The loading is summarized in Table 4.8.

If we focus on the load applied in the z -direction, the stiffeners only play a role in improving the bending stiffness in this direction. The displacements obtained from 3-D FEM simulations shown in Fig. 4.6. It is seen that the effect of the stiffeners is to lower the displacement.

The optimization problem's goal will be to create an equivalent plate without the rib with the material properties modified such that the stiffness (and hence displacement) of

Table 4.6: Dimensions of single stiffener cases

Stiffener Type	a_i	w_i	h_i
Small Stiffener	1 [cm]	1 [cm]	1 [cm]
Large Stiffener	1 [cm]	1 [cm]	3 [cm]

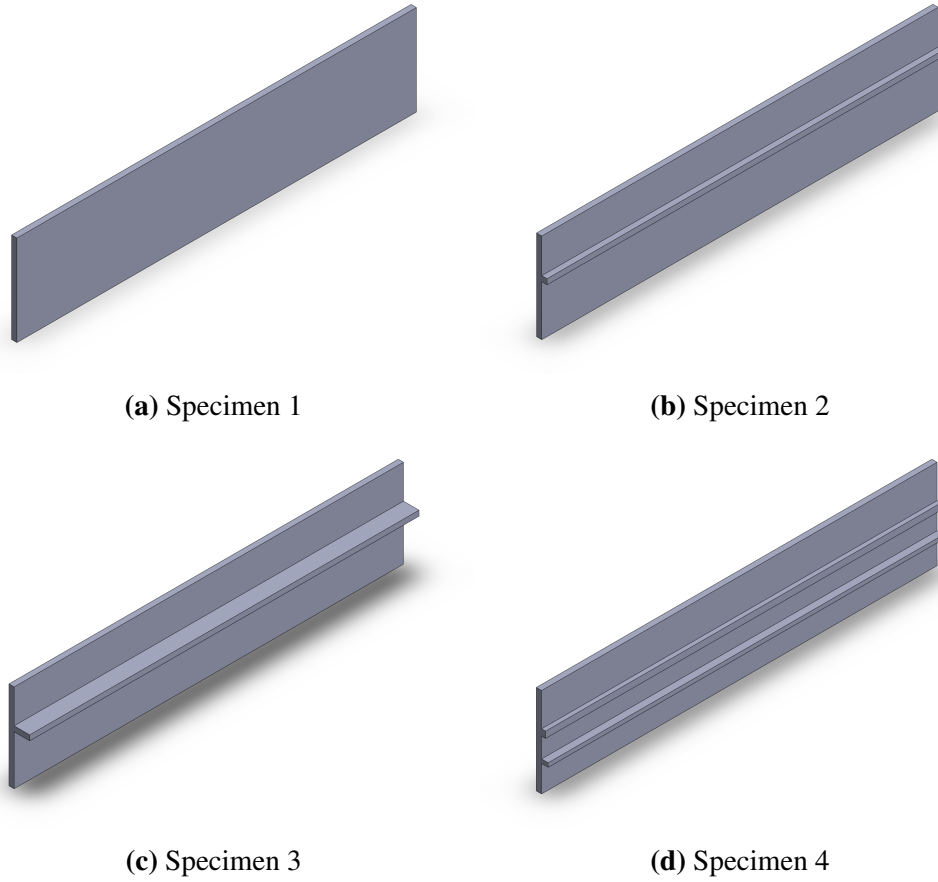


Figure 4.5: Test cases used in this work

the equivalent plate matches that of the original plate with stiffener.

4.1.4 Results

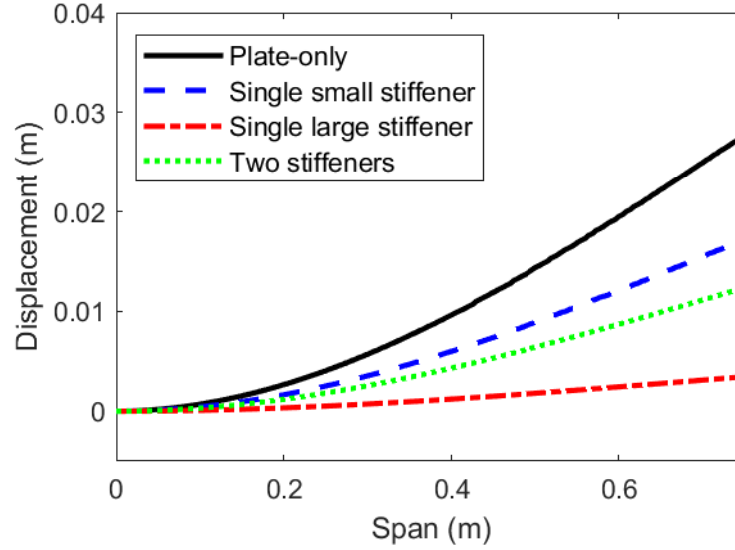
In Section 4.1.2, three methods to perform stiffness matching are proposed. This section discusses the results and applicability of the methods. For ease of reading, the expected outcomes from the three methods are repeated here:

Table 4.7: Dimensions of two stiffeners case

Stiffener location	a_i	w_i	h_i
Upper stiffener	1 [cm]	1.2 [cm]	0.75 [cm]
Lower stiffener	-3.5 [cm]	0.75 [cm]	1.25 [cm]

Table 4.8: Loading Conditions

Loading case number	F_x	F_y	F_z
Case 1	1×10^6 [N]	0	0
Case 2	0	5×10^4 [N]	0
Case 3	0	0	2×10^2 [N]

**Figure 4.6:** 3-D FEM simulations for loading case 3

1. Method 1: Analytically matches bending stiffness S_{33} at the cost of a slight mismatch in axial stiffness S_{11} . It is expected that the displacement results for load case 2 (force along the y -direction) will match since S_{33} is correct.
2. Method 2: Matches bending stiffness S_{44} . It is expected that the displacement results for load case 3 (force along the z -direction) will match.
3. Method 3: Matches both bending stiffness S_{44} and torsional stiffness S_{22} . As with Method 2, it is expected that the displacement results for load case 3 will match.

First, **specimen 2** (Fig. 4.5b) results will be discussed. This specimen has a small stiffener which drastically increases the bending stiffness (S_{44}), with some increase in the other stiffnesses.

- The displacement as a function of span for load case 1 and load case 2 for **method 1** are compared to 3-D FEM results in Fig. 4.7a and Fig. 4.7b, respectively. As seen, using method 1, the displacement for load case 2 matches, whereas that of load case 1 has some error.
- The displacement as a function of span for load case 2 and load case 3 for **method 2** are compared to 3-D FEM results in Fig. 4.8a and Fig. 4.8b, respectively. As seen, using method 2, the displacement for load case 3 matches, whereas that of load case 2 has some error.
- The results of **method 3** for load case 2 and load case 3 are very similar to those of method 2 as seen in Fig. 4.9a and Fig. 4.9b.
- The results of **method 3** for load case 1, however, has a large discrepancy. This is seen in Fig. 4.10. In an effort to simultaneously match both S_{22} and S_{44} , the optimization resulted in a large axial stiffness (S_{11}).

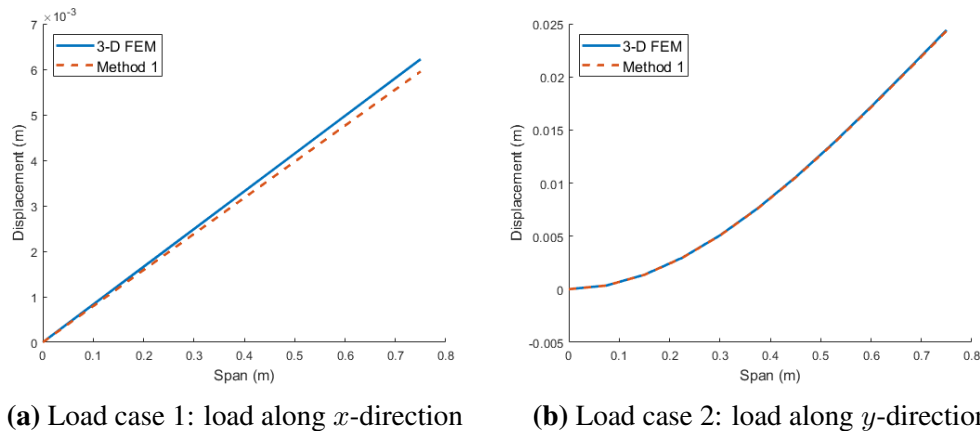
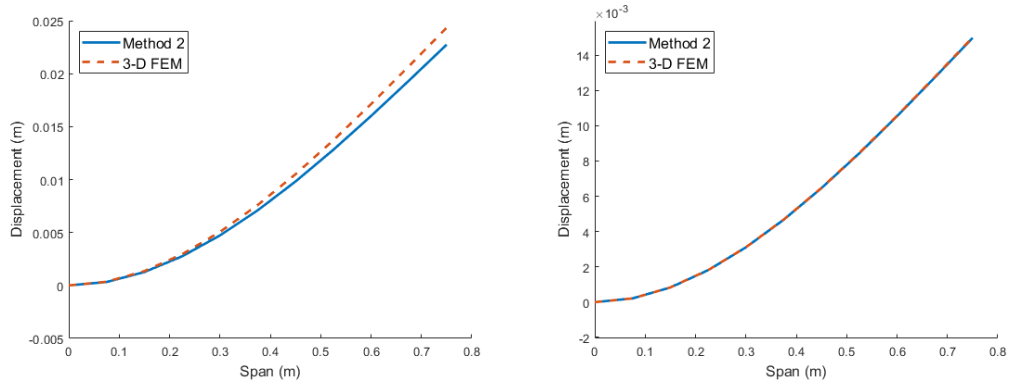


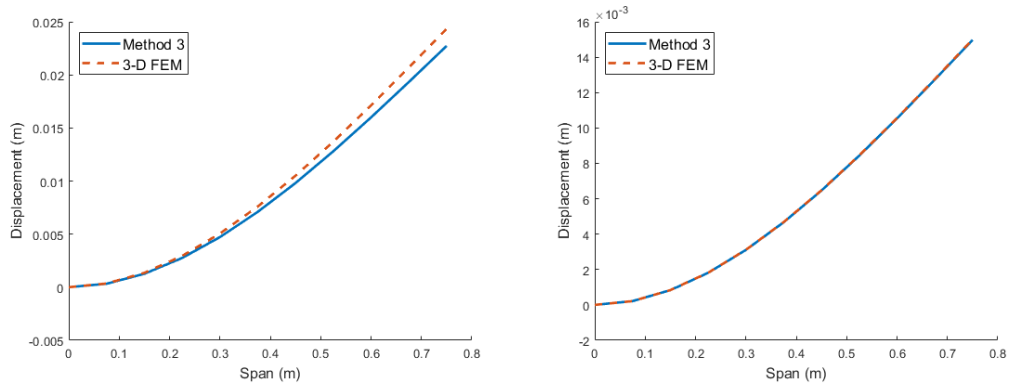
Figure 4.7: Specimen 2, method 1 displacement results for load cases 1 and 2

For **specimen 3** (Fig. 4.5c), the results are qualitatively similar to those of specimen 2. The displacement values are smaller as specimen 3 has a larger stiffener than specimen 2. The displacement vs. span plots are combined and shown in Figs. 4.11a, 4.11b and 4.11c.



(a) Load case 2: load along y -direction (b) Load case 3: load along z -direction

Figure 4.8: Specimen 2, method 2 displacement results for load cases 2 and 3



(a) Load case 2: load along y -direction (b) Load case 3: load along z -direction

Figure 4.9: Specimen 2, method 3 displacement results for load cases 2 and 3

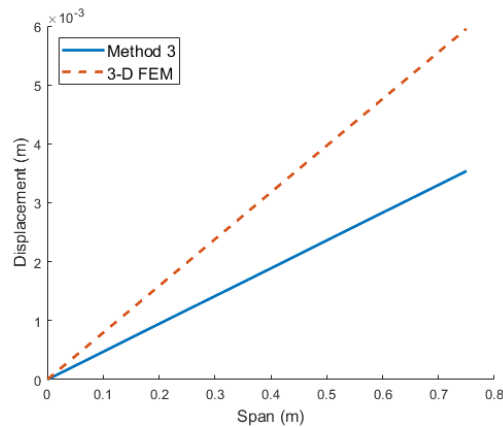


Figure 4.10: Specimen 2, method 3 displacement results for load case 1

Method 2 (matches S_{44}) results are not shown here since method 3 matches both S_{22} and S_{44} .

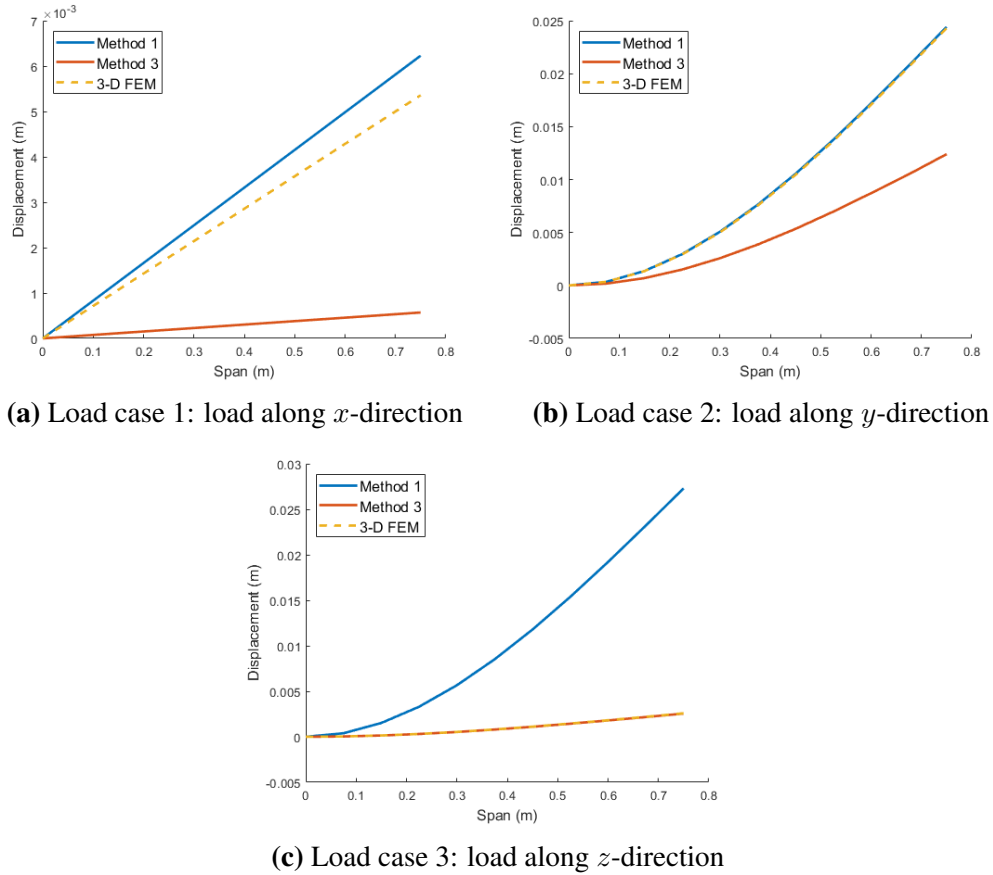
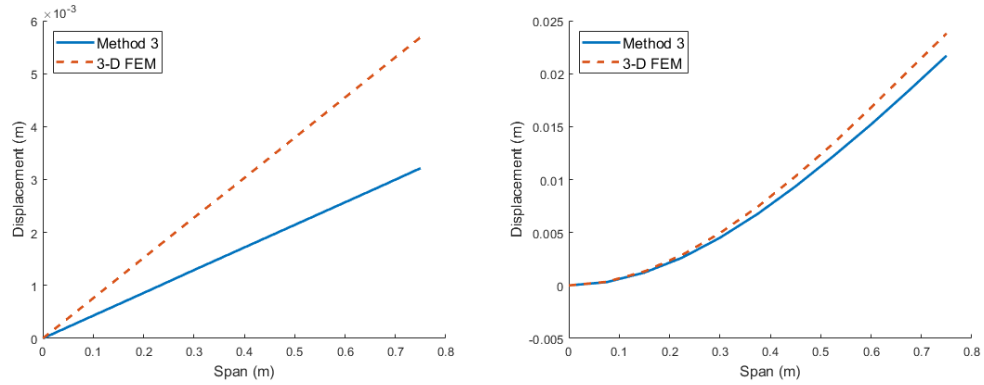


Figure 4.11: Specimen 3 displacement vs. span results

For **specimen 4** (Fig. 4.5d), the results are qualitatively similar to those of both specimen 2 and specimen 3. The displacement values are smaller than specimen 2, but larger than specimen 3. This behavior is consistent with the 3-D FEM results shown in Fig. 4.6. The displacement vs. span plots are combined and shown in Fig. 4.12a, Fig. 4.12b and Fig. 4.12c. The results being similar, for conciseness, method 1 and method 2 results are not shown here.

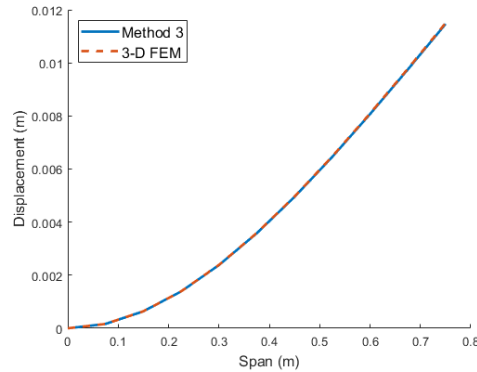
4.1.5 Summary

A method has been developed to smear the properties of a stiffener onto the base-plate locally. Unlike plate smearing approaches that assume a stiffener of constant dimension uniformly spaced on the plate, this method allows for discrete control over the stiffeners'



(a) Load case 1: load along x -direction

(b) Load case 2: load along y -direction



(c) Load case 3: load along z -direction

Figure 4.12: Specimen 4 displacement vs. span results

dimensions, number, and location.

The method is based on *stiffness matching*, where the stiffness of the cross-section with stiffener is matched to a cross-section without the stiffener by locally modifying the material properties. The stiffness of cross-sections is computed using VABS, which can handle arbitrary geometry and anisotropic materials. The stiffness matching is formulated as an optimization problem to allow for the process to be automated.

Three optimization formulations using orthotropic material are presented and compared. It is found that an analytical solution exists if it is desired to recover displacements due to out-of-plane bending accurately. It is possible to recover in-plane bending displacement with minimal loss of axial displacement accuracy by using a gradient-based optimizer with positive material bounds. To simultaneously recover both in-plane bend-

ing displacement and torsional displacement, the material bounds have to be relaxed to allow for negative values. The material obtained is not physical but mathematically possible. Using orthotropic materials, it is not possible to match in-plane bending, out-of-plane bending, and torsion simultaneously.

For the most part, this confirms our Hypothesis 1.1, stating that *locally modifying the portion of the equivalent structure where the stiffener exists allows for different stiffener topologies, dimensions, and spacing, and the anisotropic material properties of the composite equivalent structure can be found by a stiffness matching minimization problem*. The limitation lies in not being able to match in-plane bending, out-of-plane bending, and torsion simultaneously. The method can be used to obtain equivalent plates accounting for stiffeners by having regions of orthotropic materials. This is useful to design structures such as aircraft ribs that require a plate/shell analysis subject to stress and buckling constraints.

4.2 RQ 1.2 – 3-D Wingbox to 1-D

The gap this research question addresses relate to the computation of beam cross-sectional properties. The literature approaches to obtain beam properties for dynamic response analysis rely on the generation and execution of a shell model. For structural analysis, higher-order beam theory has not been used in aircraft wing stiffness computation accounting for airfoil shape and composites. To address these gaps, the research question was:

Research Question 1.2

How to compute beam cross-sectional properties for a wingbox airfoil cross-section of arbitrary shape and material definition?

It was proposed to use VABS to compute the cross-sectional properties. The hypothesis is stated as:

Hypothesis 1.2

If

VAM-based VABS is applied to an aircraft wingbox cross-section

Then,

beam cross-sectional properties of a wingbox airfoil of arbitrary shape can be calculated

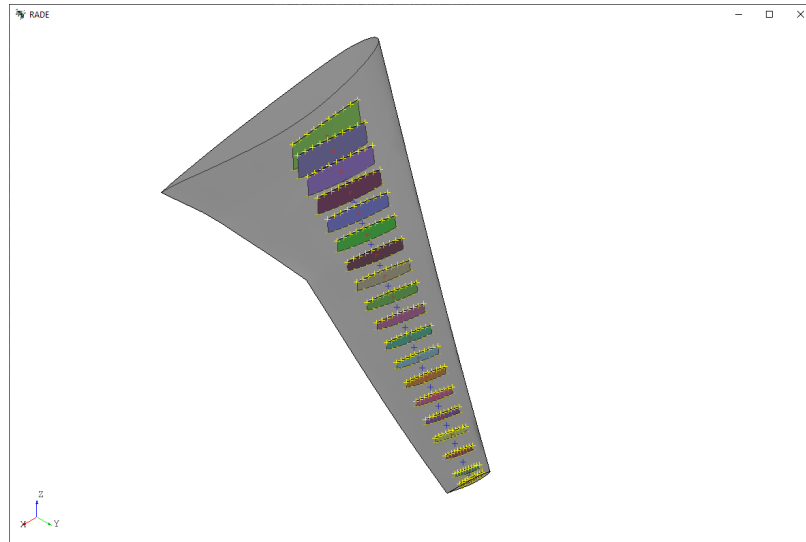
4.2.1 Information from 3-D Geometry

This section aims to provide a method to obtain the beam model from the 3-D geometry directly. This avoids generating 3-D shell models that can be time-consuming to generate in an automated manner. Fig. 4.13 shows the information available from the 3-D geometry:

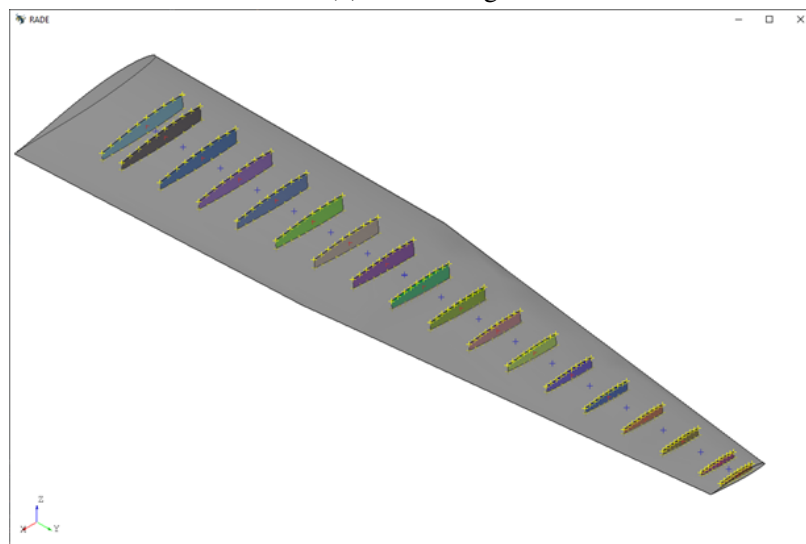
1. **Beam axis:** A series of nodes along a 1-D curve. In this work, we connect the rib CGs to generate the beam axis. They are shown as red cross marks in Fig. 4.13.
2. **Cross-sections OML:** In this work, points on the OML of the rib surface are extracted. These are shown as yellow cross marks in Fig. 4.13.
3. **Load nodes:** The loads are applied on the beam as a piecewise uniform distributed load along the wingspan. The aerodynamic loads are aggregated to a series of points along the span of the wing. The points chosen in this work are the midpoint between two ribs, seen as blue cross marks in Fig. 4.13b. This allows for the concentrated load to be distributed to the beam section between two ribs.

4.2.2 VABS for Cross-Sectional Analysis

As described in Section 2.3.1, VAM can be used to obtain beam cross-sectional properties rigorously. VABS requires two cross-sectional quantities to compute the mass and stiffness matrices for each cross-section:



(a) CRM wing



(b) PEGASUS concept wing

Figure 4.13: Information from 3-D geometry needed to generate the beam model

1. Shape of the cross-section as a 2-D mesh
2. Material definition and distribution over the cross-section

In addition, VABS requires the following information about how the cross-section relates with respect to to the rest of the structure:

1. Curvature of the 1-D beam line

2. Oblique angles to relate the cross-section orientation with respect to the 1-D beam line

All the necessary inputs to VABS are described in greater detail by Yu [191]. Fig. 4.14 shows the process of computing the cross-sectional properties. The points on the rib OML obtained from the 3-D surface geometry are the cross-section midline points. Given the thicknesses of the front spar, rear spar, top skin, and bottom skin, the midline points are offset outwards and inwards to generate a hollow cross-section, as seen in Fig. 4.15a. The 2-D cross-section is meshed with triangular elements using DistMesh, as seen in Fig. 4.15b. The mesh size is chosen such that there are at least five elements through the cross-section. In this work, we consider metallic components. Every 2-D mesh element is assigned Aluminium as the material. It should be noted that using metallic components is a simplification done in this work. VABS has no such restriction and can be used to analyze composite components.

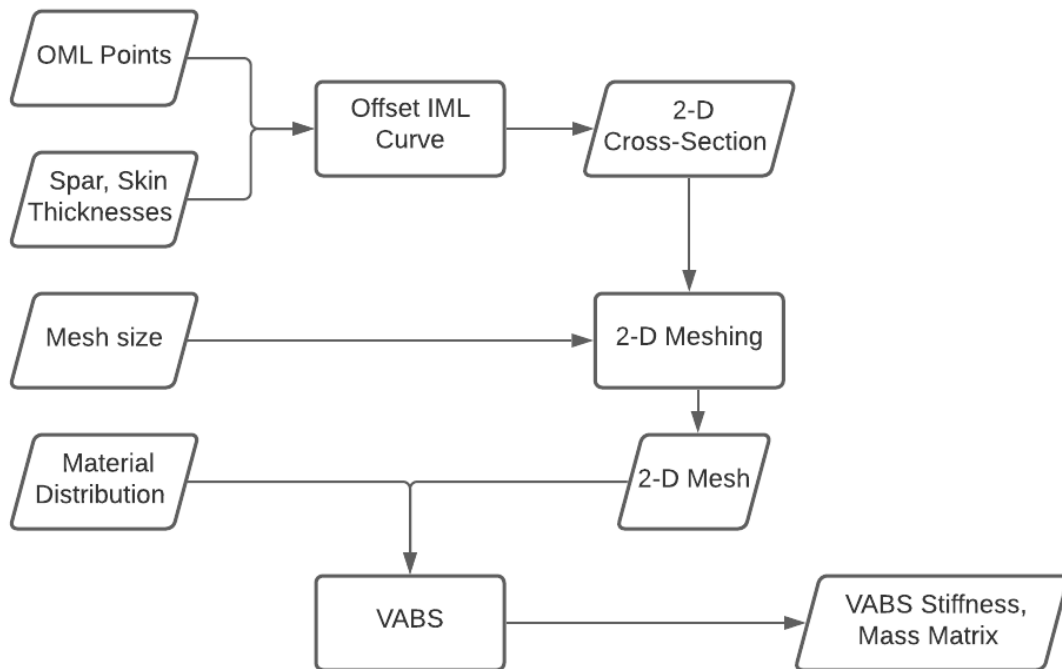


Figure 4.14: Computation of wingbox cross-sectional properties using VABS

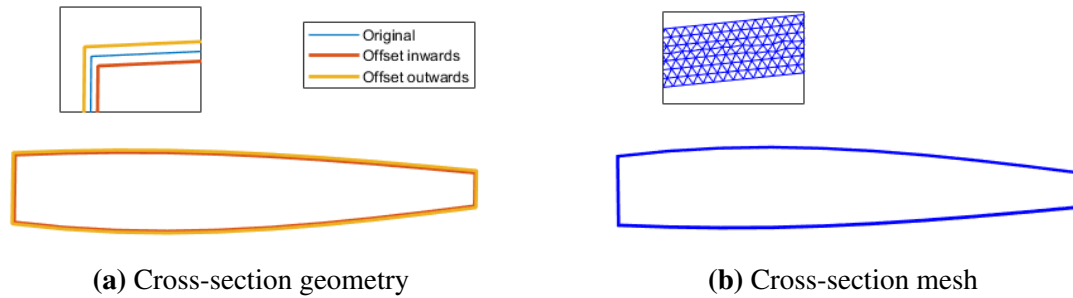
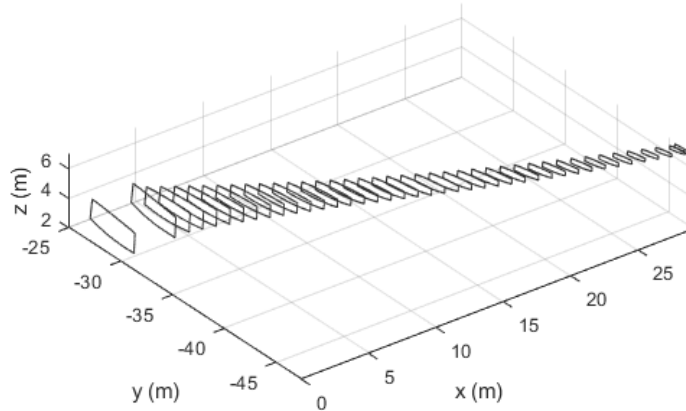


Figure 4.15: 2-D cross-section and mesh used as input for VABS

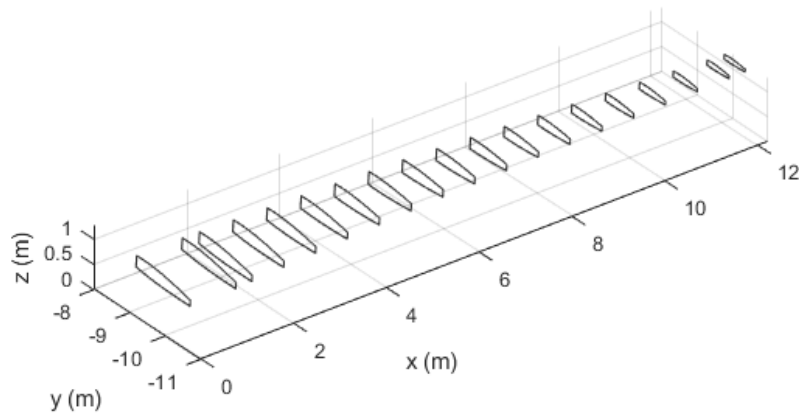
With the 2-D mesh and material definition, VABS is run to obtain the stiffness and mass matrices at every ‘rib’ cross-section along the beam’s span. Fig. 4.16 shows the beam representation.

It should be noted that in VAM’s literature, some small parameters are not considered. One such parameter is the taper, an important planform variable for aircraft wings. However, when slices of the aircraft wingbox are taken to obtain the 2-D cross-sections on which VABS analysis is performed, taper effect is accounted for due to the change in dimensions of the cross-sections. Instantaneous taper changes, such as a stepped beam, would incur error as VAM does not consider that a small parameter. For aircraft wings, it is rare to find instantaneous changes in the taper. Thus, VABS may be used for the cross-sectional analysis for the problem under consideration.

It should also be noted that that stringers on the skin are geometric entities seen in the cross-section. If the dimensions and spacing of the stringers are available, it is possible to include them in the 2-D mesh, as seen in Fig. 4.17. However, the stringers have a minimal effect on the global response of the wingbox. The primary function of the stringers is to resist the buckling of the shell panel. The stringers can therefore be treated in-isolation when setting up buckling constraints for each shell panel.



(a) CRM wing



(b) PEGASUS concept wing

Figure 4.16: Beam representation

4.2.3 Limitation of using VABS for Sizing

Using VABS to obtain the stiffness and mass matrices and further obtain the stress requires a 2-D mesh generation for each design candidate. The finite difference method to obtain the gradient is inefficient as the number of design variables increases. To be efficiently used in the design process, mesh deformation and the adjoint of VABS has to be derived. Deriving the adjoint for VABS is considered out-of-scope for this work. Instead, the cross-section is assumed to be a hollow rectangular box for which analytical formulae exist for the stiffness

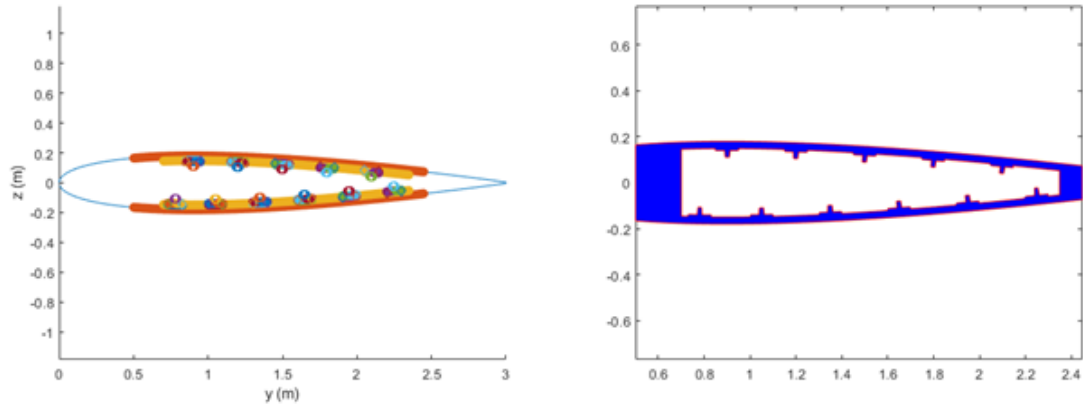


Figure 4.17: 2-D mesh of cross-section with stringers

matrix. This is discussed next.

4.2.4 Rectangular Box Wingbox

Consider a typical cross-section seen in Fig. 4.18. The upper and lower portions of the cross-section are curves instead of straight lines. This curvature adds to the complexity, and no analytical formulae exist to compute the stiffness matrix. Assumptions have to be made to create a rectangular box cross-section seen in the right of Fig. 4.18. The width w is fixed by the chosen structural topology (front and rear spar locations) and can be computed as

$$w = \frac{w_1 + w_2}{2} \quad (4.11)$$

Determining the height h is more challenging due to the curvature. One possible option is to average the heights at several locations on the top and bottom skin curves, as seen in Fig. 4.18. The height is computed as

$$h = \frac{h_1 + h_2 + \dots + h_{10}}{10} \quad (4.12)$$

The thickness variables t_{left} , t_{right} , t_{up} , and t_{down} of the front spar, rear spar, top skin, and bottom skin respectively are design variables in the optimization. Fig 4.19 shows the

process to obtain the box cross-sectional properties. The analytical formulae are given in Appendix F.

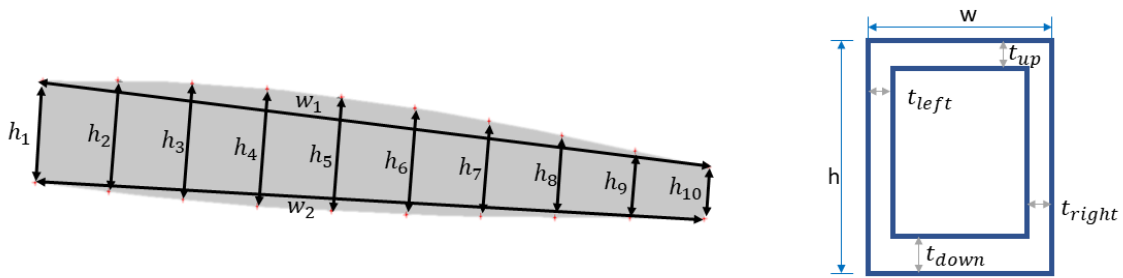


Figure 4.18: Rectangular box cross-section assumption and parameters

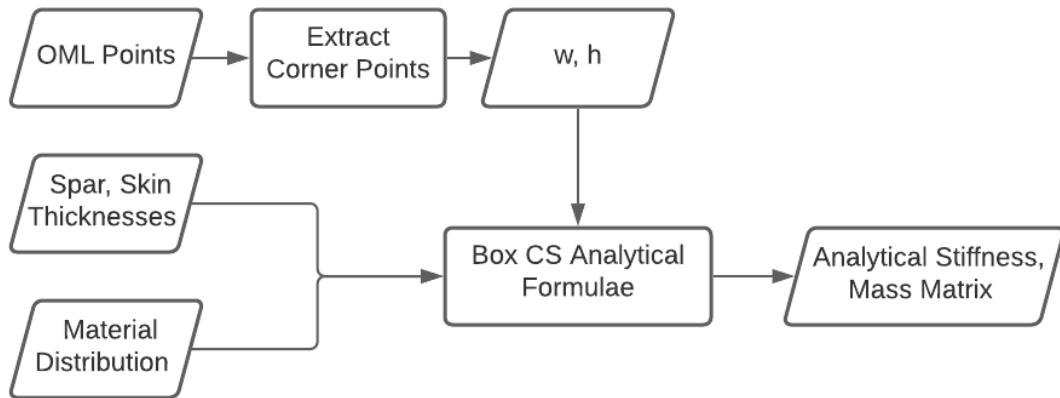


Figure 4.19: Computation of wingbox box cross-sectional properties

Stiffness Matching

As seen in Section 4.2.2, VABS provides an accurate way to obtain the stiffness matrix of aircraft wings. However, its use in design is limited due to the lack of an efficient way to obtain gradient with respect to design variables. On the other hand, the rectangular box cross-section allows for efficient gradients to be obtained using the adjoint method but lacks accuracy. Hence, a procedure is proposed to correct the stiffness of the rectangular box cross-section using VABS.

Consider the flowchart shown in Fig. 4.20. The VABS stiffness matrix, S_{VABS} , is obtained from the 2-D mesh (Fig. 4.15a), and the material definition. The analytical stiffness matrix, $S_{analytical}$, is calculated with the material definition, width, height, and thicknesses using known standard Euler-Bernoulli beam theory formulae. These are presented in Appendix F. Stiffness matching intends to ensure the two stiffness matrices are as close to each other as possible.

$$\begin{aligned} & \underset{w,h}{\text{minimize}} \quad S_{VABS} - S_{analytical} \\ & \text{subject to} \quad \text{Bounds on } w, h \end{aligned} \tag{4.13}$$

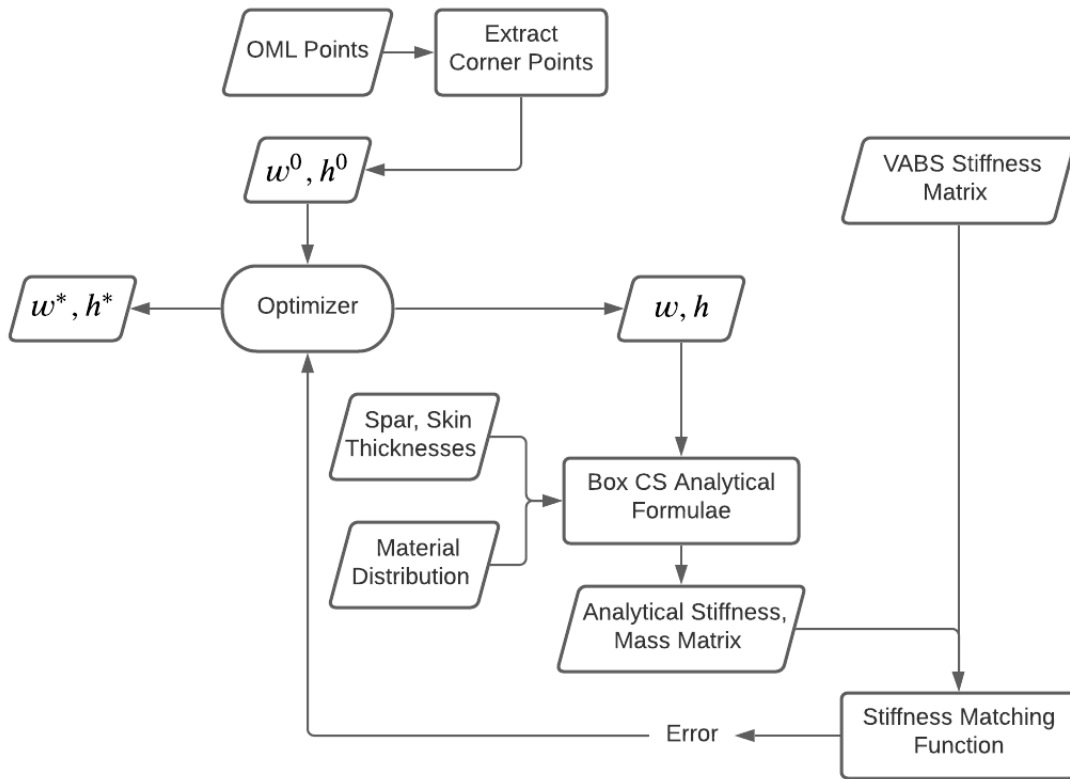


Figure 4.20: Flowchart to correct the rectangular box cross-section stiffness with information from VABS

In general, the 6×6 stiffness matrix has 21 independent elements. Matching the 21 components is impossible, with only the width and height as the design variables. However,

the majority of the deformation of aircraft wing occurs due to up-down bending and torsion. It has also been shown that the coupling between bending and torsion is important [192, 193]. Hence, a sub-matrix from the 6×6 stiffness matrix is considered as given in Eq. 4.14.

$$\begin{aligned} & \underset{w,h}{\text{minimize}} \quad \left\| \begin{bmatrix} EI_{xx} & EI_{xy} \\ EI_{xy} & GJ \end{bmatrix}_{\text{VABS}} - \begin{bmatrix} EI_{xx} & EI_{xy} \\ EI_{xy} & GJ \end{bmatrix}_{\text{analytical}} \right\|_F \quad (4.14) \\ & \text{subject to} \quad \text{Bounds on } w, h \end{aligned}$$

Based on the above discussion, the hypothesis for this research question is modified to include the provision of using a box cross-section with stiffness corrected by VABS:

Modified Hypothesis 1.2

If
the aircraft wingbox cross-section is treated as a box cross-section with analytical expressions to compute an analytical stiffness matrix,

And
a stiffness matching optimization problem modifying the width and height converges on the objective function that is the matrix Frobenius norm of the difference between the VAM-based VABS computed stiffness matrix on the wingbox cross-section and the analytical stiffness matrix

Then,
beam cross-sectional properties of a wingbox airfoil of arbitrary shape can be calculated using the resulting width and height

4.2.5 Experiments: Cross-Section Properties Computation and Stiffness Matching

The claim made by Hypothesis 1.2 is that VABS can be used to compute the cross-sectional properties of the wingbox. Information from the 3-D geometry (Section 4.2.1) can be used to generate the necessary inputs to VABS.

Consider the PEGASUS concept wing's root and tip cross-sections shown in Fig. 4.16b. When the method described in Section 4.2.2 is applied, the resulting stiffness matrices are given in Table 4.9 and Table 4.10.

Table 4.9: PEGASUS root rib stiffness matrix

1.55×10^9	56.77×10^3	-12.64×10^3	5.42×10^{-5}	-17.38×10^6	167.45×10^6
56.77×10^3	466.41×10^6	1.67×10^6	167.22×10^{-3}	-14.08×10^3	-526.11×10^3
-12.64×10^3	1.67×10^6	26.28×10^6	-66.84×10^{-3}	47.94×10^3	121.78×10^3
54.18×10^{-6}	167.22×10^{-3}	-66.84×10^{-3}	23.84×10^6	15.01	7.1753
-17.38×10^6	-14.08×10^3	47.94×10^3	15.01	19.35×10^6	-2.90×10^6
167.43×10^6	-526.11×10^3	121.78×10^3	7.18	-2.90×10^6	369.56×10^6

Table 4.10: PEGASUS tip rib stiffness matrix

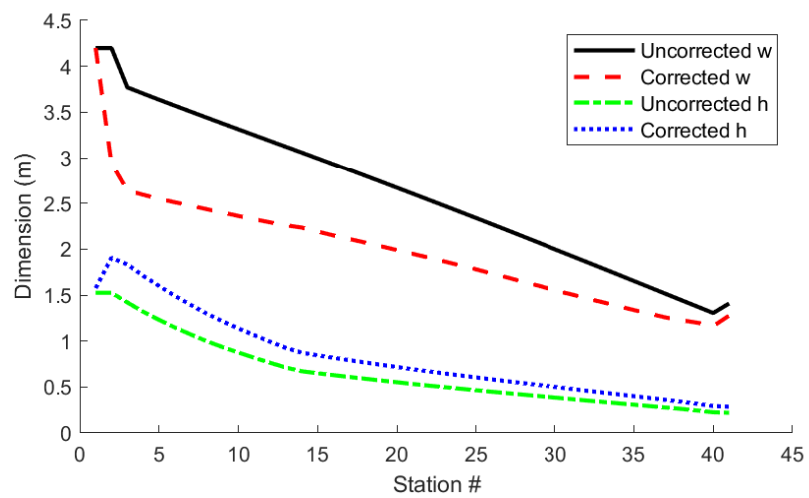
60.14×10^7	4.35×10^3	-2.17×10^3	32.50×10^{-6}	-2.57×10^6	25.68×10^6
4.35×10^3	180.49×10^6	677.59×10^3	224.31×10^{-3}	-5.12×10^3	-102.15×10^3
-2.17×10^3	677.59×10^3	11.02×10^6	-134.34×10^{-3}	6.10×10^3	51.37×10^3
32.50×10^{-6}	224.31×10^{-3}	-134.34×10^{-3}	1.48×10^6	9.07	2.80
-2.57×10^6	-5.12×10^3	6.10×10^3	9.07	1.20×10^6	-168.48×10^3
25.68×10^6	-102.15×10^3	51.37×10^3	2.80	-168.48×10^3	21.53×10^6

From Table 4.9 and Table 4.10, the following qualitative observations are made:

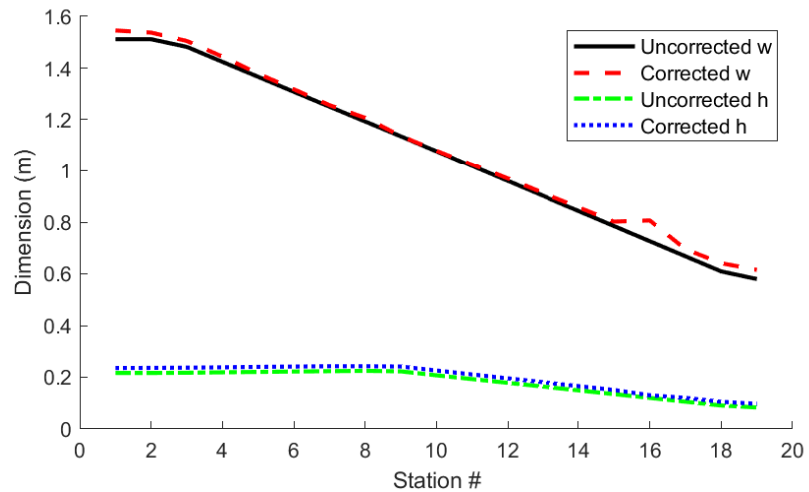
- The diagonal values of the matrix are non-zero
- One of the bending stiffness values (5,5) is much larger than the other bending stiffness value (6,6). This is due to the airfoil having a much larger chord than the thickness
- The values of the root cross-section are larger than the values of the tip cross-section

A further claim Hypothesis 1.2 makes on the use of a box cross-section with width and height corrected to match the VABS stiffness values through an optimization problem given in Eq. 4.14.

Fig. 4.21 compares the widths and heights before and after the stiffness matching procedure. For the PEGASUS wing, which only has a small taper, the width and height changes were minimal. However, for the CRM wing that has a considerable amount of sweep and taper, the changes are more pronounced.



(a) CRM wing



(b) PEGASUS concept wing

Figure 4.21: Comparison of the widths and heights of the rectangular box cross-section before and after the stiffness has been corrected

It is indeed seen that the optimization problem claimed in Hypothesis 1.2 successfully modifies the widths and heights of the box cross-section to match the stiffness values of VABS. Thus Hypothesis 1.2 is validated. However, no claim can be made on the accuracy of the cross-sectional values computed on the structural response of the wing. Experiments to check this are deferred to Section 4.3 for the displacement response and Section 4.4 for the stress field response.

4.3 RQ 1.3 – 1-D Analysis

Representing the wingbox structure (Fig. 2.1) as curved shell panels is standard in the literature and the industry; and has shown to be well suited for the structural analysis of such structures[120, 32]. In this section, a case will be made to support simplifying the wingbox structure to a beam model.

Consider the wireframe view of the PEGASUS wingbox shell model in Fig. 4.22a. It is observed that the wingbox without the ribs consists primarily of the upper skin, lower skin, front spar, and rear spar. The skins are curved surfaces following the airfoil shape truncated by the spars. A slice through the wingbox would have a 2-D cross-section similar to that shown in Fig. 4.22b. Thus, in the absence of ribs, the wingbox is a series of such cross-sections with varying dimensions. Such a structure is well-suited to be idealized as a non-prismatic beam.

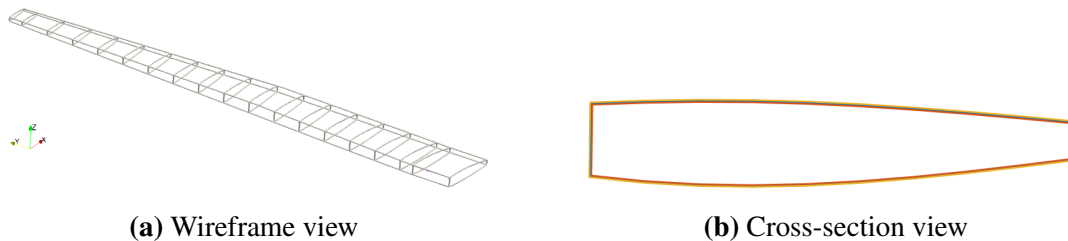


Figure 4.22: PEGASUS wingbox

It was seen in literature that 1-D beam theories do not work well in the presence of aperiodicities. Due to this, the inclusion of the ribs in the wingbox is challenging. Instead,

in this work, the effect of neglecting the ribs will be considered. It was also seen in the literature that aircraft sizing is done neglecting the ribs and produces reasonably good estimates of the weight [112, 176]. These effects will be studied further and quantified. The research question here was stated as:

Research Question 1.3a

How much accuracy is lost in the structural response and sizing calculations of the aircraft wingbox when its ribs are neglected?

Research Question 1.3b

How accurate is the displacement response when the wingbox structure is represented as a beam model?

In this dissertation, we hypothesize that the aircraft wingbox can be simplified to a non-prismatic beam by removing the ribs. To justify this hypothesis, it is essential to quantify the ribs' influence on the structural response. This is done next in Section 4.3.1.

In RQ 1.2, a method was proposed to obtain the beam cross-sectional properties. In Section 4.3.2, a 1-D beam model is generated using the properties. Experiments are run to validate the beam model's accuracy by comparing it to a higher-fidelity shell model.

4.3.1 Influence of Ribs on the Structural Response of the Wingbox

In this section, the ribs' influence on the structural response of the wingbox will be quantified. The experimental philosophy that will be followed is to monitor the structural response of the wingbox with two models:

1. A wingbox model with skin, spars, and ribs
2. A wingbox model with only skin and spars.

The response due to the following analyses will be monitored:

- Modal frequencies response
- Static response to 1g load
- Dynamic response to a gust
- Sizing weights due to 1g load

For each analysis, the structural model's response with the ribs will be compared to that without the ribs. The data will show the ribs' influence on the structural response of the wingbox.

Test 1: Modal Response of a 'Wing-Like' Structure

A 'wing-like' structure described in Section D.1 was considered. For this model, 3-D solid elements FEM was used to perform the analysis. The modal frequencies without the rib were treated as the baseline values. A single rib was added at an inboard cross-section: cross-section 2. The thickness of this rib was varied from $0m$ (no rib) to $0.5m$ in steps of $0.05m$. For each thickness, modal analysis was run. Fig. 4.23 shows the results. The y -axis shows the percent change in the modal response compared to the baseline value.

As seen, for a rib thickness of $0m$, there is no change in any modal frequencies. The torsional mode frequency of the structure dramatically increases when even a thin rib is added. After that, increasing the thickness of the rib linearly increases the torsional mode frequency. It is also seen that the bending mode frequencies are less affected by the ribs. This study shows that the structure's torsional stiffness can be increased by inserting very thin ribs without significantly affecting the bending stiffnesses.

Test 2: Static Load Response

Consider the PEGASUS wing concept described in Appendix D.2. For this aircraft's wingbox, two *Nastran shell models*- one with ribs and one without ribs. It was ensured that both

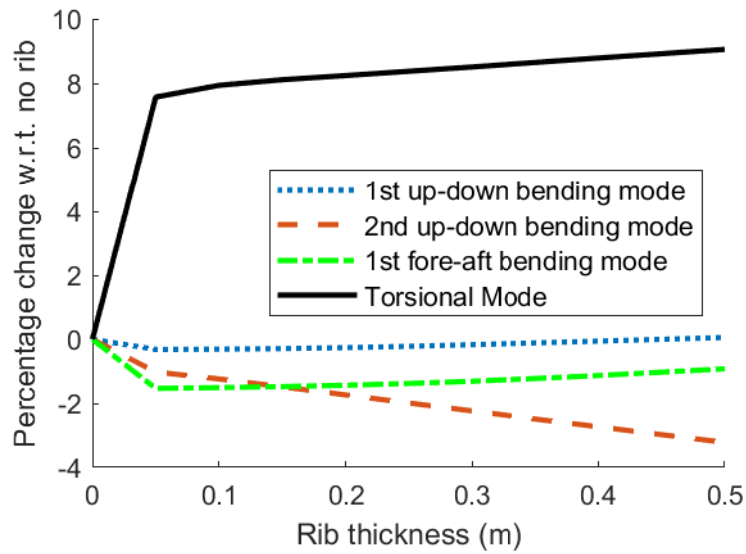


Figure 4.23: Modal response due to insertion of a rib

models have the same thicknesses of the skin and spars. The structure was subjected to 1g aerodynamic loads obtained from AVL. Fig. 4.24 compares the displacement response of the two models. It is seen qualitatively that the displacement response is similar. Fig. 4.25 shows the response for nodes along the span of the wing. It is seen that the displacement in the z -direction is similar. However, the torsional rotation of the model without ribs is larger (maximum error of around 5 degrees) than that with ribs.

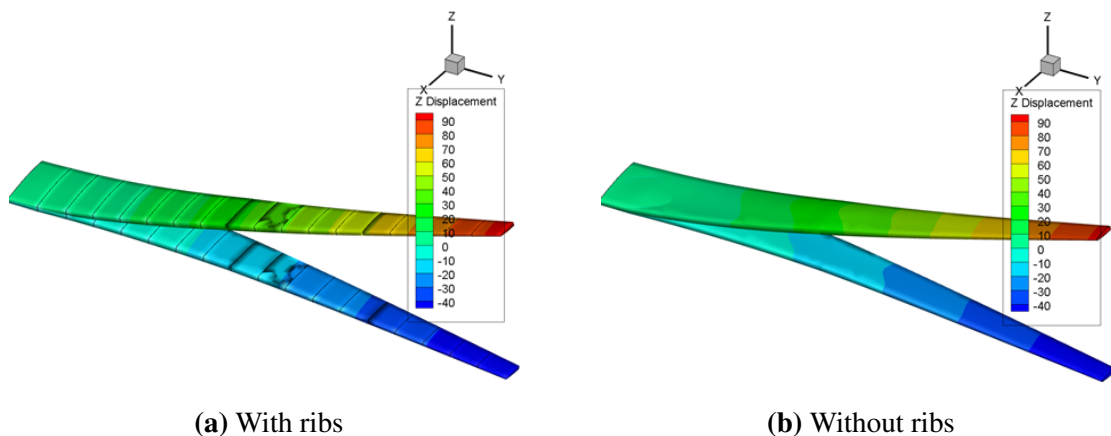


Figure 4.24: Qualitative comparison of static response displacement contour of PEGASUS concept wing subjected to 1g loads

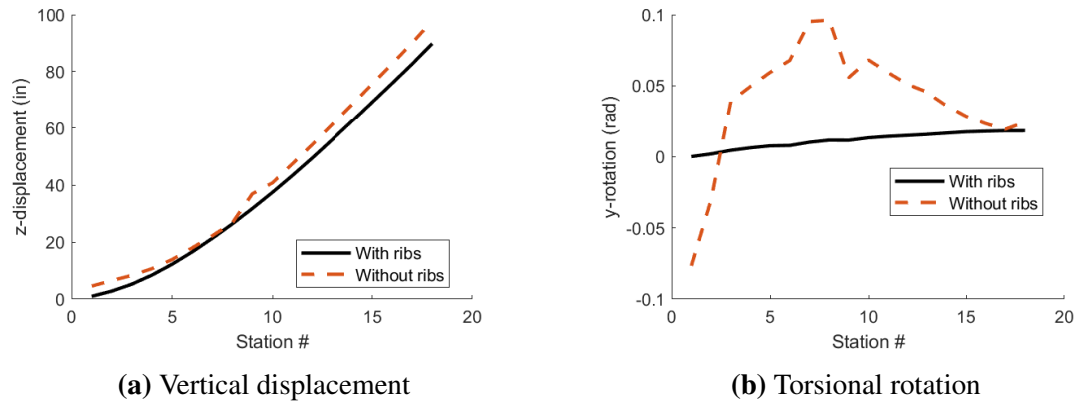


Figure 4.25: Comparison of static response of nodes along PEGASUS concept wing span subjected to 1g loads

Test 3: Gust Response

Consider the same PEGASUS wing concept considered in the previous experiment. Two SOL146 (gust analysis) shell models were created in Nastran- one where the entire shell model is used, and one where Guyan Reduction [81] is used to statically reduce the model to a series of ‘ASET’ nodes on a 1-D curve along the span of the wing. Since Guyan Reduction uses the shell model containing the ribs, it is expected to capture the torsional stiffness better than purely a beam model that does not have the ribs.

The response of a node at the CG of wingtip rib is shown in Fig. 4.26. As seen in Fig. 4.26a, the vertical displacement for the shell model and the ASET model match very well. The ASET model over-predicts the torsional stiffness as seen in Fig. 4.26b.

Test 4: Sizing for 1g Loads

We once again consider the same PEGASUS concept wing. The structure was subjected to 1g aerodynamic loads obtained from AVL. The components of the wingbox structure were sized to withstand the loads. Sizing was carried out using a commercial tool- Hypersizer. The mass of the wingbox was set as the objective function. The following failure mode constraints were setup in Hypersizer:

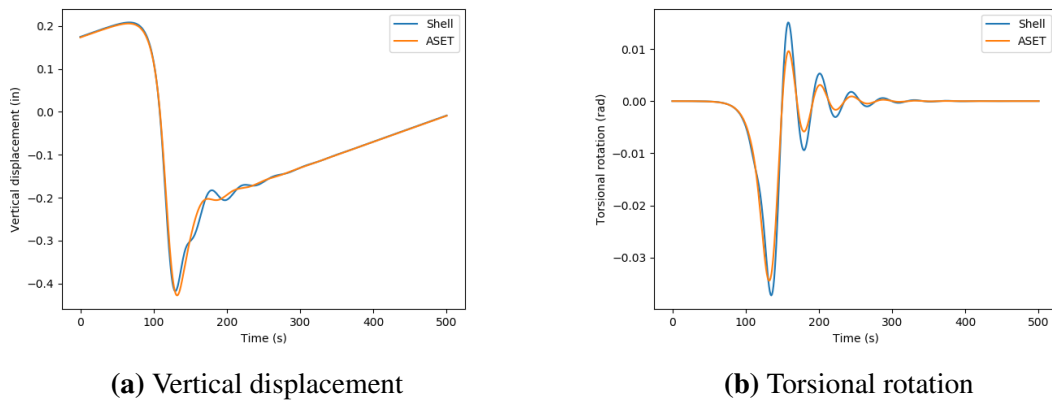


Figure 4.26: Comparison of gust response of tip node PEGASUS concept wing

- Isotropic material strength failure
- Panel buckling failure
- Crippling failure

Table 4.11 compares the masses of the structural components of the PEGASUS wing. The following observations can be made:

1. The mass of the ribs is a small percent of the overall mass (5.6% for the case shown)
2. In the absence of ribs, the other components bear the load the rib would have and hence are sized to be thicker
3. The difference in weight of the structure in the absence of rib is small (2.04% for the case shown)

Table 4.11: Static sizing of components of PEGASUS wing subjected to 1g loads. All masses in lbs

	Upper Skin	Lower Skin	Ribs	Spars	Total
With ribs	760.86	616.75	87.83	102.90	1568.34
Without ribs	844.65	637.68		118.63	1600.96

Table 4.12 compares the masses of the structural components for the CRM wing, from which similar observations can be made.

Table 4.12: Static sizing of components of CRM wing subjected to 1g loads. All weights in lbs

	Upper Skin	Lower Skin	Ribs	Spars	Total
With ribs	26808.27	14746.52	4220.94	2095.19	47870.92
Without ribs	30327.49	16929.32		2919.23	50176.05

Summary

From the preceding tests, it was seen that the structural response that the ribs impacted the most was the torsional rotation. The role of the rib in the overall wingbox is to increase the torsional stiffness of the wingbox. Accurately capturing the torsional rotation response is critical in aeroelastic studies [193]. Thus for aeroelastic studies, using a non-prismatic beam model consisting only of skins and spars would not be adequate. The test on sizing the wingbox structure showed that in the absence of the ribs, the skins and spars size to larger thicknesses and bear the loads that would have been borne by the ribs. It was also seen that the final mass obtained when sized without ribs is only slightly heavier than that obtained with the ribs. Thus, it may be possible for early structural sizing to neglect the ribs and simplify the wingbox to a non-prismatic beam.

4.3.2 Experiment: Displacement Comparison to Shell Model

In this section, the displacement response of the beam model will be compared to a higher-fidelity shell model to determine the accuracy of the beam model. The test case geometries are the PEGASUS concept wing described in Appendix D.2 and the CRM wing described in Appendix D.3. For each case, a shell model is created in Nastran using RADE. 1g loads from AVL are applied to both models. Three beam models are considered:

1. Beam model generated using VABS- VbS

2. Beam model with box cross-section

3. Beam model with box cross-section corrected by VABS- BbcVS

Fig. 4.27 shows the comparison of the displacement response of the beam model generated using VABS against that of a Nastran shell model. It is seen that the displacement response is quite accurate. The tip displacement error is 4.22% for the CRM wing and 0.57% for the PEGASUS wing.

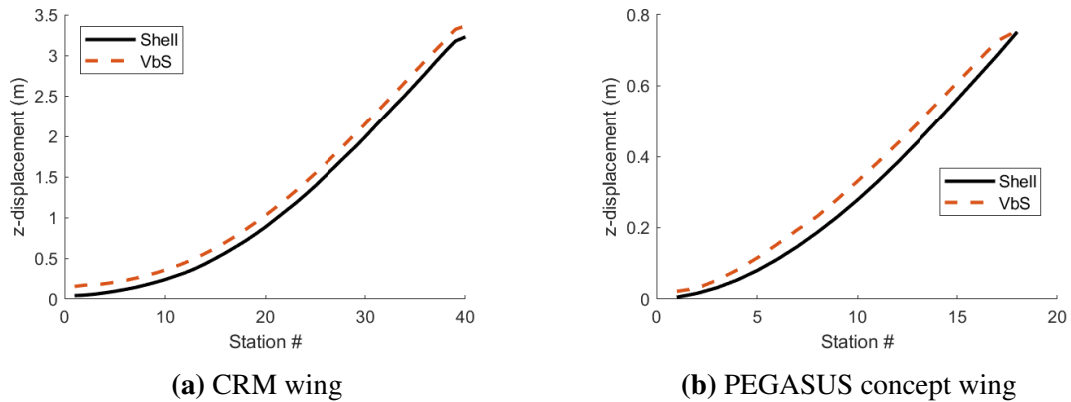
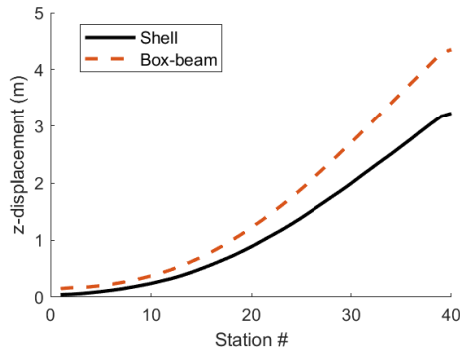


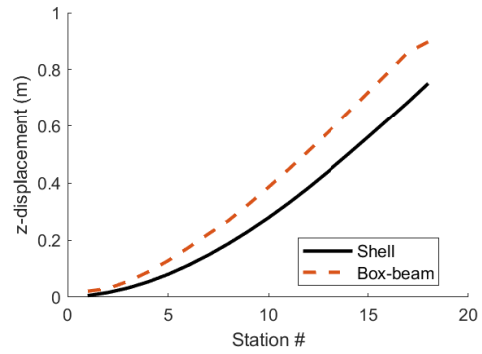
Figure 4.27: Displacement response comparison between Nastran shell model and VbS model

Next, we consider the rectangular box-beam. The width and height at each cross-section are computed using the averaging method shown in Fig. 4.18. Fig. 4.28 compares the displacement response of the box cross-section beam against Nastran shell model. As seen, this assumption does poorly in predicting the displacement. The tip displacement error is 34.86% for the CRM wing and 19.45% for the PEGASUS wing.

Finally we consider the box cross-section beam corrected by VABS, the BbcVS model, following the stiffness matching process described in Section 4.2.4. Fig. 4.29 shows the displacement response. As seen, when the stiffness matching correction is applied, the BbcVS model displacement response matches that of the Nastran shell model accurately. The tip displacement error between the shell model and BbcVS model is 9.77% for the CRM wing and 1.29% for the PEGASUS wing.

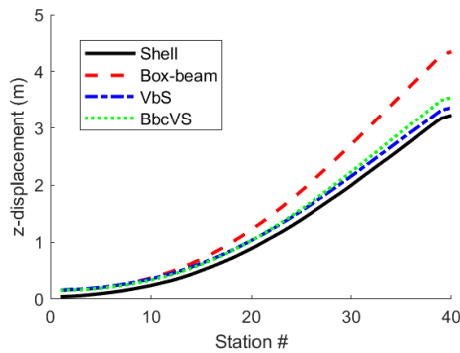


(a) CRM wing

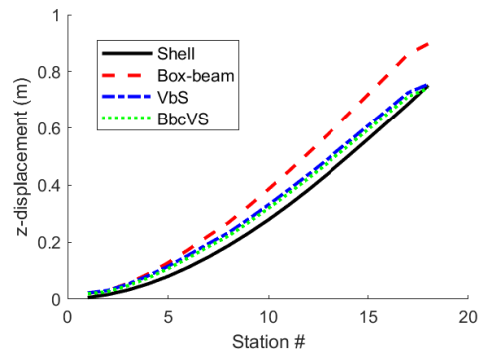


(b) PEGASUS concept wing

Figure 4.28: Displacement response comparison between Nastran shell model and rectangular box-beam model when averaged height method is used (Fig. 4.18)



(a) CRM wing



(b) PEGASUS concept wing

Figure 4.29: Displacement response comparison between Nastran shell model, VbS model, rectangular box-beam model, and BbcVS model

4.4 RQ 1.4 – 3-D Stress/Strain Recovery

The 1-D analysis solution must now be used to obtain the 3-D stress and strain fields on the structure. This section addresses the 3-D recovery. The research and hypothesis are repeated here:

Research Question 1.4

How can stress and strain field time-history computations be made accurate and efficient when the aircraft wingbox structure is subjected to dynamic loads?

Hypothesis 1.4

If
VAM-based VABS is applied to aircraft wings,
Then,
it accurately computes stress and strain field time histories.

4.4.1 Experiment: Stress Comparison to Higher-Fidelity Methods

In this section, the stress response of the beam model will be compared to higher-fidelity models to determine the accuracy of the beam model.

Toy Problem: 'Wing-like' geometry

We consider a 'wing-like' geometry described in Section D.1. Fig. 4.30 qualitatively shows the comparison of von-Mises stress contour on the four cross-sections. It is seen that VABS captures the stress contours accurately for cross-sections two and three. It should be noted that the fourth cross-section is at the tip where a load is applied. The local effect of a large force applied to this cross-section causes differences in the von-Mises stress contour plot. The first cross-section is the root where a fixed boundary condition is applied. Such differences are common near the boundaries. The beam theory is accurate at regions away from the boundary, as in cross-sections two and three.

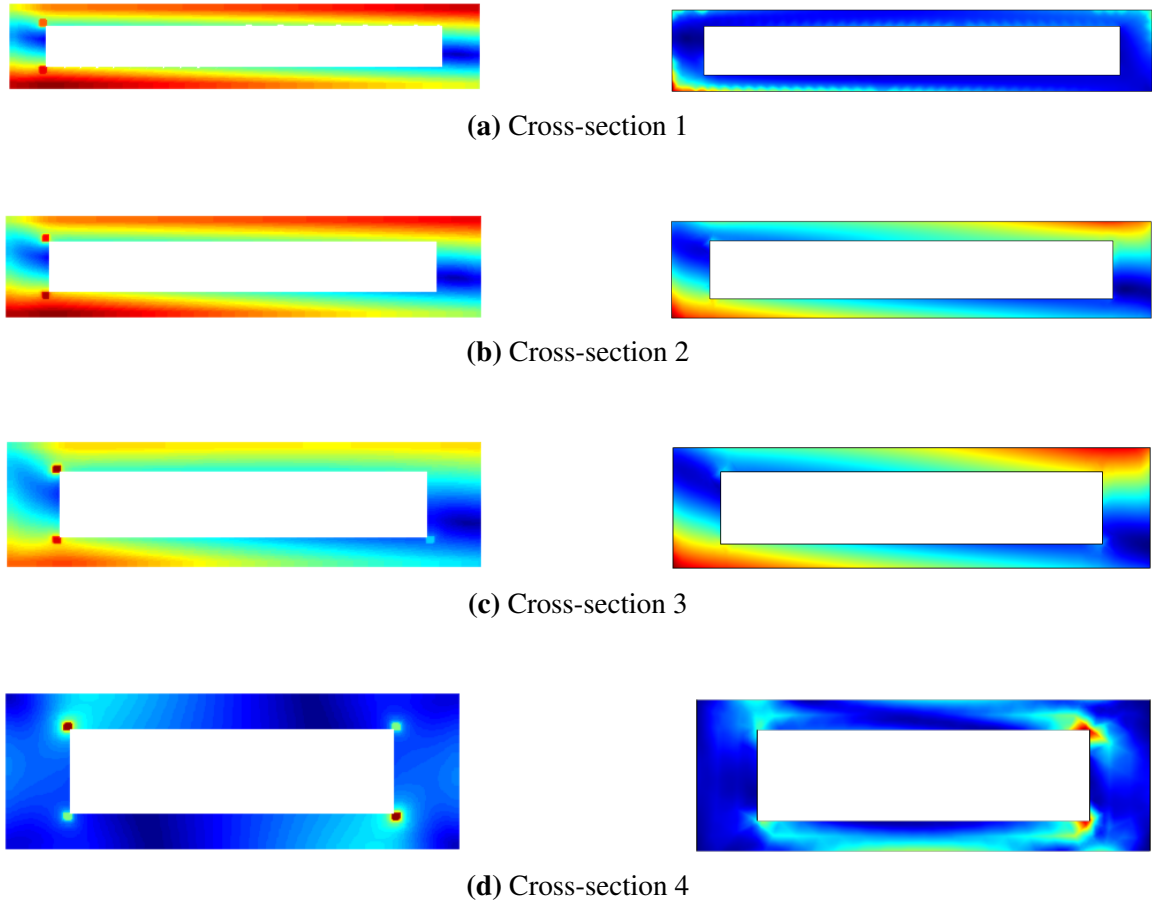


Figure 4.30: von-Mises stress comparison between VABS beam model (left) and 3-D solid element FEM model (right)

Table 4.13 compares the average von-Mises stress, and displacements. Case 1 loading is such that the stresses in the structure are below the yield stress. For case 2, the loads produce stress far higher than the yield stress. It is seen that for case 1, the von-Mises stress error is around or less than 1.5%, which is acceptable given the time-saving benefits of the beam code as compared to 3-D solid element FEM. For case 2, the error is higher. This is to be expected as beam theory assumes small strains. The strains produced by the loading of case 2 is large, and the stresses are beyond the yield stress. For design-optimization, the stresses in the structure will be constrained to be below the yield stress. Hence, the results of case 1 show the beam code to be adequate for optimization. It should also be noted that

the stresses produced by the beam are higher than those from 3-D FEM. This leads to a conservative structure, which is desirable in the early stages of aircraft design.

Table 4.13: Comparison of displacement and stress response of the geometry seen in Fig. D.2e

				von-Mises Stress (Pa)			Displacement (m)		
				3-D FEM	Beam	% Error	3-D FEM	Beam	% Error
Case 1	Fx	0	N CS2	6.13×10^7	6.20×10^7	-1.19	2.66×10^{-2}	2.45×10^{-2}	7.81
	Fy	0	N CS3	3.40×10^7	3.41×10^7	-0.09	1.29×10^{-1}	1.26×10^{-1}	2.5
	Fz	1.00×10^6	N CS4				2.38×10^{-1}	2.35×10^{-1}	1.42
Case 2	Fx	0	N CS2	3.49×10^8	3.79×10^8	-8.49	2.93×10^{-1}	2.34×10^{-1}	20.16
	Fy	1.00×10^7	N CS3	2.00×10^8	2.20×10^8	-9.66	1.38	1.17	15.20
	Fz	5.00×10^6	N CS4				2.48	2.16	12.93

PEGASUS Wing

Consider the PEGASUS concept wing described in Appendix D.2. 1g aerodynamic loads are computed from AVL and applied to the structure. A Nastran SOL 101 shell model is created for comparison.

Fig. 4.31 compares the von-Mises stress contours qualitatively on the shell and beam model. It is seen that there is excellent agreement in the stress values, except for a shell panel on the front spar root section. Here, a local high-stress concentration is observed for the shell model. We believe it to be an artifact of the SPC constraint at the root.

Fig. 4.32 compares the average von-Mises stress at each cross-section along the span of the wing. As seen, the maximum error is at the root where the local high-stress concentration is seen. The average error neglecting the root section is 4.84%.

4.4.2 Stress Recovery for Box Cross-Sections

In RQ 1.2 on the computation of cross-sectional properties, it was seen that a box cross-section was assumed as an alternate to VbS. This was done as an adjoint to VABS has not been implemented and hence would be a computational bottleneck during sizing. VABS

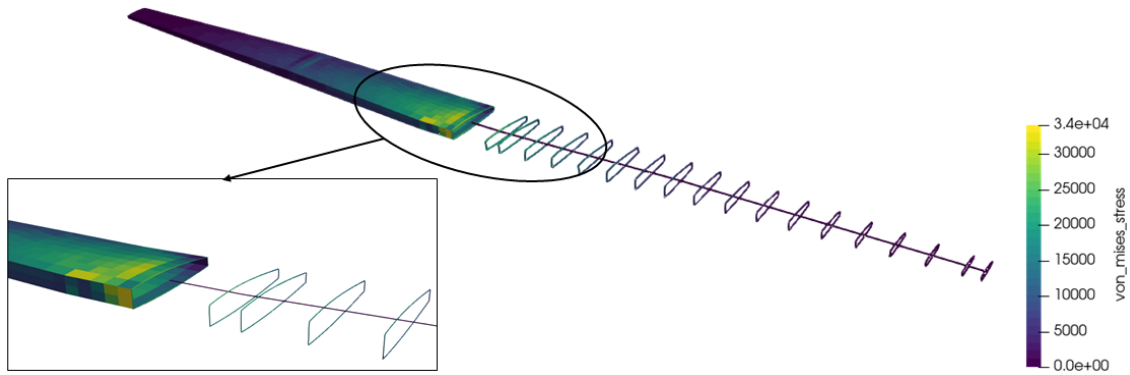


Figure 4.31: von-Mises stress contour comparison of shell and VABS beam model

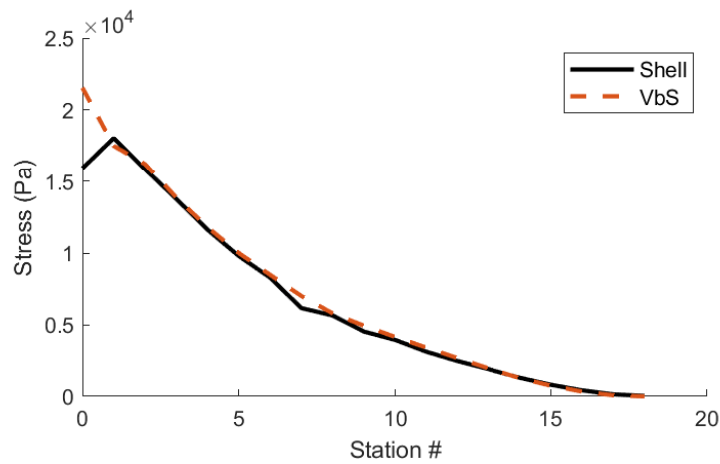


Figure 4.32: von-Mises stress comparison of shell and VbS

was used to correct the cross-sectional properties such that the analytical stiffness of the box cross-section matches the stiffness computed by VABS.

Similarly, for the 3-D stress recovery, using VABS directly would be a computational bottleneck. It is proposed to use the box cross-section corrected by VABS for the 3-D recovery. Hypothesis 1.4 is modified as:

Modified Hypothesis 1.4
<p>If</p> <p style="padding-left: 40px;">the aircraft wingbox cross-section is treated as a box cross-section,</p> <p>And</p>

the box cross-section has been stiffness matched (Hyp 1.2),

Then,

the accuracy of the stress field time history computed using analytical equations improves significantly.

Standard analytical Euler-Bernoulli beam theory formulae exists to compute the stress fields. These are described next.

Stress Field Computation Formulae

The beam theory described in Section A tracks the states defined in Table 2.3. For node $k = 1, \dots, n$ and time $t = t_0, \dots, t_{\text{final}}$, the following information is obtained:

$$\vec{x}(k, t) = \begin{bmatrix} \vec{r}(k, t) \\ \vec{\theta}(k, t) \\ \vec{F}(k, t) \\ \vec{M}(k, t) \\ \vec{r}(k, t) \\ \vec{\theta}(k, t) \end{bmatrix} \quad (4.15)$$

This resultant state vector is obtained in the inertial XYZ frame. From the state vector, the set of internal forces and moments can be computed in the chord-span-normal (csn) frame

by performing the following transformation:

$$\vec{M}_{csn} = [T]\vec{M}_{XYZ} \quad (4.16)$$

$$\vec{F}_{csn} = [T]\vec{F}_{XYZ} \quad (4.17)$$

where

$$\vec{M}_{csn} = \begin{bmatrix} M_c(k, t) \\ M_s(k, t) \\ M_n(k, t) \end{bmatrix}, \vec{F}_{csn} = \begin{bmatrix} F_c(k, t) \\ F_s(k, t) \\ F_n(k, t) \end{bmatrix} \quad (4.18)$$

The internal forces and moments at each cross-section are used to compute the state of stress in the beam. At each cross-section, points $j = 1, \dots, 12$ are considered as shown in Fig. 4.33. The locations of these points, $x_{c,j}$ and $x_{n,j}$ along with the local chord, c , and normal, n , directions respectively, are specified as inputs to the simulation and are directly dependent on the design variables shown in Fig. 4.18.

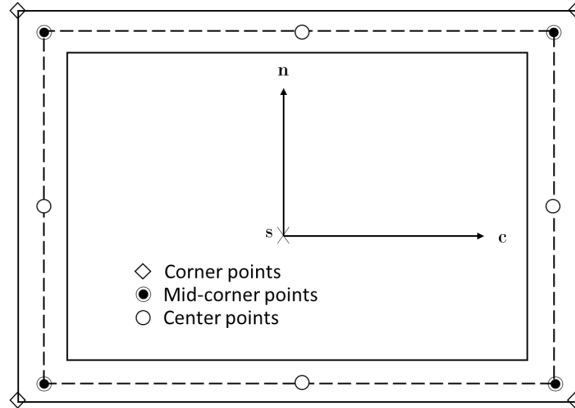


Figure 4.33: Points in each beam cross-section where stresses are computed

Given a cross-section k , the equations to compute the beam state of stress is described next. At the four corner points, the axial stress, σ_{ss} for a corner point j at time t is computed

by

$$\sigma_{ssk,j,t}^{corner} = \frac{N_{k,t}}{A_i} - x_{n,j} \frac{M_{c_{k,t}}}{EI_{cc_k}} + x_{c,j} \frac{M_{n_{k,t}}}{EI_{nn_k}} \quad (4.19)$$

The corner points, however, do not consider the torsional stresses due to the shear flow resulting from torsion within the beam. For that, given a mid-line and assuming a closed thin-walled square section, the shear flow and torsional shear can be assumed to be constant and equal to:

$$q_{k,t} = \frac{T_{k,t}}{A} \longrightarrow \tau_{s_{k,j,t}}^{mid} = \frac{T_{k,t}}{2A \cdot t_{k,j}} \quad (4.20)$$

For the mid-corner points, a resultant shear is calculated by computing the von-Mises resultant shear flow of both flanges that intersect the corner:

$$(\tau_{r_{k,j,t}}^{mid})^2 = (\tau_{s_{k,p,t}}^{mid})^2 + (\tau_{s_{k,q,t}}^{mid})^2 - \tau_{s_{k,p,t}}^{mid} \cdot \tau_{s_{k,q,t}}^{mid}$$

where p and q are flanges that intersect at the corner j . Next, an axial stress resultant is computed, taking into account the position of the corner points with respect to the neutral axis:

$$\sigma_{ssk,j,t}^{mid} = \frac{N_{k,t}}{A_k} - \left(x_{n,j} - \frac{t_{k,p}}{2} \right) \frac{M_{c_{k,t}}}{EI_{cc_k}} + \left(x_{c,j} - \frac{t_{k,q}}{2} \right) \frac{M_{n_{k,t}}}{EI_{nn_k}}$$

where p and q are flanges that intersect at the corner j . After both the shear and normal stresses are computed, a net stress is obtained by generating a von-Mises resultant at the corners, since the torsion and normal stress are perpendicular to each other:

$$(\sigma_{vmk,j,t}^{mid})^2 = (\sigma_{ssk,j,t}^{mid})^2 + (\tau_{r_{k,j,t}}^{mid})^2 - \sigma_{ssk,j,t}^{mid} \cdot \tau_{r_{k,j,t}}^{mid} \quad (4.21)$$

At the center of the flanges, the loads are assumed to be mostly composed of shear loads. These points were set up in place to capture beam stresses that lie along or close to the neutral axis of the beam. A shear flow through a cross section of total thickness t is

calculated by:

$$q = \tau \cdot t \longrightarrow \tau = \frac{V \cdot Q}{It} \quad (4.22)$$

$$\tau_{c_{k,t}} = \frac{V_{c_{k,t}} \cdot Q_{n_k}}{I_{nn_k} \cdot (t_{top,k} + t_{bottom,k})}, \tau_{n_{k,t}} = \frac{V_{n_{k,t}} \cdot Q_{c_k}}{I_{cc_k} \cdot (t_{right,k} + t_{left,k})} \quad (4.23)$$

The shear flow occurs due to torsional and transverse loads. Fig. 4.34 shows the convention and combination of loads that is used. The shear stress is calculated by combining torsional and force shear stresses specific to each flanges direction:

$$\tau_{r_{c,k,t}} = \tau_{s_{c,k,t}} + \tau_{c_{k,t}} \quad (4.24)$$

$$\tau_{r_{n,k,t}} = \tau_{s_{n,k,t}} + \tau_{n_{k,t}} \quad (4.25)$$

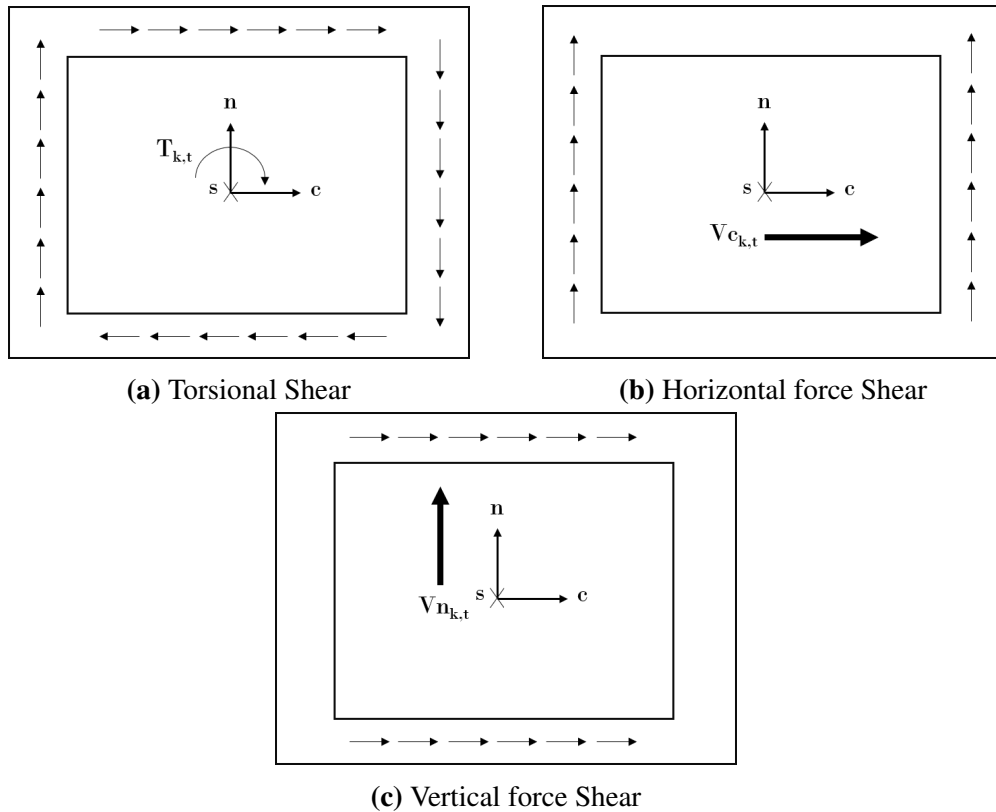


Figure 4.34: Shear sign convention

This results in a stress matrix of the size and composition shown in Fig. 4.35. As a

result, the following five sets of stress constraints for the box beam are constructed:

$$g_{vmj,k,t} = \frac{\sigma_{vmk,j,t}^{mid}}{\sigma_y} - 1 \quad (4.26)$$

$$g_{ssj,k,t} = \pm \frac{\sigma_{ssk,j,t}^{corner}}{\sigma_y} - 1 \quad (4.27)$$

$$g_{centj,k,t} = \pm \frac{\tau_{rk,j,t}^{cent}}{\sigma_y} - 1 \quad (4.28)$$

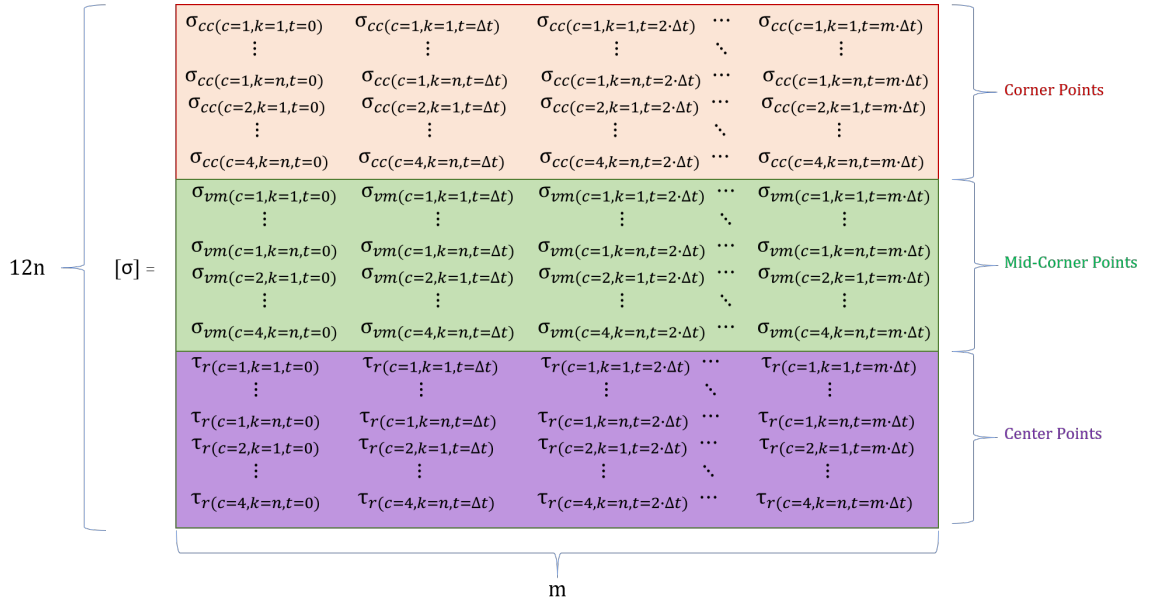


Figure 4.35: Generalized Stress matrix

Experiment: Stress Comparison to Shell and VABS Beam Models

Consider again the PEGASUS concept wing described in Appendix D.2, with 1g loads applied on it. Stresses are computed at the following regions:

- **Shell model:** The 3-D surfaces have a mesh that has either triangular or quadrilateral elements. At every mesh node location, stresses are computed.
- **VbS model:** On each cross-section 20 points are used to define the upper and lower skin curvatures. Stresses are computed on the 20 points.

- Rectangular box-beam models:** From among the 20 points used to define the points for VbS model, 4 points correspond to the intersection of upper skin and front spar, upper skin and rear spar, lower skin and front spar, and lower skin and rear spar respectively. The 4 points form a quadrilateral and stresses are recovered at these 4 points.

Fig. 4.36 compares the structural responses of the VbS model and the BbcVS model. As seen in Fig. 4.36a, the displacement magnitude matches very well. Fig. 4.36b compares the axial stress. It is seen, as expected, that the top surface is under compression and the bottom surface is in tension. In the zoomed portion the differences between the cross-sectional geometry assumption between the VbS model and the BbcVS model is apparent. Similarly, Fig. 4.36c compares the von-Mises stresses.

Fig. 4.37 compares the relative error of the average von-Mises stress at each cross-section along the span of the wing. It is seen that the stresses predicted by E-B theory match well outboard. At inboard sections, the stresses are underpredicted.

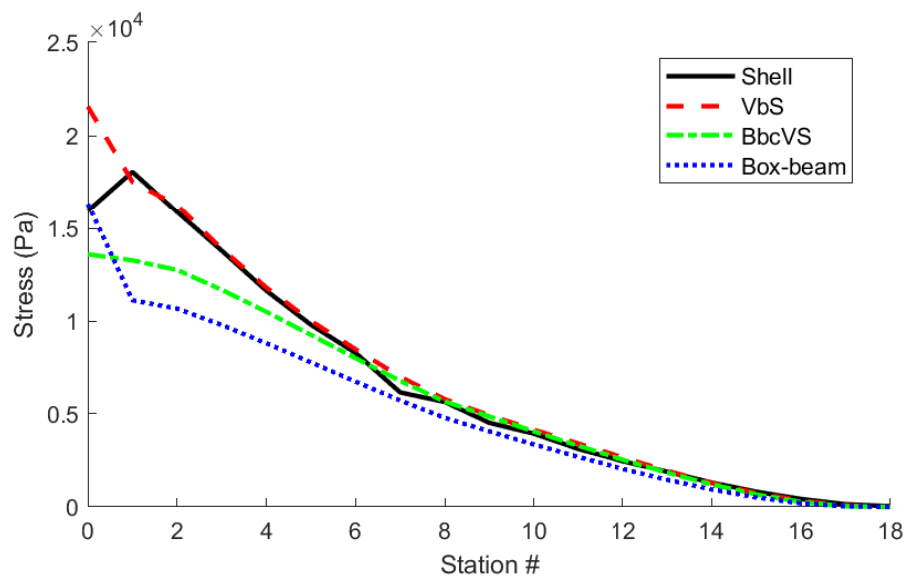
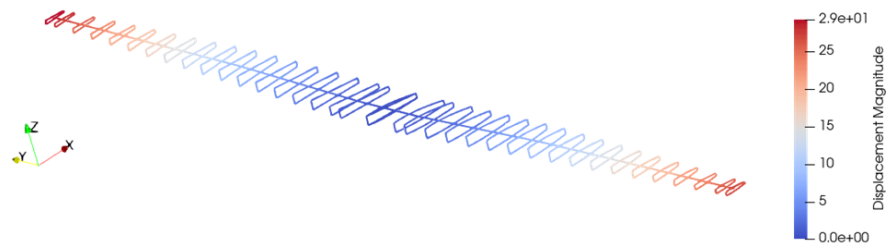
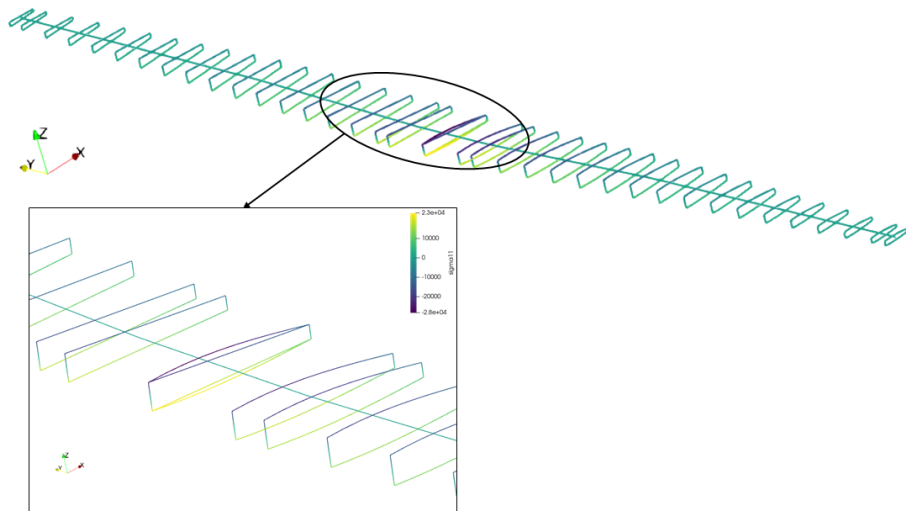


Figure 4.37: von-Mises stress comparison of shell and beam models

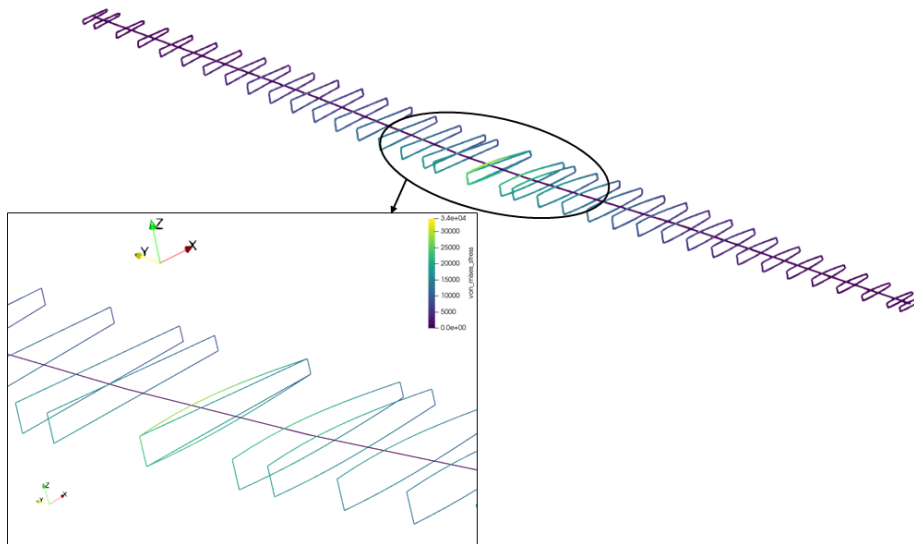
Referring to Fig. 4.28, the rectangular cross-section is created from the two horizontal lines seen. The curvature of the airfoil is such that the locations of points furthest away



(a) Displacement magnitude



(b) Axial stress



(c) von-Mises Stress

Figure 4.36: Comparison between VbS model and BbcVS model for the PEGASUS concept

from the neutral axis does not fall inside the rectangle. This is also seen in the zoomed portion of Fig. 4.36c. We attribute the underprediction of stresses in the BbcVS model to this aspect.

4.5 Structural Analysis Computation Time

Consider the PEGASUS aircraft wing described in Section D.2. Table 4.14 describes the computational time of the operations carried out by RADE to execute a shell model analysis using Nastran. As seen, the process of generating a 3-D surface representation of the wingbox involves the parametric generation of the OML, followed by the generation of the main wing and center wing surfaces. These operations for the wing under consideration take 31.34 seconds. In order to obtain realistic aerodynamic loads, an AVL model is created and executed by RADE. These tasks take 84.51 seconds. Finally, the 3-D surface is meshed, a Nastran model is generated and executed in 38.05 seconds. The static structural analysis (SOL 101) time in Nastran (8.01 seconds) is a small percentage (5.238%) of the time taken for the whole process (153.9 seconds).

If we consider the structural sizing process, it involves running the model at different thicknesses' values until a design is found that has the lowest weight and satisfies the structural failure constraints. For the shell model, the mesh does not change when the thicknesses are changed. The Nastran model's PSHELL cards are updated with the new thickness values. This takes about 2 seconds in RADE. Re-running the Nastran analysis takes about 8 seconds. Thus a new candidate design can be evaluated in about 10 seconds.

Consider next the computational time for the same geometry and loads using beam models. The beam model also requires the 3-D surface representation of the wingbox. This was shown to be 31.34 seconds in Table 4.14. The time to extract the information from the 3-D geometry needed to generate the beam model (Fig. 4.13) was 0.12 seconds.

For the VbS model, the execution time for the various tasks are shown in Table 4.15. The table also compares the execution time of operations that can be run in parallel (2-D

Table 4.14: 3-D geometry, aerodynamics and shell model execution time

Task	Time (seconds)
Generate OML time	13.79
Main wing geometry generation time	16.79
Center wing geometry generation time	0.76
AVL generation time	2.11
AVL execution time	82.4
Nastran model generation time	26.79
Nastran model execution time	8.014
Mesh generation time	3.25
Total	153.9

mesh generation, VABS cross-sectional analysis, and 3-D stress recovery) to running the same operations serially. It is seen that for the few cross-sections of the Pegasus wing, the communication overhead when running in parallel results in mesh generation being slower. Running VABS in parallel is shown to reduce the total execution time, particularly for the 3-D stress recovery. The beam model generation step involves using CasADi[190] to create symbolic containers for the beam parameters, the residual equations, and the loads. This is described in detail in a prior work [46] and in Appendix G. The total execution time from OML to structural response takes 137.87 seconds.

As before, we consider the time required to obtain the structural response of a new design candidate. Unlike the shell model, when the thicknesses are changed, a new 2-D mesh must be generated for each cross-section (alternatively, mesh deformation can be used). VABS cross-sectional analysis, the 1-D analysis, and the 3-D stress recovery must be re-run. Thus, a new candidate design can be evaluated in 17.71 seconds, which is slower than the shell model.

It should be noted that VABS is ‘embarrassingly parallelizable’ in the sense that all the cross-sectional analyses can be computed in-parallel if the requisite computational re-

Table 4.15: VbS model execution time

Task	Time (seconds)	
	Serial	Parallel
Extract beam from geometry time	0.118	
Offset to create 2-D cross-sections	2.196	
Compute VABS parameters	1.047	
Compute mesh	3.392	2.545
VABS run	8.893	6.842
Beam model gen	0.943	
1-D analysis	0.018	
3-D stress recovery	37.813	8.316

sources are available. The computation of the mass and stiffness matrices for the cross-section can be run in-parallel to obtain the necessary information to generate the 1-D beam model. Once the 1-D analysis has been run (which constitutes a very small fraction of the overall computational time- Table 4.15), the stress recovery can be parallelized over not only cross-sections but also over time steps in the dynamic simulation. Thus, the beam-based method would scale better than shell-based methods.

We now consider structural analysis using the analytical box-beam involves three operations- the beam model generation, 1-D analysis, and 3-D stress recovery. Table 4.16 shows the execution time. For the beam that has been corrected by VABS- the BbcVS model, the execution time is given in Table 4.17.

It is seen that the time taken to generate the symbolic representation for the beam model using CasADi is 2.79 seconds for the analytical beam and 0.94 seconds for the VABS beam. This difference is due to the beam model having to construct symbolics for the beam parameters, residual equations and loads, and stresses. Once the symbolics is constructed, it is seen that the execution time of the 1-D analysis ($\mathcal{O}(10^{-2})$ seconds) and 3-D stress recovery ($\mathcal{O}(10^{-3})$ seconds) are short. The total execution time from OML to structural

response takes 118.77 seconds.

Table 4.16: Box cross-section beam model execution time

Task	Time (seconds)
Extract beam from geometry time	0.118
Beam model gen	2.784
1-D analysis	0.018
3-D stress recovery	0.002

We have seen previously that correcting the analytical beam using VABS results in much greater accuracy. Including the time taken to generate the VABS mesh, run cross-sectional analysis and correct the box cross-section properties, the total execution time from OML to structural response takes 131.95 seconds. Once again, we consider the time required to obtain the structural response of a new design candidate. VABS correction and beam model generation are one-time operations. Thus, a new candidate design can be evaluated in $\mathcal{O}(10^{-2})$ seconds, which is significantly faster than the shell model, while incurring a small loss of accuracy.

4.6 RQ 2.1 – Gradient with Adjoint Method²

In this section, the necessary gradient information for optimization of the structural analysis method of RQ 1 will be derived. As seen in the literature, an efficient method to compute the gradient is the adjoint method. The general adjoint equation and gradient computation equation for dynamic simulations solved with the BDF scheme was presented in Section 3.5.2. The adjoint variable is solved at each time-step using Eq. 3.10. Four quantities are required here:

- $\frac{\partial \mathbf{R}}{\partial \mathbf{x}}$ - the Jacobian matrix of the derivative of the residual equations with respect to the

²The method and results for the solid rectangular cross-section beam case have been published in a prior work [194]

Table 4.17: BbcVS model execution time

Task	Time (seconds)
Extract beam from geometry time	0.118
Offset to create 2-D cross-sections	2.196
Compute VABS parameters	1.047
Compute mesh	2.545
VABS run	6.842
Correct box CS properties	0.545
Beam model gen	2.790
1-D analysis	0.018
3-D stress recovery	0.003

state variables

- $\frac{\partial \mathbf{R}}{\partial \dot{\mathbf{x}}}$ - the Jacobian matrix of the derivative of the residual equations with respect to the first time derivative of the state variables
- $\frac{\partial F_i}{\partial \mathbf{x}}$ - the vector of derivatives of the function of interest with respect to the state variables
- $\frac{\partial F_i}{\partial \dot{\mathbf{x}}}$ - the vector of derivatives of the function of interest with respect to the first time derivative of the state variables

The required gradient is then computed using Eq. 3.11. Two additional quantities are required here:

- $\frac{\partial F_i}{\partial \mu}$ - the vector of derivatives of the function of interest with respect to the design variables
- $\frac{\partial \mathbf{R}}{\partial \mu}$ - the matrix of derivatives of the residual equations with respect to the design variables

In summary, to solve a different system six quantities are required: $\frac{\partial \mathbf{R}}{\partial \mathbf{x}}$, $\frac{\partial \mathbf{R}}{\partial \dot{\mathbf{x}}}$, $\frac{\partial F_i}{\partial \mathbf{x}}$, $\frac{\partial F_i}{\partial \dot{\mathbf{x}}}$, $\frac{\partial F_i}{\partial \mu}$, and $\frac{\partial \mathbf{R}}{\partial \mu}$. A general adjoint solver can thus be implemented.

In this section, the adjoint method derived will be applied to specific residual equations. First, the method is illustrated on a simple spring-mass-damper system in Section 4.6.1. Next, the nonlinear beam theory of Appendix A is considered. The approach to obtain the gradient of the stresses with respect to the design variables using the adjoint method is presented. The modified KS constraint aggregation function to aggregate stresses over cross-sections and time steps is also presented here.

Appendix F contains the standard analytical formulae used to obtain the stiffness and mass matrices to be used in the beam code for a box cross-section. Analytical equations are used to compute the stresses in the beam, and further, the strength-based failure constraints are shown. Assuming a solid beam and only axial stresses, all the terms' analytical expressions are obtained in Section 4.6.2. The method is then generalized to a box cross-section, including axial, shear, and torsional stresses in Section 4.6.3.

4.6.1 Illustration on Spring-Mass-Damper System

The GDE of a spring-mass-damper (SMD) system is written as:

$$m\ddot{x} + c\dot{x} + kx = 0 \quad (4.29)$$

where m is the mass of the spring, c the damping constant, and k the spring stiffness. This system can be re-written as a first order set of equations as:

$$R_1 = m\dot{x}_2 + cx_2 + kx_1 = 0 \quad (4.30)$$

$$R_2 = x_2 - \dot{x}_1 = 0 \quad (4.31)$$

The state vector and its time derivative are represented as:

$$\mathbf{x} = \begin{Bmatrix} x_1 \\ x_2 \end{Bmatrix}, \dot{\mathbf{x}} = \begin{Bmatrix} \dot{x}_1 \\ \dot{x}_2 \end{Bmatrix} \quad (4.32)$$

The function of interest is chosen to be the integral of the potential energy

$$f = \sum_{i=1}^n \delta_i \frac{1}{2} k x_{1_i}^2 = \sum_{i=1}^n F_i \quad (4.33)$$

To propagate a system of equations forward in time using the BDF scheme, two jacobian matrices ($\frac{\partial \mathbf{R}}{\partial \mathbf{x}}$ and $\frac{\partial \mathbf{R}}{\partial \dot{\mathbf{x}}}$) are needed. For the SMD system, they are given by

$$\frac{\partial \mathbf{R}}{\partial \mathbf{x}_i} = \begin{bmatrix} \frac{\partial R_1}{\partial x_1} & \frac{\partial R_1}{\partial x_2} \\ \frac{\partial R_2}{\partial x_1} & \frac{\partial R_2}{\partial x_2} \end{bmatrix} = \begin{bmatrix} k & c \\ 0 & 1 \end{bmatrix} \quad (4.34)$$

$$\frac{\partial \mathbf{R}}{\partial \dot{\mathbf{x}}_i} = \begin{bmatrix} \frac{\partial R_1}{\partial \dot{x}_{1_i}} & \frac{\partial R_1}{\partial \dot{x}_{2_i}} \\ \frac{\partial R_2}{\partial \dot{x}_{1_i}} & \frac{\partial R_2}{\partial \dot{x}_{2_i}} \end{bmatrix} = \begin{bmatrix} 0 & m \\ -1 & 0 \end{bmatrix} \quad (4.35)$$

Table 4.18: SMD parameters

m	c	k	n	δ_i
2.5	0.2	5.0	10	1×10^{-3}

In addition to $\frac{\partial \mathbf{R}}{\partial \mathbf{x}}$ and $\frac{\partial \mathbf{R}}{\partial \dot{\mathbf{x}}}$, to solve the adjoint system, two more vectors ($\frac{\partial F_i}{\partial \mathbf{x}}$ and $\frac{\partial F_i}{\partial \dot{\mathbf{x}}}$)

are needed. For the SMD system, they are given by:

$$\frac{\partial F_i}{\partial \mathbf{x}_i} = \begin{Bmatrix} \frac{\partial F_i}{\partial x_{1_i}} \\ \frac{\partial F_i}{\partial x_{2_i}} \end{Bmatrix} = \begin{Bmatrix} \delta_i k x_{1_i} \\ 0 \end{Bmatrix} \quad (4.36)$$

$$\frac{\partial F_i}{\partial \mathbf{x}_i} = \begin{Bmatrix} \frac{\partial F_i}{\partial \dot{x}_{1_i}} \\ \frac{\partial F_i}{\partial \dot{x}_{2_i}} \end{Bmatrix} = \begin{Bmatrix} 0 \\ 0 \end{Bmatrix} \quad (4.37)$$

Finally to obtain the gradient of the function of interest with respect to design variables, the vector $\frac{\partial F_i}{\partial \mu}$, and the matrix $\frac{\partial \mathbf{R}}{\partial \mu}$. For the SMD system, these are given by

$$\frac{\partial F_i}{\partial \mu} = \frac{\partial F_i}{\partial k} = \frac{1}{2} x_{1_i}^2 \quad (4.38)$$

$$\frac{\partial \mathbf{R}}{\partial \mu} = \begin{Bmatrix} \frac{\partial R_1}{\partial k} \\ \frac{\partial R_2}{\partial k} \end{Bmatrix} = \begin{Bmatrix} x_{1_i} \\ 0 \end{Bmatrix} \quad (4.39)$$

Table 4.19 compares the accuracy of the gradient computation against finite-difference when solving the system for the parameters given in Table 4.18 and second order accurate BDF ($p = 2$).

Table 4.19: SMD adjoint results

f	Finite-difference $\frac{\partial f}{\partial k}$	Adjoint $\frac{\partial f}{\partial k}$
8.666966423590475	1.160819927186196	1.160579582598164

4.6.2 Gradient of a Solid Beam subjected to Axial Stress

In this section, the following two simplifications are made:

- Cross-section is assumed to be a solid rectangle

- Only axial stress failure constraint is considered

For each cross-section (k) and time (i), the maximum axial stress can be found using Euler-Bernoulli beam theory. It occurs at the location furthest away from the neutral axis and is given by:

$$\sigma_k^i = \frac{M}{I} y = \frac{M_{2k}^i}{\frac{w_k h_k^3}{12}} \frac{h_k}{2} = \frac{6M_{2k}^i}{w_k h_k^2} \quad (4.40)$$

where M_{2k}^i is the moment about the y-axis at cross-section k and time i . The corresponding stress constrain is given by:

$$g_k^i = \frac{\sigma_k^i}{\sigma_y} - 1 \leq 0, i = 0, \dots, n, k = 1, \dots, n_n \quad (4.41)$$

The moment in Eq. 4.40 can be either positive or negative depending on the loading on the beam. To account for both, two sets of stress constraints are imposed:

$$\begin{aligned} g_{1,k}^i &= \frac{6M_{2k}^i}{w_k h_k^2 \sigma_y} - 1 \leq 0, i = 0, \dots, n, k = 1, \dots, n_n \\ g_{2,k}^i &= \frac{-6M_{2k}^i}{w_k h_k^2 \sigma_y} - 1 \leq 0, i = 0, \dots, n, k = 1, \dots, n_n \end{aligned} \quad (4.42)$$

The above results in a very large number of constraints ($2nn_n$). A large number of constraints makes it harder for the optimizer to converge. Hence, constraint aggregation methods are used [180]. One possible constraint aggregation will be the the KS function given by

$$c_{KS} = m + \frac{1}{\rho_{KS}} \ln \left[\sum_{k=1}^{n_n} e^{\rho_{KS}(g_k - m)} \right] \quad (4.43)$$

with $m = \max g_k$, ρ_{KS} a constraint aggregation parameter. Note that the above equation is conventionally used when constraints are aggregated over space.

The peak stress on the beam could occur at any time instant between 0 and T . As it is not possible to know apriori which time instant the peak load occurs, the constraint aggregation must also be done over time. The KS functional in Eq. 4.43 can be modified

to integrate over time as well:

$$c_{KS} = m + \frac{1}{\rho_{KS}} \ln \left[\sum_{i=0}^n \sum_{k=1}^{n_n} e^{\rho_{KS}(g_k^i - m)} \right] \quad (4.44)$$

where $m = \max g_k^i$. With the definition in Eq. 4.44, the two stress constraints defined in Eq. 4.42 can be aggregated into the following two functions:

$$\begin{aligned} c_{1,KS} &= m + \frac{1}{\rho_{KS}} \ln \left[\sum_{i=0}^n \sum_{k=1}^{n_n} e^{\rho_{KS}(g_{1,k}^i - m)} \right] \\ c_{2,KS} &= m + \frac{1}{\rho_{KS}} \ln \left[\sum_{i=0}^n \sum_{k=1}^{n_n} e^{\rho_{KS}(g_{2,k}^i - m)} \right] \end{aligned} \quad (4.45)$$

As previously said in Section 4.6.1 the adjoint system requires six quantities: $\frac{\partial \mathbf{R}}{\partial \mathbf{x}}$, $\frac{\partial \mathbf{R}}{\partial \dot{\mathbf{x}}}$, $\frac{\partial F_i}{\partial \mathbf{x}}$, $\frac{\partial F_i}{\partial \dot{\mathbf{x}}}$, $\frac{\partial F_i}{\partial \mu}$, and $\frac{\partial \mathbf{R}}{\partial \mu}$. The Jacobians $\frac{\partial \mathbf{R}}{\partial \mathbf{x}}$ and $\frac{\partial \mathbf{R}}{\partial \dot{\mathbf{x}}}$ are obtained using CasADi during the forward solve. CasADi also provides the term $\frac{\partial \mathbf{R}}{\partial \mu}$. The remaining three terms are derived analytically next. The derivative of the function of interest (aggregated stress constraints) w.r.t the design variables h_k and w_k are:

$$\begin{aligned} \frac{\partial c_{1,KS}}{\partial h_k} &= \frac{1}{\rho_{KS}} \frac{1}{\sum_{i=0}^n \sum_{k=1}^{n_n} e^{\rho_{KS}(g_{1,k}^i - m)}} \sum_{i=0}^n e^{\rho_{KS}(g_{1,k}^i - m)} \rho_{KS} \frac{\partial}{\partial h_k} \left(\frac{6M_{2k}^i}{w_k h_k^2 \sigma_y} - 1 \right) \\ &= \frac{\sum_{i=0}^n e^{\rho_{KS}(g_{1,k}^i - m)}}{\sum_{i=0}^n \sum_{k=1}^{n_n} e^{\rho_{KS}(g_{1,k}^i - m)}} \frac{-12M_{2k}^i}{w_k h_k^3 \sigma_y} \end{aligned} \quad (4.46)$$

$$\begin{aligned} \frac{\partial c_{1,KS}}{\partial w_k} &= \frac{1}{\rho_{KS}} \frac{1}{\sum_{i=0}^n \sum_{k=1}^{n_n} e^{\rho_{KS}(g_{1,k}^i - m)}} \sum_{i=0}^n e^{\rho_{KS}(g_{1,k}^i - m)} \rho_{KS} \frac{\partial}{\partial w_k} \left(\frac{6M_{2k}^i}{w_k h_k^2 \sigma_y} - 1 \right) \\ &= \frac{\sum_{i=0}^n e^{\rho_{KS}(g_{1,k}^i - m)}}{\sum_{i=0}^n \sum_{k=1}^{n_n} e^{\rho_{KS}(g_{1,k}^i - m)}} \frac{-6M_{2k}^i}{w_k^2 h_k^2 \sigma_y} \end{aligned} \quad (4.47)$$

and

$$\begin{aligned}\frac{\partial c_{2,KS}}{\partial h_k} &= \frac{1}{\rho_{KS}} \frac{1}{\sum_{i=0}^n \sum_{k=1}^{n_n} e^{\rho_{KS}(g_{1,k}^i - m)}} \sum_{i=0}^n e^{\rho_{KS}(g_{1,k}^i - m)} \rho_{KS} \frac{\partial}{\partial h_k} \left(\frac{-6M_{2k}^i}{w_k h_k^2 \sigma_y} - 1 \right) \\ &= \frac{\sum_{i=0}^n e^{\rho_{KS}(g_{1,k}^i - m)}}{\sum_{i=0}^n \sum_{k=1}^{n_n} e^{\rho_{KS}(g_{1,k}^i - m)}} \frac{12M_{2k}^i}{w_k h_k^3 \sigma_y}\end{aligned}\quad (4.48)$$

$$\begin{aligned}\frac{\partial c_{2,KS}}{\partial w_k} &= \frac{1}{\rho_{KS}} \frac{1}{\sum_{i=0}^n \sum_{k=1}^{n_n} e^{\rho_{KS}(g_{1,k}^i - m)}} \sum_{i=0}^n e^{\rho_{KS}(g_{1,k}^i - m)} \rho_{KS} \frac{\partial}{\partial w_k} \left(\frac{-6M_{2k}^i}{w_k h_k^2 \sigma_y} - 1 \right) \\ &= \frac{\sum_{i=0}^n e^{\rho_{KS}(g_{1,k}^i - m)}}{\sum_{i=0}^n \sum_{k=1}^{n_n} e^{\rho_{KS}(g_{1,k}^i - m)}} \frac{6M_{2k}^i}{w_k^2 h_k^2 \sigma_y}\end{aligned}\quad (4.49)$$

The derivative of the aggregated stress constraints with respect to state vector \mathbf{x} is given by

$$\begin{aligned}\frac{\partial c_{1,KS}}{\partial \mathbf{x}_i} &= \frac{1}{\rho_{KS}} \frac{\partial}{\partial \mathbf{x}_i} \left(\ln \left[\sum_{i=0}^n \sum_{k=1}^{n_n} e^{\rho_{KS}(g_{1,k}^i - m)} \right] \right) \\ &= \frac{6e^{\rho_{KS}(g_{1,k}^i - \max g_{1,k}^i)}}{\sigma_y w_k h_k^2 \sum_{i=0}^n \sum_{k=1}^{n_n} e^{\rho_{KS}(g_{1,k}^i - m)}}\end{aligned}\quad (4.50)$$

and

$$\begin{aligned}\frac{\partial c_{2,KS}}{\partial \mathbf{x}_i} &= \frac{1}{\rho_{KS}} \frac{\partial}{\partial \mathbf{x}_i} \left(\ln \left[\sum_{i=0}^n \sum_{k=1}^{n_n} e^{\rho_{KS}(g_{2,k}^i - m)} \right] \right) \\ &= \frac{6e^{\rho_{KS}(g_{2,k}^i - \max g_{2,k}^i)}}{\sigma_y w_k h_k^2 \sum_{i=0}^n \sum_{k=1}^{n_n} e^{\rho_{KS}(g_{2,k}^i - m)}}\end{aligned}\quad (4.51)$$

The derivative of the aggregated stress constraints with respect to the derivative of the state vector $\dot{\mathbf{x}}$ is given by

$$\begin{aligned}\frac{\partial c_{1,KS}}{\partial \dot{\mathbf{x}}} &= \mathbf{0} \\ \frac{\partial c_{2,KS}}{\partial \dot{\mathbf{x}}} &= \mathbf{0}\end{aligned}\quad (4.52)$$

The derivative of the aggregated stress constraint, $c_{1,KS}$, with respect to design variables (h_k and w_k) is computed using the adjoint method and compared with those computed using central difference. Using complex-step method would produce better results. Ten beam cross-sections (n_n) are used for this test case. The results for the are shown in Table 4.20. The gradients obtained are good enough to be used for optimization.

Table 4.20: Gradient comparison between adjoint method and central differences (step-size: 1×10^{-8}) for 20 design variables for stress aggregated constraint $c_{1,KS}$

DV	Finite Difference	Adjoint	Error (%)
h_1	-0.04169	-0.04169	-0.00269
h_2	-0.03141	-0.03142	-0.00833
h_3	-0.02626	-0.02627	-0.0106
h_4	-0.02376	-0.02376	-0.01268
h_5	-0.02232	-0.02233	-0.01492
h_6	-0.02035	-0.02036	-0.01883
h_7	-0.01548	-0.01548	-0.0301
h_8	-0.00636	-0.00637	-0.09516
h_9	0.00057	0.000561	1.516774
h_{10}	0.000775	0.000769	0.73688
w_1	-0.0693	-0.0693	-0.00179
w_2	-0.0426	-0.0426	-0.00563
w_3	-0.02918	-0.02918	-0.00725
w_4	-0.02155	-0.02155	-0.00906
w_5	-0.01639	-0.0164	-0.01192
w_6	-0.01191	-0.01191	-0.01821
w_7	-0.00699	-0.00699	-0.03754
w_8	-0.00199	-0.00199	-0.16605
w_9	0.00045	0.000446	0.897364
w_{10}	0.000264	0.000263	0.697847

Table 4.21: Comparison of time (in seconds) to compute the gradient between finite-difference and adjoint method

# DV	FD Time (s)	Adjoint Time (s)
20	6.58	0.32
40	17.78	0.32
100	87.24	0.66
500	1989.55	2.70
1000	7917.03	5.34

Table 4.21 compares the time to compute the gradient using finite-difference and adjoint method as the number of design variables scales. As the number of design variables increases, the time to compute the gradient using finite-difference method becomes infeasible.

4.6.3 Gradient of a Box-Beam using Automatic Differentiation

The computation of stress fields on the box cross-section was described in Section 4.4.2. Constraint aggregation methods are then used to generate the KS functions that will be used for optimization. It should be noted that the aggregation is occurring over the $j = 1, \dots, 4$ points where the stresses were computed, the $k = 1, \dots, n$ cross-sections of the beam, and the $t = 0, \dots, n_T$ time steps of the dynamic simulation.

$$c_{vm,KS} = m + \frac{1}{\rho_{KS}} \ln \left[\sum_{j=1}^4 \sum_{k=1}^n \sum_{t=0}^{n_T} e^{\rho_{KS}(g_{vmj,k,t} - m)} \right] = m + \frac{1}{\rho_{KS}} \ln A_{vm} \quad (4.53)$$

$$c_{ss,KS} = m + \frac{1}{\rho_{KS}} \ln \left[\sum_{j=1}^4 \sum_{k=1}^n \sum_{t=0}^{n_T} e^{\rho_{KS}(g_{ssj,k,t} - m)} \right] = m + \frac{1}{\rho_{KS}} \ln A_{ss} \quad (4.54)$$

$$c_{cent,KS} = m + \frac{1}{\rho_{KS}} \ln \left[\sum_{j=1}^4 \sum_{k=1}^n \sum_{t=0}^{n_T} e^{\rho_{KS}(g_{centj,k,t} - m)} \right] = m + \frac{1}{\rho_{KS}} \ln A_{cent} \quad (4.55)$$

Each of the stress constraints defined can have hundreds of expressions dependent on

geometric properties, state variables, or external dimensions. To calculate the different sets of derivatives needed, automatic differentiation (AD) package CasADi was used. The procedure to obtain the gradients using AD is explained in detail in Appendix G. As a simplified explanation, Fig. 4.38 shows a diagram that illustrates the basic premise behind the calculation of the symbolic gradients.

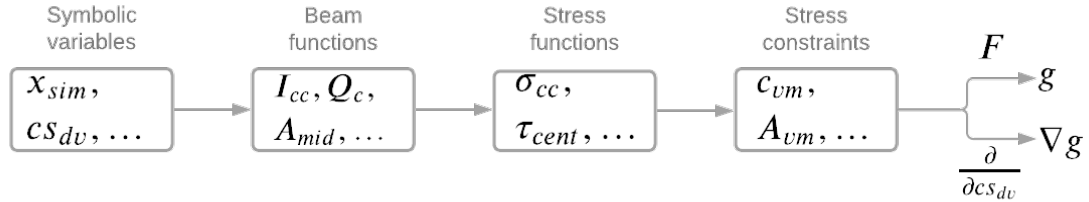


Figure 4.38: Workflow summary for symbolic gradients and functions

Given a set of specific symbolic variables of interest, such as the thickness distribution in the beam or the corner points, functions at the beam level, such as beam stiffness expressions, are constructed. These are then used to construct stress functions representing the equations given in Section 4.4.2 and the constraint aggregation functions given in this section. With these expressions at hand, CasADi can then be used to provide function objects associated with them. These function objects can then be used in conjunction with data obtained by forward-solving and backward-solving the model to generate proper constraint values and gradients associated with the state of deformation of the beam.

The derivative of the aggregated stress constraint $c_{vm,KS}$ with respect to the 16 design variables are computed using the adjoint method and compared with those computed using the central difference method. A tip load of $F_x = 1 \times 10^6 N$ and $F_z = 1 \times 10^6 N$ is applied. The simulation was run for 3 seconds with a time step of 0.01 seconds. The results are shown in Table 4.22. The gradients obtained have the right sign and order of magnitude, and thus may be used for optimization.

It should be noted that using the finite-difference method as a validation tool may be prone to errors. The errors are due to the finite-difference method being very sensitive to

Table 4.22: Gradient comparison between adjoint method and central differences (step-size: 1×10^{-8}) for 16 design variables for von-Mises stress aggregated constraint $c_{vm,KS}$

DV	Finite Difference	Adjoint	Error (%)
t_{left1}	-0.14267	-0.14268	0.00505
t_{left2}	-0.03586	-0.03587	0.021513
t_{left3}	0.001537	0.001519	-1.21537
t_{left4}	0.001505	0.001488	-1.12154
t_{top1}	-2.72883	-2.72898	0.005573
t_{top2}	-0.64338	-0.64348	0.016194
t_{top3}	0.002966	0.002918	-1.61295
t_{top4}	0.004861	0.004807	-1.10627
t_{right1}	-0.14268	-0.14269	0.006823
t_{right2}	-0.03596	-0.03597	0.02369
t_{right3}	0.00125	0.001236	-1.1515
t_{right4}	0.001358	0.001342	-1.13942
t_{bot1}	-2.72883	-2.72898	0.005666
t_{bot2}	-0.64336	-0.64346	0.016564
t_{bot3}	0.002986	0.00294	-1.53316
t_{bot4}	0.004865	0.004812	-1.09163

the chosen step-size and the region of the design space at which the gradient is computed. Thus, finite-difference serves as a check and verifies the sign and order of magnitude of the gradient, as previously stated. Future work will implement a complex-step approach to validate the gradient obtained from the adjoint method.

4.6.4 Summary

This section specialized the general adjoint method towards gradient computation for dynamic simulations with the BDF time-marching scheme. A simple spring-mass-damper system illustrated the method. Constraint aggregation methods were extended to find the

maximum stress over every cross-section and over every time-step for Euler-Bernoulli-like stress recovery relations. AD provided the necessary terms for the computation of the gradient of the aggregated stress constraints with respect to the thickness design variables. The gradient had a good agreement when compared to that computed by the finite difference method. The adjoint method showed good scalability as the number of design variables increased.

4.7 RQ 2.2 – Structural Optimization³

The structural optimization method is shown in Fig. 4.39. The material, width, and height of each cross-section are external fixed inputs to the box-beam cross-sectional properties computation. The load time history and nodes along the 1-D beamline are external fixed inputs to the beam solver. For the computation of stresses, the solver needs to know the four extreme corner points of the quadrilateral cross-section. At each iteration, the optimizer gives a new guess for the thickness design variables. The adjoint method derived in the previous section enabled gradient computation of the stress constraints and weight objective function required for structural optimization.

In Section 4.7.1, the cross-section is simplified to a solid rectangular cross-section. In Section 4.7.2, structural optimization of a box cross-section is described.

4.7.1 Optimization of a Solid Rectangular Cantilever Beam

The test case here will be a non-prismatic cantilever beam subjected to dynamic loads. The beam's cross-section is simplified to be a rectangular-beam, with loads applied at the principal axes. These assumptions simplify the problem and allow us to focus on testing the method. The beam axis is aligned along the x-axis, and a sinusoidal load is applied at the beam tip along the z-axis to simulate dynamic loads.

³The method and results for the solid rectangular cross-section beam case have been published in a prior work [194]

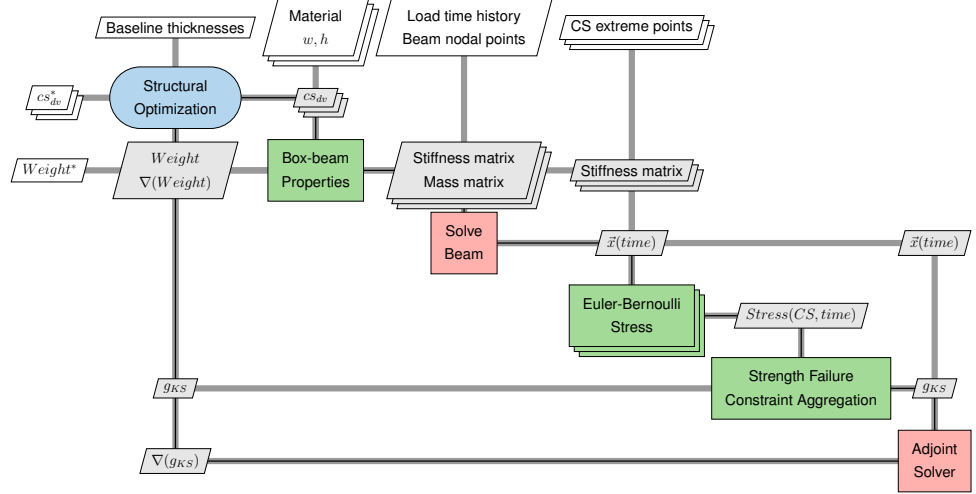


Figure 4.39: Structural optimization XDSM

The beam is discretized into a finite number of nodes (n_n). At each node, a rectangular cross-section of width (w_k) and height (h_k) is defined. Thus there are $2n_n = n_\mu$ design variables. The optimization problem is setup as:

$$\begin{aligned}
 & \underset{w_k, h_k}{\text{minimize}} && \text{mass}(w_k, h_k) \\
 & \text{subject to} && \mathbf{R}(\mu, \mathbf{x}, \dot{\mathbf{x}}, t, P, E) = \mathbf{0} \\
 & && c_{1,KS} \leq 0 \\
 & && c_{2,KS} \leq 0 \\
 & && h_{min} \leq h_k \leq h_{max} \\
 & && b_{min} \leq b_k \leq b_{max} \\
 & \text{data} && P(t)(kN), E(GPa), \sigma_y(MPa), \rho(kg/m^3)
 \end{aligned} \tag{4.56}$$

where $x \in \mathbb{R}^{18n_n}$, $\dot{x} \in \mathbb{R}^{18n_n}$, $\mu \in \mathbb{R}^{2n_n}$, $P(t)$ is the applied external load as a function of time, E , ρ and σ_y the Young's modulus density, and yield stress of the material of the beam respectively, and $c_{1,KS}$, $c_{2,KS}$ are the constraint aggregation of the stress failure criteria over space and time.

A MATLAB package OPTI [195], which implements an interior-point method algo-

Table 4.23: Parameters used for solid rectangular cross-section optimization studies

Parameter	Value	Unit
E	70×10^9	Pa
σ_y	276×10^6	Pa
ρ	2700	$\frac{kg}{m^3}$
h_{min}	0.4	m
h_{max}	5.0	m
w_{min}	0.2	m
w_{max}	5.0	m

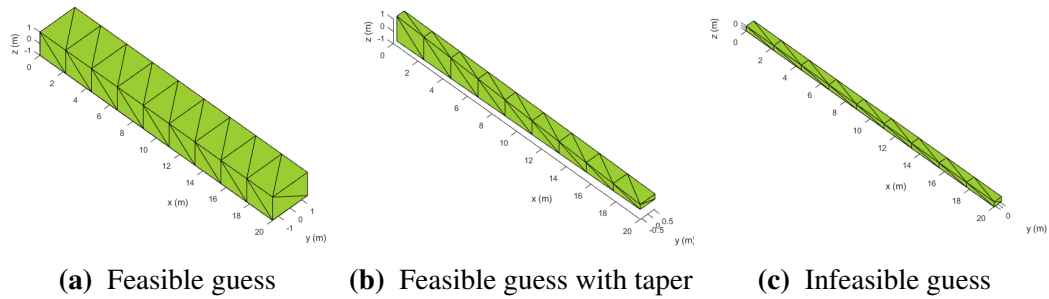
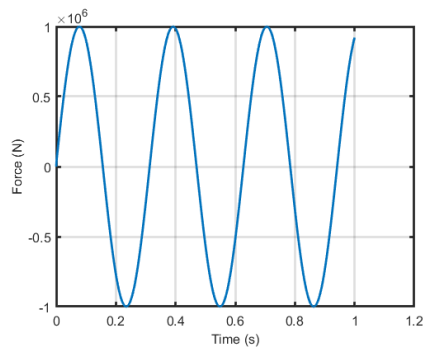


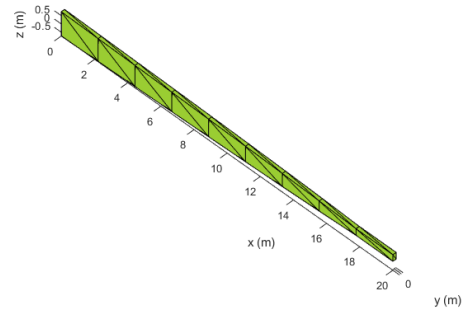
Figure 4.40: Initial guesses given to the optimizer

rithm, is used to perform optimization. The parameters chosen for the optimization run are given in Table 4.23. The first set of optimization runs are performed with ten beam sections. The loading is a sinusoidal tip load of $F_z = 1 \times 10^6 \sin(20\delta_i i)$. The loading is shown in Fig. 4.41a. The optimizer is run with three initial guesses shown in Fig. 4.40. The results for the three optimization runs are tabulated in Table 4.24. The optimizer converges to the same solution (shown in Fig. 4.41b) in all three cases. This shows the robustness of the method to initial guesses. When starting from an infeasible design (Fig. 4.40c), the optimizer requires more iterations to converge.

The second set of optimization runs compare static load sizing to dynamic load sizing. A constant tip load of $F_z = 1 \times 10^6$ N is applied. In the static case, a static solver is used, which drives the time derivatives ($\dot{\mathbf{x}}$) to zero and converges to the equilibrium deflection.



(a) Dynamic sinusoidal tip load



(b) Optimum solution for a tip loaded cantilever beam

Figure 4.41: Optimization of a cantilever beam subjected to sinusoidal tip load

Table 4.24: Optimization results for different initial guesses

Guess	Algorithm	Min Weight Value	# iterations	# func calls	# gradient calls	Time to solve (s)
Fig. 4.40a	opti: IP	10273.00	136	147	147	73.15
Fig. 4.40b	opti: IP	10273.00	164	197	165	91.07
Fig. 4.40c	opti: IP	10272.75	258	333	259	153.21

In the dynamic case, the DAEs are marched forward in time. The displacement oscillates and damps out as time progresses. Table 4.25 compares the optimization results for these two runs. As seen, the effect of dynamics causes the weight of the optimum structure to increase. The heights of the cross-sections for the dynamic simulation constant load case are greater than those for the static case, as seen in Fig. 4.42.

Table 4.25: Comparison of structural sizing for static and dynamic loads

Simulation Type	Loading Condition	Initial Guess	Optimum weight (N)
Static	Constant Tip Load	Fig. 4.40b	10942.00
Dynamic	Constant Tip Load	Fig. 4.40b	11705.00

4.7.2 Optimization of a Box-Beam ‘Wing-Like’ Structure

The test case here will be the ‘wing-like’ geometry shown previously in Fig. F.1a. There are four cross-sections, each with four design variables. The structure is cantilevered at

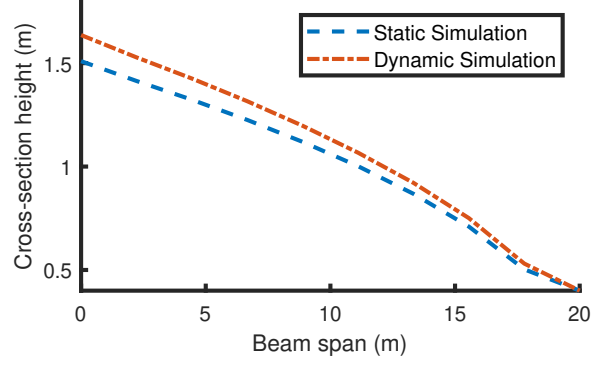


Figure 4.42: Cross-section height distribution along span of the beam for static and dynamic constant tip loading

cross-section 1 at the end left. The optimization problem is setup as:

$$\begin{aligned}
 & \underset{t_{left,k}, t_{top,k}, t_{right,k}, t_{bot,k}}{\text{minimize}} && \text{mass}(t_{left,k}, t_{top,k}, t_{right,k}, t_{bot,k}) && k = 1, \dots, 4 \\
 & \text{subject to} && \mathbf{R}(\mu, \mathbf{x}, \dot{\mathbf{x}}, t, P, E) = \mathbf{0} \\
 & && c_{1,vm,KS} \leq 0, c_{2,ss,KS,tn} \leq 0 \\
 & && c_{3,ss,KS,c} \leq 0, c_{4,cent,KS,tn} \leq 0, c_{5,cent,KS,c} \leq 0 \\
 & && 0.003 \leq t_{left,k} \leq 0.25 && k = 1, \dots, 4 \\
 & && 0.003 \leq t_{top,k} \leq 1.5 && k = 1, \dots, 4 \\
 & && 0.003 \leq t_{right,k} \leq 0.25 && k = 1, \dots, 4 \\
 & && 0.003 \leq t_{bot,k} \leq 1.5 && k = 1, \dots, 4 \\
 & \text{data} && P(t)(\text{N}), E(\text{Pa}), \sigma_y(\text{Pa}), \rho(\text{kg/m}^3) \\
 & && && (4.57)
 \end{aligned}$$

Where $P(t)$ is the applied external load as a function of time, E , ρ and σ_y the Young's modulus density, and yield stress of the material of the beam respectively, and $c_{1,vm,KS}$, $c_{2,ss,KS,tn}$, $c_{3,ss,KS,c}$, $c_{4,cent,KS,tn}$, and $c_{5,cent,KS,c}$ are the constraint aggregation of the stress failure criteria over space and time.

Study 1: Static Loading

Consider sizing the structure for the following settings:

- Tip load of $F_x = 0\text{N}$, $F_y = 0\text{N}$, $F_z = 2 \times 10^6\text{N}$
- Midpoint von-Mises stress constraints
- Initial guess to optimizer set to the upper bounds
- Aluminium material with properties: $E = 70 \times 10^9\text{Pa}$, $\rho = 2700\text{kg/m}^3$, $\sigma_y = 276 \times 10^6\text{Pa}$

Matlab's `fmincon` function was used to perform the optimization with the objective and constraint gradients supplied. The optimizer converged in 70 iterations satisfying constraints with a tolerance of 9.764×10^{-7} . The optimizer execution time was 7.7 seconds. Fig. 4.44b through Fig. 4.44e show the von-Mises stresses on cross-sections 1 through 4 respectively when the optimum solution is analyzed using a higher fidelity tool- VABS [132]. It is seen that the stresses on cross-sections 1, 2, and 3 are close-to but lower than the yield stress of $2.76 \times 10^8\text{ Pa}$. However, on cross-section 4, the stresses are higher than the yield stress. This is due to the beam stress assumptions made that cannot accurately capture the stress at a tip cross-section where zero moments are. The thicknesses of the two webs and two flanges as a function of the span is shown in Fig. 4.44a. We see a gradual decrease of thickness along the top and bottom flange span due to the internal pitching moment buildup from the vertical tip load. Since the applied loads are at the wingtip, the resulting internal torsional moment sized the webs, with a section that experiences an increased thickness far from the wing's root. Fig. 4.43 shows the moment and internal shear plots for the loads during loading for Study 1.

The thickness distributions resulting from the load in Case 1 show tendencies of sizing the top and bottom flanges from the axial stress generated by the moment buildup due to

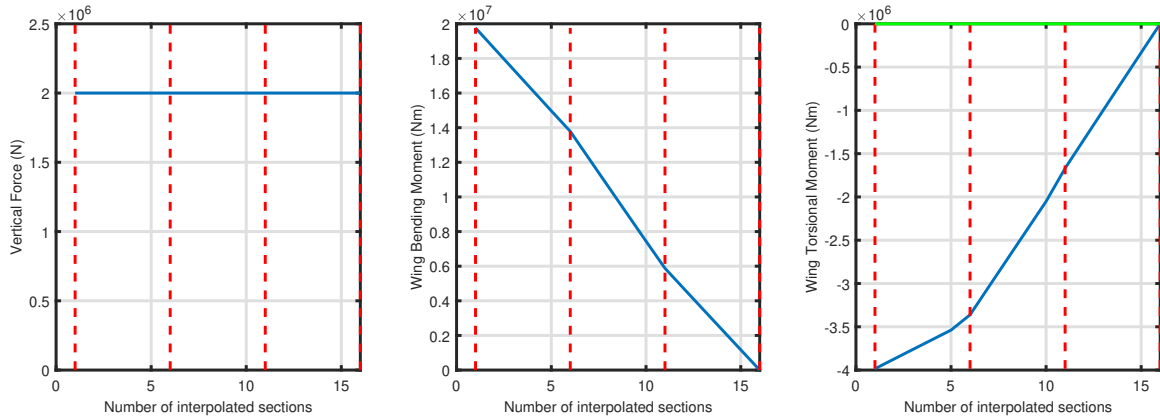


Figure 4.43: Study 1 bending moment, torsional moment and shear loads with interpolated section numbers and highlighted main sections in red

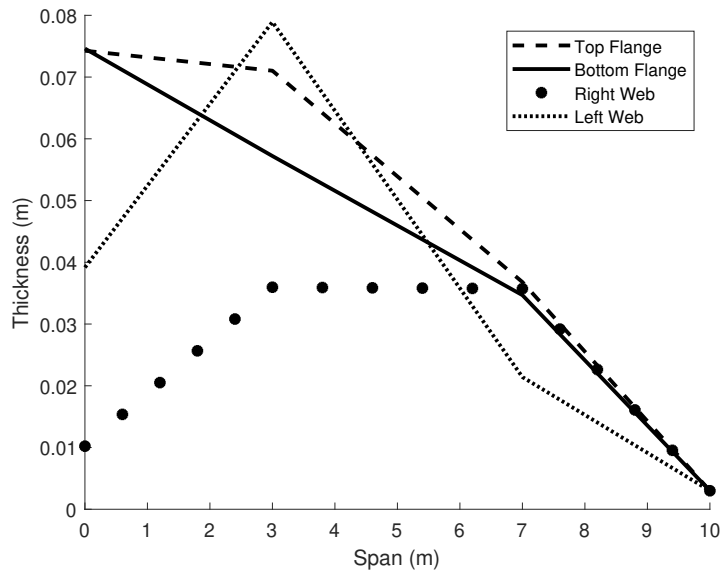
the tip load F_z , tapering down as span increases. This behavior follows the M_y vs span seen in Fig. 4.43.

Another interesting feature of the thickness distribution in Case 1 comes from the thickness buildup far from the root from the left and right webs; this as a combination of the mild increase of the internal torsional moment also seen in Fig. 4.43, as well as the shear stress coming from the applied vertical load. Since in the left web the direction of the vertical load shear matches the direction of the torsional shear, and in the right web they are opposite, there is an appreciable thickness difference between both of them, as seen in Fig. 4.44a.

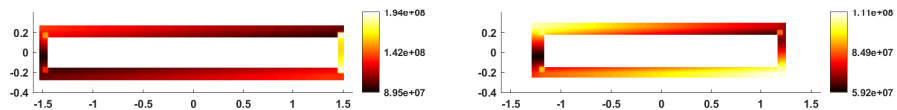
Study 2: Static Loading

Consider sizing the structure for the following settings:

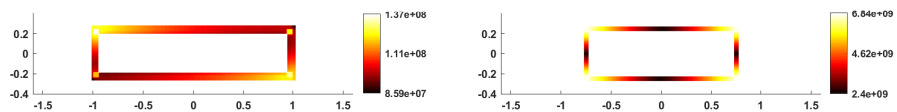
- Tip load in ‘lift, drag, and moment directions of $F_x = 0\text{N}$, $F_y = 1 \times 10^5\text{N}$, $F_z = 2 \times 10^6\text{N}$, $M_x = 1 \times 10^6\text{N m}$, $M_y = 0\text{N m}$, $M_z = 0\text{N m}$
- Initial guess to optimizer set to the upper bounds
- Aluminium material with properties: $E = 70 \times 10^9\text{Pa}$, $\rho = 2700\text{kg/m}^3$, $\sigma_y = 276 \times 10^6\text{Pa}$



(a) Thickness as a function of span



(b) von-Mises stress on cross-section 1 (c) von-Mises stress on cross-section 2



(d) von-Mises stress on cross-section 3 (e) von-Mises stress on cross-section 4

Figure 4.44: Optimum solution for study 1

The following five constraint cases were considered:

1. Corner points axial stress only
2. Midpoint von-Mises stress only
3. Flange shear stress only
4. Midpoint von-Mises stress, and flange shear stress
5. Midpoint von-Mises stress, corner point axial stress, and flange shear stress

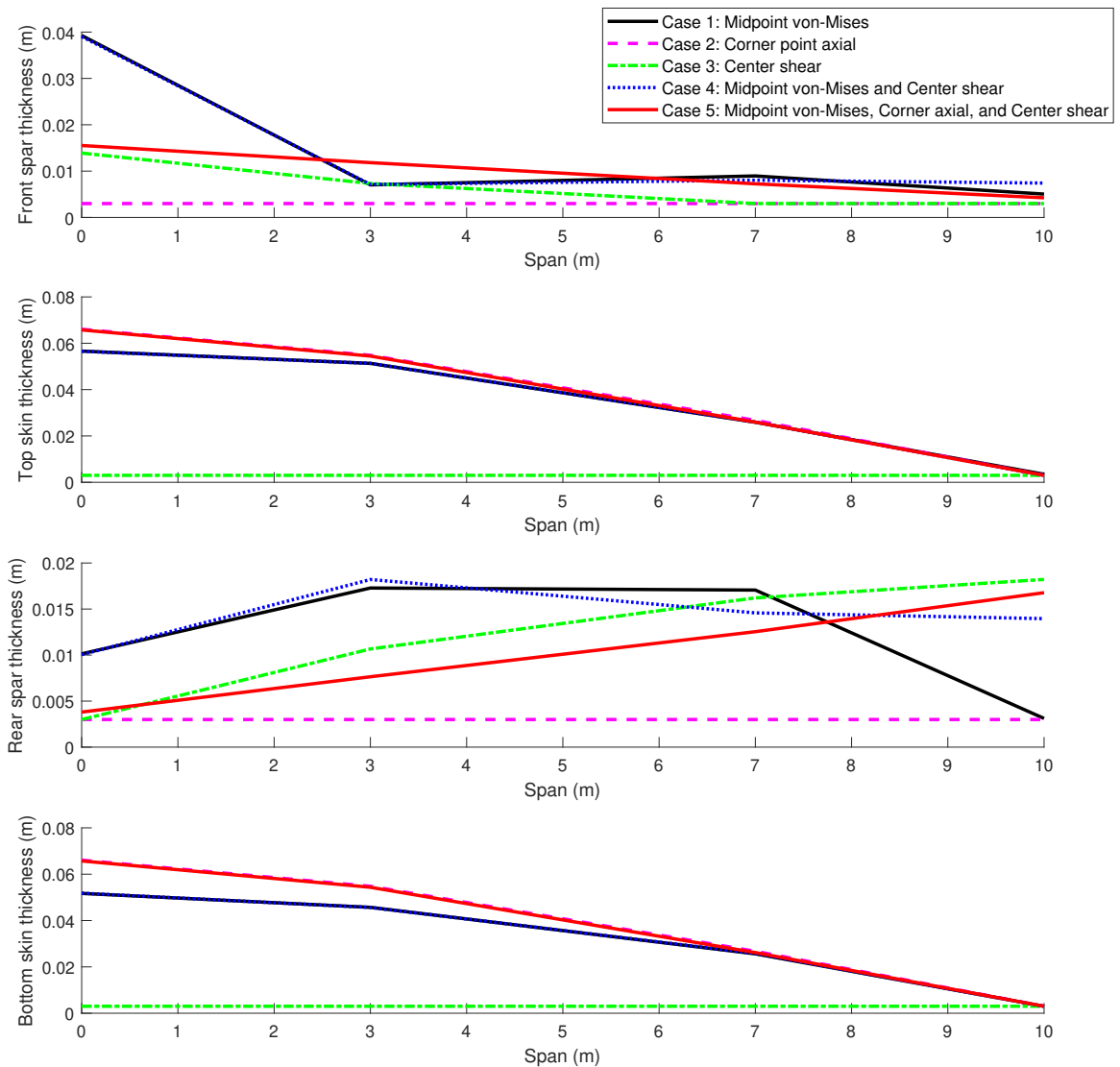


Figure 4.45: Solutions for different constraints in study 2

Fig. 4.45 compares the optimum solution thicknesses obtained. As seen, the behavior of the different constraints is as expected from a beam theory:

1. Axial stresses only depend on distance from the neutral point. The optimizer favors increasing the top and bottom flange thicknesses, while the left and right webs are at the lower bounds, as their thicknesses do not affect axial stress with the loading profile considered, as $F_z > F_y$, while also $I_{zz} > I_{yy}$.
2. With respect to the von-Mises only stress analysis, the top and bottom flanges were still sized by the axial stress component in the von-Mises resultant. The shear flow in the right and left webs did contribute to their final sized thickness. Fig. 4.46 shows that the internal torsional moment has a large negative value at the root while having a positive value at the tip. This difference in signs and magnitudes sizes the right and left webs differently.
3. If only the flange shear is used to size the beam, top and bottom flanges are sized to its minimum. This is due to not having to deal with axial stress and dealing with relatively low shear stress due to the cross-sectional inertia in the top-bottom direction. On the other hand, the webs did get a size increment due to the shear stresses from two sources- the torsional shear and the force shear- which size the right web. Unlike torsional shear, which depends on the torsional loads, shear loads depend on the shear forces experienced by the beam, which are constant along its span, as seen in Fig. 4.46. Also, since the torsion at the tip is non-zero, it sizes one of the flanges to counter the stresses. This constraint results in the lowest sized weight.
4. When the von-Mises corner points include the shear at the center of the flanges, it results in thicker left and right webs with even the tip section sized, resulting in a lesser need of top-bottom flange thickness.
5. If all constraints are enabled, the beam ends up with the highest weight, and thickness develops along all the different flanges, with a similar outcome of Case 4.

Table 4.26: Comparison of structural sizing for different constraints

	Case 1	Case 2	Case 3	Case 4	Case 5
Optimizer Iterations	133	44	30	111	87
Optimum Weight (kg)	4901.52	5275.87	624.85	4917.23	5386.58
Constraint tolerance	9.14×10^{-8}	9.13×10^{-7}	5.14×10^{-7}	6.13×10^{-8}	8.97×10^{-7}
Execution Time (s)	12.039	6.138	2.955	12.688	12.544

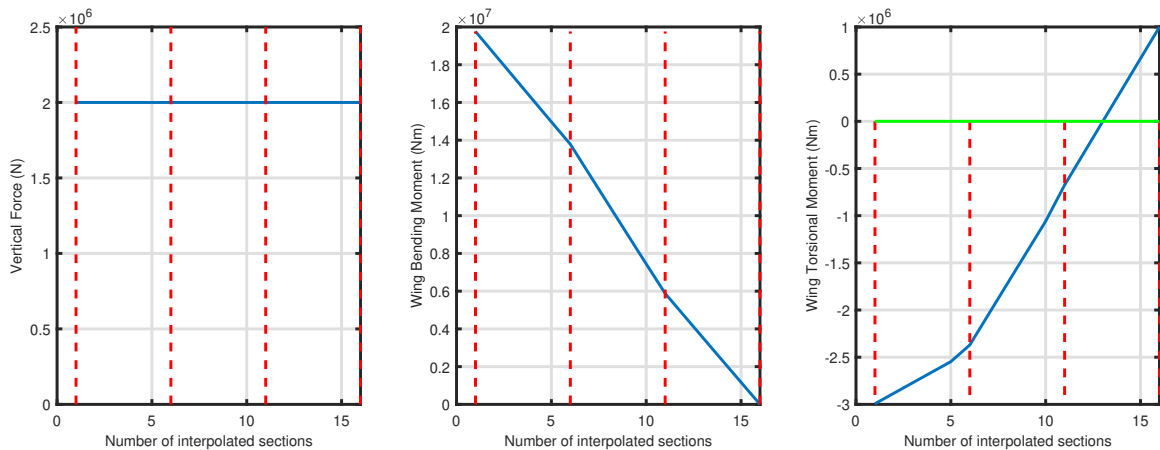
**Figure 4.46:** Study 2 bending moment, torsional moment and shear loads with interpolated section numbers and highlighted main sections in red

Table 4.26 compares the sizing for the different constraints. As seen in Fig 4.46, the tip loading is consistent with Study 2 specified tip loads and shows the variation of shear. As expected, the case that uses all constraints ends up with the highest thickness for all sections, as it took into account every high point of stress within the beam.

Study 3: Constant Load Dynamic Analysis

Consider the same settings as in Study 2. The tip load is held constant throughout the dynamic analysis. Stress constraints are imposed on midpoint von-Mises stress, corner point axial stress, and flange shear stress. The simulation is run for 5 seconds with a step size of 0.01 seconds.

Table 4.27 compares the sizing for static analysis against that for dynamic analysis. It is seen that the weight increased by 10.8% due to the dynamics. The optimizer execution

time is much longer for dynamics.

Table 4.27: Comparison of structural sizing for static and dynamic analysis

	Static	Dynamic
Optimization Iterations	87	174
Weight (kg)	5386.58	5935.87
Execution time (s)	12.54	335.57

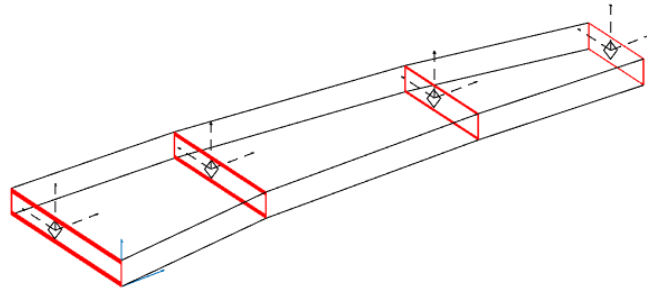
The breakdown of execution time is given in Table 4.27. The generation of the symbolic beam model is a one-time cost. After that, at each iteration of the optimizer, it is seen that the forward solver and each gradient computation using the adjoint solver are on the same order of magnitude. The computational time is higher due to the five stress gradient computations. It was seen previously in Table 4.26 that the optimum point found considering only the midpoint von-Mises stresses and that found considering all three (von-Mises, axial, and shear) produce comparable results. Thus, larger optimization problems considering only the von-Mises stress constraint would yield acceptable results with a far lower computational cost.

Table 4.28: Breakdown of computation time (in seconds) of dynamic solver

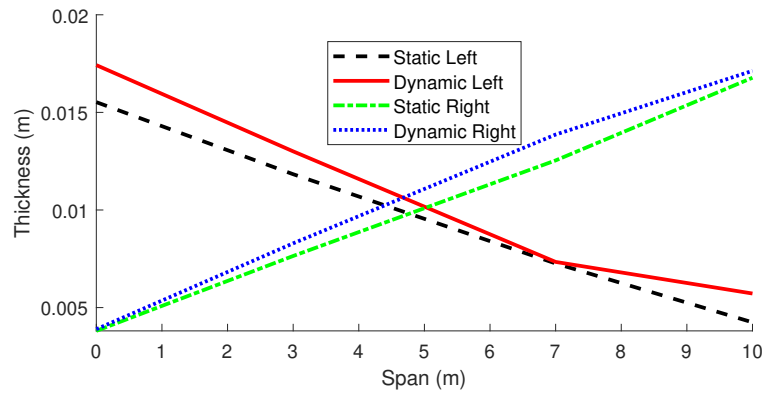
Task	Time (seconds)
Generate symbolic beam model	47.53
Time marching forward solve	3.12
von-Mises stress gradient	3.90
Compressive axial stress gradient	3.92
Tensile axial stress gradient	3.82
Postitive shear stress gradient	4.15
Negative shear stress gradient	4.10

The optimum results are shown in Fig. 4.47. It is seen that all four thicknesses have been sized to larger values when comparing to a static analysis. The top and bottom flange

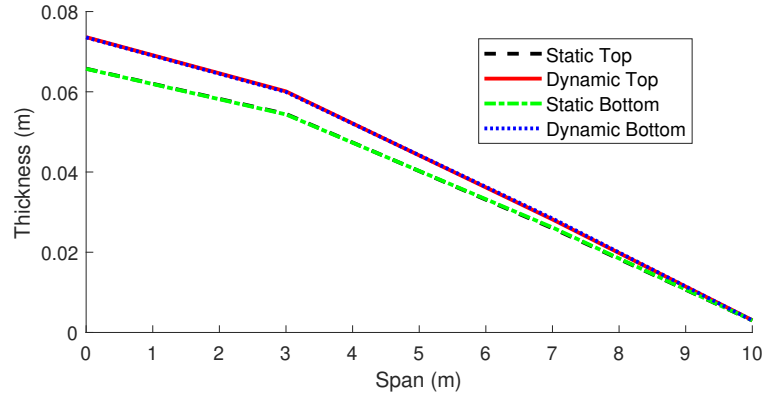
thicknesses are symmetric, and hence the plot lines overlap.



(a) 3-D view



(b) Web thicknesses



(c) Flange thickness

Figure 4.47: Optimum solution for study 3

CHAPTER 5

APPLICATION

Referring back to the overall research objective of this dissertation:

Research Objective
Develop a framework for aircraft wing design that <ol style="list-style-type: none">1. Dimensionally reduces complex 3-D structures to produce a low DoF structural analysis model2. Obtain the gradient of the structural analysis model in the time-domain

The beam-based structural analysis and optimization method described in Section 3 is used to size the wingbox structure. The process is shown as an XDSM in Fig. 5.1. First, a 3-D surface representation of the geometry is generated by RADE from the OpenVSP OML model. RADE then extracts the IML points at each rib location. The IML points are offset using the given baseline thickness to create the 2-D cross-sections seen in Fig. 4.15. The required beam curvature, frame angles, and oblique angles [191] for VABS are computed. At this stage, VABS can be run in-parallel over all cross-sections to obtain the stiffness and mass matrices.

Next, the stiffness correction procedure described in Section 4.2.4 is applied to obtain new values of the width and height of the rectangular box cross-section. The corrected widths and heights are used in all further computations of the box cross-section's cross-sectional properties.

The beam model described in Appendix A is generated using CasADi as described in Appendix G. The beam model is now used for structural optimization. The optimizer

controls the upper skin's thicknesses, lower skin, front spar, and rear spar of each cross-section. At each iteration, the thicknesses and corrected widths and heights are used to compute the beam's stiffness and mass matrices. The input load time-history is applied on the beam and time-marched using the 2nd order BDF scheme described in Algorithm 1. The time history of beam states obtained from the 1-D beam analysis is used to obtain the E-B stresses described in Section 4.4.2.

The stresses are aggregated over every cross-section and over every time-step. The beam model uses the created symbolic definition through automatic differentiation to obtain the quantities required to solve Eq. 3.10. The adjoint solver time marches from t_{final} to t_0 and solves for the adjoint variable λ at each time step. The gradient of the constraints w.r.t. the thickness design variables are computed using Eq. 3.11. The optimizer (fmincon in Matlab) uses these gradients to find a new guess for the design variables. The optimization iterations continue till a minimum weight design is found that satisfies the constraints to a tolerance of 1×10^{-7} .

Notes on implementation:

1. The RADE toolkit is implemented in python. The first analysis box of the XDSTM (Fig. 5.1) where the structural geometry is built occurs in RADE, and hence in python. RADE exports tables containing the 3-D coordinates of points on the rib IML, and the beam axis nodal 3-D coordinates. The structural analysis and optimization method proposed in this thesis is implemented in MATLAB. MATLAB reads the tables exported by RADE and builds the information needed to run VABS, and create a beam model
2. The 1-D analysis used in this thesis comes from Drela [53]. Drela implemented the beam equations, along with an unsteady aerodynamic theory and control laws in a commercial tool named ASWING. It should be noted that this thesis did not use ASWING directly. ASWING's documentation provides in-detail all the equations needed. The beam theory structural dynamics equations from ASWING were

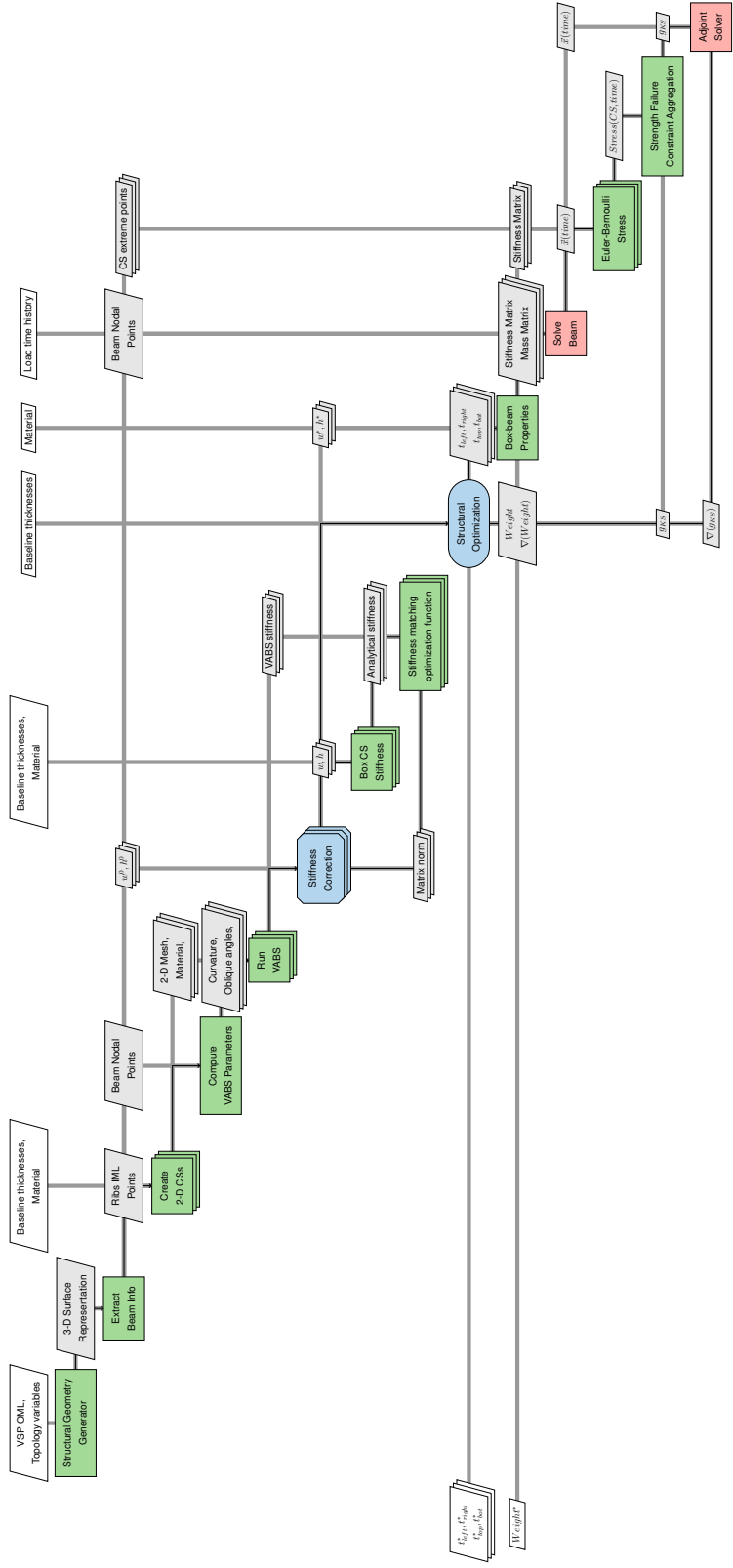


Figure 5.1: XDSM for structural optimization of wingbox using analytical beam corrected by VABS

implemented in MATLAB, verified and validated for use in this thesis.

3. The loads on the aircraft are obtained in this work using either Nastran or AVL. Static loads (1.0g, -1.0g, 2.5g loads) are obtained running AVL with AVL setting the angle of attack and elevator deflection in order to obtain the aircraft trim settings for the given flight condition and static maneuver. To obtain dynamic gust loads, Nastran SOL 146 is used. Details of the gust simulation are provided in Section 5.2.1. The structure is idealized as a beam when running SOL 146. It should be noted that the structure could have been treated as a shell model, or a Guyan reduction [81] reduced shell model. It was found that the loads obtained from all three representations are comparable. As the scope of this thesis is focused on performing structural analysis and optimization, the accuracy of the loads is not a priority. The beam representation in Nastran provides realistic loads while being computationally tracktable.
4. In the overall implementation in MATLAB, the structural geometry information, and the loads (static load cases, or dynamic load time history) are the two external inputs obtained from RADE. Once this information is available, the rest of the framework executes automatically, and optimizes the structure for the given loads.

5.1 Static Load Optimization

In this section, the optimization method described is applied to size the structure for static loads. The geometry considered is the PEGASUS concept wing described in Appendix D.2. The baseline OML with values shown in Table D.3, and structural topology variable values shown in Table D.4 will be used. Two critical loading conditions on an aircraft wing are the 2.5g and -1.0g maneuvers [188, 32]. These maneuvers are typically used for static sizing of the aircraft. The PEGASUS wing will be sized for these maneuvers using the optimization framework described in this work.

AVL is used to trim the aircraft at 2.5g and -1.0g, assuming a TOGW of 41005 lbs,

altitude of 20000 ft, and Mach number 0.5. This provides the aerodynamic loading for the two conditions. The aerodynamic lift and moment distribution is shown in Fig. 5.2. It is seen how the 2.5g maneuver distribution has a large positive value, and the -1.0g maneuver has a large negative value. The aircraft's weight provides inertial relief for the 2.5g maneuver but adds on in the -1.0g maneuver.

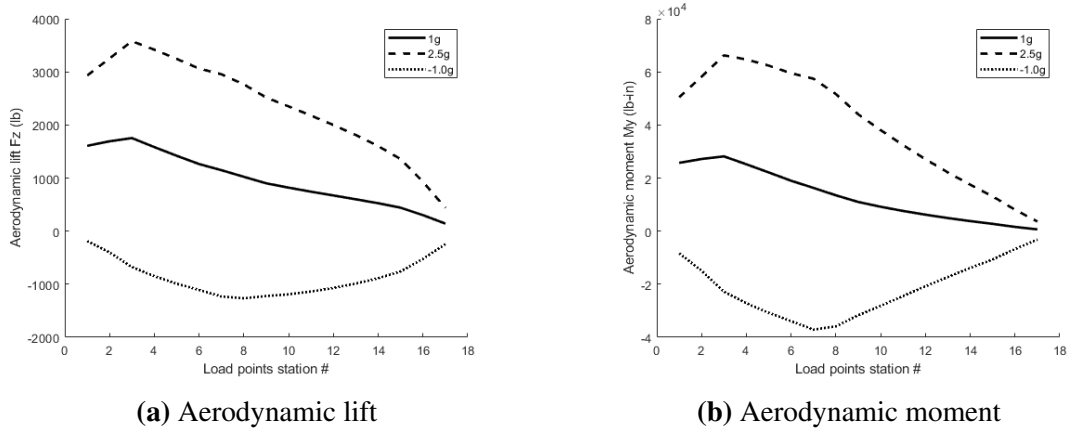


Figure 5.2: Aerodynamic load distribution for the PEGASUS wing

The chosen rib spacing of 28 inches results in 18 ribs for which IML points are extracted. The root rib is replicated at the $y = 0$ symmetry plane to create a center wingbox inside the fuselage. The design variables optimization problem are shown in Table 5.1. The material is assumed to be Aluminium. Two constraints are setup- the aggregated von-Mises stress-based strength failure criteria for the 2.5g and -1.0 loading conditions, respectively.

It should be noted the regions close to the tip of the wingbox are subjected to lower loads and hence results in very thin structures. If freedom is given to the optimizer, it will thin the structure to an extent that makes manufacturing the part difficult. The concept of *minimum gauge* exists specifying the lower limit of allowable thickness of the manufacturing process. This lower limit value can be incorporated as lower bound side constraints in the optimization problem. The lower bounds used in this thesis are given in Table 5.1.

The sizing results of the beam-based methods must be compared to that produced by a higher DoF model. A Nastran SOL 101 shell model was created with the same geometry

Table 5.1: Design variables for optimization of PEGASUS wing

Variable	Description	Number	Lower bound
t_{fs}	Front spar thickness at a cross-section	19	0.001 m/0.04 in
t_{us}	Upper skin thickness at a cross-section	19	0.001 m/0.04 in
t_{ls}	Lower skin thickness at a cross-section	19	0.001 m/0.04 in
t_{rs}	Rear spar thickness at a cross-section	19	0.001 m/0.04 in
Total design variables		76	

(with ribs) and aerodynamic loading. The Nastran .bdf file was linked with Hypersizer for optimization. Hypersizer uses the internal loads produced by Nastran and optimizes the thickness of the structure. Material failure constraints were setup in Hypersizer for an unstiffened panel concept. Four iterations between Nastran and Hypersizer were performed to ensure convergence on the optimized structure.

Fig. 5.3 shows the optimized thickness distribution from the beam-based optimization and compared to that produced by the shell-based Hypersizer optimization. It is seen that there is excellent agreement in the thickness distribution for the skins. The largest discrepancy is at the root section of the front spar (Fig. 5.3c). Hypersizer sizes this section to a large value. The section immediately outboard has a much smaller value. Referring back to Fig. 4.31, it was at the root section of the front spar that a region of high local stress was seen. This high-stress results in the large thickness seen in Fig. 5.3c. The beam model does not have this non-physical high-stress region, and thus, we see a smooth decrease in thickness from the root to the tip. The rear spar (Fig. 5.3d) is sized to a larger value by the beam model as compared to the shell model due to the shear stress constraints.

The total wing weight predicted by the beam-based optimization is 405.64 kg. The shell-based Hypersizer optimization predicts 392.62 kg for the skin and spars and 38.89 kg for the ribs, resulting in a total weight of 431.51 kg. It is again seen that the ribs account for a relatively small percent (9.01%) of the total weight. The error between the beam weight and shell weight is 6%. The results are summarized in Table 5.2, and a comparison of the

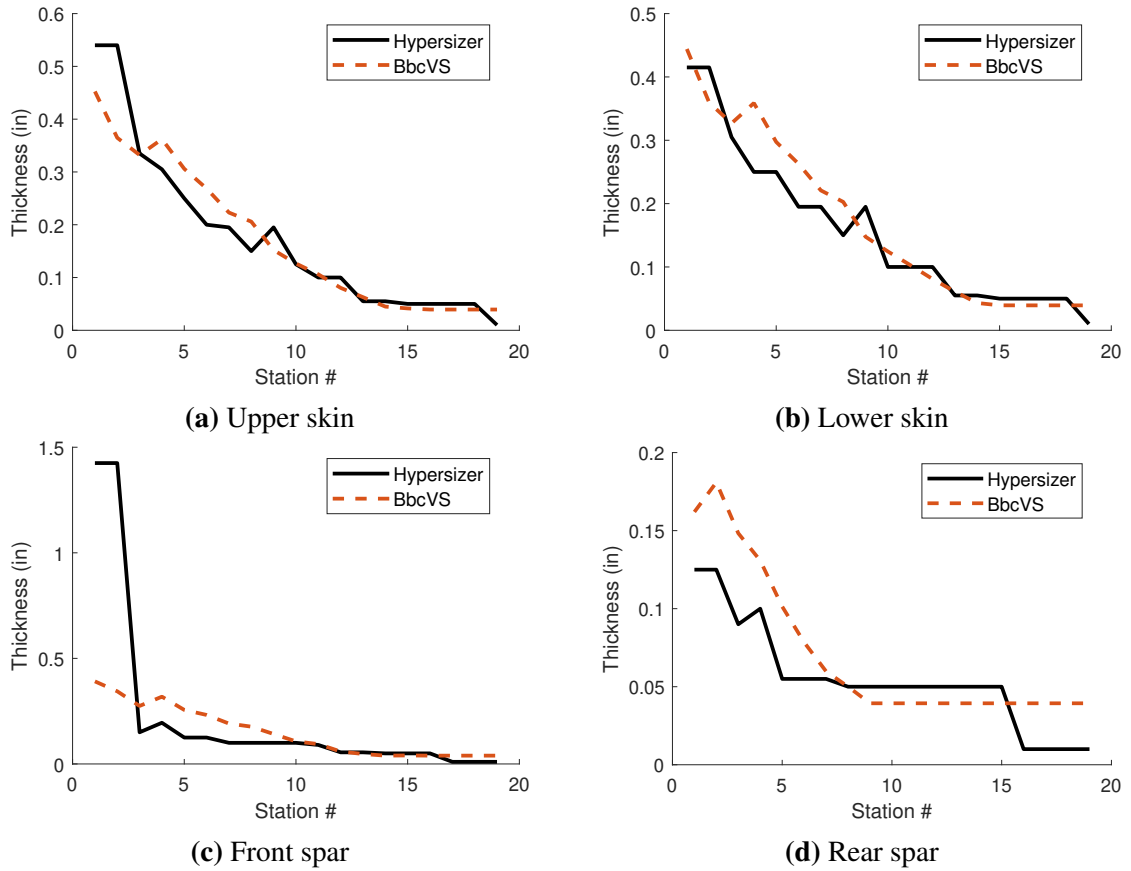


Figure 5.3: Static sizing thickness distribution

computational time needed to reach the optimum.

Table 5.2: Weight and computational time comparison for static sizing

Analysis	Weight (kg)	Optimization time (seconds)
Beam	405.64	85.89
Shell	431.51	656.4
	6% error	7.64X speed-up

5.2 Dynamic Load Optimization

This section considers the same PEGASUS wing sized for 2.5g and -1.0g loads, as in Section 5.1. Optimization is now done for dynamic loads instead of static loads. Nastran SOL 146 is used to simulate a gust and obtain the load as a function of time. A gust or other

dynamic aeroelastic simulation depends on the user's parameters, which in turn depend on 14 CFR 25.341 requirements.

5.2.1 Gust Simulation

In this work, we consider a one-minus cosine gust. As a test case example, we consider the one minus cosine gust defined in 14 CFR 25.341(a)(2):

$$U = \frac{U_{ds}}{2} \left[1 - \cos \left(\frac{\pi s}{H} \right) \right] \quad (5.1)$$

where $0 \leq s \leq 2H$ is the distance penetrated into the gust (feet), U_{ds} the design gust velocity in equivalent airspeed, and H the gust gradient which is the distance (feet) parallel to the airplane's flight path for the gust to reach its peak velocity. To comply with 14 CFR 25.341 regulations, the aircraft must have satisfactory performance when handling gusts of gradient distances ranging from 30 ft to 350 ft. The design gust velocity (in accordance with 14 CFR 25.341(a)(4)) is given by:

$$U_{ds} = U_{ref} F_g \left(\frac{H}{350} \right)^{\frac{1}{6}} \quad (5.2)$$

where U_{ref} is the reference gust velocity in equivalent airspeed, and F_g the flight profile alleviation factor. Multiple reference gust velocities between must be considered depending on the altitude. The different values of U_{ref} and H result in a combinatorial problem. For each case, a gust simulation must be run. In this work, we demonstrate for a single gust run. The flight profile alleviation factor also depends on the altitude. Table 5.3 gives the chosen gust settings.

For the dynamic analysis, a practical value of 0.02 is assumed for structural damping, constant through the frequency range from 0 Hz to 10.0 Hz. The simulation is designed to delay the application of the gust for 0.2 seconds to observe if the response has damped out sufficiently during the previous period in the periodic Fourier solution. Consequently,

a total simulation time of 5 seconds was given to ensure that the response damps out adequately before the next period begins. The study for both cases also focuses on the 11 first elastic modes of the wing and uses the Modified Givens Method normalized to their maximum displacements to obtain the modes.

Table 5.3: Gust simulation settings

Parameter	Value	Unit
Altitude	25000	ft
Mach number	0.5	
Reference gust velocity	30	ft/s
Gust distance	350	ft
Total simulation time	5	s
Reduced frequencies	[0.001, 0.01, 0.05, 0.1, 0.2, 0.5, 1.]	

The aircraft is trimmed at cruise using elevator and angle of attack using Nastran and AVL, and the gust is initiated at 1 second. Fig. 5.4 shows the aerodynamic lift as a function of time for an inboard and outboard section of the wing. As expected, the effect of dynamics is more pronounced at the outboard section.

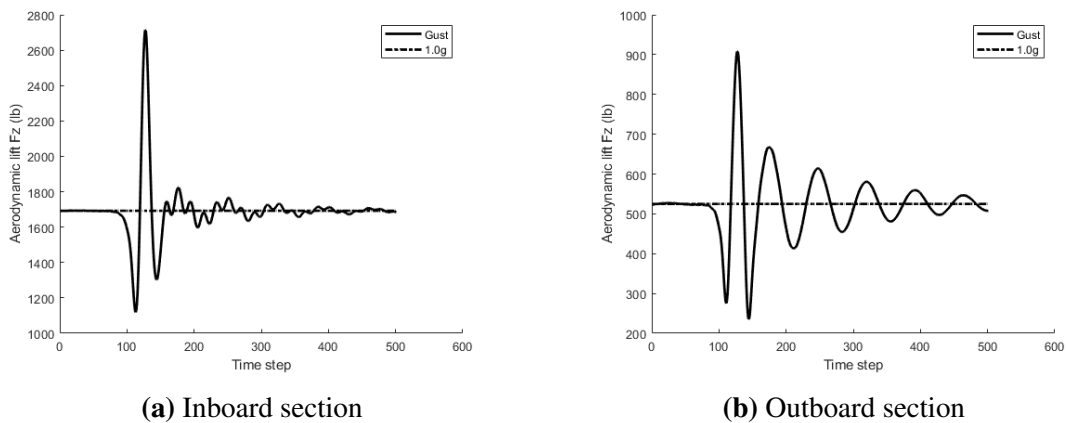


Figure 5.4: Gust load time history for the PEGASUS wing

5.2.2 Optimization

The optimization design variables are the same as the static loading case, shown in Table 5.1. The entire gust load time history is provided, and a dynamic simulation is run. A single von-Mises stress-based strength failure criteria aggregated over every cross-section and every time-step is used as the constraint.

Fig. 5.5 compares the four components' thicknesses between the static and dynamic sizing cases. The upper and lower skins' inboard stations are sized by the static cases, whereas the gust loads size the outboard sections. The magnitude of the torsion and shear moment on the spars is larger for the gust loads than the static maneuvers, resulting in larger thicknesses.

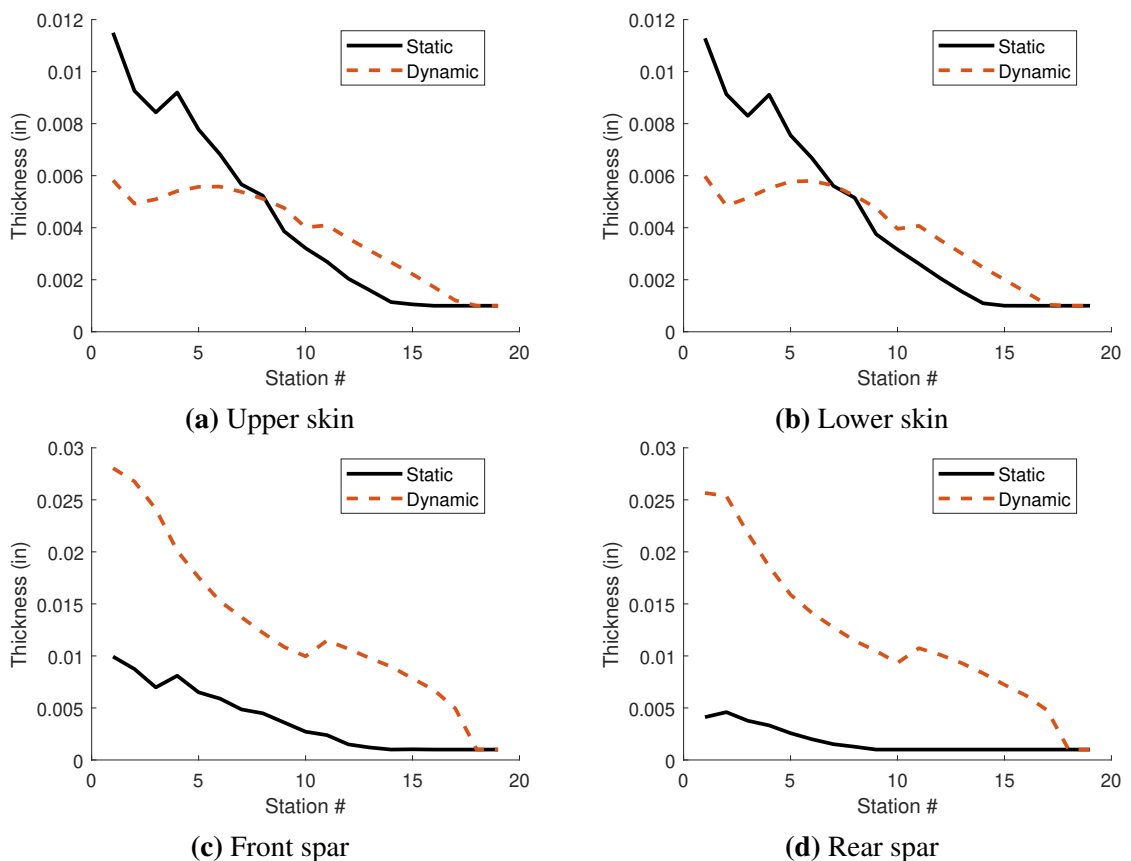


Figure 5.5: Comparison of thicknesses between static maneuvers sizing and gust sizing

The optimized area of the cross-sections and beam section weights as a function of

the span is shown in Fig. 5.6a, and compared to the static maneuvers sizing. The upper and lower skin has a larger surface area than the front and rear spars. Thus, the larger thicknesses of the static maneuvers give a larger area on the inboard stations. As expected, in Fig. 5.6b, the static maneuvers size the inboard portions of the wing, whereas the gust sizes the outboard portions of the wing.

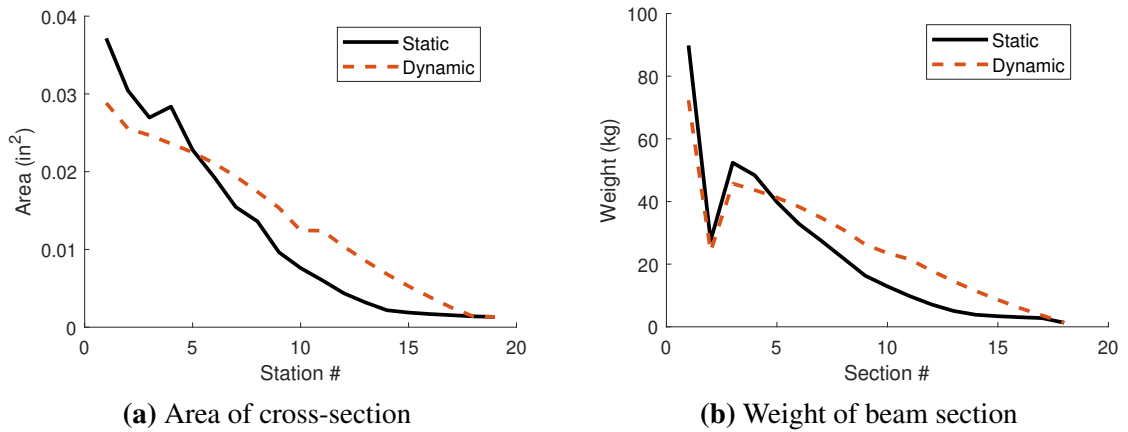


Figure 5.6: Comparison of area and weights between static maneuvers sizing and gust sizing

The results of sizing are summarized in Table 5.4. It is seen that the dynamic optimization is significantly slower than the static one. The computational expense is due to two dynamic simulations performed at each iteration- one for the forward solve and one for the adjoint.

Table 5.4: Weight and computational time comparison for static sizing

Type of Simulation	Weight (kg)	Optimization time (seconds)
Static	405.64	85.89
Dynamic	465.90	409.52

The beam-based structural analysis method with adjoint for gradient computation allows for the dynamic optimization to be computationally faster than the static shell-based Hypersizer optimization.

CHAPTER 6

SUMMARY

This section discusses the main findings of this work. The need to account for the dynamic loads specified by Code of Federal Regulations (CFR) while simultaneously achieving low structural weight for fuel efficiency in early-stage aircraft design motivated the following question:

Motivating Question

How to account for dynamics while maintaining computational efficiency in structural analysis and optimization of early-stage aircraft wing design?

This formed the basis for the research objective of this dissertation, stated below:

Research Objective

Develop a framework for aircraft wing design that

1. Dimensionally reduces complex 3-D structures to produce a low DoF structural analysis model
2. Obtain the gradient of the structural analysis model in the time-domain

The literature was explored to determine the state-of-the-art pertaining to

- The generation of dynamic loads
- Reduction methods to account for intricate load-bearing features such as stiffeners
- Reduction methods to obtain a low DoF model

- Structural failure computation
- Multi-disciplinary optimization, and sizing of aircraft wings

The gaps found in the literature are summarized below:

Gaps in the literature
<ul style="list-style-type: none"> • Dynamic Loads <ul style="list-style-type: none"> – Gap 1: Coupling the loads generation with structural failure computation – Gap 2: Systematic extraction of beam stiffness constants accounting for couplings without running higher fidelity tools • Internal Structure <ul style="list-style-type: none"> – Gap 3: Creating equivalent 2-D structures for stiffeners of varying topology, dimensions and rib spacing • Structural Analysis <ul style="list-style-type: none"> – Gap 4: Existing 1-D beam theories do not work well in the presence of aperiodicity along the span of the beam – Gap 5: Simple beam theories used for stress recovery with limited considerations for airfoil shape and composites – Gap 6: Using VAM for structural analysis of aircraft wings • Multi-Disciplinary Optimization (MDO) <ul style="list-style-type: none"> – Gap 7: MDO methods simplify simulations to statics <ul style="list-style-type: none"> * Gap 7a: Adjoint in the time-domain applied to aircraft structural optimization * Gap 7b: Constraint aggregation methods not extended for dynamics

The research follows the two points of the research objective- (1) structural analysis, and (2) structural optimization.

Gap 3 pertains to the absence of a method to create equivalent 2-D structures for stiffeners of varying topology, dimensions, and rib spacing. Such stiffeners are standard on the rib, as seen in Fig. 3.1. The following research question was posed to address this gap:

Research Question 1.1

How can an equivalent plate be created that accounts for stiffeners of varying topology, dimensions and non-uniform spacing?

It was hypothesized that a local smearing approach to creating a composite structure with anisotropic properties allows for stiffeners of varying dimensions and topology to be smeared. This approach does not assume any stiffener spacing as it is possible to smear any number of stiffeners. A stiffness matching optimization problem was posed to obtain the values of the anisotropic properties, where the stiffness of the built-up section was matched to the stiffness of the equivalent section. The hypothesis for RQ 1.1 was stated as:

Hypothesis 1.1

If

1. smearing the stiffener of the built-up structure to the corresponding portion of the equivalent structure, thereby, accounting for the effects of stiffeners of varying topology, dimensions and spacing, and subsequently,
2. the anisotropic material properties of the composite equivalent structure computed as a stiffness matching minimization problem

converges to within first order optimality criteria,

Then,

the structural response of this equivalent structure matches that of the built-up structure.

An experiment consisted of stiffeners of varying numbers and dimensions being smeared onto the base plate. The stiffness matching process showed that it was possible to obtain anisotropic material properties such that the stiffness matching optimization problem minimized the error to zero. Next, the structural response of the built-up structure was compared against the response of the equivalent structure. It was seen that in the direction of interest (out-of-plane bending) the response was accurate, thus validating Hypothesis 1.1. RQ 1.1 successfully enabled the dimensional reduction of 3-D features to 2-D.

With the 3-D features of stiffeners and stringers smeared, the 3-D wingbox now consists of skin, spars, and ribs represented as curved surfaces. Gap 2 addresses the lack of a method to extract a low DoF model (a beam model) properties directly from the 3-D surface wingbox without the necessity of creating and executing a higher DoF model or relying on assumptions of the cross-sectional shape and material distribution. RQ 1.2 was posed as:

Research Question 1.2

How to compute beam cross-sectional properties for a wingbox airfoil cross-section of arbitrary shape and material definition?

It was hypothesized that a higher-order beam theory, VAM-based VABS, can be used to obtain the cross-sectional properties. In the literature, VAM was successfully applied in the analysis and design of rotorcraft blades, but not aircraft wings. This gap, Gap 6, is also addressed in RQ 1.2. A limitation of VABS was noted in that the adjoint has not been implemented. This limitation creates a bottleneck for structural optimization. It was hypothesized that a box cross-section with known analytical formulae and a one-time stiffness matching correction allows for the box-beam's stiffness to match the stiffness calculated by

VABS. The hypothesis for RQ 1.2 was stated as:

Modified Hypothesis 1.2

If

the aircraft wingbox cross-section is treated as a box cross-section with analytical expressions to compute an analytical stiffness matrix,

And

a stiffness matching optimization problem modifying the width and height converges on the objective function that is the matrix Frobenius norm of the difference between the VAM-based VABS computed stiffness matrix on the wingbox cross-section and the analytical stiffness matrix

Then,

beam cross-sectional properties of a wingbox airfoil of arbitrary shape can be calculated using the resulting width and height

Two aircraft were chosen as test cases in this dissertation:

1. A conventional large twin-aisle commercial transport-based aircraft: the CRM
2. A novel distributed electric propulsion aircraft: the PEGASUS concept

A parametric geometry creation tool, RADE, was used to create a surface representation of the 3-D geometry. Information from the 3-D geometry was used as input to VABS, which successfully calculated the beam stiffness and mass matrices. Further, the stiffness matching optimization problem minimized the error between the box cross-section bending and torsion stiffness sub-matrix and the VABS stiffness matrix, thus validating hypothesis 1.2. Overall, RQ 1.2 allowed for the reduction of a 3-D wingbox to a 1-D beam.

Now that a 1-D model exists, it is necessary to apply dynamic loads on the model and obtain the dynamic response. However, a limitation exists in the literature- aperiodicities

along the beam's span cause numerical errors in the 1-D analysis (Gap 4). No robust method has been found to deal with this gap, and thus an alternate method was chosen-neglecting the ribs. The influence of the ribs on the wingbox had to be quantified. RQ 1.3 was stated as:

Research Question 1.3a

How much accuracy is lost in the structural response and sizing calculations of the aircraft wingbox when its ribs are neglected?

Research Question 1.3b

How accurate is the displacement response when the wingbox structure is represented as a beam model?

Two shell models, one with ribs and one without, were created, and their response was tested. It was seen that the primary effect of the rib on the global response of the wing is on the torsional stiffness. The absence of the ribs causes an over-prediction of the torsional rotation of the wingbox. However, in the lift-direction, the z-displacement and stress response and the two models' sizing were comparable. Thus, for the application of non-prismatic beams to early-stage aircraft structural sizing and weight prediction, neglecting the ribs would not incur large errors.

RQ 1.3 also bore the burden of validating the cross-sectional properties found by RQ 1.2. RQ 1.2 merely showed that it was possible to obtain the properties. In RQ 1.3, loads were applied to the models, and their displacement response was compared. If the stiffness properties were correctly computed, the shell model's displacement response should match that of the beam model. When VbS was used, it was seen that when the PEGASUS concept wing and the CRM were subjected to 1g loads, the displacement response was accurate

with a tip-displacement error of 4.22% for the CRM wing and 0.57% for the PEGASUS wing. For the box cross-section, the response was inaccurate with a tip displacement error of about 20%. However, when the stiffness matching correction was applied to the box cross-section to create the BbcVS model, the error was reduced to 9.77% for the CRM wing and 1.29% for the PEGASUS wing. Thus, it validated hypothesis 1.2 and showed the capability to obtain accurate displacement response from beam models.

In gap 5, it was seen that the literature uses simple beam theories to recover the stresses. Such beam theories struggle to accurately capture stress concentrations, account for composite materials, or apply to arbitrary cross-sectional shapes. Higher-order beam theories have been used to obtain the aircraft's loads accurately, but not coupled with structural failure computation. To address this gap, RQ 1.4 was stated as:

Research Question 1.4

How can stress and strain field time-history computations be made accurate and efficient when the aircraft wingbox structure is subjected to dynamic loads?

As before, it was hypothesized that VABS could accurately compute the stress fields needed to compute structural failure. The box cross-section assumption is also under consideration here. Hypothesis 1.4 is stated as

Modified Hypothesis 1.4

If
the aircraft wingbox cross-section is treated as a box cross-section,
And
the box cross-section has been stiffness matched (Hyp 1.2),
Then,

the accuracy of the stress field time history computed using analytical equations improves significantly.

As with the displacement matching of RQ 1.2, to test hypothesis 1.4, the beam's stress field response was compared against that computed by a shell model. The PEGASUS concept wing was used as the test case. The maximum error was at the root where the local high-stress concentration was seen. The average error neglecting the root section was 4.84%. The stiffness matching correction applied to the box cross-section created the BbcVS model which had a higher but still acceptable error. Thus, hypothesis 1.4 was validated and showed the capability to obtain accurate stress field responses from beam models.

The above four research questions allowed for a structural analysis method. Starting from the 3-D geometry, a low DoF model was generated. The loads were applied to the model, and 3-D stress fields were obtained.

A final experiment was carried out to check for computational efficiency. It was seen that for a single analysis, both the VbS model and the BbcVS were only slightly faster than the shell model. For many-query applications where thicknesses are modified the VbS is the least efficient method. On the other hand, the BbcVS, is very efficient at accepting new thicknesses and obtaining the stress field response. Thus the BbcVS model provides the right trade-off between accuracy and computational efficiency to be used for sizing.

The literature on multi-disciplinary optimization methods showed that gradient-based optimization methods are computationally efficient to size a structure with many design variables. Further, obtaining the gradient can be done efficiently using the adjoint method. However, as stated in Gap 7, the methods have been applied to static analysis and optimization. The adjoint method for dynamic simulations had not been applied to aircraft sizing (Gap 7a). Further, constraint aggregation techniques needed to deal with many structural constraints had not been extended for dynamics (Gap 7b). To address these gaps, the re-

search question is stated as:

Research Question 2.1

How can the gradient of aggregated strength-based failure criteria be computed efficiently during structural dynamic simulations?

The use of computationally efficient beam models alleviates the time and storage requirements for dynamic simulations. The KS constraint aggregation has a simple extension to extend to aggregate over both spatial and temporal domains. Thus Hypothesis 2.1 is posed as:

Hypothesis 2.1

If
low DoF beam models, in place of high DoF shell models are used to represent the structure,
Then,
the computational cost (runtime and memory) reduces significantly.
And if
the spatial Kreisselmeier–Steinhauser (KS) constraint aggregation function is extended to include temporal aspects,
Then,
accurate predictions of the maximum strength constraint violation during the dynamic simulation are obtained.
Finally, if
the six quantities (Eq. 3.10 and Eq. 3.11) required for the adjoint method are computed for the beam model and the modified Kreisselmeier–Steinhauser (KS) con-

straint aggregation function,

Then,

the gradient of aggregated strength-based failure criteria can be computed efficiently during structural dynamic simulations.

A general adjoint solver was implemented for the BDF scheme. It was found that the solver requires six quantities. Table 6.1 summarizes the computation of the six terms for the three cases on which the solver was validated. For all three cases, the gradient computed by the adjoint solver was compared against finite-differences. The maximum error was 1.16%. Scalability studies were performed by increasing the number of design variables. It was seen that finite-difference scales poorly, while the adjoint method scales well as expected. These experiments validate hypothesis 2.1.

Table 6.1: Quantities required for adjoint solver

	$\frac{\partial \mathbf{R}}{\partial \mathbf{x}}$	$\frac{\partial \mathbf{R}}{\partial \dot{\mathbf{x}}}$	$\frac{\partial F_i}{\partial \mathbf{x}}$	$\frac{\partial F_i}{\partial \dot{\mathbf{x}}}$	$\frac{\partial \mathbf{R}}{\partial \mu}$	$\frac{\partial F_i}{\partial \mu}$
Spring-Mass-Damper	Analytical	Analytical	Analytical	0	Analytical	Analytical
Solid rectangular cross-section	AD with CasADi	AD with CasADi	Analytical	0	Analytical	Analytical
Box cross-section	AD with CasADi	AD with CasADi	AD with CasADi	0	AD with CasADi	AD with CasADi

Finally, standard optimization methods were used to size the structure for static and dynamic loads. The optimization was validated using a simple ‘wing-like’ toy problem. It was seen, as expected, that the optimization produces larger thicknesses when dynamic simulation is performed instead of a static simulation for the same load.

A flowchart summary of relationship of the gaps, research questions and experiments is shown in Fig. 6.1. Having validated all the hypotheses and addressed the gaps (except Gap 4), the proposed structural analysis and optimization method was applied to size the PEGASUS wing. Two studies were performed:

1. **Sizing for static loading of 2.5g and -1.0g-** It was seen that the proposed approach produces a 6% error compared to the shell-based method, but with a 7.8x speed-up.

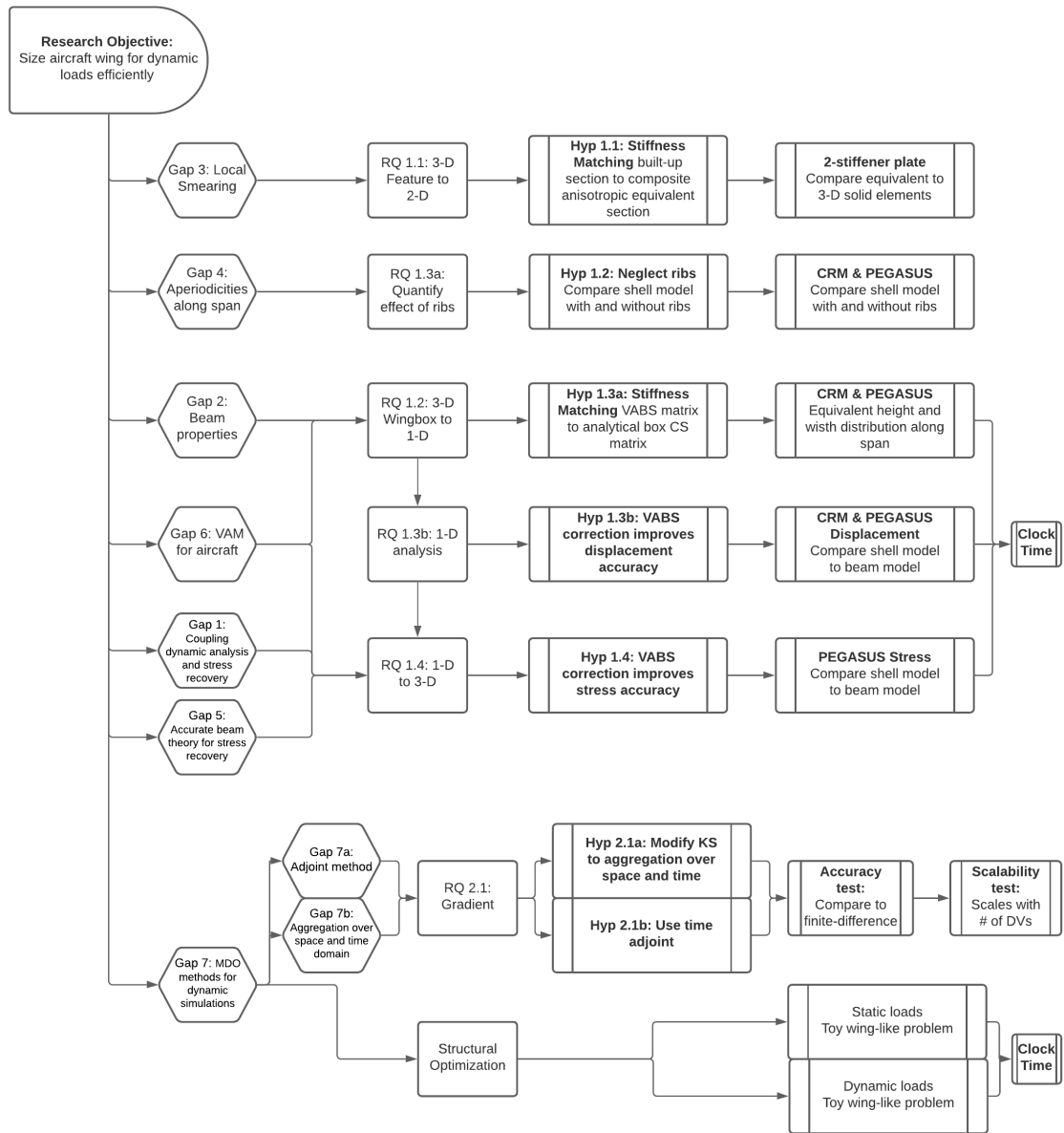


Figure 6.1: Summary of research

2. **Sizing for dynamic gust loads-** It was seen, as expected, that the optimization algorithm sized the outboard sections of the wing to thicknesses larger than those seen for static sizing.

Overall, the proposed method works well as an early-stage structural weight estimation tool. With the ribs neglected, the resulting thickness distribution would be less accurate as compared to a higher-fidelity model. However, the thickness distribution obtained from the proposed method can be used as an initial guess when running higher-fidelity methods, and thus helps improve the overall design cycle-time.

CHAPTER 7

CONCLUDING REMARKS

7.1 Limitations and Future Work

In this dissertation, simplifying assumptions were made or the studies were scoped to be more manageable. For this method to have more significant practical applications, the assumptions must be relaxed, and the scope expanded. These aspects are discussed in this chapter.

7.1.1 Applicability of Beam Theory

A fundamental assumption of beam theory is that the structure is slender – VAM indeed uses the fact that the cross-sectional dimension is much smaller than the beam’s length. The slenderness assumption holds for the two test cases considered in this dissertation – the CRM wing and the PEGASUS concept wing. More generally, the aerodynamic benefits of high aspect ratio wings have spurred unconventional aircraft concepts that have slender wings. However, it should be noted that for low aspect ratio wings or wings with large chord length, the structure cannot be considered slender. A popular aircraft concept that features a large chord is the blended-wing body (BWB) concept. Future work must test the applicability of beam theory for the structural analysis and optimization of such aircraft. It should also be noted that some small parameters are not considered in VAM’s derivation. One such parameter is the taper, an important planform variable for aircraft wings. The lack of consideration of taper in VAM’s derivation could explain why the method worked better for the PEGASUS concept wing than the CRMwing. Further investigation is necessary to quantify the effect of taper.

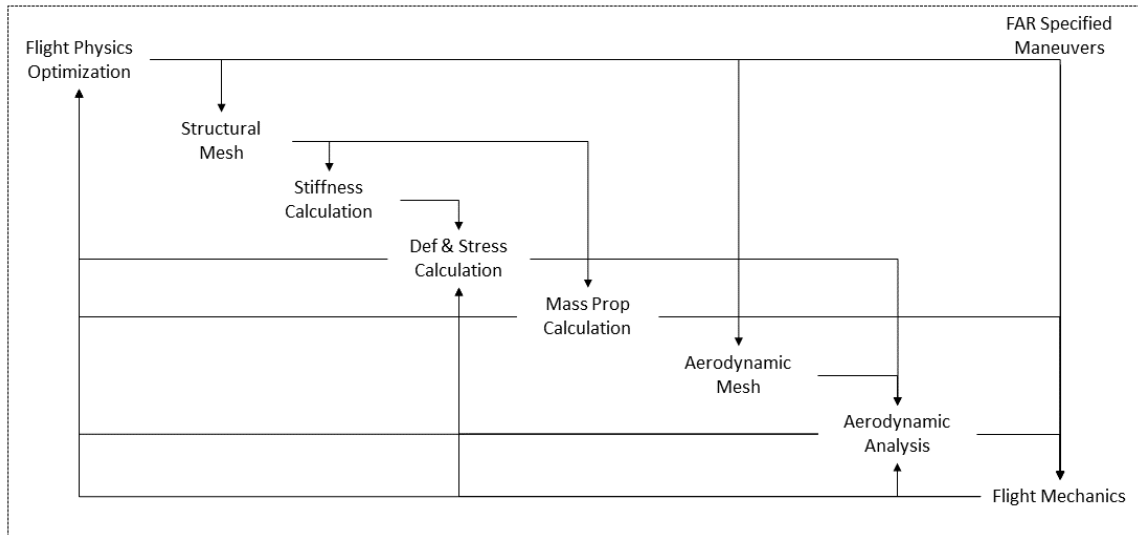


Figure 7.1: Coupled aircraft early-stage design process (Repeated from Fig. 1.5)

7.1.2 Aero-Servo Elastic MDAO

Consider the motivating coupled framework described in Section 1, repeated in Fig. 7.1. In this dissertation, a claim was made that such a coupled framework was impractical due to the computational expensive structural failure computation. Through the course of this work, it was shown that the proposed approach allows for efficient structural failure computation. Thus, the proposed approach is an enabler for the framework. However, this work did not implement or test the coupled framework. Implementation and testing of the coupled framework is another proposed future work. Some limitations and challenges still exist for this framework to be practical. These are discussed next.

Buckling constraints

This dissertation simplified the structural sizing only to consider strength failure constraints. Another important failure mode is buckling [180, 165, 32]. As described in Section 3.1, the stiffeners are the primary components that resist buckling. This dissertation proposed a method to smear stiffeners locally, thus allowing for stiffeners of varying topology, dimensions, and spacing to be used. It is, however, noted that considering such

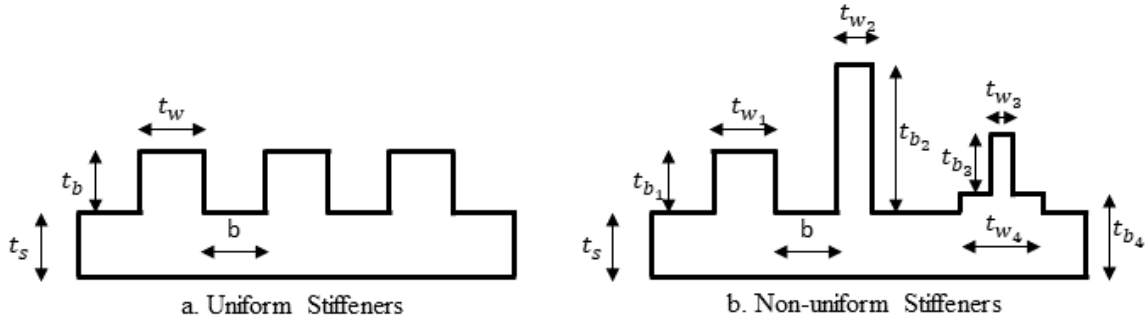


Figure 7.2: Dimensionality of stiffeners

stiffeners is not a necessity.

Consider the design variables for stiffeners shown in Fig. 7.2. For uniform stiffeners on a panel, the design variables are the thickness of the skin t_s , the stiffener spacing b , the stiffener height t_b , and the stiffener width t_w . The notional non-uniform stiffener on the hand has ten design variables. It should be noted that each panel has stiffener design variables. Thus, non-uniform stiffeners lead to a very large number of design variables for the optimization problem. For early-stages of design, it is acceptable to assume uniform stiffeners and use the smearing approach described in Section 2.1.1. In either case, the stiffener design variables and buckling constraints must be included in the optimization.

An approach to consider buckling of skin panels and rib crushing is described in Niu [110]. The buckling loads can be computed from the 1-D analysis responses. After that, shell buckling equations of the smeared anisotropic structure can be used to check failure and impose constraints. A method to consider buckling for tow-steered composite aircraft wing was described by Guimaraes et al. [196].

Flutter constraints

Flutter is a crucial consideration in aircraft design [197, 198]. To capture flutter requires an accurate prediction of the bending-torsion coupling of the wingbox. It is seen in the literature that beam models have been used to predict the flutter response accurately [199]. The beam models in the literature (Section 2.2.4) were generated using either Guyan reduction

or the displacement matching approach. This dissertation's proposed method advocates for a new method to generate the stickmodel directly from the 3-D geometry. However, the method does not capture the torsional stiffness accurately. A method to overcome this limitation is proposed as future work (Section 7.1.3). If successful, the proposed method would result in a beam model used for flutter computations.

Kennedy [197, 198] described a method to impose a flutter constraint and use gradient-based optimization methods to size the structure. The structural model used in the work was a shell model. The method is readily adaptable to beams. Lupp et al. [200, 201, 199] described a gradient-based flutter constraint method using beams.

Aero-servo-elasticity

In this work, the dynamic loads were obtained externally and supplied to the structural solver. In the framework described in Fig. 7.1, the loads' generations is coupled with the stress computation. Accurate computation of dynamic loads for aircraft using beam models is well established in the literature [202]. As with flutter, it requires an accurate representation of torsional stiffness and bending-torsion coupling.

Summary of Future Work for AeroServoElasticity

It is seen that implementation of the coupled framework of Fig. 7.1 requires (at least) three aspects beyond the scope of this thesis to be considered: 1) dynamic load generation, 2) flutter constraints, and 3) buckling constraints. The current limitation for all three is the lack of inclusion of the ribs. The following section proposes potential ways to include the ribs.

7.1.3 Ribs in the Wingbox

As was noted in Gap 4, the presence of aperiodicities along the beam's span causes numerical issues for the 1-D analysis. Ribs in the wingbox are an example of such an aperiodicity.

The rib is a solid section with stiffness larger than the cross-sections immediately before and after it. This results in a beam with soft-stiff sections along the span. It was seen that the presence of these aperiodicities causes the condition number to increase and results in a singular Jacobian matrix when solving the 1-D analysis.

In this dissertation, the ribs were neglected, and the wingbox simplified to a non-prismatic beam hollow beam without aperiodicities. The inclusion of the ribs is essential to compute the torsional stiffness of the wing accurately. The bending-torsion coupling is particularly crucial for composite high-aspect wings. Two potential solutions are discussed next.

Pre-Conditioners

As noted earlier, the 1-D analysis fails due to the Jacobian matrix becoming singular. A method in linear algebra called *preconditioning* is available in the literature. The preconditioner matrix, P for a matrix A is a matrix such that $P^{-1}A$ has a lower condition number than A . The Jacobian matrix's analytical form for the 1-D beam residual equations (Section A) is available. A potential future work would be to demonstrate that a preconditioner matrix can be constructed robustly for the Jacobian matrix such that the aperiodicities along the span do not result in a singular matrix.

Multi-Fidelity Field Surrogate Approach

Another potential solution side-steps the problem of an ill-conditioned Jacobian matrix. It was seen that a shell model could be used to compute the structural response of the wingbox accurately. The drawback was the high computational time of the high DoF shell model for dynamic simulations.

A popular solution in the literature to obtain high accuracy and computationally efficient models is to replace the high-fidelity simulations with a *surrogate model* [203]. The surrogate model is an inexpensive-to-evaluate model designed to mimic the output of a

more complex and expensive model. There are two factors to consider in using surrogate models:

1. **Training cost:** The cost to run the simulation many times to gather the data needed for training
2. **Accuracy:** How faithfully the surrogate model predicts the actual simulation response

There is a trade-off between accuracy and cost in the field of surrogate modeling. Generally speaking, the more data available to train the surrogate, the more accurate the model would be. However, generating more data requires running the simulation many more times, resulting in a higher cost. Since surrogate models are meant to replace simulations, collecting large volumes of data can be computationally prohibitive. One must carefully balance the surrogate model accuracy with its training cost, mostly the computational cost of creating the training dataset.

Most surrogate modeling literature focuses on the prediction of scalars. Review of such models is found in Forrester and Keane [204], Queipo et al. [205], Yondo et al. [206], and Bhosekar and Ierapetritou [207]. On the other hand, structural responses require predicting field quantities (such as displacements, stresses, and strains), which bring additional difficulties. A relatively recent solution to field surrogate model generation is to employ a Reduced Order Model (ROM) [208, 209, 210]. While ROM's work well for field quantities, the high computational cost of creating the training dataset persists, and in fact, exacerbated as compared to scalar surrogate models.

A way to address the dilemma between accuracy and training cost is to build a surrogate model using multiple data sources. Consider a scenario with two fidelities of models available to capture the response of the system:

1. A high-fidelity (high accuracy) computationally expensive physics-based model
2. A lower-fidelity computationally inexpensive physics-based model

The low fidelity model could be inaccurate in two aspects:

1. Inability to capture one (or more) physical phenomenon
2. Less accurate response values

For example, in the aerodynamics load generation, it is possible to obtain loads using CFD. CFD can accurately compute the lift and drag on the aircraft. However, CFD is a computationally expensive simulation. One could use a lower-fidelity Doublet Lattice Method (DLM). DLM gives less accurate values for the lift on the wing and fails to account for viscous drag, drastically underpredicting the wing's total drag. However, DLM is computationally inexpensive and can provide large volumes of data quickly.

A recent idea in field surrogate models is to combine data from different fidelities of simulation, a so-called *multi-fidelity surrogate model* [211]. The idea is to obtain two datasets: a few data samples from the high-fidelity model and many data samples from the low-fidelity model. The sparse high-fidelity data provides accuracy while the dense low-fidelity data provides a useful approximation of the rest of the design space. Thus, an accurate surrogate model is obtained at a lower overall computational cost.

In the context of the present work, the 'low-fidelity' model is the proposed beam model that is inaccurate at capturing the torsional response due to the ribs' absence. The 'high-fidelity' model is the shell model. The beam model is computationally efficient, whereas the shell model is computationally expensive. The multi-fidelity field surrogate model can be trained running a few samples of the expensive shell model and many samples of the cheap beam model. The process is shown notionally in Fig. 7.3. The generated field surrogate can then be used for structural optimization.

A challenge to combining beam model data with shell model data is that the two fields are topologically inconsistent. A recent method to create multi-fidelity field surrogates with topologically inconsistent fields based on manifold alignment was developed by Perron et al [212].

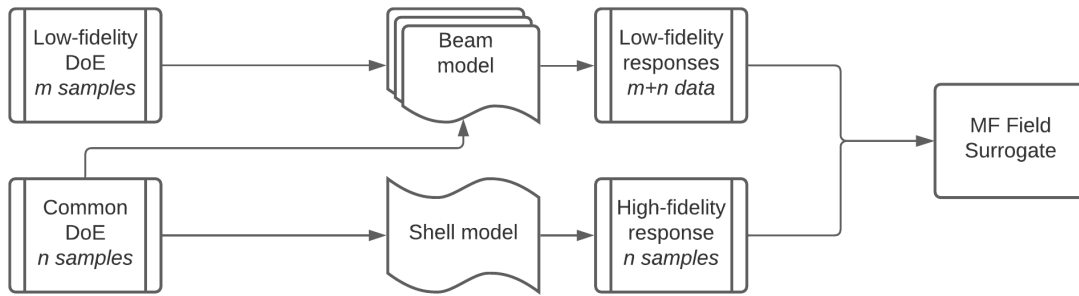


Figure 7.3: Notional structural multi-fidelity field surrogate model

7.1.4 Additional Experiments to Validate the Method

The experiments run to validate the accuracy of the proposed structural analysis method focused on the displacement and stress response of the aircraft wings (CRM and PEGASUS concept) subjected to a 1g aerodynamic loads. It is essential to test the wings' modal response to test the wings' dynamic response thoroughly. Thus, the proposed future work is to generate the beam model described in this thesis and run modal analysis using GEBT [133]. The resulting frequencies should be compared against a higher-fidelity shell model run with Nastran SOL 103. It is expected that the fore-aft bending modes and the up-down bending modes would be accurate, but the torsional mode would be inaccurate.

In Section 5.2, the PEGASUS concept wing was sized subjected to dynamic gust loads. It was seen, as expected, that the dynamic loads sized the outboard portions of the wings. The experiment served as a verification of the method. However, to validate the method, it is essential to compare it to a higher-fidelity method. It is proposed as future work to develop a framework that reduces the dynamic loads into static critical load cases. The aircraft wing must be sized for the load cases using a shell model, and the resulting weight and thickness distributions compared to those produced by the beam model.

7.2 Conclusions

The work presented in this dissertation explored the use of dimensional reduction for structural analysis and sizing of aircraft wings. Existing methods simplify the problem to statics and/or make assumptions on the structural geometry or material distribution.

A structural analysis method was proposed that relies on only the 3-D geometry as the input and systematically

1. Reduces the 3-D features to 2-D, capturing the effects of stiffeners of varying topology, dimensions, and spacing in the base plate
2. Reduces the 3-D wingbox to a 1-D beam

The key step in these reduction steps was the novel stiffness matching method used in this work. Stiffness matching ensured the simplified structure's energy matched the complex structure's energy, and thus the structural response was also matched. The dynamics were solved in 1-D, and recovery relations were used to obtain the 3-D stress fields for the computation of failure metrics. Spatial constraint aggregation techniques in the literature were extended to the temporal domain to accurately constrain the maximum stress occurring at any point of the structure and at any time step of the dynamic simulation. A general adjoint solver was implemented for BDF time-marching scheme. The terms the adjoint solver required for the aggregated strength constraints were computed using Automatic Differentiation (AD).

The aviation industry will continue to move towards higher aspect ratio wings, employ more composites, and use simulation-driven methods and optimization techniques to design aircraft. The proposed approach provides improvements on the existing methods in the literature – it is computationally efficient, provides reasonable accuracy for early-stage structural sizing and weight prediction, and includes dynamic effects. The computational efficiency makes it well-suited for many-query applications like optimization, design space exploration, uncertainty quantification, and generating data for surrogate modeling.

Appendices

APPENDIX A

NONLINEAR TIMOSHENKO BEAM THEORY

The beam theory used in this work was described by Drela [53] in the aero-servo-elastic tool ASWING. The ASWING manual provides all the equations of the beam theory. This appendix summarizes the equations and algorithmically organizes them. In this dissertation, the equations were implemented in Matlab and used for all studies.

The structural dynamics formulation for this work uses a nonlinear beam theory, including shear deformation [53, 213, 214, 54], for which the discretized equations are presented here for completeness.

It is necessary to model the flexibility of all aircraft surfaces: wings, fuselage, horizontal tail, and vertical tail. The flexible surfaces are treated as beam joined together to form a stickmodel, as shown in Fig. A.1.

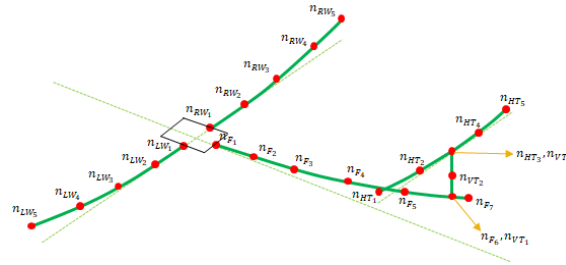


Figure A.1: Aircraft stick model

A.1 Definitions of Matrices

There exist two axis frames in the formulation:

1. A global XYZ inertial frame
2. A body-fixed xyz frame
3. Local csn frames for each beam segment

A matrix $\bar{\bar{T}}_i$ is defined that transforms a vector from body-fixed axes to local csn axes as

$$\begin{Bmatrix} ()_c \\ ()_s \\ ()_n \end{Bmatrix}_i = \bar{\bar{T}}_i \begin{Bmatrix} ()_x \\ ()_y \\ ()_z \end{Bmatrix}_i \quad (\text{A.1})$$

To avoid a singular matrix, the transformation sequence is different for surface beam and for fuselage beam. For a surface beam, the Euler angles are applied in the order φ, ψ, ϑ to give $\bar{\bar{T}}_i^{surface}$. For a fuselage beam, the Euler angles are applied in the order ψ, φ, ϑ to give $\bar{\bar{T}}_i^{fuselage}$. Finally we define a matrix $\bar{\bar{T}}_E$ which transforms a vector from the body-fixed axes to the inertial axes via a backward sequence $\Phi, -\Theta, \Psi$ as

$$\begin{Bmatrix} ()_X \\ ()_Y \\ ()_Z \end{Bmatrix}_i = \bar{\bar{T}}_E \begin{Bmatrix} ()_x \\ ()_y \\ ()_z \end{Bmatrix}_i \quad (\text{A.2})$$

The above transformation is required to couple the structural dynamics equations to the flight dynamics equations.

As seen in Fig. A.1, each beam consists of a number of nodes. The curvature matrix relates the beam to the xyz frame. The curvature of i'th node is given by

$$\bar{\bar{K}}_i^{surface} = \begin{bmatrix} \cos \phi & \cos \theta & 0 & -\sin \theta \\ -\sin \phi & 1 & 0 & 0 \\ \cos \phi & \sin \theta & 0 & \cos \theta \end{bmatrix}_i \quad (\text{A.3})$$

$$\bar{\bar{K}}_i^{fuselage} = \begin{bmatrix} \cos \theta & 0 & -\cos \psi & \sin \theta \\ 0 & 1 & \sin \psi \\ \sin \theta & 0 & \cos \psi & \cos \theta \end{bmatrix}_i \quad (\text{A.4})$$

The complete stiffness matrix is a 6×6 of the form:

$$\begin{bmatrix} S_{11} & S_{12} & S_{13} & S_{14} & S_{15} & S_{16} \\ S_{21} & S_{22} & S_{23} & S_{24} & S_{25} & S_{26} \\ S_{31} & S_{32} & S_{33} & S_{34} & S_{35} & S_{36} \\ S_{41} & S_{42} & S_{43} & S_{44} & S_{45} & S_{46} \\ S_{51} & S_{52} & S_{53} & S_{54} & S_{55} & S_{56} \\ S_{61} & S_{62} & S_{63} & S_{64} & S_{65} & S_{66} \end{bmatrix} \quad (\text{A.5})$$

ASWING simplifies the above matrix to ignore the coupling between the axial and bending terms to produce two sub-matrices. $\bar{\bar{E}}_i$ is the moment/curvature stiffness submatrix of i 'th node defined as

$$\bar{\bar{E}}_i = \begin{bmatrix} EI_{cc} & EI_{cs} & EI_{cn} \\ \cdot & GJ & EI_{sn} \\ \cdot & \cdot & EI_{nn} \end{bmatrix}_i \quad (\text{A.6})$$

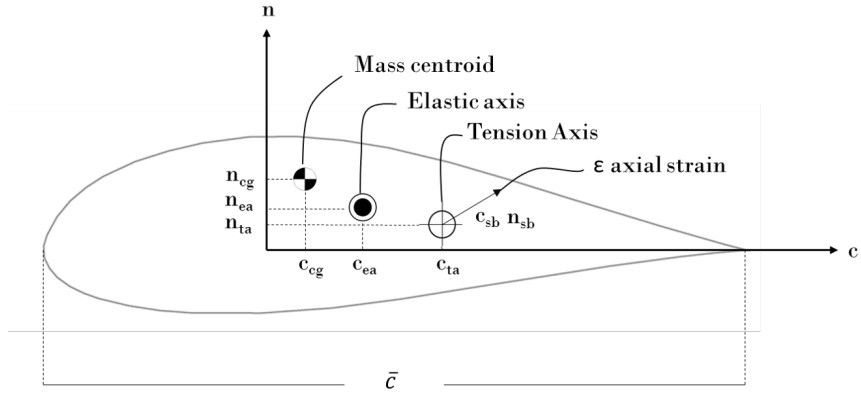


Figure A.2: Cross section properties. Figure based on [53].

$\bar{\bar{S}}_i$ is the axial stiffness submatrix of i'th node defined as

$$\bar{\bar{S}}_i = \begin{bmatrix} \frac{1}{GK_c} & 0 & 0 \\ \cdot & \frac{1}{EA} & \\ \cdot & \cdot & \frac{1}{GK_n} \end{bmatrix}_i \quad (\text{A.7})$$

In general, a wingbox cross-section has the properties shown in Fig. A.2. The origin of the c-n axis shown is where the beam axis passes through the cross-section. The mass centroid, elastic axis, and tension axis are, in general, distinct. An offset matrix of i'th node to tension and elastic axes of the corresponding cross-section is defined as:

$$\bar{\bar{D}}_i = \begin{bmatrix} 0 & -n_{ea} & 0 \\ n_{ta} & 0 & -c_{ta} \\ 0 & c_{ea} & 0 \end{bmatrix}_i \quad (\text{A.8})$$

A.2 Residual System of Equations

With a state vector defined as $X = \{\vec{r}, \vec{\theta}, \vec{F}, \vec{M}, \vec{u}, \vec{\omega}\}^T$, the governing structural equations can be written in residual form as $R(X, \dot{X}) = 0$, where the quantities in \dot{X} are the time derivatives of the quantities in X . First order finite differencing can be used to relate the states to their derivatives as follows:

$$X_n = \frac{1}{t_n - t_{n-1}} X_n + \frac{-1}{t_n - t_{n-1}} X_{n-1} \quad (\text{A.9})$$

For each node there are 18 variables to be solved for. If n is the number of nodes for a flexible surface, each flexible surface has $18n$ unknowns. The equations to solve the system are:

1. Element equations

- (a) $3(n-1)$ Force equilibrium equations
- (b) $3(n-1)$ Moment equilibrium equations
- (c) $3(n-1)$ Moment-curvature relationships
- (d) $3(n-1)$ Strain-displacement relationships

2. Boundary conditions

- (a) 6 conditions at the root
- (b) 6 conditions at the tip

3. Nodal equations

- (a) $3n$ transformations: $\vec{r}_i = \vec{u}_i$
- (b) $3n$ transformations: $\vec{\theta}_i = [C] \vec{\omega}_i$ (matrix C relates the Euler angle rates to angular velocities)

In addition, there are 12 equation-variable pairs for each “joint” in the system. Joints are used to transfer forces and moments from one beam to the other. They also enforce the constraints that the relative position and orientation between the beams (at the joint) must remain invariant.

The force and moment equilibrium equations in discretized form are

$$\vec{F}_{i+1} - \vec{F}_i + f_a \Delta s + \Delta \vec{F} = 0 \quad (\text{A.10})$$

$$\vec{M}_{i+1} - \vec{M}_i + m_a \Delta s + \Delta \vec{M} + \Delta \vec{r} \times \vec{F}_a = 0 \quad (\text{A.11})$$

where $(\)_a$ refers to an average defined as $\frac{1}{2} ((\)_i + (\)_{i+1})$, and f_a and m_a are the distributed force and moment for an element. These loads comprise aerodynamic, propulsive and inertial loads. Further,

$$\vec{F}_a = \frac{1}{2} (\vec{F}_{i+1} + \vec{F}_i) \quad (\text{A.12})$$

$$\vec{f}_a = f (\vec{\theta}, \vec{\omega}, \vec{\dot{\omega}}, \vec{r}, \vec{u}, \vec{\dot{u}}) \quad (\text{A.13})$$

$$\vec{m}_a = f (\vec{\theta}, \vec{\omega}, \vec{\dot{\omega}}, \vec{r}, \vec{u}, \vec{\dot{u}}) \quad (\text{A.14})$$

$$\Delta \vec{r} = \vec{r}_{i+1} - \vec{r}_i \quad (\text{A.15})$$

$$\Delta s = (1 + \epsilon_s) \Delta s^0 \quad (\text{A.16})$$

where ϵ_s is the axial strain, and Δs^0 the arc length of the element in the undeformed configuration.

First consider the computation of the nodal acceleration. Algorithm 2 shows the computation steps. $\vec{V}_{ac} = \{U, V, W\}^T$ is the gross aircraft velocity in body-fixed axes, and $\vec{\Omega}_{ac} = \{P, Q, R\}^T$ the gross aircraft angular rates in body-fixed axes.

The inertial force and moment are calculated as shown in Algorithm 3. μ is the mass per unit length of the element, $[i]$ the mass moment of inertia tensor per unit length, $\vec{\alpha}^0$ the acceleration of the rigid body, and $\vec{\Omega}$ the aircraft rigid body angular velocity.

Algorithm 2: Calculate nodal acceleration

- 1 Read nodal quantities: $\vec{r}_i, \vec{u}_i, \vec{\omega}_i, \vec{\omega}_i$
 - 2 Read element quantities: $\Delta \vec{r}_{CG}^i$
 - 3 Read aircraft quantities: $\vec{A}_0, \vec{\Omega}, \vec{\alpha}_0$
 - 4 Read number of nodes on the beam n
 - 5 Pre-allocate variables: $a_{CG} : 3 \times (n - 1), a_i : 3 \times n$
 - 6 Compute acceleration at the node as
$$\vec{a}_i = \vec{A}_0 + \vec{u}_i + \vec{\alpha}_0 \times \vec{r}_i + \vec{\Omega} \times (\vec{\Omega} \times \vec{r}_i) + 2\vec{\Omega} \times \vec{u}_i$$
 - 7 Compute the acceleration at the location of the center of gravity for each element
$$\vec{a}_{CG}^i$$
 - 8 **for** $i = 1 \rightarrow n - 1$ **do**
 - 9
$$\vec{a}_{CG}^i = \frac{1}{2}(\vec{a}_i + \vec{a}_{i+1}) + [\vec{\alpha}_0 + \frac{1}{2}(\vec{\omega}_i + \vec{\omega}_{i+1})] \times \Delta \vec{r}_{CG}^i + \vec{\Omega} \times (\vec{\Omega} \times \Delta \vec{r}_{CG}^i) + [\frac{1}{2}(\vec{\omega}_i + \vec{\omega}_{i+1})] \times \left\{ [\frac{1}{2}(\vec{\omega}_i + \vec{\omega}_{i+1})] \times \Delta \vec{r}_{CG}^i \right\}$$
 - 10 **end**
 - 11 **return** \vec{a}_{CG}
-

Algorithm 3: Calculate inertial loads

- 1 Read nodal quantities: $\vec{T}_i, \vec{\omega}_i, \vec{\omega}_i$
 - 2 Read element quantities: $\vec{\mu}^i, \vec{v}^i, \vec{a}_{CG}^i, \Delta \vec{r}_{CG}^i$
 - 3 Read aircraft quantities: $\vec{T}_E, \vec{\alpha}_0$
 - 4 Read number of nodes on the beam n
 - 5 Pre-allocate variables: $f_{acc} : 3 \times (n - 1), m_{acc} : 3 \times (n - 1)$
 - 6 **for** $i = 1 \rightarrow n - 1$ **do**
 - 7
$$\vec{f}_{acc}^i = \vec{\mu}^i * \left(\vec{T}_E^T \begin{pmatrix} 0 \\ 0 \\ -9.81 \end{pmatrix} - \vec{a}_{CG}^i \right)$$
 - 8
$$T \iota T = \left[\frac{1}{2} \vec{T}_i^T + \vec{T}_{i+1}^T \right] \vec{v}^i \left[\frac{1}{2} \vec{T}_i + \vec{T}_{i+1} \right]$$
 - 9
$$\vec{m}_{acc}^i = \Delta \vec{r}_{CG}^i \times \vec{f}_{acc}^i - T \iota T \left(\vec{\alpha}_0 + \left[\frac{1}{2}(\vec{\omega}_i + \vec{\omega}_{i+1}) \right] \right) - \left(\vec{\Omega} + \left[\frac{1}{2}(\vec{\omega}_i + \vec{\omega}_{i+1}) \right] \right) \times \left\{ T \iota T \left(\vec{\Omega} + \left[\frac{1}{2}(\vec{\omega}_i + \vec{\omega}_{i+1}) \right] \right) \right\}$$
 - 10 **end**
 - 11 **return** f_{acc}, m_{acc}
-

The offset of the center of gravity of the section from the csn origin expressed in xyz was shown in Fig. A.2. The effect is taken into account through the term r^{cg} defined as:

$$\vec{r}^{cg} = c^{cg}\hat{c} + n^{cg}\hat{n} \quad (\text{A.17})$$

The external loads, nodal average reactions, and length of the beam beam are computed as shown in Algorithm 4.

Algorithm 4: Calculate beam elemental quantities required by residual equations

```

1 Pre-allocate variables:
   $f : 3 \times (n - 1), m : 3 \times (n - 1), F_{av} : 3 \times (n - 1), \Delta s : 1 \times (n - 1)$ 
2 Calculate total loading for  $i = 1 \rightarrow n$  do
3    $\vec{f}^i = \vec{f}_{acc}^i + \vec{f}_{aero}^i$ 
4    $\vec{m}^i = \vec{m}_{acc}^i + \vec{m}_{aero}^i$ 
5 end
6 Calculate average nodal reactions for  $i = 1 \rightarrow n - 1$  do
7    $\vec{F}_{av}^i = \frac{1}{2}\vec{F}_i + \vec{F}_{i+1}$ 
8 end
9 Calculate length of element for  $i = 1 \rightarrow n - 1$  do
10   $\Delta r = \vec{r}_{i+1} - \vec{r}_i$ 
11   $\Delta s^i = \|\Delta r\|_2$ 
12 end
13 return  $f, m, F_{av}, \Delta s$ 

```

Finally, the strains are computed as as shown in Algorithm 5.

Algorithm 5: Calculate Strains in csn axes

```

1 Read nodal quantities:  $\vec{F}_i, \vec{M}_i, \vec{T}_i, \vec{D}_i, \vec{S}_i$ 
2 Read number of nodes on the beam  $n$ 
3 Pre-allocate variables:  $F^{csn} : 3 \times n, M^{csn} : 3 \times n, M'^{csn} : 3 \times n, \epsilon^{csn} : 3 \times n$ 
4 for  $i = 1 \rightarrow n$  do
5    $\vec{F}_i^{csn} = \vec{T}_i \vec{F}_i$ 
6    $\vec{M}_i^{csn} = \vec{T}_i \vec{M}_i$ 
7    $M_i'^{csn} = \vec{M}_i^{csn} + \vec{D}_i^T \vec{F}_i^{csn}$ 
8    $\epsilon_i^{csn} = \vec{S}_i \vec{F}_i^{csn} + \vec{D}_i \vec{E}_i^{-1} M_i'^{csn}$ 
9 end
10 return  $\epsilon^{csn}$ 

```

To create a square system to solve, six more equations are needed. The moment-curvature relations for an element are defined as:

$$\frac{1}{2} ([K]_i + [K]_{i+1}) (\vec{\theta}_{i+1} \vec{\theta}_i) = \frac{1}{2} ([K^0]_i + [K^0]_{i+1}) \left(\vec{\theta}_{i+1}^0 \vec{\theta}_i^0 \right) + \frac{\Delta s}{2} ([E]_i + [E]_{i+1}) \left\{ \begin{array}{c} M'_c \\ M'_s \\ M'_n \end{array} \right\}_a \quad (\text{A.18})$$

where

$$\left\{ \begin{array}{c} M'_c \\ M'_s \\ M'_n \end{array} \right\}_a = \frac{1}{2} ([T]_i \vec{M}_i + [T]_{i+1} \vec{M}_{i+1}) + \frac{1}{2} ([D]_i [T]_i \vec{F}_i + [D]_{i+1} [T]_{i+1} \vec{F}_{i+1}) \quad (\text{A.19})$$

The strain-displacement relations for an element are defined as:

$$\vec{r}_{i+1} - \vec{r}_i = \Delta s^0 \left(\frac{1}{2} [T]_{i+1} + [T]_i \right) \left[\left\{ \begin{array}{c} 0 \\ 1 \\ 0 \end{array} \right\} + \left(\bar{S} [T] \vec{F} \right)_a + \left([D^T] [E^{-1}] \left\{ \begin{array}{c} M'_c \\ M'_s \\ M'_n \end{array} \right\} \right)_a \right] \quad (\text{A.20})$$

The final residual system of equations is populated as shown in Algorithm 6. The residuals are arranged as a $18 \times n$ matrix for easy visualization. When solving the residuals, the matrix is reshaped into a $18n \times 1$ vector.

Algorithm 6: Populating matrix of residuals

1 Pre-allocate variables: $\mathfrak{R} : 18 \times n$

2 **for** $i = 1 \rightarrow n$ **do**

3 **if** $i \leq n - 1$ **then**

4 Force equilibrium equation: $\mathfrak{R}(1 : 3)^i = \vec{F}_{i+1} - \vec{F}_i + \vec{f}^i \Delta s^i + \Delta \vec{F}_{ext}^i$

5 Moment equilibrium equation:

$$\mathfrak{R}(4 : 6)^i = \vec{M}_{i+1} - \vec{M}_i + \vec{m}^i \Delta s^i + \Delta \vec{M}_{ext}^i + (\vec{r}_{i+1} - \vec{r}_i) \times \vec{F}_{av}^i$$

6 Moment-curvature relationship: $\mathfrak{R}(7 : 9)^i =$

$$\begin{aligned} & \left[\frac{1}{2}(\bar{K}_i + \bar{K}_{i+1}) \right] \left[\vec{\theta}_{i+1} - \vec{\theta}_i \right] - \left[\frac{1}{2}(\bar{K}_{0i} + \bar{K}_{0i+1}) \right] \left[\vec{\theta}_{0i+1} - \vec{\theta}_{0i} \right] - \\ & \left[\frac{1}{2}(\bar{E}_{i+1}^{-1} + \bar{E}_i^{-1}) \right] \left[0.5(M'_{i+1}{}^{csn} + M_i{}^{csn}) \right] \Delta s^i + \\ & \begin{bmatrix} t_{\kappa_c} & 0 & 0 \\ 0 & t_{\kappa_s} & 0 \\ 0 & 0 & t_{\kappa_n} \end{bmatrix} \left\{ \left[\frac{1}{2}(\bar{K}_i + \bar{K}_{i+1}) \right] \left[\bar{K}_{i+1}^{-1} \bar{T}_{i+1} \vec{\omega}_{i+1} - \bar{K}_i^{-1} \bar{T}_i \vec{\omega}_i \right] \right\} + \\ & \begin{bmatrix} t_{\kappa_c} & 0 & 0 \\ 0 & t_{\kappa_s} & 0 \\ 0 & 0 & t_{\kappa_n} \end{bmatrix} \left\{ (\bar{K}_{i+1} - \bar{K}_i) \left[\frac{1}{2}(\bar{K}_{i+1}^{-1} \bar{T}_{i+1} \vec{\omega}_{i+1}) + \bar{K}_i^{-1} \bar{T}_i \vec{\omega}_i \right] \right\} \end{aligned}$$

7 Strain-displacement relationship: $\mathfrak{R}(10 : 12)^i =$

$$\begin{aligned} & (\vec{r}_{i+1} - \vec{r}_i) - \Delta s_0^i \left[\frac{1}{2}(\bar{T}_{i+1} + \bar{T}_i) \right]^T \left[\frac{1}{2} \left(\begin{Bmatrix} 0 \\ 1 \\ 0 \end{Bmatrix} + \epsilon_i^{csn} + \begin{Bmatrix} 0 \\ 1 \\ 0 \end{Bmatrix} + \epsilon_{i+1}^{csn} \right) \right] + \\ & \begin{bmatrix} t_{\gamma_c} & 0 & 0 \\ 0 & t_{\gamma_s} & 0 \\ 0 & 0 & t_{\gamma_n} \end{bmatrix} \left\{ (\vec{u}_{i+1} - \vec{u}_i) - \left[\frac{1}{2}(\vec{\omega}_{i+1} + \vec{\omega}_i) \right] \times (\vec{r}_{i+1} - \vec{r}_i) \right\} \end{aligned}$$

8 Nodal equations: $\mathfrak{R}(13 : 15)^i = \vec{u}_i - \vec{r}_i$, $\mathfrak{R}(16 : 18)^i = \vec{\omega}_i - \bar{T}_i^T \bar{K}_i \vec{\theta}_i$

9 **end**

10 **else**

11 Nodal equations: $\mathfrak{R}(13 : 15)^i = \vec{u}_i - \vec{r}_i$, $\mathfrak{R}(16 : 18)^i = \vec{\omega}_i - \bar{T}_i^T \bar{K}_i \vec{\theta}_i$

12 BC at fixed end: $\mathfrak{R}(1 : 3)^i = \vec{r}_1 - \vec{r}_1^{spec}$, $\mathfrak{R}(4 : 6)^i = \vec{\theta}_1 - \vec{\theta}_1^{spec}$

13 BC at free end: $\mathfrak{R}(7 : 9)^i = \vec{F}_n - \vec{F}_n^{spec}$, $\mathfrak{R}(10 : 12)^i = \vec{M}_n - \vec{M}_n^{spec}$

14 **end**

15 **end**

16 **return** \mathfrak{R}

APPENDIX B

RAPID AIRFRAME DESIGN ENVIRONMENT (RADE)

A supporting tool used in this work is the Rapid Airframe Design Environment (RADE) toolkit [188], developed at the Aerospace Systems Design Laboratory (ASDL). A flowchart of the capabilities of RADE is shown in Fig. B.1.

RADE contains a module for parametric variation of a baseline OML through the Open-VSP API, where aerodynamic shape variables such as span, sweep, chord, area, aspect ratio, twist, among others, can be defined. An example is shown in Fig. B.2a, where a baseline horizontal tail (gold) was changed to a planform with a larger sweep angle, higher aspect ratio, and smaller taper ratio.

Once the OML is defined, RADE has an automated capability to create a structural topology within the bounds of the OML. This is also a parametric implementation, and RADE has a library of various topological categories, each with its own set of parameters. Fig. B.2b shows a simple two spar wingbox for the horizontal tail (HT) in which variation of the front and rear spar locations, rib spacing, and rib orientation can be defined. The RADE structural geometry module then organizes the spars, ribs, and skin parts into an assembly hierarchy, in which various definitions can be made for the discretization of surfaces to set up material and sectional properties. A structural mesh can also be created automatically with definitions supplied by the user, including desired mesh size, growth rates, curvature rules, and element types. Example meshes for both configurations can be seen plotted on top of each other in the right side portion of the HT in Fig. B.2b. The structural model generation capabilities of RADE are not limited to a single component or section of the aircraft. Fig. D.8 shows structural geometry layout and mesh for the wing, horizontal tail, and vertical tail within a fused representation of the OML for the Common Research Model (CRM).

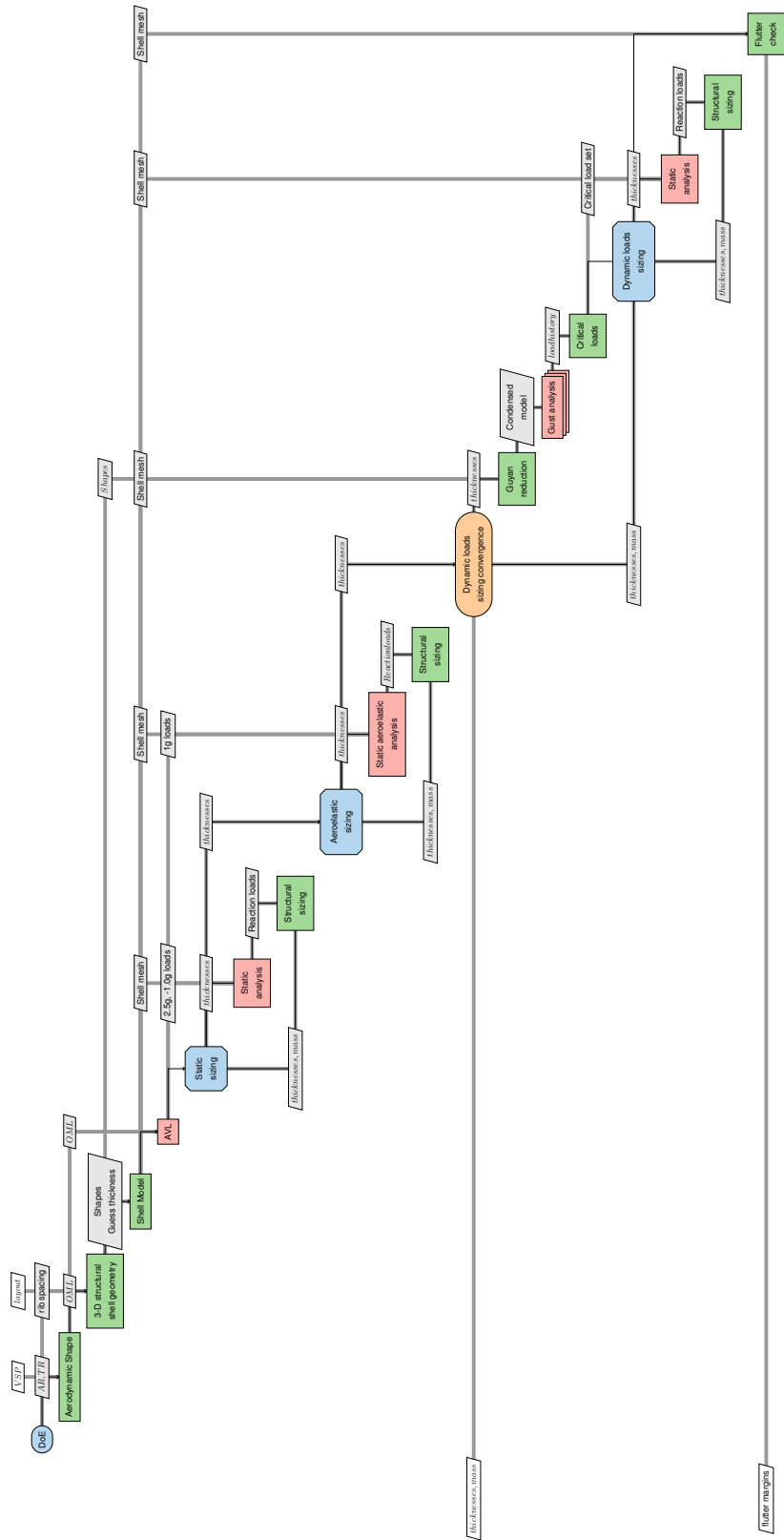


Figure B.1: XDSM for structural sizing using RADE

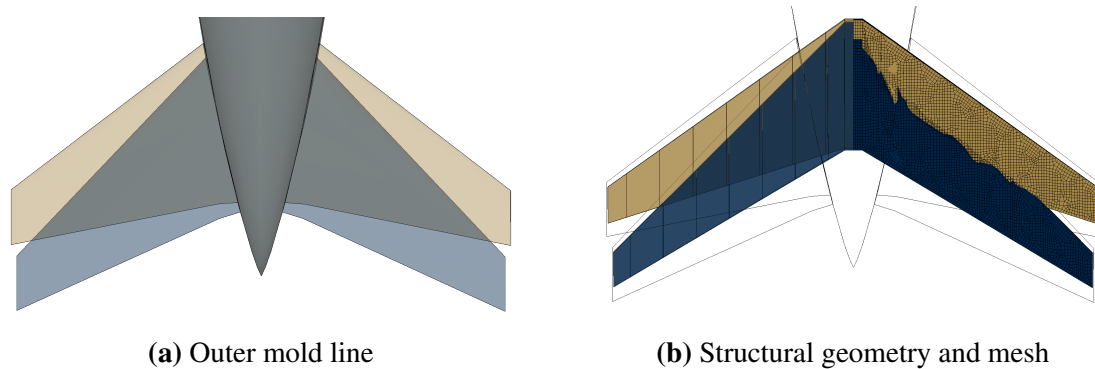


Figure B.2: Parametric features of the geometry pre-processor shown for a horizontal tail of the CRM aircraft

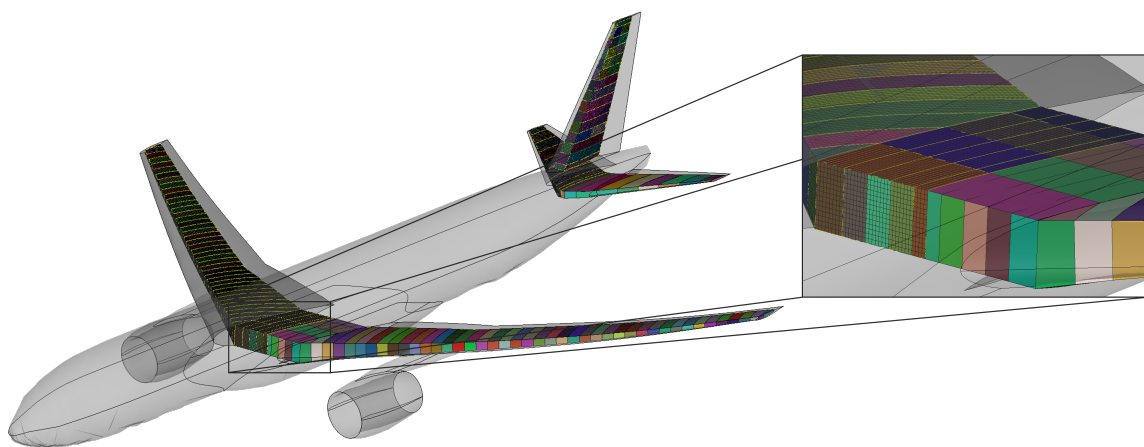


Figure B.3: Parametric mesh generation capability: geometry and mesh of mesh of wing and empennage of the CRM

RADE can also generate an AVL file based on the modified OML to compute realistic aerodynamic loads. Fig. B.4 shows an AVL model for the B777 aircraft. AVL is used to obtain cruise loads, and loads at static maneuver conditions of such as 2.5g and -1.0g.

Inertial loads associated with components and subsystems such as engines, control surfaces, actuators, and hydraulic lines are implemented through concentrated masses. Fig. B.5 shows a structural layout for the HT with two concentrated masses for the two actuators of the elevator. The elevator structure itself is treated as a concentrated mass attached to the rear spar, and therefore its stiffness in the system is neglected. Thus, the mass of the subsystems is accounted for in structural sizing.

The transfer of aerodynamic loads to the structure is by integrating surface pressures to

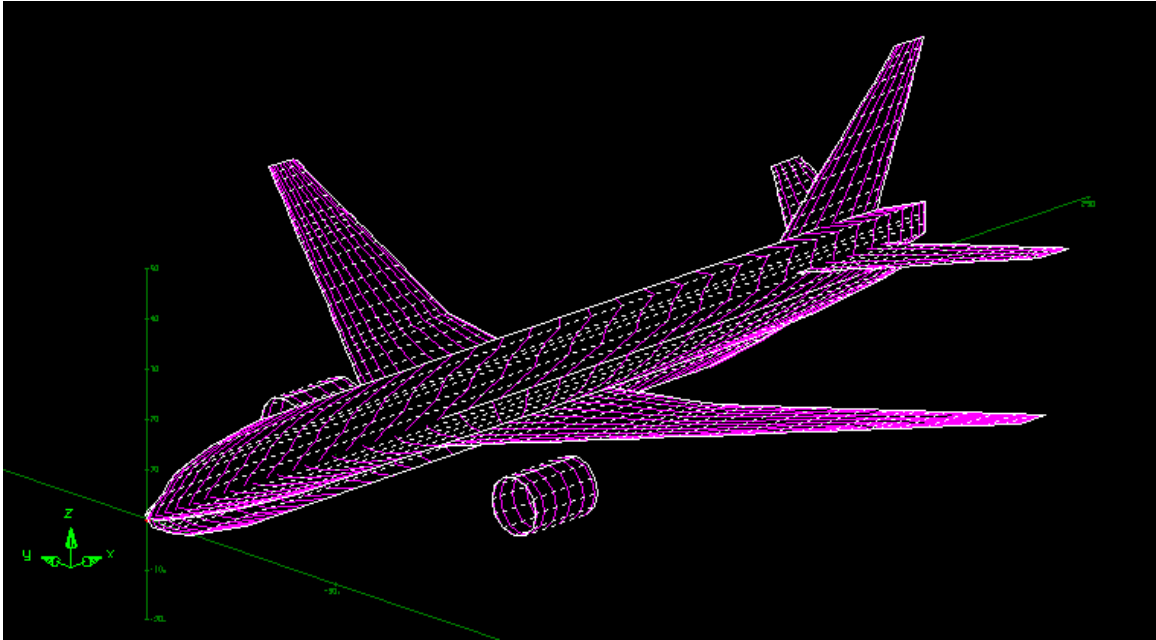


Figure B.4: AVL model of a B777

reference points along the span of a wing-like component. A module in RADE [188, 215] estimates the elastic axis and sets these reference points at the intersection of this line with rib components. The forces and moments associated with each reference point are then distributed to the structure via rigid body elements at key intersecting nodes between the rib and skin.

RADE also provides a module to translate data required for structural analysis with Nastran in the form of .bdf file, or structural sizing with Hypersizer. RADE executes the code and obtains responses of interest. Along with stress, strain, and deflection distributions calculated in Nastran, potential component-based outputs from HyperSizer include

- Optimal sectional dimensions (skin thickness, stiffener height,...)
- Margins of safety
- Critical failure mode (categorization)
- Critical failure method (failure equation)

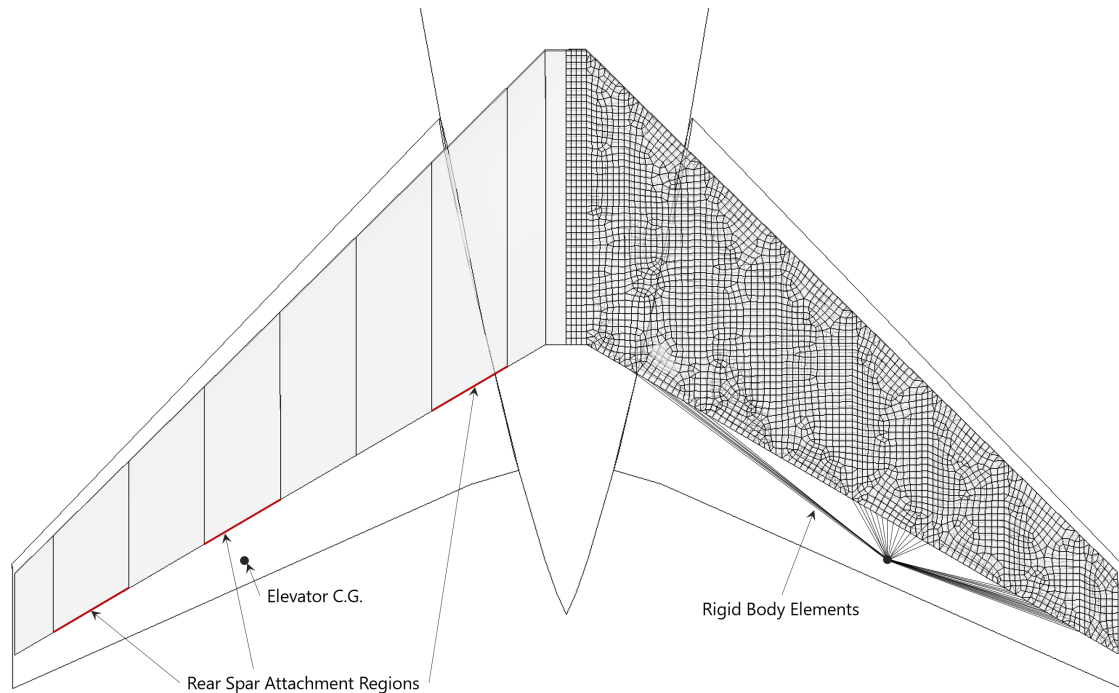


Figure B.5: Subsystems treated as concentrated masses and attached to the structure via rigid body elements

Sizing in RADE is done in three stages. First, the structure is sized for rigid aerodynamic loads provided by AVL for 2.5g and -1.0g maneuvers. The shell model structure and loads are given to Nastran SOL 101 for static load analysis. The internal loads computed by Nastran are used by Hypersizer to size the structure.

Next, the structure is sized for static aeroelastic conditions. Nastran SOL 144 is used for aeroelastic static load analysis. The main difference between SOL 101 and SOL 144 is the allocation of control constraints in SOL 144, which specify angles of attack, net pitching moment at the neutral point, and total load factor, which condition the interaction of the generated aerodynamic mesh with the mission conditions.

Recently the capabilities of RADE were extended to include dynamic aeroelastic simulations [216]. Nastran SOL 146 is used for gust analysis. The user supplies the following gust parameters:

- Total simulation time (must include enough time for gust dissipation)

- Structural damping (assumed 0.02 throughout all the frequency range)
- Time-step of the simulation (0.01 seconds for 5 seconds)
- Number of vibrational modes to take into account (11 wing modes)
- Shape of the gust, either one-minus-cosine or sharp

RADE executes SOL 146 and extracts a set of deflections from each node recorded for each time-step specified.

For the dynamic simulations to be computationally tractable, RADE uses Guyan Reduction[81]. However, the most difficult part is to select the degrees of freedom that are expected to be ‘unloaded’, and that requires careful analysis of the structure in question. For that, Nastran with the ASET card allows a custom set of nodes to take into account as the loaded nodes and generate the required reduced system according to the selected nodes and degrees of freedom. The reduced stiffness matrix, \mathbf{K}_{ASET} is also obtained from Nastran. The following were the different degrees of freedom considered:

- All nodes where the loads are applied, connected with the structure by the rigid body (RBE3) elements
- The nodes where the engines are connected
- The nodes at the front and rear spars

Apart from the ASET implementation’s speed bonus, it also provides an efficient way to obtain the loads on the structure during a dynamic simulation.

$$\vec{f}_{applied}(t) = \mathbf{K}_{ASET} \cdot \vec{d}_{ASET}(t) \quad (\text{B.1})$$

The loads computed include the applied loads through the FORCE and MOMENT cards and the inertial, aerodynamic, and other loads that give rise to the deflections observed after the analysis finishes. Thus the load time-history due to gusts can be computed. Such a load

history can then be used to find critical load cases, which then can be employed to size the structure. As before, Hypersizer is used for structural sizing.

Finally, a Nastran SOL 145 flutter check is performed, using the same aerodynamic and structural mesh as previous solutions. It performs a PK-method flutter analysis, which allows the estimation of divergent modes in the aircraft structure given a set of flight conditions.

APPENDIX C

VARIATIONAL ASYMPTOTIC METHOD (VAM)

The theoretical foundation for using the VAM method for composite beams was originally developed by Hodges [125]. A code named Variational Asymptotic Beam Sectional Analysis (VABS) was developed based on the theory. This appendix presents the equations from the relevant papers [191, 133, 132, 151, 125, 139].

C.1 Cross-Sectional Analysis using VAM

The behavior of beams is governed by the extended Hamilton's Principle as shown

$$\int_{t_1}^{t_2} [\delta(\mathcal{K} - \mathcal{U}) + \overline{\delta\mathcal{W}}] dt = 0 \quad (\text{C.1})$$

where t_1 and t_2 are arbitrary fixed times, \mathcal{K} is the kinetic energy, \mathcal{U} is the internal energy, δ is the Lagrangian variation for a fixed time, and $\overline{\delta\mathcal{W}}$ is the virtual work by applied loads.

As seen in Fig. C.1, a beam can be represented by a reference line r measured by x_1 , and a reference cross-section which has all the points perpendicular to the undeformed reference line and along with the x_α coordinates. The orthonormal triad of unit vectors \mathbf{b}_i is specified at each point along r , such that $\mathbf{b}_1(\mathbf{x}_1)$ always remains tangential to the undeformed reference curve. The position vector of any point in the undeformed beam $\hat{\mathbf{r}}$ is given as

$$\hat{\mathbf{r}}(x_1, x_2, x_3) = \mathbf{r}(x_1) + x_\alpha \mathbf{b}_\alpha(x_1) \quad (\text{C.2})$$

where \mathbf{r} is the position vector of the points along the reference line. After deformation, the particle that had position vector $\hat{\mathbf{r}}$ in the undeformed state now has the position vector $\hat{\mathbf{R}}$ in the deformed state. Another orthonormal triad \mathbf{B}_i for deformed configuration are specified at each point along \mathbf{R} which is related to \mathbf{b}_i as $\mathbf{B}_i = C_{ij}^{Bb} \mathbf{b}_j$. The position vector of an

arbitrary point in the deformed state denoted by $\hat{\mathbf{R}}(x_1, x_2, x_3)$ can now be expressed as

$$\hat{\mathbf{R}}(x_1, x_2, x_3) = \mathbf{R}(x_1) + x_\alpha \mathbf{B}_\alpha(x_1) + w_i(x_1, x_2, x_3) \mathbf{B}_i(x_1) \quad (\text{C.3})$$

where the functions w_i are the warping displacements, subject to constraints

$$\begin{aligned} \langle w_i(x_1, x_2, x_3) \rangle &= 0 \\ \langle w_{2,3}(x_1, x_2, x_3) - w_{3,2}(x_1, x_2, x_3) \rangle &= 0 \end{aligned} \quad (\text{C.4})$$

for unique warping solutions, where

$$\langle \cdot \rangle = \int_{-\frac{b}{2}}^{\frac{b}{2}} \int_{-\frac{h}{2}}^{\frac{h}{2}} (\cdot) dx_2 dx_3$$

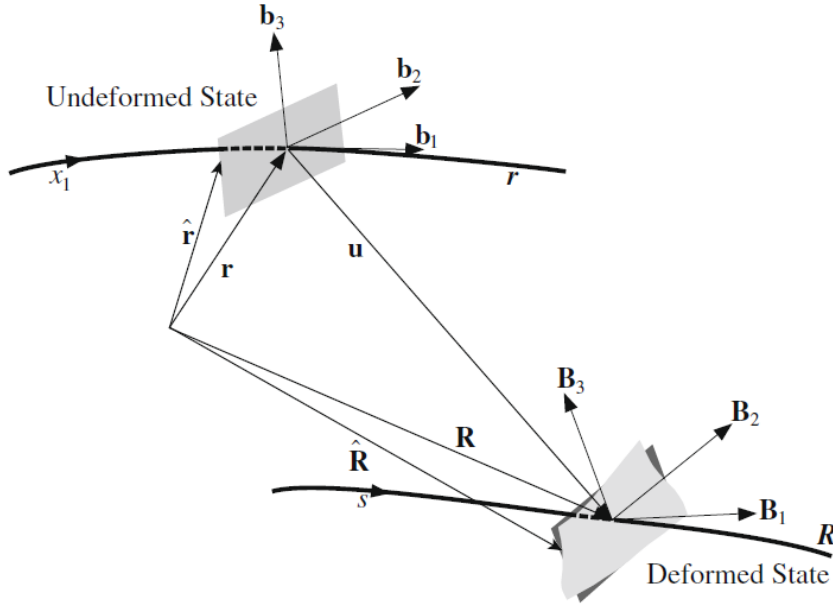


Figure C.1: Schematic of Beam Deformation

It is possible to write the 3-D formulation of the extended Hamilton's Principle (Eq. C.1) in terms of 1-D beam displacements, rotations and warping defined in Eq. C.3. Strain

energy is written as

$$\mathcal{U} = \int_0^L \langle \langle \sigma^T \Gamma \rangle \rangle dx_1 \quad (\text{C.5a})$$

$$\langle \langle \bullet \rangle \rangle = \langle \bullet \sqrt{g} \rangle \quad (\text{C.5b})$$

assuming that the material is linearly elastic and thus satisfies Hooke's law

$$\sigma = \mathcal{D}\Gamma \quad (\text{C.6})$$

where Γ is the 3-D strain and is written as $\Gamma = [\Gamma_{11} \ 2\Gamma_{12} \ 2\Gamma_{13} \ \Gamma_{22} \ 2\Gamma_{23} \ \Gamma_{33}]^T$. Here, x_i represents the beam coordinate frame such that the unit vector x_1 points along the span of the beam and x_2, x_3 are corresponding cross-sectional coordinates for the cross section. Warping functions are assumed to be of the order of the strain with assumption of small local rotations. Thus, the product of warping and 1-D generalized strains may be neglected and the 3-D strain field can be written as

$$\Gamma = \Gamma_a w + \Gamma_\epsilon \bar{\epsilon} + \Gamma_R w + \Gamma_\ell w' \quad (\text{C.7})$$

where Γ_a is a 6×3 matrix, sparsely populated with operators of derivatives with respect to the cross-sectional coordinates as described in Eq. (C.8). The other symbols (i.e., Γ_ϵ , Γ_R and Γ_ℓ) are defined in Eqs. (C.9), (C.10) and (C.11), respectively. These symbols in Eq.

(C.7) are further defined and derived in Ref. [125].

$$\Gamma_a = \begin{bmatrix} 0 & 0 & 0 \\ \frac{\partial}{\partial x_2} & 0 & 0 \\ \frac{\partial}{\partial x_3} & 0 & 0 \\ 0 & \frac{\partial}{\partial x_2} & 0 \\ 0 & \frac{\partial}{\partial x_3} & \frac{\partial}{\partial x_2} \\ 0 & 0 & \frac{\partial}{\partial x_3} \end{bmatrix} \quad (\text{C.8})$$

$$\Gamma_\epsilon = \frac{1}{\sqrt{g}} \begin{bmatrix} 1 & 0 & x_3 & -x_2 \\ 0 & -x_3 & 0 & 0 \\ 0 & x_2 & 0 & 0 \\ 0 & 0 & 0 & 0 \\ 0 & 0 & 0 & 0 \\ 0 & 0 & 0 & 0 \\ 0 & 0 & 0 & 0 \end{bmatrix} = \frac{1}{\sqrt{g}} \bar{\Gamma}_\epsilon = \sum_{i=0}^4 g_i \bar{\Gamma}_\epsilon \quad (\text{C.9})$$

$$\Gamma_\ell = \frac{1}{\sqrt{g}} \begin{bmatrix} 1 & 0 & 0 \\ 0 & 1 & 0 \\ 0 & 0 & 1 \\ 0 & 0 & 0 \\ 0 & 0 & 0 \\ 0 & 0 & 0 \end{bmatrix} = \frac{1}{\sqrt{g}} \bar{\Gamma}_\ell = \sum_{i=0}^3 g_i \bar{\Gamma}_\ell \quad (\text{C.10})$$

$$\Gamma_R = \frac{1}{\sqrt{g}} \begin{bmatrix} \Gamma_{hR} & -k_3 & k_2 \\ k_3 & \Gamma_{hR} & -k_1 \\ -k_2 & k_1 & \Gamma_{hR} \\ 0 & 0 & 0 \\ 0 & 0 & 0 \\ 0 & 0 & 0 \end{bmatrix} = \frac{1}{\sqrt{g}} \bar{\Gamma}_R = \sum_{i=0}^3 g_i \bar{\Gamma}_R \quad (\text{C.11})$$

where

$$\Gamma_{hR} = k_1 \left(x_3 \frac{\partial}{\partial x_2} - x_2 \frac{\partial}{\partial x_3} \right) \quad (\text{C.12})$$

A detailed derivation of the 3-D strains and the expressions for strain energy density (strain energy per unit length) is presented in Ref. [125]. The derivation for the strain energy density and warping constraints were updated by Yu et al. [132]. Further, to do the dimen-

sional reduction, one must rely on the inherent small parameters that are generally present in a beam geometry. Denoting the characteristic radius of initial curvature or twist by R , the two small geometric parameters are b/l and b/R . Therefore, using the finite element discretization of the warping field [125]

$$w(x_1, x_2, x_3) = S(x_2, x_3) V(x_1) \quad (\text{C.13})$$

$$w = [w_1 \quad w_2 \quad w_3]^T$$

where $S(x_2, x_3)$ are the finite-element shape functions, the expression for the strain energy from Eq. (C.5) can be rewritten as

$$2U = V^T E V + 2V^T (D_{a\epsilon} \bar{\epsilon} + D_{aR} V + D_{a\ell} V') + \bar{\epsilon}^T D_{\epsilon\epsilon} \bar{\epsilon} + V^T D_{RR} V \quad (\text{C.14})$$

$$+ V'^T D_{\ell\ell} V' + 2V^T D_{R\epsilon} \bar{\epsilon} + 2V'^T D_{\ell\epsilon} \bar{\epsilon} + 2V^T D_{R\ell} V'$$

The matrices in the above equation are defined carefully with the order of magnitude written in subscript as

$$D_{a\epsilon} = \langle (\Gamma_a S)^T D \bar{\Gamma}_\ell S \rangle \quad (\text{C.15})$$

$$= \langle (\Gamma_a S)^T D \bar{\Gamma}_\epsilon \rangle$$

$$D_{aR} = \langle (\Gamma_a S)^T D \bar{\Gamma}_R S \rangle \quad (\text{C.16})$$

$$D_{a\ell} = \langle (\Gamma_a S)^T D \bar{\Gamma}_\ell S \rangle \quad (\text{C.17})$$

$$\begin{aligned}
D_{\epsilon\epsilon} &= \langle\langle \Gamma_\epsilon^T D\Gamma_\epsilon \rangle\rangle \\
&= \langle \frac{1}{\sqrt{g}} \bar{\Gamma}_\epsilon^T D\bar{\Gamma}_\epsilon \rangle \\
&= \langle g_0 \bar{\Gamma}_\epsilon^T D\bar{\Gamma}_\epsilon \rangle + \langle g_1 \bar{\Gamma}_\epsilon^T D\bar{\Gamma}_\epsilon \rangle + \langle g_2 \bar{\Gamma}_\epsilon^T D\bar{\Gamma}_\epsilon \rangle \\
&\quad + \langle g_3 \bar{\Gamma}_\epsilon^T D\bar{\Gamma}_\epsilon \rangle + \langle g_4 \bar{\Gamma}_\epsilon^T D\bar{\Gamma}_\epsilon \rangle \\
&= D_{\epsilon\epsilon_0} + D_{\epsilon\epsilon_1} + D_{\epsilon\epsilon_2} + D_{\epsilon\epsilon_3} + D_{\epsilon\epsilon_4}
\end{aligned} \tag{C.18}$$

$$\begin{aligned}
D_{RR} &= \langle\langle (\Gamma_R S)^T D\Gamma_R S \rangle\rangle \\
&= \langle \frac{1}{\sqrt{g}} (\bar{\Gamma}_R S)^T D\bar{\Gamma}_R S \rangle \\
&= \langle g_0 (\bar{\Gamma}_R S)^T D\bar{\Gamma}_R S \rangle + \langle g_1 (\bar{\Gamma}_R S)^T D\bar{\Gamma}_R S \rangle + \langle g_2 (\bar{\Gamma}_R S)^T D\bar{\Gamma}_R S \rangle \\
&= D_{RR_2} + D_{RR_3} + D_{RR_4}
\end{aligned} \tag{C.19}$$

$$\begin{aligned}
D_{\ell\ell} &= \langle\langle (\Gamma_\ell S)^T D\Gamma_\ell S \rangle\rangle \\
&= \langle \frac{1}{\sqrt{g}} (\bar{\Gamma}_\ell S)^T D\bar{\Gamma}_\ell S \rangle \\
&= \langle g_0 (\bar{\Gamma}_\ell S)^T D\bar{\Gamma}_\ell S \rangle + \langle g_1 (\bar{\Gamma}_\ell S)^T D\bar{\Gamma}_\ell S \rangle + \langle g_2 (\bar{\Gamma}_\ell S)^T D\bar{\Gamma}_\ell S \rangle \\
&= D_{\ell\ell_2} + D_{\ell\ell_3} + D_{\ell\ell_4}
\end{aligned} \tag{C.20}$$

$$\begin{aligned}
D_{R\epsilon} &= \langle\langle (\Gamma_R S)^T D\Gamma_\epsilon \rangle\rangle \\
&= \left\langle \frac{1}{\sqrt{g}} (\bar{\Gamma}_R S)^T D\bar{\Gamma}_\epsilon \right\rangle \\
&= \langle g_0 (\bar{\Gamma}_R S)^T D\bar{\Gamma}_\epsilon \rangle + \langle g_1 (\bar{\Gamma}_R S)^T D\bar{\Gamma}_\epsilon \rangle + \langle g_2 (\bar{\Gamma}_R S)^T D\bar{\Gamma}_\epsilon \rangle + \langle g_3 (\bar{\Gamma}_R S)^T D\bar{\Gamma}_\epsilon \rangle \\
&= D_{R\epsilon_1} + D_{R\epsilon_2} + D_{R\epsilon_3} + D_{R\epsilon_4} \\
D_{R\epsilon_{i+1}} &= \langle g_i (\bar{\Gamma}_R S)^T D\bar{\Gamma}_\epsilon \rangle
\end{aligned} \tag{C.21}$$

$$\begin{aligned}
D_{\ell\epsilon} &= \langle\langle (\Gamma_\ell S)^T D\Gamma_\epsilon \rangle\rangle \\
&= \left\langle \frac{1}{\sqrt{g}} (\bar{\Gamma}_\ell S)^T D\bar{\Gamma}_\epsilon \right\rangle \\
&= \langle g_0 (\bar{\Gamma}_\ell S)^T D\bar{\Gamma}_\epsilon \rangle + \langle g_1 (\bar{\Gamma}_\ell S)^T D\bar{\Gamma}_\epsilon \rangle + \langle g_2 (\bar{\Gamma}_\ell S)^T D\bar{\Gamma}_\epsilon \rangle + \langle g_3 (\bar{\Gamma}_\ell S)^T D\bar{\Gamma}_\epsilon \rangle \\
&= D_{\ell\epsilon_1} + D_{\ell\epsilon_2} + D_{\ell\epsilon_3} + D_{\ell\epsilon_4}
\end{aligned} \tag{C.22}$$

$$\begin{aligned}
D_{R\ell} &= \langle\langle (\Gamma_R S)^T D\Gamma_\ell S \rangle\rangle \\
&= \left\langle \frac{1}{\sqrt{g}} (\bar{\Gamma}_R S)^T D\bar{\Gamma}_\ell S \right\rangle \\
&= \langle g_0 (\bar{\Gamma}_R S)^T D\bar{\Gamma}_\ell \rangle + \langle g_1 (\bar{\Gamma}_R S)^T D\bar{\Gamma}_\ell \rangle + \langle g_2 (\bar{\Gamma}_R S)^T D\bar{\Gamma}_\ell \rangle \\
&= D_{R\ell_2} + D_{R\ell_3} + D_{R\ell_4}
\end{aligned} \tag{C.23}$$

and finally,

$$\begin{aligned}
E &= \langle \langle (\Gamma_a S)^T D \Gamma_a S \rangle \rangle \\
&= \langle (\Gamma_a S)^T D (\Gamma_a S) \sqrt{g} \rangle \\
&= \underbrace{\langle (\Gamma_a S)^T D \Gamma_a S g_0 \rangle}_{E_0} + \underbrace{\langle (\Gamma_a S)^T D \Gamma_a S g_1 \rangle}_{E_1} \\
&= E_0 + E_1
\end{aligned} \tag{C.24}$$

After substituting the values obtained above in Eq. (C.14), the total strain energy that is to be considered is therefore

$$\begin{aligned}
2U &= (V_0 + V_1 + V_2)^T (E_0 + E_1) (V_0 + V_1 + V_2) \\
&\quad + 2(V_0 + V_1 + V_2)^T (D_{a\epsilon}) \bar{\epsilon} \\
&\quad + 2(V_0 + V_1 + V_2)^T (D_{aR}) (V_0 + V_1 + V_2) \\
&\quad + 2(V_0 + V_1 + V_2)^T (D_{a\ell}) (V'_0 + V'_1 + V'_2) \\
&\quad + \bar{\epsilon}^T (D_{\epsilon\epsilon_0} + D_{\epsilon\epsilon_1} + D_{\epsilon\epsilon_2} + D_{\epsilon\epsilon_3} + D_{\epsilon\epsilon_4}) \bar{\epsilon} \\
&\quad + (V_0 + V_1 + V_2)^T (D_{RR_2} + D_{RR_3} + D_{RR_4}) (V_0 + V_1 + V_2) \\
&\quad + (V'_0 + V'_1 + V'_2)^T (D_{\ell\ell_2} + D_{\ell\ell_3} + D_{\ell\ell_4}) (V'_0 + V'_1 + V'_2) \\
&\quad + 2(V_0 + V_1 + V_2)^T (D_{R\epsilon_1} + D_{R\epsilon_2} + D_{R\epsilon_3} + D_{R\epsilon_4}) \bar{\epsilon} \\
&\quad + 2(V'_0 + V'_1 + V'_2)^T (D_{\ell\epsilon_1} + D_{\ell\epsilon_2} + D_{\ell\epsilon_3} + D_{\ell\epsilon_4}) \bar{\epsilon} \\
&\quad + 2(V_0 + V_1 + V_2)^T (D_{R\ell_2} + D_{R\ell_3} + D_{R\ell_4}) (V'_0 + V'_1 + V'_2)
\end{aligned} \tag{C.25}$$

The terms are now split into orders for the asymptotic analysis. It is important to note that the definitions of the symbols are such that the order of any symbol is the sum of all the numbers that appear as subscripts in that symbol. While minimizing the strain energy, one needs to also consider the constraints due to warping mentioned in Eq. (C.4) which are

represented in terms of discretized warping variables as

$$V^T D_c = 0 \quad (\text{C.26})$$

The kernel of Γ_a, ψ , from Hodges [125] can be used during the development such that

$$\begin{aligned} \Gamma_a \psi = 0 &\implies E_0 \Psi = 0 \\ \psi &= S \Psi \end{aligned} \quad (\text{C.27})$$

Zeroth-Order Analysis

From Eq. (C.25), the zeroth-order energy can be obtained as

$$2U_0 = V_0^T E_0 V_0 + 2V_0^T D_{a\epsilon} \bar{\epsilon} + \bar{\epsilon}^T D_{\epsilon\epsilon_0} \bar{\epsilon} \quad (\text{C.28})$$

Keeping track of the warping constraints, the final equation for zeroth-order warping is therefore

$$E_0 V_0 + D_{a\epsilon} \bar{\epsilon} = 0 \quad (\text{C.29})$$

After considering singularities of E_0 [125], the final solution is

$$V_0 = \hat{V}_0 \bar{\epsilon} \quad (\text{C.30})$$

The substitution of the zeroth-order warping solutions in the strain energy expression yields the asymptotically correct zeroth-order strain energy which is given by the expression

$$2U_0 = \bar{\epsilon}^T D_{\epsilon\epsilon_1} \bar{\epsilon} + (V_0'^T D_{\ell\epsilon_1} + V_0^T D_{R\epsilon_1}) \bar{\epsilon} + 2V_0^T D_{aR_1} V_0 \quad (\text{C.31})$$

This approximation contains no corrections due to the transverse shear strains. So, the stiffness matrix obtained from this approximation is analogous to the Euler-Bernoulli

stiffness matrix such that S in the equation shown below depicts the 4×4 stiffness matrix

$$\begin{pmatrix} F_1 \\ M_1 \\ M_2 \\ M_3 \end{pmatrix} = \underbrace{\begin{bmatrix} S_{11} & S_{12} & S_{13} & S_{14} \\ S_{21} & S_{22} & S_{23} & S_{24} \\ S_{31} & S_{32} & S_{33} & S_{34} \\ S_{41} & S_{42} & S_{43} & S_{44} \end{bmatrix}}_S \begin{pmatrix} \gamma_{11} \\ \kappa_1 \\ \kappa_2 \\ \kappa_3 \end{pmatrix} \quad (\text{C.32})$$

Note this this stiffness matrix accounts for corrections due to initial curvature and pre-twist, unlike conventional Euler-Bernoulli stiffness matrix.

C.1.1 First-Order Analysis

The warping is now perturbed and substituted back in the strain energy. Now, the relevant terms in the strain energy are those through second-order. However, after the substitution of the zeroth-order warping solutions in the strain energy expression, the zeroth-order strain energy is a constant and does not feature in the first-order warping calculation. So, the expression for strain energy after removing the zeroth-order terms can be written as

$$\begin{aligned} 2U_1 = & \bar{\epsilon}^T D_{e\epsilon_1} \bar{\epsilon} + (V_0^{T} D_{\ell\epsilon_1} + V_0^{T} D_{R\epsilon_1}) \bar{\epsilon} \\ & + 2V_0^T D_{aR_1} V_0 + \cancel{V_1^T E_0 V_0} + V_0^T E_1 V_0 + \cancel{V_0^T E_0 V_1} + 2V_0^T D_{a\ell_1} V_0' \end{aligned} \quad (\text{C.33})$$

Further, the second-order terms in the strain energy can be combined and written in the following expression as

$$\begin{aligned}
2U_2 = & \bar{\epsilon} D_{\epsilon\epsilon_2} \bar{\epsilon} + (\cancel{2V_2^T D_{a\epsilon}} + 2V_1'^T D_{\ell\epsilon_1} + 2V_0'^T D_{\ell\epsilon_2} + 2V_1^T D_{R\epsilon_1} + 2V_0^T D_{R\epsilon_2}) \bar{\epsilon} \\
& + 2V_1^T D_{aR_1} V_0 + V_0^T D_{RR_2} V_0 + \cancel{V_2^T E_0 V_0} + V_1^T E_1 V_0 + 2V_0^T D_{aR} V_1 \\
& + V_1^T E_0 V_1 + V_0^T E_1 V_1 + \cancel{V_0^T E_0 V_2} + 2V_1^T D_{al} V_0' \\
& + 2V_0^T D_{R\ell_2} V_0' + 2V_0^T D_{al} V_1'
\end{aligned} \tag{C.34}$$

The canceled terms in the above two equations are results of Eq. (C.29). As expected the second-order warping plays no part in the second-order strain energy. After considerations of the warping constraints, the final equation for V_1 is

$$\begin{aligned}
E_0 V_1 = & (D_c (\Psi^T D_c)^{-1} \Psi^T - \Delta) (D_R \bar{\epsilon} + D_S \bar{\epsilon}') \\
D_R = & E_1 \hat{V}_0 + (D_{aR} + D_{aR}^T) \hat{V}_0 + D_{R\epsilon_1} \\
D_S = & (D_{al} - D_{al}^T) \hat{V}_0 - D_{\ell\epsilon_1}
\end{aligned} \tag{C.35}$$

The solution after removing the singularities of E_0 may be written as

$$V_1 = V_{1R} \bar{\epsilon} + V_{1S} \bar{\epsilon}' \tag{C.36}$$

Only the terms related with V_1 are relevant in the process of the minimization of the strain energy. After performing integration by parts with respect to x_1 to get rid of the derivatives

of V_1 , the relevant terms are

$$\begin{aligned}
\mathcal{F} &= V_1^T E_0 V_1 + 2V_1^T (E_1 V_0 + D_{a\epsilon_1} \bar{\epsilon} + (D_{aR} + D_{aR}^T) V_0 + D_{R\epsilon_1} \bar{\epsilon}) \\
&\quad + 2V_1^T ((D_{al} - D_{al}^T) V_0' - D_{\ell\epsilon_1} \bar{\epsilon}') \\
&= V_1^T E_0 V_1 + 2V_1^T (E_1 \hat{V}_0 + (D_{aR} + D_{aR}^T) \hat{V}_0 + D_{R\epsilon_1} \bar{\epsilon}) \\
&\quad + 2V_1^T ((D_{al} - D_{al}^T) \hat{V}_0 - D_{\ell\epsilon_1} \bar{\epsilon}') \\
&= V_1^T E_0 V_1 + 2V_1^T D_R \bar{\epsilon} + 2V_1^T D_S \bar{\epsilon}'
\end{aligned} \tag{C.37}$$

Keeping the constraints in mind, one can use the standard procedure of the calculus of variations to solve for the warping field. Hence

$$\begin{aligned}
E_0 V_1 &= (D_c (\Psi^T D_c)^{-1} \Psi^T - \Delta) (D_R \bar{\epsilon} + D_S \bar{\epsilon}') \\
V_1 &= V_{1R} \bar{\epsilon} + V_{1S} \bar{\epsilon}'
\end{aligned} \tag{C.38}$$

where Ψ is the kernel matrix for E_0 and D_c is the constraint matrix associated with warping (i.e., $E_0 \Psi = 0$ and $V^T D_c = 0$, respectively). Using this, we may now obtain the second-order asymptotically correct strain energy as

$$2U = \bar{\epsilon}^T A \bar{\epsilon} + 2\bar{\epsilon}^T B \bar{\epsilon}' + \bar{\epsilon}'^T C \bar{\epsilon}' + 2\bar{\epsilon}^T D \bar{\epsilon}' \tag{C.39}$$

The matrices in the above equation are defined as

$$\begin{aligned}
A &= \hat{V}_0^T D_{a\epsilon} + D_{\epsilon\epsilon_0} + \hat{V}_0^T E_1 \hat{V}_0 + 2\hat{V}_0^T D_{aR_1} \hat{V}_0 + D_{\epsilon\epsilon_1} + 2\hat{V}_0^T D_{R\epsilon_1} \\
&\quad + D_{\epsilon\epsilon_2} + \hat{V}_0^T D_{RR_2} \hat{V}_0 + 2\hat{V}_0^T D_{R\epsilon_2} + V_{1R}^T \bar{D}_R \\
B &= \hat{V}_0^T D_{al_1} \hat{V}_0 + D_{\ell\epsilon_1}^T \hat{V}_0 + D_{\ell\epsilon_2}^T \hat{V}_0 + \hat{V}_0^T D_{R\ell_2} \hat{V}_0 + \frac{1}{2} (V_{1R}^T \bar{D}_S + D_R^T V_{1S}) \\
&\quad + (\hat{V}_0^T D_{al_1} + D_{\ell\epsilon_1}^T) V_{1R} \\
C &= \hat{V}_0^T D_{\ell\ell_2} \hat{V}_0 + V_{1S}^T \bar{D}_S \\
D &= (\hat{V}_0^T D_{al} + D_{\ell\epsilon_1}^T) V_{1S}
\end{aligned} \tag{C.40}$$

where

$$\begin{aligned}\bar{D}_R &= (D_c(\Psi^T D_c)^{-1} \Psi^T + \Delta) D_R \\ \bar{D}_S &= (D_{al} + D_{al}^T) \hat{V}_0 + D_{\ell\epsilon_1}\end{aligned}\tag{C.41}$$

To summarize the minimization process, the strain energy functional thus formed in Eq. (C.25) is minimized with respect to the warping functions and the warping solutions are further perturbed to obtain asymptotically correct second order approximations of the strain energy, Eq. (C.39), respectively. The Generalized Timoshenko (GT) transformation now follows to convert Eq. (C.39) into the following form

$$2U = \epsilon^T X \epsilon + 2\epsilon^T Y \gamma_s + \gamma_s^T G \gamma_s\tag{C.42}$$

where X , Y and G are unknowns to be found to fit Eq. (C.39) in the GT (i.e. shear deformable) model, Eq. (C.42). Here matrices X , Y , and G are of the size 4×4 , 4×4 , and 2×2 , respectively. The transformation procedure involves applying 1-D kinematic equations, constitutive law, and static equilibrium equations. The result is a system of nonlinear algebraic equations with unknowns consisting of stiffness matrices X , Y , and G . Because the strain energy, Eq. (C.42) is a quadratic form involving generalized strain measures, one obtains a physically linear one-dimensional model. The cross-sectional stress resultants are

linear in the 1-D generalized strains and can be written in the form

$$\begin{Bmatrix} F_1 \\ F_2 \\ F_3 \\ M_1 \\ M_2 \\ M_3 \end{Bmatrix} = \begin{bmatrix} X & Y \\ Y^T & G \end{bmatrix} \begin{Bmatrix} \epsilon \\ \gamma_s \end{Bmatrix} \quad (\text{C.43})$$

After rearranging the terms in the equation above, one obtains a 1-D constitutive law relating the 1-D generalized resultant forces on the beam cross section to the 1-D generalized strains as

$$\begin{Bmatrix} F_1 \\ F_2 \\ F_3 \\ M_1 \\ M_2 \\ M_3 \end{Bmatrix} = \underbrace{\begin{bmatrix} S_{11} & S_{12} & S_{13} & S_{14} & S_{15} & S_{16} \\ S_{21} & S_{22} & S_{23} & S_{24} & S_{25} & S_{26} \\ S_{31} & S_{32} & S_{33} & S_{34} & S_{35} & S_{36} \\ S_{41} & S_{42} & S_{43} & S_{44} & S_{45} & S_{46} \\ S_{51} & S_{52} & S_{53} & S_{54} & S_{55} & S_{56} \\ S_{61} & S_{62} & S_{63} & S_{64} & S_{65} & S_{66} \end{bmatrix}}_S \begin{Bmatrix} \gamma_{11} \\ 2\gamma_{12} \\ 2\gamma_{13} \\ \kappa_1 \\ \kappa_2 \\ \kappa_3 \end{Bmatrix} \quad (\text{C.44})$$

where S is the 6×6 sectional stiffness matrix. The Eq. (C.44) can be written in a condensed form as

$$\begin{Bmatrix} F \\ M \end{Bmatrix} = \begin{bmatrix} A & B \\ B^T & D \end{bmatrix} \begin{Bmatrix} \gamma \\ \kappa \end{Bmatrix} \quad (\text{C.45})$$

where A, B and D are the 3×3 sub-matrices of the stiffness matrix S and have no relation with the matrices used in laminate theory. $F = [F_1 \ F_2 \ F_3]^T$, $M = [M_1 \ M_2 \ M_3]^T$, $\gamma = [\gamma_{11} \ 2\gamma_{12} \ 2\gamma_{13}]^T$ and $\kappa = [\kappa_1 \ \kappa_2 \ \kappa_3]^T$ as shown. Apart from this, one also obtains the 6×6 inertia matrix $[I]$ from the cross-sectional analysis as part of the Eq. (C.46) which is written as

$$\begin{Bmatrix} P \\ H \end{Bmatrix} = [I] \begin{Bmatrix} V \\ \Omega \end{Bmatrix} \quad (\text{C.46})$$

C.2 1-D Beam Analysis with GEBT

GEBT is based on a mixed formulation. The variational statement in Eq. C.1, after substituting values for \mathcal{K} , \mathcal{U} and $\overline{\delta\mathcal{W}}$ from Ref. [133], is rewritten as a variational statement in the mixed formulation in Eq. C.47.

$$\begin{aligned} & \int_{t_1}^{t_2} \int_0^l \left\{ \left(\overline{\delta\dot{q}} + \tilde{\Omega}\overline{\delta q} + \tilde{V}\overline{\delta\psi} \right) P + \left(\overline{\delta\dot{\psi}} + \tilde{\Omega}\overline{\delta\psi} \right) H - \left(\overline{\delta q}' + \tilde{K}\overline{\delta q} + (\tilde{e}_1 + \tilde{\gamma})\overline{\delta\psi} \right) F \right. \\ & \left. - \left(\overline{\delta\psi}' + \tilde{K}\overline{\delta\psi} \right) M + \overline{\delta q}^T f + \overline{\delta\psi}^T m \right\} dx_1 dt = \int_0^l \left(\overline{\delta q}^T \hat{P} + \overline{\delta\psi}^T \hat{H} \right) \Big|_{t_1}^{t_2} dx_1 \\ & - \int_{t_1}^{t_2} \left(\overline{\delta q}^T \hat{F} + \overline{\delta\psi}^T \hat{M} \right) \Big|_0^l dt \end{aligned} \quad (\text{C.47})$$

To proceed, the constitutive law from Eq. C.45 and the momentum-velocity relations containing the mass-matrix from Eq. C.46 are required. Further, to derive the mixed formu-

lation, the kinematic differential relations in Eq. C.48 are incorporated into the variational statement in Eq. C.47 with the help of Lagrange multipliers and using the calculus of variations.

$$u' = C^{bB}(e_1 + \gamma) - e_1 - \tilde{k}u \quad (\text{C.48a})$$

$$\dot{u} = C^{bB}V - v - \tilde{\omega}u \quad (\text{C.48b})$$

$$c' = Q^{-1}(\kappa + k - C^{bB}k) \quad (\text{C.48c})$$

$$\dot{c} = Q^{-1}(\Omega - C^{bB})\omega \quad (\text{C.48d})$$

where Q is a set of Wiener-Milenković rotation parameters defined in Ref [217]. Following Wang [217], after identifying Lagrange multipliers associated with the kinematic differential equations in C.48, one obtains

$$\begin{aligned} & \int_0^l \left\{ \delta u_a'^T F_a + \overline{\delta \psi}_a'^T M_a + \delta u_a^T (\dot{P}_a + \tilde{\omega}_a P_a) + \overline{\delta \psi}_a^T \left[\dot{H}_a + \tilde{\omega}_a H_a + \tilde{V}_a P_a - C^{aB}(\tilde{e}_1 + \tilde{\gamma}) F_B \right] \right. \\ & - \overline{\delta F}_a^T \left[C^{aB}(e_1 + \gamma) - C^{ab}e_1 \right] - \overline{\delta F}_a'^T u_a - \overline{\delta M}_a'^T c_a - \overline{\delta M}_a^T Q_a^{-1} C^{ab} \kappa \\ & \left. + \overline{\delta P}_a^T (-\dot{u}_a + V_a - v_a - \tilde{\omega}_a u_a) + \overline{\delta H}_a^T (\Omega_B - \omega_B - C^{ba} Q_a \dot{c}_a) - \delta u_a^T f_a - \overline{\delta \psi}_a^T m_a \right\} dx_1 = \\ & \left(\delta u_a^T \hat{F}_a + \overline{\delta \psi}_a^T \hat{M}_a - \overline{\delta F}_a^T \hat{u}_a - \overline{\delta M}_a^T \hat{c}_a \right) \Big|_0^l \end{aligned} \quad (\text{C.49})$$

The variational statement in Eq. C.49 is further treated using a suitable 1-D finite element discretization. Following Ref. [133], the system of equations, thus formed, is solved using the Newton-Raphson method along with a line search algorithm to ensure global convergence. Hence, solutions for the beam 1-D displacement variables are obtained.

APPENDIX D

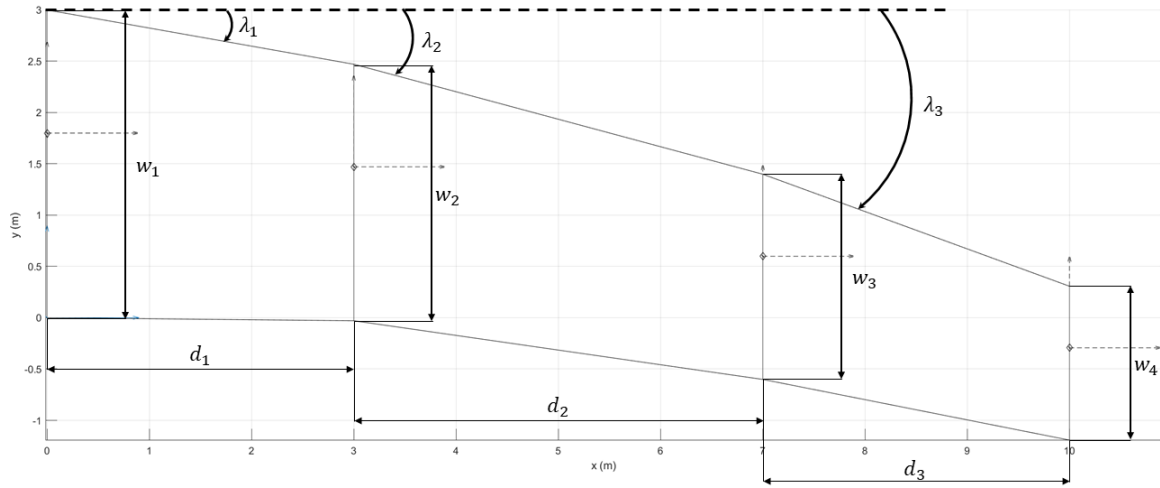
DESCRIPTION OF TEST CASE GEOMETRIES

In this appendix, the baseline geometries used as test cases in this paper are described. Three geometries are considered- a ‘Wing-Like’ Box Beam, the PEGASUS concept aircraft, and the Common Research Model (CRM). Details of the geometric parametrization, baseline values, load application mechanism, and 3-D views of the structure are shown.

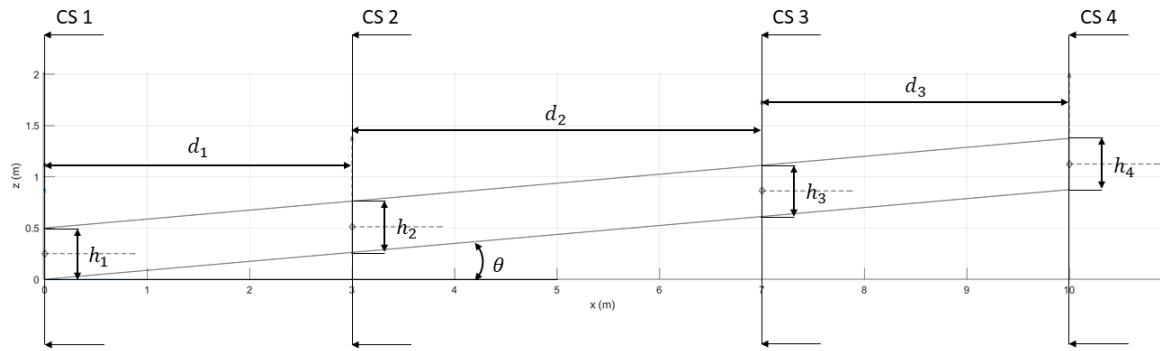
D.1 ‘Wing-Like’ Box Beam

The parametrization of the box beam is shown in Fig. D.1. It consists of four cross-sections and three trapezoidal sections. Each cross-section i is rectangular in shape with h_i and w_i as the width and height respectively. The spar and skin thicknesses are denoted by t_i and b_i , respectively. Three sweep angles, λ_1 , λ_2 , and λ_3 are used for each of the sections. A single dihedral angle, θ is used.

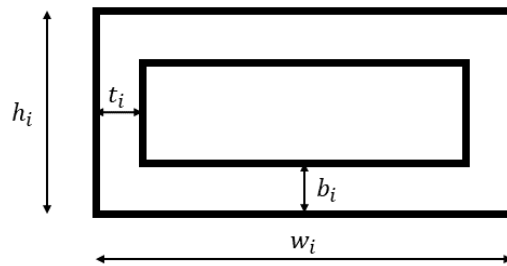
From the parametrization described above, five structures were created as shown in Fig. D.2. The structures are chosen so as to test different aspects of an aircraft wing planform. The simplest is that of a prismatic beam, shown in Fig. D.2a. Fig D.2b is a geometry where the cross-section of the beam is tapered from root to tip. Sweep and dihedral cases are shown in Fig. D.2c and Fig. D.2d respectively. Fig. D.2e shows the most complex geometry which combines taper, sweep and dihedral to generate a structure resembling that of an aircraft wing. The distance between the cross-sections- d_1 , d_2 , and d_3 , and the heights of the cross-sections- h_1 , h_2 , h_3 , and h_4 are held constant for all five geometries. The values are given in Table D.1. The dimensions of the widths of the cross-section- w_1 , w_2 , w_3 , and w_4 , sweep angles- λ_1 , λ_2 , λ_3 , and dihedral angle- θ differ for the five geometries. The values are shown in Table D.2.



(a) Top view

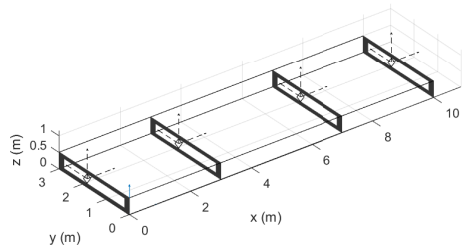


(b) Side view

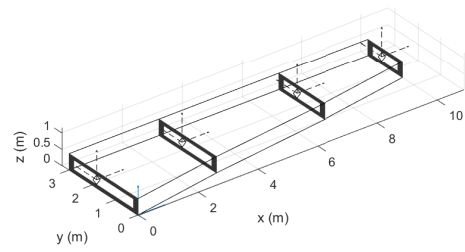


(c) Cross-section i

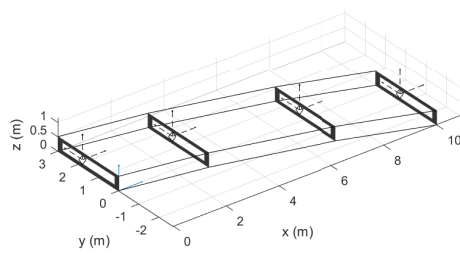
Figure D.1: Box beam geometry parametrization



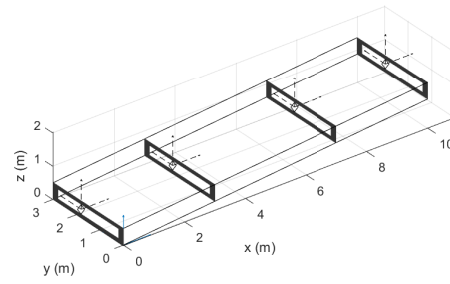
(a) Prismatic



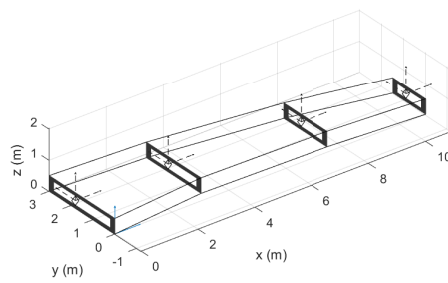
(b) Taper-only



(c) Sweep-only



(d) Dihedral-only



(e) Combined taper, sweep and dihedral

Figure D.2: Box beam geometries considered

Table D.1: Dimensions held constant for all five geometries shown in Fig. D.2

d_1	d_1	d_1		
3 m	4 m	3 m		
h_1	h_2	h_3	h_4	
0.5 m	0.5 m	0.5 m	0.5 m	

Table D.2: Dimensions varied for the five geometries shown in Fig. D.2

Parameter	Prismatic	Taper-only	Sweep-only	Dihedral-only	Combined
w_1 (m)	3	3	3	3	3
w_2 (m)	3	2.5	3	3	2.5
w_3 (m)	3	2	3	3	2
w_4 (m)	3	1.5	3	3	1.5
λ_1 (deg)	0	0	10	0	10
λ_2 (deg)	0	0	15	0	15
λ_3 (deg)	0	0	20	0	20
θ (deg)	0	0	0	5	5

D.2 PEGASUS Concept Aircraft

The geometry manager used in this work is facilitated through the Rapid Airframe Design Environment (RADE) toolkit [188], developed at the Aerospace Systems Design Laboratory (ASDL). RADE contains a module for parametric variation of a baseline OML through the OpenVSP API, where aerodynamic shape variables such as span, sweep, chord, area, aspect ratio, twist, among others can be defined. The OpenVSP model for the Pegasus wing is shown in Fig. D.3. The PEGASUS wing baseline OML variable values and flight conditions are shown in Table D.3.

Once the OML is defined, RADE has an automated capability to create a structural topology within the bounds of the OML. This is also a parametric implementation, and RADE has a library of various topological categories, each with its own set of parameters.

Table D.3: Baseline OML & flight condition values for PEGASUS aircraft

Parameter	Value	Unit
Planform area	586.33280	<i>ft</i> ²
Span	80.58962	<i>ft</i>
Aspect ratio	11.0596	-
Taper ratio	0.986	-
TOGW	41005	<i>lbs</i>
Altitude	20000	<i>ft</i>
Mach number	0.5	-

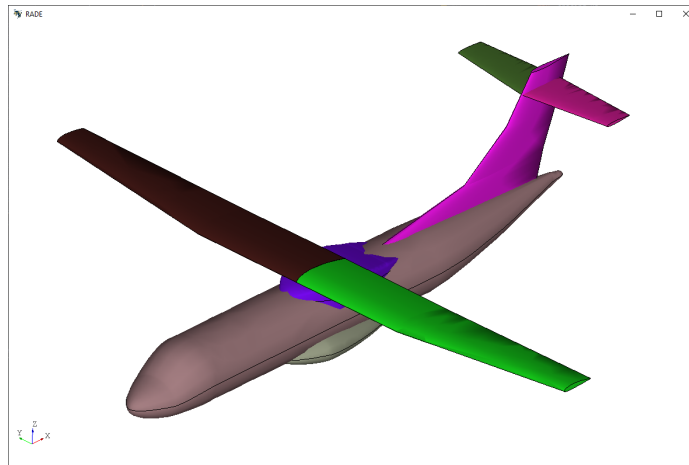


Figure D.3: OpenVSP model of the PEGASUS aircraft

The RADE structural geometry module then organizes the spars, ribs, and skin parts into an assembly hierarchy, in which various definitions can be made for the discretization of surfaces to set up material and sectional properties. A structural mesh can also be created automatically with definitions supplied by the user, including desired mesh size, growth rates, curvature rules, and element types. The structural topology variable values are shown in Table D.4.

Fig. D.4 show a wireframe view of the PEGASUS wingbox. The wingbox is divided into two portions:

1. **Center wingbox:** This portion of the wingbox extends from the intersection of the

Table D.4: Baseline structural topology values

Parameter	Value	Unit
Front spar chord normalized loc	0.18	-
Rear spar chord normalized loc	0.75	-
Rib spacing	28	in
Rib roll	0	deg
Rib yaw	0	deg
Root rib span normalized loc	0.08	-
Tip rib span normalized loc	0.995	-

fuselage outer skin to the symmetry plane at the center of the fuselage.

2. **Main wingbox:** The portion of the wingbox inside the wing from the root rib to the tip rib

For the chosen rib spacing of 28 inches, there are 18 ribs. Wingbox stations are numbered from 0 to 19, with 0 being the symmetry plane, 1 the root rib, and 19 the tip rib. The chosen front and rear spar normalized locations give a wingbox whose size compared to the wing OML are shown in Fig. D.5.

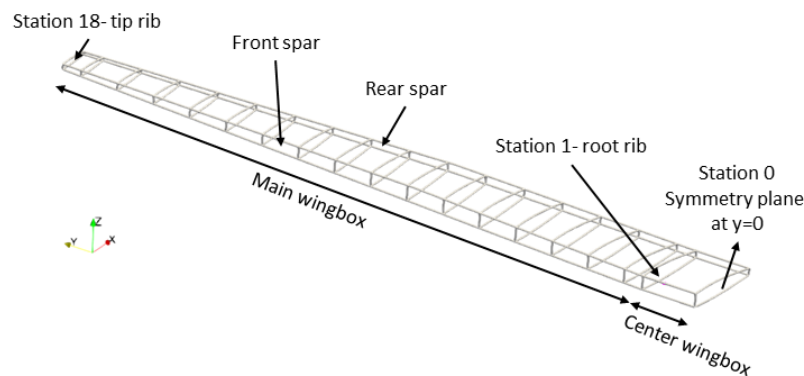


Figure D.4: Wireframe view of the PEGASUS wingbox

RADE sets up a series of nodes along the CG of each rib. These nodes are the load application points. Point forces and moments are applied along these nodes and transferred

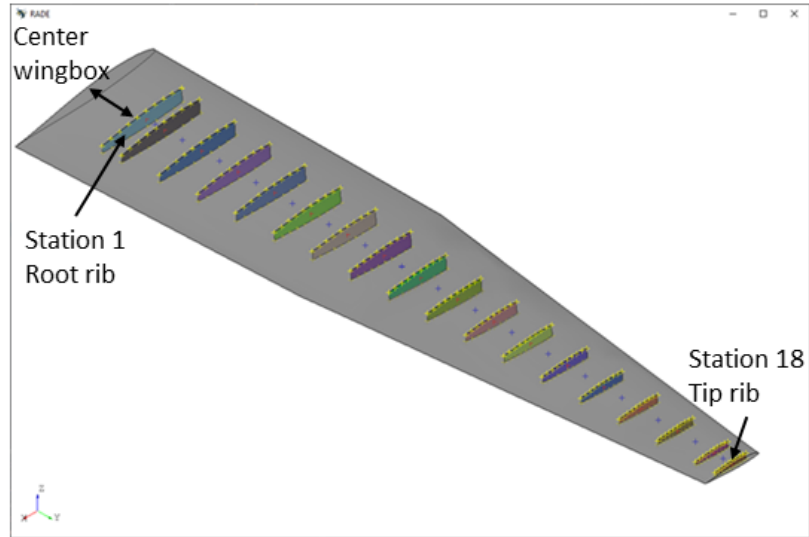


Figure D.5: Wing OML and ribs view of the PEGASUS wingbox

to the skin, spars and ribs through RBE3 elements. This is shown in Fig. D.6a. As in the shell model with ribs, in the shell model where the ribs have been removed a series of nodes are created on a 1-D line connecting the CGs of the cross-sections. The loads are applied at these nodes and distributed via RBE3 elements to the skin and spar. This is shown in Fig. D.6b.

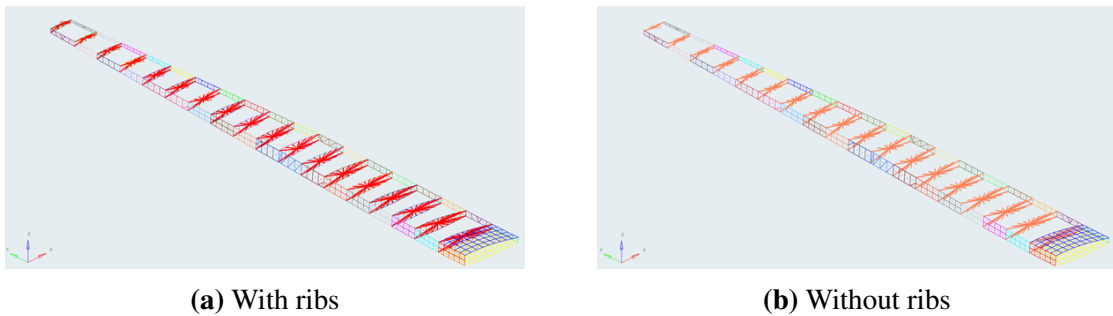


Figure D.6: PEGASUS concept wing shell models

Finally, RADE also creates an AVL model to compute aerodynamic loads. Fig. D.7 shows the AVL model for the PEGASUS aircraft. The fuselage is treated as a cruciform. The four electric engines on the wings are neglected in the AVL model.

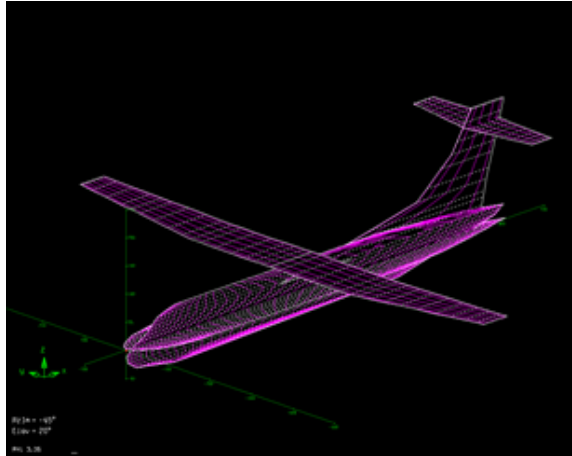


Figure D.7: AVL model of the PEGASUS aircraft

D.3 Common Research Model (CRM) Aircraft

The RADE toolkit is used to generate the 3-D structural representation of the Common Research Model (CRM) wing as well. The CRM is an “open-source configuration based on a transonic transport configuration designed to fly at a cruise Mach number of $M=0.85$ with a nominal lift condition of $CL=0.50$, and at a Reynolds number of $Rn=40$ million per reference chord”. Fig. D.8 shows structural geometry layout and mesh for the wing, horizontal tail, and vertical tail within a fused representation of the OML. The baseline OML, structural topology variables of the CRM wing are given in Table D.5 and Table D.6.

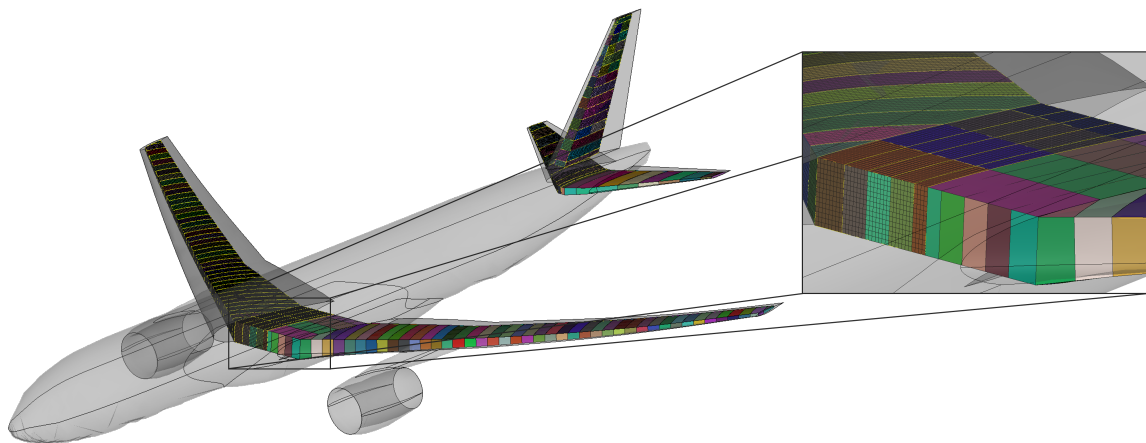


Figure D.8: Geometry and mesh of mesh of wing and empennage of the CRM

Table D.5: Baseline OML & flight condition values

Parameter	Value	Unit
Planform area	4444.38127	<i>ft</i> ²
Span	193.34768	<i>ft</i>
Aspect ratio	8.3325	-
Taper ratio	0.86031	-
Leading edge sweep	37	<i>deg</i>
TOGW	650000	<i>lbs</i>
Altitude	30000	<i>ft</i>
Mach number	0.8	-

Table D.6: Baseline structural topology values

Parameter	Value	Unit
Front spar chord normalized loc	0.17	-
Rear spar chord normalized loc	0.68	-
Rib spacing	32	in
Rib roll	0	deg
Rib yaw	-10	deg
Root rib span normalized loc	0.1	-
Tip rib span normalized loc	0.995	-

APPENDIX E

1-D ANALYSIS IMPLEMENTATION VERIFICATION AND VALIDATION

The nonlinear Timoshenko beam theory described in Appendix A was implemented in Matlab. This appendix provides verification and validation cases for the implementation.

E.1 Comparison to known Analytical Formulae

The code was first validated using simple static load conditions for which analytical solutions exist. Table E.1 shows the analytical cases considered and Fig. E.1 the error.

Table E.1: Analytical test cases to validate beam code

Case	Loading	Deflection Analytical Formula
Self-weight	$q = \rho A(\text{beam span})$	$\delta = \frac{qL^4}{8EI}$
Concentrated load	Tip load F	$\delta = \frac{FL^3}{3EI}$
Concentrated moment	Tip moment M	$\delta = \frac{ML^2}{2EI}$
Uniformly distributed load	UDL q	$\delta = \frac{qL^4}{8EI}$
Uniformly varying load	UVL q	$\delta = \frac{qL^4}{30EI}$

A dynamic simulation was performed where the structure was initialized at the jig shape and subjected to gravity. As seen in Fig. E.2, the simulation reaches steady-state at the self-weight solution. At time 7.5 seconds, the model was then subjected to a free-fall which should simulate weightlessness. As seen, the simulation reaches steady-state back at the jig shape.

E.2 Representative Business Jet

Next, a representative business jet was represented as a stickmodel as shown in Fig. E.3a. The tip displacement and leading edge up rotation for the wing was validated with data

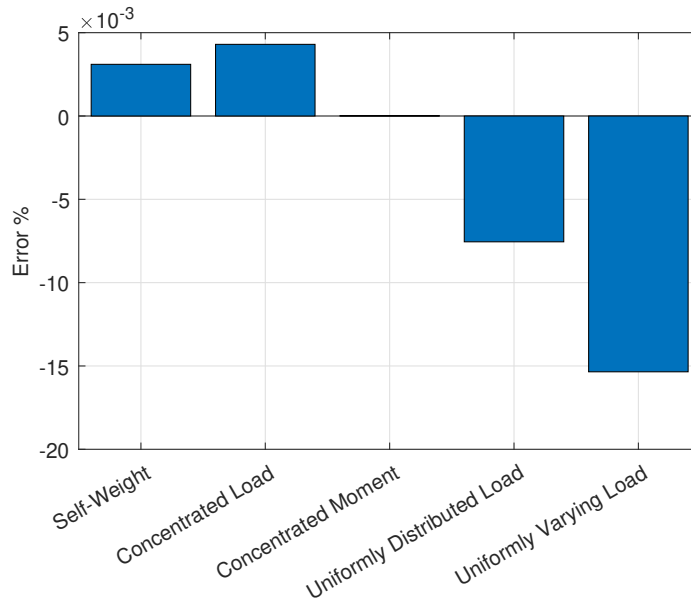


Figure E.1: Error between implemented code and known analytical solution for static loads

provided by a business jet manufacturer, as seen in Fig. E.3b. Note, the axes have been normalized to protect proprietary data.

E.3 ‘Wing-Like’ Box Beam

Next, a wing-like structure is used. Section D.1 describes the parametrization of the structure used to validate the code. The results from the beam code were compared against those from 3-D solid elements FEM model.

In this validation study, the thicknesses of the spars- $t_1, t_2, t_3,$ and $t_4,$ and the thicknesses of the skin- $b_1, b_2, b_3,$ and b_4 are held constant to values shown in Table E.2. Fig. D.2 shows the five geometries considered.

Table E.2: Thicknesses of spars and skin for validation study

t_1	t_1	t_1	t_1
0.2 m	0.2 m	0.2 m	0.2 m
b_1	b_1	b_1	b_1
0.1 m	0.1 m	0.1 m	0.1 m

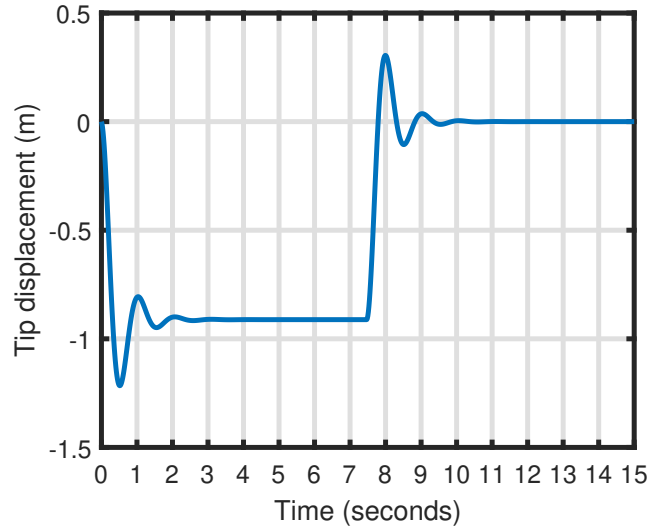


Figure E.2: Dynamic simulation. At 0 seconds, gravity is turned on. At 7.5 seconds, the beam let into free-fall.

The geometries are created with 3-D solid elements, with the mesh having about 200,000 elements. A fixed boundary condition is used at one end, and tip loads are applied at the other end. The average displacements over cross-sections 2, 3, and 4 are measured in 3-D FEM, and compared against the beam axis displacements. The values are shown in Table E.3 for three loading conditions.

Table E.3: Comparison of displacements (m) for validation study

	Loading (N)		Prismatic		Taper-only		Sweep-only		Dihedral-only		Combined	
			3-D FEM	Beam	3-D FEM	Beam	3-D FEM	Beam	3-D FEM	Beam	3-D FEM	Beam
Case 1	Fx 0	CS2	0.025139	0.0229	0.025967	0.024538	0.0268	0.025119	0.025448	0.022894	0.026579	0.024502
	Fy 0	CS3	0.10974	0.1058	0.12195	0.120345	0.1213	0.120572	0.11108	0.105869	0.12873	0.125516
	Fz 1.00E+06	CS4	0.19627	0.1876	0.22239	0.220482	0.22173	0.219244	0.19858	0.187801	0.23837	0.234978
Case 2	Fx 0	CS2	0.12853	0.113618	0.13218	0.12191	0.13705	0.124094	0.12919	0.112809	0.1339	0.12122
	Fy -1.00E+06	CS3	0.56642	0.524786	0.62145	0.596382	0.62462	0.593538	0.56729	0.51973	0.64476	0.611695
	Fz 5.00E+06	CS4	1.0099	0.930288	1.1289	1.091077	1.1361	1.077246	1.0097	0.920347	1.1854	1.137097
Case 3	Fx 0	CS2	0.29563	0.223217	0.29589	0.237945	0.31535	0.242789	0.29187	0.21942	0.29318	0.234073
	Fy -1.00E+06	CS3	1.324	1.025793	1.3628	1.155278	1.4569	1.153865	1.2949	1.003472	1.3768	1.167504
	Fz 1.00E+07	CS4	2.3168	1.813536	2.4269	2.103945	2.5931	2.086705	2.2597	1.770524	2.4759	2.155846

Case 1 loading is such that the stresses in the structure are below the yield stress. For case 2, the loads produce stress slightly higher than the yield stress, while case 3 produces stresses far above yield. It is seen in Fig. E.4 that for case 1, the error is less than 5%, which is acceptable given the time-saving benefits of the beam code as compared to 3-D

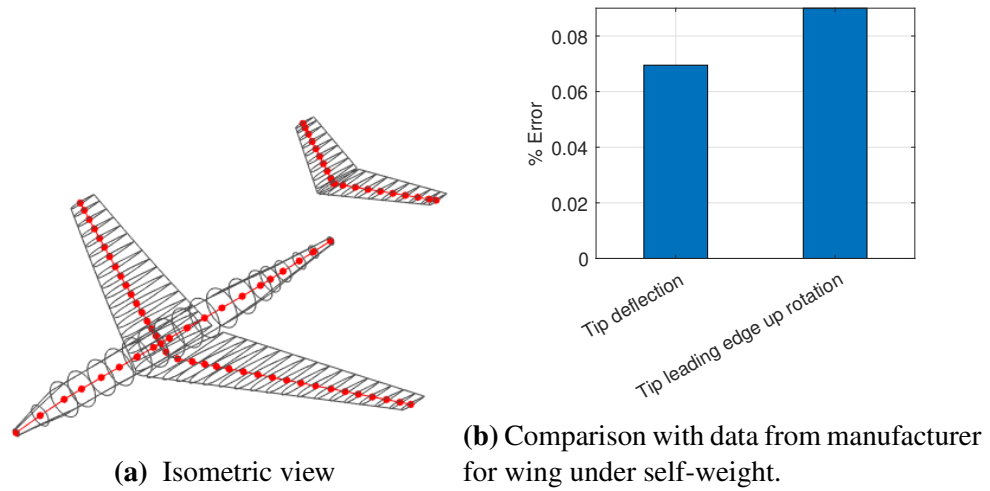


Figure E.3: Representative business jet simulation

solid element FEM. For case 2 and case 3, the error is higher. This is to be expected as beam theory assumes small strains. The strains produced by the loading of case 2 and case 3 is large, and the stresses are beyond the yield stress. For design-optimization, the stresses in the structure will be constrained to be below the yield stress. Hence, the results of case 1 show the beam code to be adequate for optimization.

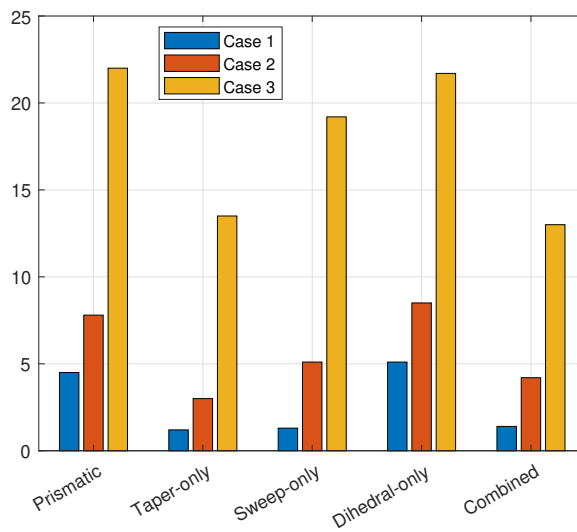


Figure E.4: Percentage error of displacements for validation study

APPENDIX F

CROSS-SECTIONAL PROPERTIES OF A BOX-BEAM

F.1 Objective Function

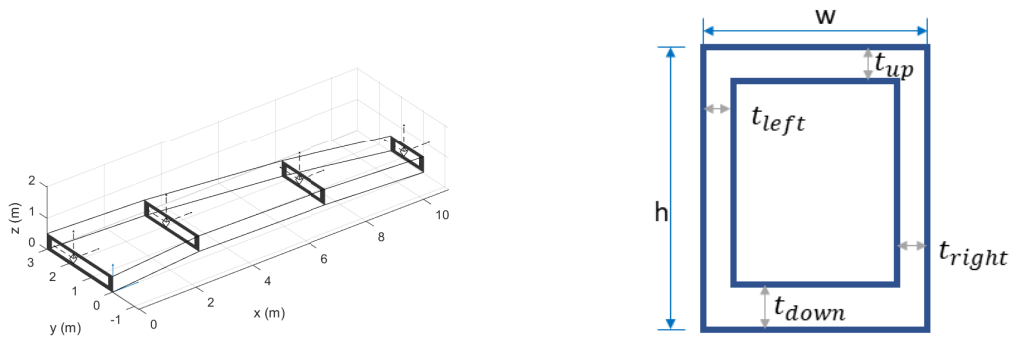
The objective function has been adjusted as the total wing weight, which is given by the following equations:

$$f_m = \sum_{i=1}^{n-1} m_i$$

$$m_i = \rho \cdot V_i \longrightarrow V_i = \frac{1}{3} \cdot s_i \cdot (A_{i+1} + A_i + \sqrt{A_i \cdot A_{i+1}})$$

F.2 Box-Beam Cross-Sectional Properties Computation

Consider a box cross-section beam such as seen in Fig. F.1a. The geometry has typical aircraft wing planform features such as taper, dihedral, and sweep. Each cross-section is a hollow rectangle.



(a) ‘Wing-like’ geometry used in this work

(b) Rectangular box cross-section assumption and parameters

Figure F.1: Wingbox and cross-section

In general, the beam axis can be chosen to be at any location within the cross-section. This makes the beam axis location potentially different from the elastic axis, the tension

axis, and the geometric CG, as shown in Fig. A.2. The design variables of each box cross-section i of the beam are shown in Fig. F.1b and can be defined by the following quantities:

- h_i : height
- w_i : width
- $t_{top,i}$: top thickness
- $t_{bot,i}$: bottom thickness
- $t_{right,i}$: right thickness
- $t_{left,i}$: left thickness

The moment/curvature stiffness submatrix, Eq. A.6, used in the equations defined in Section A are about the local beam csn frame. We first compute the cross-sectional properties about the inertial XYZ frame and then transform it to the local csn frame.

We use the notation $(-)_{j,i}$ to denote a property at cross-sectional i and component j can be top, left, bottom, or right corresponding to 1, 2, 3, or 4 respectively. The area of the cross-section in inertial XYZ frame is given by:

$$A_i = A_{1,i} + A_{2,i} + A_{3,i} + A_{4,i} \quad (\text{F.1})$$

where

$$A_{1,i} = t_{top,i} \cdot w_i \quad (\text{F.2})$$

$$A_{2,i} = t_{left,i} \cdot (h_i - t_{top,i} - t_{bot,i}) \quad (\text{F.3})$$

$$A_{3,i} = t_{bot,i} \cdot w_i \quad (\text{F.4})$$

$$A_{4,i} = t_{right,i} \cdot (h_i - t_{top,i} - t_{bot,i}) \quad (\text{F.5})$$

The area moments of inertia in the inertial XYZ frame are given by:

$$I_{xx,i} = \sum_{j=1}^4 I_{xx,j,i} + A_i \cdot (x_{i,j,x} - c_{ea,x,i})^2 \quad (\text{F.6})$$

$$I_{zz,i} = \sum_{j=1}^4 I_{zz,j,i} + A_i \cdot (x_{i,j,z} - n_{ea,z,i})^2 \quad (\text{F.7})$$

$$I_{xz,i} = \sum_{j=1}^4 -A_i \cdot (x_{i,j,z} - n_{ea,z,i}) \cdot (x_{i,j,x} - c_{ea,x,i}) \quad (\text{F.8})$$

where the terms of the top flange are given by:

$$I_{xx,1,i} = \frac{w_i \cdot t_{top,i}^3}{12} \quad (\text{F.9})$$

$$I_{zz,1,i} = \frac{w_i^3 \cdot t_{top,i}}{12} \quad (\text{F.10})$$

$$x_{i,1,z} = \frac{h_i - t_{top,i}}{2} \quad (\text{F.11})$$

$$x_{i,1,x} = 0 \quad (\text{F.12})$$

The terms of the left web are given by

$$I_{xx,2,i} = \frac{t_{left,i} \cdot (h_i - t_{top,i} - t_{bot,i})^3}{12} \quad (\text{F.13})$$

$$I_{zz,2,i} = \frac{t_{left,i}^3 \cdot (h_i - t_{top,i} - t_{bot,i})}{12} \quad (\text{F.14})$$

$$x_{i,2,z} = \frac{h}{2} - t_{top,i} - \frac{h_i - t_{top,i} - t_{bot,i}}{2} \quad (\text{F.15})$$

$$x_{i,2,x} = \frac{t_{left,i} - w_i}{2} \quad (\text{F.16})$$

The terms of the bottom flange are given by

$$I_{xx,3,i} = \frac{w_i \cdot t_{bot,i}^3}{12} \quad (F.17)$$

$$I_{zz,3,i} = \frac{w_i^3 \cdot t_{bot,i}}{12} \quad (F.18)$$

$$x_{i,3,z} = \frac{t_{bot,i} - h_i}{2} \quad (F.19)$$

$$x_{i,3,x} = 0 \quad (F.20)$$

The terms of the right web are given by

$$I_{xx,4,i} = \frac{t_{right,i} \cdot (h_i - t_{top,i} - t_{bot,i})^3}{12} \quad (F.21)$$

$$I_{zz,4,i} = \frac{t_{right,i}^3 \cdot (h_i - t_{top,i} - t_{bot,i})}{12} \quad (F.22)$$

$$x_{i,4,z} = \frac{h}{2} - t_{top,i} - \frac{h_i - t_{top,i} - t_{bot,i}}{2} \quad (F.23)$$

$$x_{i,4,x} = \frac{w_i - t_{right,i}}{2} \quad (F.24)$$

The modulus weighted centroid is used to compute the elastic axis, and feeds into Eq. A.1.

We make the assumption here that the tension axis coincides with the beam axis.

$$c_{ea,x,i} = \frac{\sum_{j=1}^4 A_j \cdot E_j \cdot x_{i,j,x}}{\sum_{j=1}^4 A_j \cdot E_j} \quad (F.25)$$

$$n_{ea,z,i} = \frac{\sum_{j=1}^4 A_j \cdot E_j \cdot x_{i,j,z}}{\sum_{j=1}^4 A_j \cdot E_j} \quad (F.26)$$

$$c_{ta,x,i} = 0 \quad (F.27)$$

$$n_{ta,z,i} = 0 \quad (F.28)$$

The torsional stiffness is given by:

$$J_i = \frac{2 \cdot \left((h_i - \frac{t_{top,i}}{2} - \frac{t_{bot,i}}{2}) \cdot (w_i - \frac{t_{right,i}}{2} - \frac{t_{left,i}}{2}) \right)^2}{\left(\frac{(w_i - \frac{t_{right,i}}{2} - \frac{t_{left,i}}{2})}{(\frac{t_{top,i}}{2} + \frac{t_{bot,i}}{2})} + \frac{((h_i - \frac{t_{top,i}}{2} - \frac{t_{bot,i}}{2})}{(\frac{t_{right,i}}{2} + \frac{t_{left,i}}{2})}) \right)} \quad (F.29)$$

The moment/curvature stiffness submatrix in the inertial XYZ frame is given by

$$\underline{\underline{EI_{XYZ,i}}} = \begin{bmatrix} E_i \cdot I_{xx,i} & 0 & E_i \cdot I_{xz,i} \\ 0 & G_i \cdot J_i & 0 \\ E_i \cdot I_{xz,i} & 0 & E_i \cdot I_{zz,i} \end{bmatrix} \quad (\text{F.30})$$

It is transformed into the local csn frame to be used in Eq. A.6 as

$$\underline{\underline{EI_{csn}}} = [T] \underline{\underline{EI_{XYZ}}} [T]^T \quad (\text{F.31})$$

For shear stress computation, the stiffness is given by:

$$\begin{aligned} Q_{x,i} = & w_i \cdot t_{top,i} \cdot \left(\frac{h_i}{2} - n_{ea,z,i} - \frac{t_{top,i}}{2} \right) \\ & + \frac{1}{2} \cdot t_{right,i} \cdot \left(\frac{h_i}{2} - n_{ea,z,i} - t_{top,i} \right)^2 \\ & + \frac{1}{2} \cdot t_{left,i} \cdot \left(\frac{h_i}{2} - n_{ea,z,i} - t_{top,i} \right)^2 \end{aligned} \quad (\text{F.32})$$

$$\begin{aligned} Q_{z,i} = & h_i \cdot t_{left,i} \cdot \left(\frac{w_i}{2} - c_{ea,x,i} - \frac{t_{left,i}}{2} \right) \\ & + \frac{1}{2} \cdot t_{top,i} \cdot \left(\frac{w_i}{2} - c_{ea,x,i} - t_{left,i} \right)^2 \\ & + \frac{1}{2} \cdot t_{bot,i} \cdot \left(\frac{w_i}{2} - c_{ea,x,i} - t_{left,i} \right)^2 \end{aligned} \quad (\text{F.33})$$

The center of gravity of the cross-section feeds into Eq. A.17 and is given by:

$$r_{cg,c,i} = \frac{\sum_{j=1}^4 A_j \cdot \rho_j \cdot x_{i,j,x}}{\sum_{j=1}^4 A_j \cdot \rho_j} \quad (\text{F.34})$$

$$r_{cg,n,i} = \frac{\sum_{i=1}^4 A_i \cdot \rho_i \cdot x_{i,j,z}}{\sum_{j=1}^4 A_j \cdot \rho_j} \quad (\text{F.35})$$

APPENDIX G
GRADIENT OF STRESS CONSTRAINTS USING SYMBOLIC
DIFFERENTIATION

Fig. G.1 explains the process in a DSM format. Table. G.1 shows the symbolic quantities used as independent variables for the equations formulated.

Table G.1: Symbolic variables used in the formulation for automatic differentiation

Variable	Variable Function
$\tilde{x}_{sim} \in \mathbb{R}^{[18 \cdot n \times t]}$	State vector history
$\tilde{c}_{sdv} \in \mathbb{R}^{[4 \times n]}$	Cross-Section design variables
$\tilde{c}_p \in \mathbb{R}^{[4 \times 2 \times n]}$	Corner point locations in the csn axis
$\tilde{m} \in \mathbb{R}$	Maximum stress found
$\tilde{x}_{slice} \in \mathbb{R}^{[18 \cdot n]}$	Slice of state at a given time
$\tilde{x}_{dotslice} \in \mathbb{R}^{[18 \cdot n]}$	Slice of state derivatives at a given time
$\tilde{F} \in \mathbb{R}^{[3 \times n - 1]}$	External point forces acting on the beam
$\tilde{M} \in \mathbb{R}^{[3 \times n - 1]}$	External point moments acting on the beam
$\tilde{F}_c \in \mathbb{R}^{[3 \times n - 1]}$	External distributed forces acting on the beam
$\tilde{M}_c \in \mathbb{R}^{[3 \times n - 1]}$	External distributed moments acting on the beam

Based on these different symbolic variables, geometric characteristics, and materials,

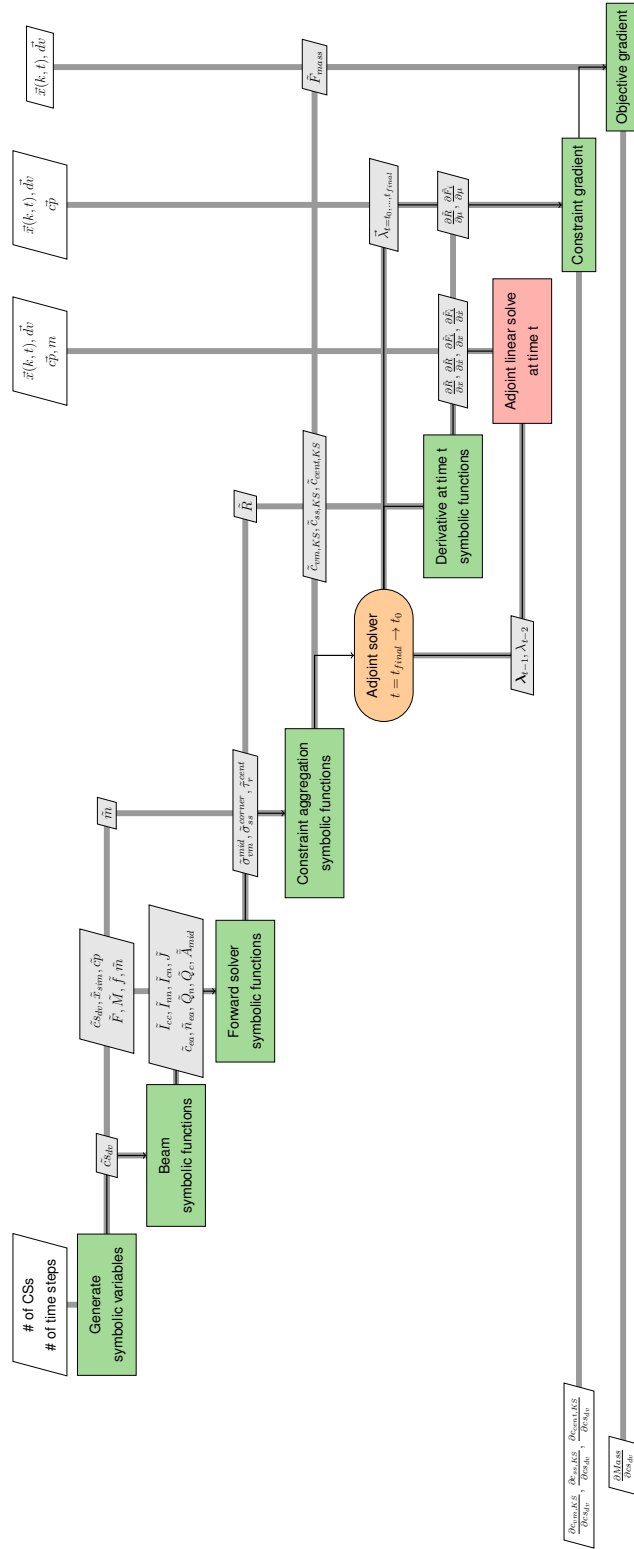


Figure G.1: XDSM for gradient computation using automatic differentiation and adjoint method

more complex functions $f_s()$ can be constructed, first at the beam level, following the mathematical expressions directly, as seen in Table. G.2.

Table G.2: Symbolic Functions at the Beam Level

Quantity	Function Reference
$c_{ea}, n_{ea} \equiv f_s(\tilde{cS}_{dv})$	Location of elastic axis with respect to geometric center
$I_{cc}, I_{cn}, I_{nn}, J \equiv f_s(\tilde{cS}_{dv})$	Cross-section second moments of inertia
$Q_n, Q_c \equiv f_s(\tilde{cS}_{dv})$	First moments of inertia
$A_{mid}^- \equiv f_s(\tilde{cS}_{dv})$	Mid cross-sectional areas

While its true that each of the preceding terms also used other variables such as rotations and translations $\vec{r}, \vec{\theta}$ and material properties E, G , those are fixed after the equations are defined, and no derivatives with respect to such quantities are calculated for the specific analysis performed.

From the equations obtained at the beam level, the stress and residual equations are constructed at the stick model level, as seen in Table. G.3.

Table G.3: Symbolic Functions at the Stick Model Level

Quantity	Function Reference
$\mathbf{R} \equiv f_s(\tilde{cS}_{dv}, \tilde{x}_{slice}, \tilde{x}_{dot\,slice}, \tilde{F}, \tilde{M}, \tilde{F}_c, \tilde{M}_c)$	Main residual equations for the stick model
$\sigma_{vmk,j,t}^{mid} \equiv f_s(I_{cc}, I_{nn}, J, c_{ea}, n_{ea}, A_{mid}) \equiv f_s(\tilde{cS}_{dv}, \tilde{x}_{sim}, \tilde{c}p)$	Von-misses stress
$\sigma_{ssk,j,t}^{corner} \equiv f_s(I_{cc}, I_{cn}, I_{nn}, c_{ea}, n_{ea}) \equiv f_s(\tilde{cS}_{dv}, \tilde{x}_{sim}, \tilde{c}p)$	Axial stress
$\tau_{rk,j,t}^{cent} \equiv f_s(I_{cc}, I_{cn}, I_{nn}, J, A_{mid}, Q_n, Q_c, A_{mid}^-) \equiv f_s(\tilde{cS}_{dv}, \tilde{x}_{sim}, \tilde{c}p)$	Flange shear stress
$F_{mass} \equiv f_s(A_{mid}, A_{mid}^-) \equiv f_s(\tilde{cS}_{dv})$	Total stick model mass

Table G.4: Symbolic Functions for Constraint Aggregation

Quantity	Function Reference
$A_{vm} \equiv f_s(\sigma_{vmk,j,t}^{mid}, \tilde{m}) \equiv f_s(\tilde{c}s_{dv}, \tilde{x}_{sim}, \tilde{c}p, \tilde{m})$	Von-misses aggregated constraint summation term
$A_{ss} \equiv f_s(\sigma_{ssk,j,t}^{corner}, \tilde{m}) \equiv f_s(\tilde{c}s_{dv}, \tilde{x}_{sim}, \tilde{c}p, \tilde{m})$	Axial aggregated constraint summation term
$A_{cent} \equiv f_s(\tau_{rk,j,t}^{center}, \tilde{m}) \equiv f_s(\tilde{c}s_{dv}, \tilde{x}_{sim}, \tilde{c}p, \tilde{m})$	Flange shear aggregated constraint summation term
$c_{vm,KS} \equiv f_s(A_{vm}, \tilde{m}) \equiv f_s(\tilde{c}s_{dv}, \tilde{x}_{sim}, \tilde{c}p, \tilde{m})$	Von-misses aggregated constraint
$c_{ss,KS} \equiv f_s(A_{ss}, \tilde{m}) \equiv f_s(\tilde{c}s_{dv}, \tilde{x}_{sim}, \tilde{c}p, \tilde{m})$	Axial aggregated constraint
$c_{cent,KS} \equiv f_s(A_{cent}, \tilde{m}) \equiv f_s(\tilde{c}s_{dv}, \tilde{x}_{sim}, \tilde{c}p, \tilde{m})$	Flange shear aggregated constraint

Table G.5: Derivative functions for optimization

Quantity	Function Reference
$\left. \begin{array}{l} \frac{\partial \mathbf{R}}{\partial \mathbf{x}_i} \equiv \frac{d\mathbf{R}}{d\tilde{x}_{slice}} \\ \frac{\partial \mathbf{R}}{\partial \mathbf{cs}_i} \equiv \frac{d\mathbf{R}}{d\tilde{c}s_{dv}} \end{array} \right\} f_s(\tilde{c}s_{dv}, \tilde{x}_{sim}, \tilde{c}p, \tilde{m})$	Matrices of residual vectors
$\left. \begin{array}{l} \frac{\partial c_{vm,KS}}{\partial \mathbf{x}_i} \equiv \frac{dc_{vm,KS}}{d\tilde{x}_{slice}} \\ \frac{\partial c_{vm,KS}}{\partial \mathbf{cs}_i} \equiv \frac{dc_{vm,KS}}{d\tilde{c}s_{dv}} \end{array} \right\} f_s(\tilde{c}s_{dv}, \tilde{x}_{sim}, \tilde{c}p, \tilde{m})$	Derivative of aggregated von-Mises constraint
$\left. \begin{array}{l} \frac{\partial c_{ss,KS}}{\partial \mathbf{x}_i} \equiv \frac{dc_{ss,KS}}{d\tilde{x}_{slice}} \\ \frac{\partial c_{ss,KS}}{\partial \mathbf{cs}_i} \equiv \frac{dc_{ss,KS}}{d\tilde{c}s_{dv}} \end{array} \right\} f_s(\tilde{c}s_{dv}, \tilde{x}_{sim}, \tilde{c}p, \tilde{m})$	Derivative of aggregated axial constraint
$\left. \begin{array}{l} \frac{\partial c_{cent,KS}}{\partial \mathbf{x}_i} \equiv \frac{dc_{cent,KS}}{d\tilde{x}_{slice}} \\ \frac{\partial c_{cent,KS}}{\partial \mathbf{cs}_i} \equiv \frac{dc_{cent,KS}}{d\tilde{c}s_{dv}} \end{array} \right\} f_s(\tilde{c}s_{dv}, \tilde{x}_{sim}, \tilde{c}p, \tilde{m})$	Derivative of aggregated axial constraint
$\left. \frac{\partial F_{mass}}{\partial \mathbf{cs}_i} \equiv \frac{dF_{mass}}{d\tilde{c}s_{dv}} \right\} f_s(\tilde{c}s_{dv})$	Derivative of total stickmodel mass

From the stress functions, the aggregated constraint functions can then be constructed as seen in Table. G.4.

Equivalent constraints can be constructed for a slice of time if \tilde{x}_{sim} is substituted with \tilde{x}_{slice} . Once the equations have been constructed, CASADI can construct the direct derivatives of the functions with respect to the design variable of choice, resulting in the derivatives shown in Table. G.5.

The usage of the derivatives within the optimization algorithm follow the workflow observed in Fig. G.1 to generate the constraint function $[\vec{g}, \nabla g] = f(\tilde{c}s_{dv}, \tilde{c}p, model)$. For

the systems of constraints and the gradients, a sequence of analyses needs to be performed. All symbolic functions are stored in a *model* object that describes the structure being simulated and contains all the relevant constants and the time history of forces and moments that perturb the structure through time. The constraint function is meant to evaluate the wing structure's failure criteria, employing the expressions previously derived. As numerical inputs, it starts with some immediate value of the cross-section design variables $\vec{c}s_{dv}$, given during optimization, and the numerical locations where the stress is evaluated. The function will forward-solve each of the load cases independently and store the state history values.

Then, using the symbolic functions of stress and stress constraints, numerical values for \vec{g} can be obtained, which is a vector construction of the values obtained from the functions in Table. G.4. The resultant constraint vector has a size of 5 by the number of running load cases specified. For the calculation of the derivatives of the stress constraints with respect to the design variables, a backward adjoint solver is used to calculate the sensitivity of the stress constraints to the evolution of the state \vec{x}_{sim} and, in combination with the symbolic functions seen in Table G.5, ∇g is finally calculated. This gradient has a size of the length of \vec{g} by the length of $\vec{c}s_{dv}$. The user can enable or disable stress constraints to verify the optimization trends with respect to different types of stress.

REFERENCES

- [1] C Mares and N Ursache, “Aircraft ground structural testing,” *Encyclopedia of Aerospace Engineering*, vol. 1-16, 2014.
- [2] F. De Florio, *Airworthiness: an introduction to aircraft certification*. Elsevier, 2010.
- [3] “Aircraft accident report ntsb/aar-04/04,” National Transportation Safety Board, [Online; accessed 20 November 2020].
- [4] *Code of Federal Regulations, Title 14, Federal Aviation Regulations, Part 25 - Airworthiness Standards: Transport Category Airplanes*, Federal Aviation Administration, 2019.
- [5] “Certifying boeing’s airplanes,” The Boeing Company., 2020.
- [6] R. S. Lineberger and A. Hussain, “Program management in aerospace and defense; still late and over budget,” *Deloitte Development LLC, New York*, 2016.
- [7] T Captain, *Can we afford our own future? why A&D programs are late and over-budget — and what can be done to fix the problem*, 2009.
- [8] I. Dörfler and O. Baumann, “Learning from a drastic failure: The case of the Airbus A380 program,” *Industry and Innovation*, vol. 21, no. 3, pp. 197–214, 2014.
- [9] A. Naikal and A. Chua, “Airbus A380: A risk management framework,” PhD thesis, 2009.
- [10] D. Greising and J. Johnsson, “Behind boeing’s 787 delays,” *Chicago Tribune*, vol. 10, 2007.
- [11] Y. Zhao, “Why 787 slips were inevitable?” *Rutgers University, New York*, 2013.
- [12] A. Flaig, “Airbus A380: Solutions to the aerodynamic challenges of designing the world’s largest passenger aircraft,” Airbus, Hamburg, Tech. Rep., 2008.
- [13] W. L. Glende, “The Boeing 777: A look back,” in *AGARD CP*, AGARD, 1998.
- [14] R. Ruben Del, *Propulsion Technologies for Future Aircraft Generations: Clean, Lean, Quiet, and Green*. 2011.

- [15] G. Rozza, D. B. P. Huynh, and A. T. Patera, “Reduced basis approximation and a posteriori error estimation for affinely parametrized elliptic coercive partial differential equations,” *Archives of Computational Methods in Engineering*, vol. 15, no. 3, 2007.
- [16] Z. Lyu, Z. Xu, and J. Martins, “Benchmarking optimization algorithms for wing aerodynamic design optimization,” in *Proceedings of the 8th International Conference on Computational Fluid Dynamics, Chengdu, Sichuan, China*, Citeseer, vol. 11, 2014.
- [17] R. Dwight and Z.-H. Han, “Efficient uncertainty quantification using gradient-enhanced kriging,” in *50th AIAA/ASME/ASCE/AHS/ASC Structures, Structural Dynamics, and Materials Conference 17th AIAA/ASME/AHS Adaptive Structures Conference 11th AIAA No*, 2009, p. 2276.
- [18] M. A. Bouhleh and J. R. Martins, “Gradient-enhanced kriging for high-dimensional problems,” *Engineering with Computers*, vol. 35, no. 1, pp. 157–173, 2019.
- [19] I. Chakraborty, T. Nam, J. R. Gross, D. N. Mavris, J. A. Schetz, and R. K. Kapania, “Comparative assessment of strut-braced and truss-braced wing configurations using multidisciplinary design optimization,” *Journal of Aircraft*, vol. 52, no. 6, pp. 2009–2020, 2015.
- [20] M. Drela, “Development of the d8 transport configuration,” in *29th AIAA Applied Aerodynamics Conference*, 2011, p. 3970.
- [21] R. H. Liebeck, “Design of the blended wing body subsonic transport,” *Journal of aircraft*, vol. 41, no. 1, pp. 10–25, 2004.
- [22] W. Silva, E. Vartio, A. Shimko, R. Kvaternik, K. Eure, and R. Scott, “Development of aeroservoelastic analytical models and gust load alleviation control laws of a sensorcraft wind-tunnel model using measured data,” in *47th AIAA/ASME/ASCE/AHS/ASC Structures, Structural Dynamics, and Materials Conference 14th AIAA/ASME/AHS Adaptive Structures Conference 7th*, 2006, p. 1935.
- [23] D. Lucia, “The sensorcraft configurations: A non-linear aeroservoelastic challenge for aviation,” in *46th AIAA/ASME/ASCE/AHS/ASC Structures, Structural Dynamics and Materials Conference*, 2005, p. 1943.
- [24] T. E. Noll, J. M. Brown, M. E. Perez-Davis, S. D. Ishmael, G. C. Tiffany, and M. Gaier, “Investigation of the helios prototype aircraft mishap volume i mishap report,” *Downloaded on*, vol. 9, p. 2004, 2004.

- [25] M. J. Patil and D. H. Hodges, “On the importance of aerodynamic and structural geometrical nonlinearities in aeroelastic behavior of high-aspect-ratio wings,” *Journal of Fluids and Structures*, vol. 19, no. 7, pp. 905–915, 2004.
- [26] G. Schuhmacher, I. Murra, L. Wang, A. Laxander, O. O’Leary, and M. Herold, “Multidisciplinary design optimization of a regional aircraft wing box,” in *9th AIAA/ISSMO Symposium on Multidisciplinary Analysis and Optimization*, p. 5406.
- [27] T. Klimmek, “Parametric set-up of a structural model for fermat configuration aeroelastic and loads analysis,” *Journal of Aeroelasticity and Structural Dynamics*, vol. 3, no. 2, 2014.
- [28] W. R. Krüger and T. Klimmek, “Definition of a comprehensive loads process in the dlr project iloads,” 2016.
- [29] N. T. Nguyen, E. Ting, and S. Lebofsky, “Inertial force coupling to nonlinear aeroelasticity of flexible wing aircraft,” in *15th Dynamics Specialists Conference*, 2016, p. 1094.
- [30] M. Karpel, B. Moulin, L. Anguita, C. Maderuelo, and H. Climent, “Aeroservoelastic gust response analysis for the design of transport aircrafts,” in *45th AIAA/ASME /ASCE/AHS/ASC Structures, Structural Dynamics & Materials Conference*, 2004, p. 1592.
- [31] C. M. Shearer, “Coupled nonlinear flight dynamics, aeroelasticity, and control of very flexible aircraft,” 2006.
- [32] G. J. Kennedy and J. R. R. A. Martins, “A parallel aerostructural optimization framework for aircraft design studies,” *Structural and Multidisciplinary Optimization*, pp. 1–23, Jan. 1, 2014, published.
- [33] T. Führer, C. Willberg, S. Freund, and F. Heinecke, “Automated model generation and sizing of aircraft structures,” *Aircraft Engineering and Aerospace Technology: An International Journal*, 2016.
- [34] C. Werner-Westphal, W. Heinze, and P. Horst, “Multidisciplinary integrated preliminary design applied to unconventional aircraft configurations,” *Journal of aircraft*, vol. 45, no. 2, pp. 581–590, 2008.
- [35] T. Zill, D. Böhnke, and B. Nagel, “Preliminary aircraft design in a collaborative multidisciplinary design environment,” in *11th AIAA Aviation Technology, Integration, and Operations (ATIO) Conference, including the AIAA Balloon Systems Conference and 19th AIAA Lighter-Than*, 2011, p. 6959.

- [36] A. Gharbi, D. Sarojini, E. Kallou, D. J. Harper, V. Petitgenet, D. Rancourt, S. I. Briceno, and D. N. Mavris, “A single digital thread approach to aircraft detailed design,” in *55th AIAA Aerospace Sciences Meeting*, 2017, p. 0693.
- [37] G. J. Burley and A. R. Mills, “The development of automated processes for the manufacture of cost-effective composite wing-boxes,” SAE Technical Paper, Tech. Rep., 1998.
- [38] G. Moors, C. Kassapoglou, S. F. M. de Almeida, and C. A. E. Ferreira, “Weight trades in the design of a composite wing box: Effect of various design choices,” *CEAS Aeronautical Journal*, vol. 10, no. 2, pp. 403–417, 2019.
- [39] C. Libove and R. E. Hubka, “Elastic constants for corrugated-core sandwich plates,” 1951.
- [40] J. M. Hedgepeth and D. B. Hall, “Stability of stiffened cylinders.,” *AIAA Journal*, vol. 3, no. 12, pp. 2275–2286, 1965.
- [41] C. Collier, P. Yarrington, and M Pickenheim, “Analysis and optimization of the grid-stiffened family of panel concepts “,” *Collier Research Corporation*, 2000.
- [42] C. Collier, P. Yarrington, and B. Van West, “Composite, grid-stiffened panel design for post buckling using hypersizer,” in *43rd AIAA/ASME/ASCE/AHS/ASC Structures, Structural Dynamics, and Materials Conference*, 2002, p. 1222.
- [43] W. Yu, “A unified theory for constitutive modeling of composites,” *Journal of Mechanics of Materials and Structures*, vol. 11, no. 4, pp. 379–411, 2016.
- [44] G. Goron, R. Duca, D. Sarojini, S. Shah, I. Chakraborty, S. I. Briceno, and D. N. Mavris, “A simulation-based framework for structural loads assessment during dynamic maneuvers,” in *17th AIAA Aviation Technology, Integration, and Operations Conference*, 2017, p. 3767.
- [45] R. Duca, D. Sarojini, S. Bloemer, I. Chakraborty, S. I. Briceno, and D. N. Mavris, “Effects of epistemic uncertainty on empennage loads during dynamic maneuvers,” in *2018 AIAA Aerospace Sciences Meeting*, 2018, p. 0767.
- [46] D. Sarojini, R. Duca, H. D. Solano, I. Chakraborty, S. I. Briceno, and D. N. Mavris, “Framework to assess effects of structural flexibility on dynamic loads developed in maneuvering aircraft,” in *2018 Aviation Technology, Integration, and Operations Conference*, 2018, p. 4147.
- [47] N. Nguyen, “Integrated flight dynamic modeling of flexible aircraft with inertial force-propulsion-aeroelastic coupling,” in *46th AIAA Aerospace Sciences Meeting and Exhibit*, 2008, p. 194.

- [48] N. Nguyen and I. Tuzcu, "Flight dynamics of flexible aircraft with aeroelastic and inertial force interactions," in *AIAA Atmospheric Flight Mechanics Conference*, 2009, p. 6045.
- [49] N. T. Nguyen, E. Ting, D. Y. Nguyen, and K. V. Trinh, "Flutter analysis of mission-adaptive wing with variable camber continuous trailing edge flap," in *55th AIAA/ASME/ASCE/AHS/SC Structures, Structural Dynamics, and Materials Conference*, 2014, p. 0839.
- [50] E. Ting, N. T. Nguyen, and K. V. Trinh, "Static aeroelastic and longitudinal trim model of flexible wing aircraft using finite-element vortex-lattice coupled solution," in *55th AIAA/ASME/ASCE/AHS/SC Structures, Structural Dynamics, and Materials Conference*, 2014, p. 0837.
- [51] M. Drela, "Method for simultaneous wing aerodynamic and structural load prediction," *Journal of aircraft*, vol. 27, no. 8, pp. 692–699, 1990.
- [52] M. R. Robert, *Theory and analysis of flight structures*, 1969.
- [53] M. Drela, "Integrated simulation model for preliminary aerodynamic, structural, and control-law design of aircraft," in *40th Structures, Structural Dynamics, and Materials Conference and Exhibit*, 1999, p. 1394.
- [54] P. J. Minguet, "Static and dynamic behavior of composite helicopter rotor blades under large deflections," PhD thesis, Massachusetts Institute of Technology, 1989.
- [55] M. Patil, D. Hodges, and C. Cesnik, "Nonlinear aeroelastic analysis of aircraft with high-aspect-ratio wings," in *39th AIAA/ASME/ASCE/AHS/ASC Structures, Structural Dynamics, and Materials Conference and Exhibit*, 1998, p. 1955.
- [56] M. J. Patil, *Nonlinear aeroelastic analysis, flight dynamics, and control of a complete aircraft*. Citeseer, 1999.
- [57] D. A. Peters and M. J. Johnson, "Finite-state airloads for deformable airfoils on fixed and rotating wings," *Asme-Publications-AD*, vol. 44, pp. 1–1, 1994.
- [58] D. Peters, D Barwey, and M. Johnson, "Finite-state airloads modeling with compressibility and unsteady free-stream," in *Proceedings of the Sixth International Workshop on Dynamics and Aeroelastic Stability Modeling of Rotorcraft Systems*, 1995, pp. 8–10.
- [59] D. A. Peters, S. Karunamoorthy, and W.-M. Cao, "Finite state induced flow models part i: Two-dimensional thin airfoil," *Journal of Aircraft*, vol. 32, no. 2, pp. 313–322, 1995.

- [60] M. J. Patil, D. H. Hodges, and C. E. S. Cesnik, “Nonlinear aeroelastic analysis of complete aircraft in subsonic flow,” *Journal of Aircraft*, vol. 37, no. 5, pp. 753–760, 2000.
- [61] ———, “Nonlinear aeroelasticity and flight dynamics of high-altitude long-endurance aircraft,” *Journal of Aircraft*, vol. 38, no. 1, pp. 88–94, 2001.
- [62] C.-S. Chang, D. H. Hodges, and M. J. Patil, “Flight dynamics of highly flexible aircraft,” *Journal of Aircraft*, vol. 45, no. 2, pp. 538–545, 2008.
- [63] R. D. Milne, *Dynamics of the deformable aeroplane*. HM Stationery Office, 1964.
- [64] R. Milne, “Some remarks on the dynamics of deformable bodies.,” *AIAA Journal*, vol. 6, no. 3, pp. 556–558, 1968.
- [65] C. M. Shearer and C. E. Cesnik, “Nonlinear flight dynamics of very flexible aircraft,” *Journal of Aircraft*, vol. 44, no. 5, pp. 1528–1545, 2007.
- [66] B. Raghavan, “Flight dynamics and control of highly flexible flying-wings,” PhD thesis, Virginia Tech, 2009.
- [67] J. Murua, R. Palacios, and J. M. R. Graham, “Applications of the unsteady vortex-lattice method in aircraft aeroelasticity and flight dynamics,” *Progress in Aerospace Sciences*, vol. 55, pp. 46–72, 2012.
- [68] I. Tuzcu, “Dynamics and control of flexible aircraft,” PhD thesis, Virginia Tech, 2001.
- [69] L. Meirovitch and I. Tuzcu, “Time simulations of the response of maneuvering flexible aircraft,” *Journal of guidance, control, and dynamics*, vol. 27, no. 5, pp. 814–828, 2004.
- [70] ———, “Unified theory for the dynamics and control of maneuvering flexible aircraft,” *AIAA journal*, vol. 42, no. 4, pp. 714–727, 2004.
- [71] I. Tuzcu and L. Meirovitch, “Effects of flexibility on the stability of flying aircraft,” *Journal of dynamic systems, measurement, and control*, vol. 127, no. 1, pp. 41–49, 2005.
- [72] L. Meirovitch and I. Tuzcu, “Control of flexible aircraft executing time-dependent maneuvers,” *Journal of guidance, control, and dynamics*, vol. 28, no. 6, pp. 1291–1300, 2005.
- [73] ———, “The lure of the mean axes,” *Journal of Applied Mechanics*, vol. 74, no. 3, pp. 497–504, 2007.

- [74] A. B. Guimarães Neto, R. G. Silva, P. Paglione, and F. J. Silvestre, “Formulation of the flight dynamics of flexible aircraft using general body axes,” *AIAA Journal*, pp. 3516–3534, 2016.
- [75] P. Hajela and J. L. Chen, “Preliminary weight estimation of conventional and joined wings using equivalent beam models,” *Journal of Aircraft*, vol. 25, no. 6, pp. 574–576, 1988.
- [76] F. H. Gern, A. H. Naghshineh-Pour, E. Sulaeman, R. K. Kapania, and R. T. Haftka, “Structural wing sizing for multidisciplinary design optimization of a strut-braced wing,” *Journal of aircraft*, vol. 38, no. 1, pp. 154–163, 2001.
- [77] G Bindolino, G Ghiringhelli, S Ricci, and M Terraneo, “Multilevel structural optimization for preliminary wing-box weight estimation,” *Journal of Aircraft*, vol. 47, no. 2, pp. 475–489, 2010.
- [78] P. Piperni, M. Abdo, and F. Fafyeke, “The application of multi-disciplinary optimization technologies to the design of a business jet,” in *10th AIAA/ISSMO Multidisciplinary Analysis and Optimization Conference*, 2004, p. 4370.
- [79] M. S. A. Elsayed, R. Sedaghati, and M. Abdo, “Accurate stick model development for static analysis of complex aircraft wing-box structures,” *AIAA journal*, vol. 47, no. 9, pp. 2063–2075, 2009.
- [80] R. Palacios, Y. Wang, A. Wynn, and M. Karpel, “Condensation of large finite-element models for wing load analysis with geometrically-nonlinear effects,” 2013.
- [81] R. J. Guyan, “Reduction of stiffness and mass matrices,” *AIAA journal*, vol. 3, no. 2, pp. 380–380, 1965.
- [82] R. CIRILLO, “Detailed and condensed finite element models for dynamic analysis of a business jet aircraft,” 2011.
- [83] W. C. Hurty, “Dynamic analysis of structural systems using component modes,” *AIAA journal*, vol. 3, no. 4, pp. 678–685, 1965.
- [84] M. R. Waszak and D. K. Schmidt, “Flight dynamics of aeroelastic vehicles,” *Journal of Aircraft*, vol. 25, no. 6, pp. 563–571, 1988.
- [85] M. C. Van Schoor and A. H. von Flotow, “Aeroelastic characteristics of a highly flexible aircraft,” *Journal of Aircraft*, vol. 27, no. 10, pp. 901–908, 1990.
- [86] D. K. Schmidt and D. L. Raney, “Modeling and simulation of flexible flight vehicles,” *Journal of Guidance, Control, and Dynamics*, vol. 24, no. 3, pp. 539–546, 2001.

- [87] J. Pedro and C. G. Bigg, “Development of a flexible embedded aircraft/control system simulation facility,” in *Proceedings of the AIAA Modeling and Simulation Technologies, Conference and Exhibit, San Francisco, CA, USA, 2005*, pp. 1–25.
- [88] M. Karpel, “Reduced-order models for integrated aeroservoelastic optimization,” *Journal of Aircraft*, vol. 36, no. 1, pp. 146–155, 1999.
- [89] M. Karpel, B. Moulin, and P. Chen, “Dynamic response of aeroservoelastic systems to gust excitation,” *Journal of Aircraft*, vol. 42, no. 5, pp. 1264–1272, 2005.
- [90] B. Moulin and M. Karpel, “Gust loads alleviation using special control surfaces,” *Journal of Aircraft*, vol. 44, no. 1, pp. 17–25, 2007.
- [91] F. Saltari, C. Riso, G. D. Matteis, and F. Mastroddi, “Finite-element-based modeling for flight dynamics and aeroelasticity of flexible aircraft,” *Journal of Aircraft*, vol. 54, no. 6, pp. 2350–2366, 2017.
- [92] R. R. Medeiros, C. E. Cesnik, and E. B. Coetzee, “Computational aeroelasticity using modal-based structural nonlinear analysis,” *AIAA Journal*, vol. 58, no. 1, pp. 362–371, 2020.
- [93] P. Geuzaine, G. Brown, C. Harris, and C. Farhat, “Aeroelastic dynamic analysis of a full f-16 configuration for various flight conditions,” *AIAA journal*, vol. 41, no. 3, pp. 363–371, 2003.
- [94] R. Palacios and C. Cesnik, “Static nonlinear aeroelasticity of flexible slender wings in compressible flow,” in *46th AIAA/ASME/ASCE/AHS/ASC Structures, Structural Dynamics and Materials Conference*, 2005, p. 1945.
- [95] C. E. Cesnik and D. H. Hodges, “Vabs: A new concept for composite rotor blade cross-sectional modeling,” *Journal of the American helicopter society*, vol. 42, no. 1, pp. 27–38, 1997.
- [96] J. A. Garcia, “Numerical investigation of nonlinear aeroelastic effects on flexible high-aspect-ratio wings,” *Journal of Aircraft*, vol. 42, no. 4, pp. 1025–1036, 2005.
- [97] D. E. Raveh, Y. Levy, and M. Karpel, “Efficient aeroelastic analysis using computational unsteady aerodynamics,” *Journal of Aircraft*, vol. 38, no. 3, pp. 547–556, 2001.
- [98] ———, “Structural optimization using computational aerodynamics,” *AIAA journal*, vol. 38, no. 10, pp. 1974–1982, 2000.

- [99] K. Jacobson, J. F. Kiviaho, M. J. Smith, and G. Kennedy, “An aeroelastic coupling framework for time-accurate analysis and optimization,” in *2018 AIAA/ASCE/AHS/ASC Structures, Structural Dynamics, and Materials Conference*, 2018, p. 0100.
- [100] T. L. Lomax, *Structural loads analysis for commercial transport aircraft: theory and practice*. American Institute of Aeronautics and Astronautics, 1996.
- [101] Y.-I. Kim and G.-J. Park, “Nonlinear dynamic response structural optimization using equivalent static loads,” *Computer Methods in Applied Mechanics and Engineering*, vol. 199, no. 9-12, pp. 660–676, 2010.
- [102] H. Lee, Y. Kim, G. Park, R. Kolonay, M. Blair, and R. A. Canfield, “Structural optimization of a joined wing using equivalent static loads,” *Journal of aircraft*, vol. 44, no. 4, pp. 1302–1308, 2007.
- [103] B.-S. Kang, G.-J. Park, and J. S. Arora, “A review of optimization of structures subjected to transient loads,” *Structural and Multidisciplinary Optimization*, vol. 31, no. 2, pp. 81–95, 2006.
- [104] B.-S. Kang, G. Park, and J. Arora, “Optimization of flexible multibody dynamic systems using the equivalent static load method,” *AIAA journal*, vol. 43, no. 4, pp. 846–852, 2005.
- [105] G.-J. Park, “Technical overview of the equivalent static loads method for non-linear static response structural optimization,” *Structural and Multidisciplinary Optimization*, vol. 43, no. 3, pp. 319–337, 2011.
- [106] E. Hong, B. You, C. Kim, and G. Park, “Optimization of flexible components of multibody systems via equivalent static loads,” *Structural and Multidisciplinary Optimization*, vol. 40, no. 1-6, pp. 549–562, 2010.
- [107] T. H. G. Megson, *Aircraft structures for engineering students*. Elsevier, 2012.
- [108] D. J. Peery, *Aircraft structures*. Courier Corporation, 2011.
- [109] J. T. Lusk, “Wing and fuselage optimization considering alternative material,” PhD thesis, University of Kansas, 2008.
- [110] C. Niu, *Airframe structural design: practical design information and data on aircraft structures*. Conmilit Press Limited Hong Kong, 1999.
- [111] D. L. Miskin and T. T. Takahashi, “Stochastic modeling of preliminary wing box structural design for stiffness,” in *2018 Aviation Technology, Integration, and Operations Conference*, 2018, p. 4002.

- [112] T. T. Takahashi and T. Lemonds, “Transport category wing weight estimation using a optimizing beam-element structural formulation,” in *53rd AIAA Aerospace Sciences Meeting*, 2015, p. 1898.
- [113] S. Altus and I. Kroo, “Concurrent wing design and flight-path optimization using optimizer-based decomposition,” in *7th AIAA/USAF/NASA/ISSMO Symposium on Multidisciplinary Analysis and Optimization*, 1998, p. 4920.
- [114] A. Ning and I. Kroo, “Tip extensions, winglets, and c-wings: Conceptual design and optimization,” in *26th AIAA Applied Aerodynamics Conference*, 2008, p. 7052.
- [115] —, “Multidisciplinary considerations in the design of wings and wing tip devices,” *Journal of Aircraft*, vol. 47, no. 2, pp. 534–543, 2010.
- [116] J. Xu and I. Kroo, “Aircraft design with active load alleviation and natural laminar flow,” *Journal of Aircraft*, vol. 51, no. 5, pp. 1532–1545, 2014.
- [117] A Elham, G La Rocca, and M. Van Tooren, “Development and implementation of an advanced, design-sensitive method for wing weight estimation,” *Aerospace Science and Technology*, vol. 29, no. 1, pp. 100–113, 2013.
- [118] P. Hajela, “Reduced complexity structural modeling for automated airframe synthesis,” 1987.
- [119] G. L. Giles, “Equivalent plate analysis of aircraft wing box structures with general planform geometry,” *Journal of Aircraft*, vol. 23, no. 11, pp. 859–864, 1986.
- [120] —, “Further generalization of an equivalent plate representation for aircraft structural analysis,” *Journal of Aircraft*, vol. 26, no. 1, pp. 67–74, 1989.
- [121] T. Krishnamurthy and B. Mason, “Equivalent plate analysis of aircraft wing with discrete source damage,” in *47th AIAA/ASME/ASCE/AHS/ASC Structures, Structural Dynamics, and Materials Conference 14th AIAA/ASME/AHS Adaptive Structures Conference 7th*, 2006, p. 2218.
- [122] E. Riks, “Buckling and post-buckling analysis of stiffened panels in wing box structures,” *International journal of solids and structures*, vol. 37, no. 46, pp. 6795–6824, 2000.
- [123] M. G. Sexstone, “Aircraft structural mass property prediction using conceptual-level structural analysis,” 1998.
- [124] R. Ajaj, M. Friswell, D Smith, and A. Isikveren, “A conceptual wing-box weight estimation model for transport aircraft,” *The Aeronautical Journal*, vol. 117, no. 1191, pp. 533–551, 2013.

- [125] D. H. Hodges, *Nonlinear composite beam theory*. American Institute of Aeronautics and Astronautics, 2006.
- [126] N. Buannic and P. Cartraud, “Higher-order effective modeling of periodic heterogeneous beams. asymptotic expansion method,” *International Journal of Solids and Structures*, vol. 38, no. 40-41, pp. 7139–7161, 2001.
- [127] ———, “Higher-order effective modeling of periodic heterogeneous beams. derivation of the proper boundary conditions for the interior asymptotic solution,” *International Journal of Solids and Structures*, vol. 38, no. 40-41, pp. 7163–7180, 2001.
- [128] J.-S. Kim and K. Wang, “Vibration analysis of composite beams with end effects via the formal asymptotic method,” *Journal of Vibration and Acoustics*, vol. 132, no. 4, p. 041 003, 2010.
- [129] A. Rajagopal and D. H. Hodges, “Asymptotic approach to oblique cross-sectional analysis of beams,” *Journal of Applied Mechanics*, vol. 81, no. 3, 2014.
- [130] H. Chen, W. Yu, and M. Capellaro, “A critical assessment of computer tools for calculating composite wind turbine blade properties,” *Wind Energy*, vol. 13, no. 6, pp. 497–516, 2010.
- [131] M. Gupta and D. H. Hodges, “Modeling thin-walled beams using vam,” in *58th AIAA/ASCE/AHS/ASC Structures, Structural Dynamics, and Materials Conference*, 2017, p. 1832.
- [132] W. Yu, D. H. Hodges, and J. C. Ho, “Variational asymptotic beam sectional analysis—an updated version,” *International Journal of Engineering Science*, vol. 59, pp. 40–64, 2012.
- [133] W. Yu and M. Blair, “Gebt: A general-purpose nonlinear analysis tool for composite beams,” *Composite Structures*, vol. 94, no. 9, pp. 2677–2689, 2012.
- [134] X. Liu, K. Rouf, B. Peng, and W. Yu, “Two-step homogenization of textile composites using mechanics of structure genome,” *Composite Structures*, vol. 171, pp. 252–262, 2017.
- [135] K. Rouf, X. Liu, and W. Yu, “Multiscale structural analysis of textile composites using mechanics of structure genome,” *International Journal of Solids and Structures*, vol. 136, pp. 89–102, 2018.
- [136] N. Liu and W. Yu, “Evaluation of smeared properties approaches and mechanics of structure genome for analyzing composite beams,” *Mechanics of Advanced Materials and Structures*, vol. 25, no. 14, pp. 1171–1185, 2018.

- [137] J. Ku, V. Volovoi, and D. Hodges, “Multilevel-multiphase optimization of composite rotor blade with surrogate model,” in *48th AIAA/ASME/ASCE/AHS/ASC Structures, Structural Dynamics, and Materials Conference*, 2007, p. 1900.
- [138] L. Li, V. V. Volovoi, and D. H. Hodges, “Cross-sectional design of composite rotor blades,” *Journal of the American Helicopter Society*, vol. 53, no. 3, pp. 240–251, 2008.
- [139] D. Hodges and W Yu, “A rigorous, engineer-friendly approach for modelling realistic, composite rotor blades,” *Wind Energy: An International Journal for Progress and Applications in Wind Power Conversion Technology*, vol. 10, no. 2, pp. 179–193, 2007.
- [140] P. W. Richards, D. T. Griffith, and D. H. Hodges, “High-fidelity modeling of local effects of damage for derated offshore wind turbines,” in *Journal of Physics: Conference Series*, IOP Publishing, vol. 524, 2014, p. 012 036.
- [141] D. Lee, D. H. Hodges, and M. J. Patil, “Multi-flexible-body dynamic analysis of horizontal axis wind turbines,” *Wind Energy: An International Journal for Progress and Applications in Wind Power Conversion Technology*, vol. 5, no. 4, pp. 281–300, 2002.
- [142] C. E. Cesnik, P. J. Senatore, W. Su, E. M. Atkins, and C. M. Shearer, “X-hale: A very flexible unmanned aerial vehicle for nonlinear aeroelastic tests,” *AIAA journal*, vol. 50, no. 12, pp. 2820–2833, 2012.
- [143] E Carrera, G Giunta, P Nali, and M Petrolo, “Refined beam elements with arbitrary cross-section geometries,” *Computers & structures*, vol. 88, no. 5-6, pp. 283–293, 2010.
- [144] E. Carrera, A. Pagani, and M. Petrolo, “Classical, refined, and component-wise analysis of reinforced-shell wing structures,” *AIAA Journal*, vol. 51, no. 5, pp. 1255–1268, 2013.
- [145] A. Pagani, “Component-wise models for static, dynamic and aeroelastic analyses of metallic and composite aerospace structures,” PhD thesis, Ph. D Thesis, 2015.
- [146] A Pagani, M Petrolo, G Colonna, and E Carrera, “Dynamic response of aerospace structures by means of refined beam theories,” *Aerospace Science and Technology*, vol. 46, pp. 360–373, 2015.
- [147] E Carrera and V. Zozulya, “Carrera unified formulation (cuf) for the micropolar beams: Analytical solutions,” *Mechanics of Advanced Materials and Structures*, pp. 1–25, 2019.

- [148] ———, “Carrera unified formulation (cuf) for the micropolar plates and shells. i. higher order theory,” *Mechanics of Advanced Materials and Structures*, pp. 1–23, 2020.
- [149] ———, “Carrera unified formulation (cuf) for the micropolar plates and shells. ii. complete linear expansion case,” *Mechanics of Advanced Materials and Structures*, pp. 1–20, 2020.
- [150] J. P. A. A. Blasques, “User’s manual for becas: A cross section analysis tool for anisotropic and inhomogeneous beam sections of arbitrary geometry,” 2012.
- [151] D. H. Hodges, “A mixed variational formulation based on exact intrinsic equations for dynamics of moving beams,” *International journal of solids and structures*, vol. 26, no. 11, pp. 1253–1273, 1990.
- [152] G. Failla and A. Santini, “On euler–bernoulli discontinuous beam solutions via uniform-beam green’s functions,” *International Journal of Solids and Structures*, vol. 44, no. 22-23, pp. 7666–7687, 2007.
- [153] G. Falsone, “The use of generalised functions in the discontinuous beam bending differential equations,” *International Journal of Engineering Education*, vol. 18, no. 3, pp. 337–343, 2002.
- [154] G. Failla and N. Impollonia, “General finite element description for non-uniform and discontinuous beam elements,” *Archive of Applied Mechanics*, vol. 82, no. 1, pp. 43–67, 2012.
- [155] W. Huang* and X. Gao, “Tresca and von mises yield criteria: A view from strain space,” *Philosophical magazine letters*, vol. 84, no. 10, pp. 625–629, 2004.
- [156] L. A. Carlsson and G. A. Kardomateas, *Structural and failure mechanics of sandwich composites*. Springer Science & Business Media, 2011, vol. 121.
- [157] R. Talreja and C. V. Singh, *Damage and failure of composite materials*. Cambridge University Press, 2012.
- [158] L. Cavagna, S. Ricci, and L. Riccobene, “A fast tool for structural sizing, aeroelastic analysis and optimization in aircraft conceptual design,” in *50th AIAA/ASME/ASCE/AHS/ASC Structures, Structural Dynamics, and Materials Conference 17th AIAA/ASME/AHS Adaptive Structures Conference 11th AIAA No*, 2009, p. 2571.
- [159] L. Cavagna, S. Ricci, and L. Travaglini, “Neocass: An integrated tool for structural sizing, aeroelastic analysis and mdo at conceptual design level,” *Progress in Aerospace Sciences*, vol. 47, no. 8, pp. 621–635, 2011.

- [160] P Piperni, M Abdo, and F Kafyeke, “The development of a multi-disciplinary wing design method,” SAE Technical Paper, Tech. Rep., 2003.
- [161] P. Piperni, M. Abdo, F. Kafyeke, and A. T. Isikveren, “Preliminary aerostructural optimization of a large business jet,” *Journal of Aircraft*, vol. 44, no. 5, pp. 1422–1438, 2007.
- [162] A. DeBlois and M. Abdo, “Multi-fidelity multidisciplinary design optimization of metallic and composite regional and business jets,” in *13th AIAA/ISSMO Multidisciplinary Analysis Optimization Conference*, 2011, p. 9191.
- [163] M Abdo, P Piperni, and F Kafyeke, “Conceptual design of stringer stiffened compression panels,” in *Proceedings of The Canadian aeronautics and space institute 50 AGM and conference*, 2003, pp. 28–30.
- [164] K. Maute, M. Nikbay, and C. Farhat, “Coupled analytical sensitivity analysis and optimization of three-dimensional nonlinear aeroelastic systems,” *AIAA journal*, vol. 39, no. 11, pp. 2051–2061, 2001.
- [165] G. J. Kennedy, “Aerostructural analysis and design optimization of composite aircraft,” PhD thesis, University of Toronto, 2012.
- [166] G. K. W. Kenway, G. J. Kennedy, and J. R. R. A. Martins, “Scalable parallel approach for high-fidelity steady-state aeroelastic analysis and adjoint derivative computations,” *AIAA Journal*, vol. 52, pp. 935–951, Jan. 1, 2014, published.
- [167] G. J. Kennedy, J. R. R. A. Martins, and J. S. Hansen, “Aerostructural optimization of aircraft structures using asymmetric subspace optimization,” in *12th AIAA/ISSMO Multidisciplinary Analysis and Optimization Conference, Victoria, BC*, AIAA-2008-5847, AIAA, Jan. 1, 2008, published.
- [168] G. J. Kennedy and J. R. R. A. Martins, “Parallel solution methods for aerostructural analysis and design optimization,” in *Proceedings of the 13th AIAA/ISSMO Multidisciplinary Analysis Optimization Conference*, AIAA 2010-9308, Fort Worth, TX, Jan. 1, 2010, published.
- [169] ———, “Aerostructural design optimization of composite aircraft with stress and local buckling constraints using an implicit structural parametrization,” in *Proceedings of CASI AERO 2011*, Montreal, Quebec, Jan. 1, 2011, published.
- [170] G. K. W. Kenway, G. J. Kennedy, and J. R. R. A. Martins, “A scalable parallel approach for high-fidelity aerostructural analysis and optimization,” in *53rd AIAA/ASME/ASCE/AHS/ASC Structures, Structural Dynamics, and Materials Conference*, AIAA-2012-1922, Honolulu, HI, Jan. 1, 2012, published.

- [171] G. J. Kennedy and J. R. R. A. Martins, “An adjoint-based derivative evaluation method for time-dependent aeroelastic optimization of flexible aircraft,” in *Proceedings of the 54th AIAA/ASME/ASCE/AHS/ASC Structures, Structural Dynamics, and Materials Conference*, Boston, MA, Jan. 1, 2013, published.
- [172] J. Hwang and J. Martins, “Geomach: Geometry-centric mdao of aircraft configurations with high fidelity,” in *12th AIAA Aviation Technology, Integration, and Operations (ATIO) Conference and 14th AIAA/ISSMO Multidisciplinary Analysis and Optimization Conference*, 2012, p. 5605.
- [173] J. R. Martins and J. T. Hwang, “Review and unification of methods for computing derivatives of multidisciplinary computational models,” *AIAA journal*, vol. 51, no. 11, pp. 2582–2599, 2013.
- [174] J. R. Martins and A. B. Lambe, “Multidisciplinary design optimization: A survey of architectures,” *AIAA journal*, vol. 51, no. 9, pp. 2049–2075, 2013.
- [175] J. P. Jasa, J. T. Hwang, and J. R. Martins, “Open-source coupled aerostructural optimization using python,” *Structural and Multidisciplinary Optimization*, vol. 57, no. 4, pp. 1815–1827, 2018.
- [176] S. S. Chauhan and J. R. R. A. Martins, “Low-fidelity aerostructural optimization of aircraft wings with a simplified wingbox model using OpenAeroStruct,” in *Proceedings of the 6th International Conference on Engineering Optimization, EngOpt 2018*, Lisbon, Portugal: Springer, 2018, pp. 418–431.
- [177] A. B. Lambe, G. J. Kennedy, and J. R. Martins, “An evaluation of constraint aggregation strategies for wing box mass minimization,” *Structural and Multidisciplinary Optimization*, vol. 55, no. 1, pp. 257–277, 2017.
- [178] N. M. Poon and J. R. Martins, “An adaptive approach to constraint aggregation using adjoint sensitivity analysis,” *Structural and Multidisciplinary Optimization*, vol. 34, no. 1, pp. 61–73, 2007.
- [179] J. Martins and N. M. Poon, “On structural optimization using constraint aggregation,” in *VI World Congress on Structural and Multidisciplinary Optimization WCSMO6, Rio de Janeiro, Brasil*, Citeseer, 2005.
- [180] G. J. Kennedy and J. E. Hicken, “Improved constraint-aggregation methods,” *Computer Methods in Applied Mechanics and Engineering*, vol. 289, pp. 332–354, 2015.
- [181] K. Boopathy and G. Kennedy, “Adjoint-based derivative evaluation methods for flexible multibody systems with rotorcraft applications,” in *55th AIAA Aerospace Sciences Meeting*, 2017, p. 1671.

- [182] K. Boopathy and G. J. Kennedy, “Parallel finite element framework for rotorcraft multibody dynamics and discrete adjoint sensitivities,” *AIAA Journal*, vol. 57, no. 8, pp. 3159–3172, 2019.
- [183] A. M. Bradley, “Pde-constrained optimization and the adjoint method,” Technical Report. Stanford University. <https://cs.stanford.edu/~ambrad...>, Tech. Rep., 2013.
- [184] S. G. Johnson, “Notes on adjoint methods for 18.335,” *Introduction to Numerical Methods*, 2006.
- [185] M. Gupta, D. Sarojini, A. Shah, and D. H. Hodges, “Beam theory for asymptotic analysis of aperiodic and inhomogeneous structures,” *AIAA Journal*, vol. 57, no. 10, pp. 4155–4168, 2019.
- [186] D. Sarojini, M. Gupta, D. H. Hodges, and D. N. Mavris, “An efficient method to dimensionally reduce aperiodic inhomogeneous 3-d structures to 1-d beam-like structures,” in *AIAA Scitech 2020 Forum*, 2020, p. 0272.
- [187] C. Collier, “Stiffness, thermal expansion, and thermal bending formulation of stiffened, fiber-reinforced composite panels,” in *34th Structures, Structural Dynamics and Materials Conference*, 1993, p. 1569.
- [188] J. A. Corman, N. Weston, C. Friedland, D. N. Mavris, and T. W. Laughlin, “A parametric multi-fidelity approach to conceptual airframe design,” in *2018 AIAA Modeling and Simulation Technologies Conference*, 2018, p. 1930.
- [189] M. Gupta, “Enhancements in analysis of beam-like structures using asymptotic methods,” PhD thesis, Georgia Institute of Technology, 2019.
- [190] J. Andersson, J. Åkesson, and M. Diehl, “Casadi: A symbolic package for automatic differentiation and optimal control,” in *Recent advances in algorithmic differentiation*, Springer, 2012, pp. 297–307.
- [191] W. Yu, “Vabs manual for users,” *Logan, Utah: Utah State University*, 2011.
- [192] O. Stodieck, J. E. Cooper, and P. Weaver, “Interpretation of bending/torsion coupling for swept, nonhomogenous wings,” *Journal of Aircraft*, vol. 53, no. 4, pp. 892–899, 2016.
- [193] M. J. Patil, D. H. Hodges, and C. E. Cesnik, “Characterizing the effects of geometrical nonlinearities on aeroelastic behavior of high-aspect ratio wings,” in *NASA Conference Publication*, NASA, 1999, pp. 501–510.

- [194] D. Sarojini, D. Rajaram, D. Solano, and D. N. Mavris, “Adjoint-based structural optimization for beam-like structures subjected to dynamic loads,” in *AIAA Scitech 2020 Forum*, 2020, p. 0273.
- [195] J. Currie, D. I. Wilson, N. Sahinidis, and J. Pinto, “Opti: Lowering the barrier between open source optimizers and the industrial matlab user,” *Foundations of computer-aided process operations*, vol. 24, p. 32, 2012.
- [196] T. A. Guimarães, S. G. Castro, C. E. Cesnik, and D. A. Rade, “Supersonic flutter and buckling optimization of tow-steered composite plates,” *AIAA Journal*, vol. 57, no. 1, pp. 397–407, 2019.
- [197] J. F. Kiviaho, K. E. Jacobson, and G. J. Kennedy, “Flutter boundary identification from time-domain simulations using the matrix pencil method,” *AIAA Journal*, vol. 57, no. 8, pp. 3639–3645, 2019.
- [198] K. E. Jacobson, J. F. Kiviaho, G. J. Kennedy, and M. J. Smith, “Evaluation of time-domain damping identification methods for flutter-constrained optimization,” *Journal of Fluids and Structures*, vol. 87, pp. 174–188, 2019.
- [199] E. Jonsson, C. Riso, C. A. Lupp, C. E. Cesnik, J. R. Martins, and B. I. Epureanu, “Flutter and post-flutter constraints in aircraft design optimization,” *Progress in Aerospace Sciences*, vol. 109, p. 100537, 2019.
- [200] C. A. Lupp, C. Cesnik, P. Beran, J. Deaton, and D. Easterling, “Including geometrically nonlinear flutter constraints in high fidelity aircraft optimization,” in *International Forum on Aeroelasticity and Structural Dynamics (IFASD 2019)*, 2019.
- [201] C. A. Lupp and C. E. Cesnik, “A gradient-based flutter constraint including geometrically nonlinear deformations,” in *AIAA Scitech 2019 Forum*, 2019, p. 1212.
- [202] C. Riso, D. Sanghi, C. E. Cesnik, F. Vetrano, and P. Teufel, “Parametric roll maneuverability analysis of a high-aspect-ratio-wing civil transport aircraft,” in *AIAA Scitech 2020 Forum*, 2020, p. 1191.
- [203] C. Audet, J. Denni, D. Moore, A. Booker, and P. Frank, “A surrogate-model-based method for constrained optimization,” in *8th symposium on multidisciplinary analysis and optimization*, 2000, p. 4891.
- [204] A. I. Forrester and A. J. Keane, “Recent advances in surrogate-based optimization,” *Progress in Aerospace Sciences*, vol. 45, no. 1-3, pp. 50–79, 2009. arXiv: 11106.2697.

- [205] N. V. Queipo, R. T. Haftka, W. Shyy, T. Goel, R. Vaidyanathan, and P. Kevin Tucker, “Surrogate-based analysis and optimization,” *Progress in Aerospace Sciences*, vol. 41, no. 1, pp. 1–28, 2005. arXiv: [arXiv:1011.1669v3](https://arxiv.org/abs/1011.1669v3).
- [206] R. Yondo, E. Andrés, and E. Valero, “A review on design of experiments and surrogate models in aircraft real-time and many-query aerodynamic analyses,” *Progress in Aerospace Sciences*, vol. 96, no. November 2017, pp. 23–61, 2018.
- [207] A. Bhosekar and M. Ierapetritou, “Advances in surrogate based modeling, feasibility analysis, and optimization: A review,” *Computers & Chemical Engineering*, vol. 108, pp. 250–267, 2018.
- [208] D. J. Lucia, P. S. Beran, and W. A. Silva, “Reduced-order modeling: New approaches for computational physics,” *Progress in aerospace sciences*, vol. 40, no. 1-2, pp. 51–117, 2004.
- [209] D. Rajaram, T. G. Puranik, S. Ashwin Renganathan, W. Sung, O. P. Fischer, D. N. Mavris, and A. Ramamurthy, “Empirical assessment of deep gaussian process surrogate models for engineering problems,” *Journal of Aircraft*, pp. 1–15, 2020.
- [210] D. Rajaram, C. Perron, T. G. Puranik, and D. N. Mavris, “Randomized algorithms for non-intrusive parametric reduced order modeling,” *AIAA Journal*, vol. 58, no. 12, pp. 5389–5407, 2020.
- [211] B. Peherstorfer, K. Willcox, and M. Gunzburger, “Survey of Multifidelity Methods in Uncertainty Propagation, Inference, and Optimization,” *SIAM Review*, vol. 60, no. 3, pp. 550–591, 2018. arXiv: [1806.10761](https://arxiv.org/abs/1806.10761).
- [212] C. Perron, D. Rajaram, and D. Mavris, “Development of a multi-fidelity reduced-order model based on manifold alignment,” in *AIAA AVIATION 2020 FORUM*, 2020, p. 3124.
- [213] M. Drela, *Aswing 5.99 technical description steady formulation*, 2015.
- [214] ———, *Aswing 5.99 technical description unsteady extension*, 2015.
- [215] J. A. Corman, D. Sarojini, A. Gharbi, and D. N. Mavris, “Estimating jig shape for an aircraft wing determined through aerodynamic shape optimization with rigid body assumptions,” in *AIAA Scitech 2019 Forum*, 2019, p. 0418.
- [216] D. Solano, D. Sarojini, J. A. Corman, and D. N. Mavris, “Structural sizing of unconventional aircraft under static and dynamic aeroelastic loading,” in *AIAA Scitech 2020 Forum*, 2020, p. 0274.

- [217] Q. Wang and W. Yu, “Geometrically nonlinear analysis of composite beams using wiener-milenković parameters,” *Journal of Renewable and Sustainable Energy*, vol. 9, no. 3, p. 033 306, 2017.
- [218] M. Gupta, D. Sarojini, A. Shah, and D. H. Hodges, “Dimensional reduction technique for analysis of aperiodic inhomogeneous structures,” in *2018 AIAA/ASCE/AHS/ASC Structures, Structural Dynamics, and Materials Conference*, 2018, p. 0698.

ACKNOWLEDGEMENT OF PRIOR PUBLICATIONS

This section acknowledges that the research described in dissertation has been previously published in the following papers by the author:

- The complexity of aircraft wingbox structure (Section 2.1) – *A Single Digital Thread Approach to Aircraft Detailed Design* [36]
- Computation of dynamic loads (Section 2.2) – *Framework to Assess Effects of Structural Flexibility on Dynamic Loads Developed in Maneuvering Aircraft* [46], *A Simulation-Based Framework for Structural Loads Assessment during Dynamic Maneuvers* [44], *Effects of Epistemic Uncertainty on Empennage Loads During Dynamic Maneuvers* [45]
- Challenges in stiffness matching (Section 4.1.1) – *Beam Theory for Asymptotic Analysis of Aperiodic and Inhomogeneous Structures* [185, 218]
- Method and results of RQ 1.1 (Section 4.1.2 and Section 4.1.3) – *An Efficient Method to Dimensionally Reduce Aperiodic Inhomogeneous 3-D Structures to 1-D Beam-Like Structures* [186]
- Method and results of RQ 2.1 and RQ 2.2 for solid rectangular beams (Section 4.6.1, Section 4.6.2, and Section 4.7.1) – *Adjoint-Based Structural Optimization for Beam-Like Structures Subjected to Dynamic Loads* [194]

This research is reprinted with permission of the American Institute of Aeronautics and Astronautics.

VITA

Darshan Sarojini is originally from India where he received his Bachelor's degree in Mechanical Engineering in 2014. He worked for a year at Indian Institute of Science where he worked on compliant bistable mechanisms. He joined the Ph.D. program in Aerospace Engineering at Georgia Institute of Technology in 2015. While pursuing the Ph.D. degree, Darshan also completed a Master's in Aerospace Engineering and a Master's in Computational Science and Engineering.

Darshan has been working on a variety of projects focused on scientific computing, specifically multi-disciplinary design optimization, aeroelasticity and loads, surrogate modeling, and reduced order models. He has worked on projects funded by Airbus, NASA, Gulfstream, and Siemens.

Darshan has been an active member of the Leadership Education and Development initiative on campus, and a student representative on the Institute Graduate Curriculum Committee. He has been an active part of the India club at Georgia Tech and helped organize cultural events on campus. His hobbies include hiking, board games, biking, and running.